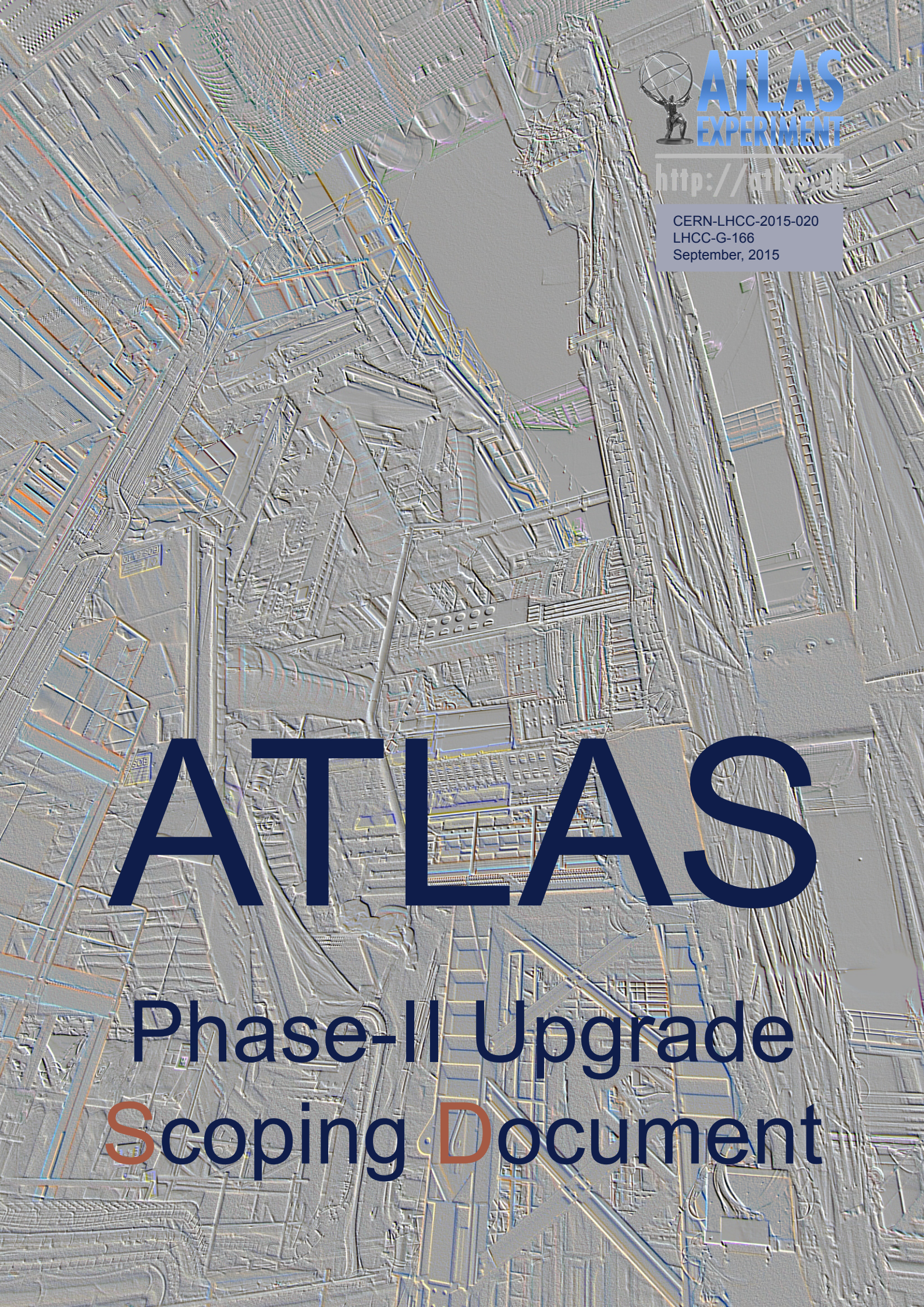

CERN-LHCC-2015-020
LHCC-G-166
September, 2015

ATLAS

Phase-II Upgrade Scoping Document

September 25, 2015
Version 1.0

ATLAS
Phase-II Upgrade

Scoping Document

Revision: 1.0
Reference: CERN-LHCC-2015-020
LHCC-G-166
Created: March 1, 2015
Last modified: September 25, 2015
Prepared by: The ATLAS Collaboration

Contents

Chapter I

Preface

The High Luminosity upgrade of the Large Hadron Collider (LHC) (HL-LHC) is currently expected to begin operations in the second half of 2026, with a nominal levelled instantaneous luminosity of $\mathcal{L} \simeq 5 \times 10^{34}\text{cm}^{-2}\text{s}^{-1}$ corresponding to an average, μ, of roughly 140 inelastic pp collisions each beam-crossing, and delivering an integrated luminosity of around 250 fb $^{-1}$ per year of operation. The ATLAS collaboration described their initial plan and goals for the corresponding Phase-II upgrade of the detector, intended to take full advantage of this accelerator upgrade, in the Letter of Intent [1] in 2012. Since that time, the accelerator team has announced the goal of achieving an ultimate luminosity of $\mathcal{L} \simeq 7.5 \times 10^{34}\text{cm}^{-2}\text{s}^{-1}$ corresponding an average $\mu = 200$ inelastic pp collisions per beam-crossing. This programme aims to provide a total integrated luminosity of 3000 fb^{-1} by 2035. The ATLAS collaboration has been refining and improving their Phase-II upgrade plans since the LoI document was submitted, incorporating lessons learnt from the initial Run 1 operation of the LHC, from further evolution of the initial design, and from the results of a task force which evaluated specific options to extend the pseudo-rapidity coverage of the inner tracking detector, and related detectors such as the muon system.

The LHC Experiment Committee (LHCC), the Upgrade Cost Group (UCG), and CERN management have agreed on a detailed plan for the review and approval of the ATLAS and CMS Phase-II upgrade projects. This plan has been described in an LHC Research Review Board (LHC-RRB) document, which is now being finalised [2]. The present document, referred to as the *Scoping Document* in this process, is intended to address a broad range of questions relevant to the initial stage of formal approval for the ATLAS Phase-II upgrade project. Three different upgrade configurations have been defined, corresponding to three costing scenarios, with total CORE costs of about 200 MCHF, 235 MCHF, and 275 MCHF respectively. These three scenarios are described in detail in the present document, including the relevant R&D and prototyping results. The current estimates of approximate total CORE project costs, manpower, schedule and the corresponding funding profile, in sufficient detail to allow a meaningful review, are also included. Finally, a list of the Technical Design Reports (TDRs) for each of the proposed Phase-II upgrades, and an overall plan with milestones and schedules for producing them, are presented. The corresponding plan and schedule for the remaining R&D and prototyping required to define final designs and provide cost and schedule estimates for the TDRs, are summarised.

The different scenarios have been designed to provide information on performance versus cost for the major cost drivers of the Phase-II upgrade, including the large inner tracker, which comprises roughly 50% of the total upgrade cost, as well as the trigger and data-acquisition system, the calorimeter systems, and the muon spectrometer. For each scoping scenario, detailed studies have been performed to estimate the expected performance for physics objects such as tracks, primary vertices, electrons, photons, muons, jets, heavy-flavour jets, and missing transverse energy. The performance is estimated for the highest instantaneous luminosity expected from the HL-LHC, with $\mu = 200$. In some cases, the performance is explored at reduced values of instantaneous luminosity corresponding to $\mu = 140$ (the nominal HL-LHC luminosity). In addition, the performance of the data-acquisition and triggering systems, and their impact on the triggering capability of ATLAS, have been parameterised in the form of a simplified trigger menu for each scenario. These results are then used to extract the expected physics performance of the Phase-II upgrade for a selected set of benchmark physics processes, covering Electroweak and Higgs boson physics, as well as searches for Supersymmetry and more exotic manifestations of new physics processes. The contributions of individual components of the upgrades can be disentangled to give an approximate estimate of the impact of the scoping scenarios on the performance and physics metrics. The final evaluations of the different scenarios, based on these performance and physics studies, are summarised in Chapter XII.

Chapter II

Overview of the ATLAS Phase-II upgrade program

This document describes the strategy of the ATLAS collaboration for its Phase-II upgrade. It provides a supplement and an update to the original Letter of Intent (LoI) [1] dating from 2012. In particular, it provides a detailed presentation of the scope and performance of the detector and trigger system upgrade for each of the three scoping scenarios defined by the ATLAS collaboration to correspond to the three cost targets defined by the CERN management at the LHC-RRB meeting of April 2015 [2].

The ATLAS LoI document addressed the Phase-II upgrade for the accelerator scenario in which the peak levelled luminosity was taken to be $\mathcal{L} \simeq 5 \times 10^{34}\text{cm}^{-2}\text{s}^{-1}$, corresponding to $\mu \simeq 140$, where μ is the the average number of collisions per crossing. Since that time, the HL-LHC project has introduced an ultimate levelled luminosity scenario with $\mathcal{L} \simeq 7.5 \times 10^{34}\text{cm}^{-2}\text{s}^{-1}$, corresponding to $\mu \simeq 200$. This scenario explores the technical limits of the LHC capabilities, and ATLAS has carried out a number of simulation studies with $\mu \simeq 200$ to ensure that the Phase-II detector upgrade is capable of taking full advantage of the ultimate luminosity.

These studies, extending techniques developed for the 2012 Run 1 data with $\mu \simeq 25$, lead to a more complete understanding of the challenges of operation at $\mu \simeq 200$, particularly in the area of mitigation of pile-up effects from these additional events. In addition, a Task Force was established by the ATLAS collaboration in early 2014 to evaluate possible extensions to the LoI detector design for Phase-II, with a particular emphasis on the regions with $|\eta| > 2.5$. The pile-up values in the range of $\mu \simeq 140 - 200$, and the greater understanding of the role of the forward region of the detector in the Phase-II physics program, have motivated a set of additions to the original LoI detector presented in 2012. This has led to the definition of the Reference scenario detector layout, optimised for luminosities up to the ultimate luminosity configuration ($\mu \simeq 200$). At the present time, this is the detector configuration which is intended to maximise the physics performance and discovery potential of the experiment during the HL-LHC period. It corresponds approximately to the 275 MCHF costing guideline [2]. The two alternative scenarios, with an approximate cost of 235 MCHF and 200 MCHF, are referred to hereafter as the Middle and Low scenarios, respectively.

The three scoping scenarios include different configurations for the upgrade of each major system in the ATLAS detector. They focus in particular on the Inner Tracker (ITk) and on the Trigger and Data Acquisition (TDAQ) systems, as these are the most expensive components of the Phase-II upgrade. The impact on performance of the three costing scenarios is assessed in this document. This in turn allows an evaluation of the physics program that could be possible in each scenario. The changes in scope for the Middle and Low scenarios have their largest impact on the triggering and reconstruction of leptons, jets, b-jets and missing transverse momentum at the higher μ values. Both triggering and reconstruction are essential to acquire the statistics needed to address critical measurements in the electroweak sector, as well as to extend the searches for new particles and new phenomena beyond the Standard Model. The impact on the physics potential is assessed using detailed studies of the expected detector performance for different physics objects, which are then parametrised to provide simple "smeared truth" simulations of the complete physics analyses with all backgrounds and signals included. This approach was developed for the ECFA 2013 [3] and 2014 [4] workshops, and is further extended here to evaluate the representative measurements and searches described in Section II.2 and, in more detail, in Chapter XI.

The preparation of the TDRs for the ATLAS upgrade projects will take place in the period from now until the end of 2017. Chapter X describes the organisation and schedule for the activity in this period, system by system. The activity will include extensive and detailed simulations, and additional iterations and refinements of the designs presented in this document. At that time, a broader range of performance studies, and physics analyses for benchmark processes, will be carried out. In the context of the Scoping Document, the studies have focused on a smaller set of physics processes, which take advantage of the full integrated luminosity possible with the HL-LHC programme. Fur-

thermore, the selection of analyses presented, which is summarised in Table 1, is tailored to explore many of the issues that are most relevant for the proposed scoping scenarios.

Chapter XII provides the overall summary of the document by integrating together the performance and physics results of Chapter XI with the detailed descriptions of the upgrades in Chapters III – VIII. This leads finally to the conclusion of the scoping exercise, where the performance and physics advantages of the Reference scenario, and the performance and physics disadvantages of the Low scenario, both relative to the Middle scenario, are briefly summarised.

II.1 Roadmap to High Luminosity LHC

The schedule for the upgrades to the LHC accelerator complex, leading to the HL-LHC, is shown in Fig. 1 [5]. This schedule has been recently updated according to the CERN Medium Term Plan (MTP) for the period 2016-2020, which was presented at the last CERN Council session [6] in June 2015. The complete accelerator and detector upgrades are expected to be progressively installed during the next two major shutdowns of the accelerator complex, defined as LS2 (currently scheduled to take place in 2019-2020 and to last for 24 months) and LS3 (currently scheduled to take place in 2024-2026 and to last for 30 months).

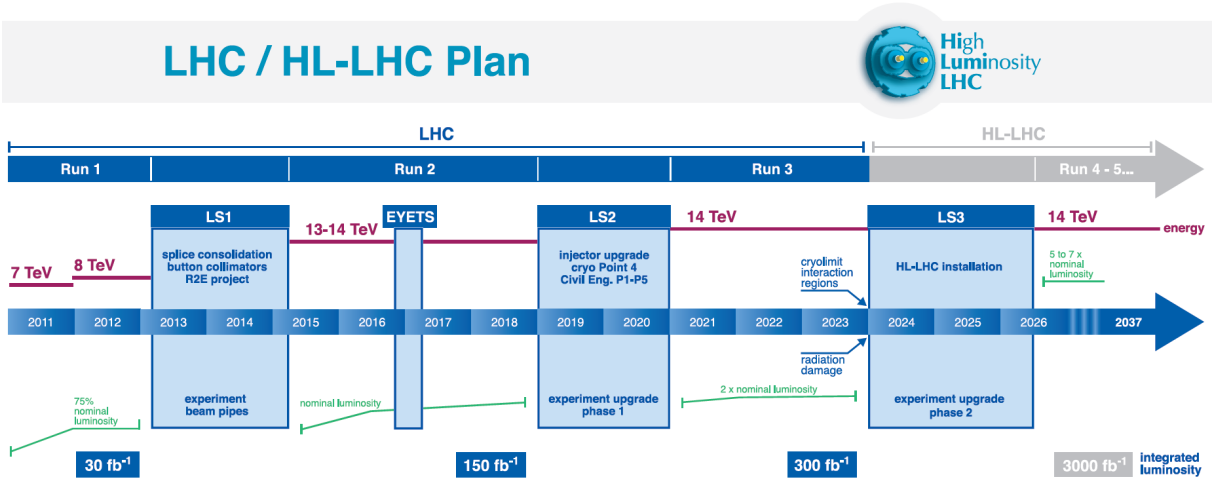

Figure 1. High Luminosity LHC plan beyond 2015, updated according to the CERN MTP for 2016-2020 (from Ref. [5])

At the beginning of the operation of the HL-LHC in the second half of 2026, it is expected that the ATLAS experiment will have acquired a data sample corresponding to an integrated luminosity of approximately 300 fb^{-1}. The target integrated luminosity for the HL-LHC program, during an operating period of roughly 10 years (with a nominal rhythm of 3 years of operation and 1 year of shutdown, or roughly 8 years of accelerator operation) is intended to provide ten times more integrated luminosity, or 3000 fb^{-1}. In order to achieve this extraordinary goal, an ultimate performance of the accelerator complex, based on achieving an instantaneous levelled luminosity of $\mathcal{L} \simeq 7.5 \times 10^{34} \mathrm{cm}^{-2}\mathrm{s}^{-1}$ and delivering more than 300 fb^{-1} per year, is required.
This scenario, which implies extended periods of operation, and therefore full performance and physics capability, at $\mu \simeq 200$, has been considered as the design goal for the Phase-II ATLAS upgrade. Most of the performance and physics results in this document are therefore evaluated at $\mu \simeq 200$, although some studies have been performed at the lower values of $\mu \simeq 140$ (corresponding

to $\mathcal{L} \simeq 5 \times 10^{34}\text{cm}^{-2}\text{s}^{-1}$) and at $\mu \simeq 80$ (the maximum pile-up conditions expected at the end of the Run 3 period before HL-LHC operation begins). Many of the features present in the Reference design scenario are essential to achieve the required trigger and reconstruction performance when operating in the highest pile-up configurations ($\mu \simeq 140-200$). The goal of optimal performance at $\mu \simeq 200$ is especially challenging given the strong dependence of critical elements of the programme on efficiently triggering and reconstructing physics processes that involve the production of the W and Z bosons, and especially Higgs bosons in a wide range of decay modes.

II.2 Performance and Physics objectives and comparative studies

The physics programme of the LHC luminosity upgrade is presented and discussed in detail in the Phase-II Upgrade LoI [1] and in the two reports submitted to the European Committee for Future Acceleartors (ECFA) [3, 4]. In this document, the trigger and offline reconstruction performance of electrons and photons, muons, jets, b-jets and $E_{\text{T}}^{\text{miss}}$ have been studied extensively in each of the scoping scenarios. The results of those studies are reported in Section XI.2.
In addition, several physics processes have been analysed to evaluate the impact of the different upgrade scenarios proposed. The physics analyses focus primarily on precision measurements for the 125 GeV Higgs boson, on vector-boson scattering, and on searches for signatures of new physics. A few selected analyses, shown in Table 1, are presented in detail in Section XI.3 to draw attention to specific components of the ATLAS upgrade programme, and to the benefits that those upgrades provide in terms of improved performance for the relevant physics objects.

Table 1. Overview of the physics analyses described in this document, and of the associated ATLAS sub-systems whose upgrades may impact the physics object performance used in those analyses. The table includes only those benchmark physics processes selected to investigate the impact of the three upgrade scoping scenarios.

Detector system	Trigger–DAQ		Inner Tracker	Inner Tracker + Muon Spectrometer	Inner Tracker + Calorimeter		
Physics Process \ Object Performance	Efficiency/ Thresholds $\mu^{\pm}$	Efficiency/ Thresholds $e^{\pm}$	b-tagging	$\mu^{\pm}$ Identification/ Resolution	Pile-up rejection	Jets	$E_{\text{T}}^{\text{miss}}$
$H \longrightarrow 4\mu$	✓			✓			
VBF $H \to ZZ^{(*)} \to \ell\ell\ell\ell$	✓	✓		✓	✓	✓	
VBF $H \to WW^{(*)} \to \ell\nu\ell\nu$	✓	✓	✓	✓	✓	✓	✓
SM VBS ssWW	✓	✓		✓	✓	✓	✓
SUSY, $\chi_1^{\pm}\chi_2^{o} \to \ell b\bar{b} + X$	✓	✓	✓	✓	✓	✓	✓
BSM $HH \to b\bar{b}b\bar{b}$			✓			✓	

Precision measurements of the Higgs boson properties at the HL-LHC will be performed through studies of all accessible Higgs boson production processes, as well as all accessible decay final states (early studies are available in [7]). To evaluate the impact of the scoping scenarios on the sensitivity, a few benchmark Higgs boson channels have been selected in this document. The

gluon-gluon production mode is probed through the decay of the Higgs boson into Z-bosons ($gg \to H \to ZZ^* \to \ell\ell\ell\ell$). The sensitivity to this process and the achievable precision of the measurements depend strongly on the performance of the lepton trigger and reconstruction. The sensitivity to Higgs bosons produced via vector-boson fusion (VBF) is studied by selecting Higgs boson decays into gauge bosons ($H \to ZZ^* \to \ell\ell\ell\ell$, $H \to WW^* \to \ell\nu\ell\nu$). The critical requirement for distinguishing this production mode from the gluon-fusion mode involves the reconstruction of forward jets. These jets preferentially populate the region $|\eta| \geq 2.5$, and provide one of the strongest arguments for enhancing the performance of the calorimeter and tracker systems in this very-forward region for the Phase-II upgrade. Mitigation of pile-up effects, *e.g.* through the correct association of the forward jets to the primary hard-scattering vertex using tracking information, is essential to the robust observation of these processes at very high μ values. The impact of the various upgrade scoping scenarios has also been assessed by studying the variation of the acceptance for Higgs boson production and decay into $ZZ \to \mu^+\mu^-\mu^+\mu^-$ final states.

The study of vector-boson scattering (VBS) is important to establish whether other mechanisms are responsible, together with the 125 GeV Higgs boson, for maintaining unitarity in this process. As for the VBF Higgs production processes, VBS processes are also characterised by the presence of high-p_{T} jets in the forward regions, whose reconstruction is essential for the analysis.

Searches for new physics include both a SUSY study and a more exotic BSM study:

- Search for the associated production of charginos and heavy neutralinos where the neutralino decays via Higgs bosons leading to final states with one lepton, two jets consistent with originating from b-quarks, and large missing transverse momentum. The discovery reach critically relies on the performance of the lepton trigger, lepton reconstruction, b-jet identification, and missing transverse momentum reconstruction.

- Search for high mass Kaluza-Klein gravitons decaying into pairs of Higgs bosons hh, with each Higgs h decaying to $b\bar{b}$. The $b\bar{b}$ system may be "boosted" and reconstructed as a large radius jet. The discovery of such a high mass resonance relies on the reconstruction performance of b-jets, and on the efficiency for reconstructing collimated ("boosted") objects originating from the decay of the resonance.

II.3 Reference and alternative scoping scenarios

The plans of the ATLAS collaboration for the HL-LHC upgrades build on the foundation of the consolidation program completed in the LS1 shutdown and on the Phase-I detector configuration that will be deployed during LS2:

- The Insertable B-Layer (IBL) Pixel detector, whose installation was successfully completed during LS1, exploits new technologies for both the detector using planar n-in-n sensors with slim edges and 3D-sensors, and a new front-end readout ASIC in 130 nm CMOS technology, the FE-I4 ASIC. This detector provides a fourth pixel layer in the Inner tracking Detector (ID).
- The Phase-I upgrades of the calorimeter trigger system [8] and of the associated LAr trigger electronics [9] improve the granularity of the calorimeter information used for the advanced electron and jet reconstruction algorithms by a factor of ten. This information is used in the state-of-the-art Field-Programmable Gate Array (FPGAs) of the Level-1 trigger (L1) trigger processors to provide improved L1 performance at Run 3 luminosities and beyond.
- The New Small Wheel (NSW) [10] replaces the first layer of end-cap muon instrumentation and provides improved triggering for high luminosity, while already meeting the very challenging Phase-II requirements.

- The Fast TracKer trigger (FTK) [11] uses hardware track reconstruction based on associative memories to perform reconstruction of tracks with transverse momenta $p_{\mathrm{T}} \geq$ 1 GeV, which are then sent to the Event Filter (EF) processing farm. This addition to the trigger provides high-quality tracking information as an input to the HLT, allowing complex track-based trigger decisions to be made very rapidly.

In most cases, the design and techniques used for the Phase-II upgrades represent an evolution from the new designs and technologies already introduced during the LS1 improvement program, which included the installation of the IBL pixel detector, and the Phase-I upgrades now being prepared for installation during LS2. This evolutionary approach leads to a relatively solid understanding of the technical challenges, as well as the uncertainties on the costs and the required resources, even at the present early stage of the Phase-II upgrade activities. The following Sections outline the elements and the scope of the ATLAS detector upgrade, which are also summarised in Tables 2-4.

II.3.1 Trigger and Data Acquisition

The strategy devised by the ATLAS collaboration for the HL-LHC upgrade of the TDAQ system is based on two levels of "custom-hardware" trigger, which allow for data streaming off-detector either after a Level-0 trigger (L0), or in some cases, at the full 40 MHz Bunch Crossing (BC) rate. The information feeds sophisticated FPGA technology to implement fast and powerful trigger algorithms, rather than using the very rigid ASIC-based approaches often used during the Run 1 operations. The primary elements of the Phase-II TDAQ system in the Reference, Middle, and Low scenarios are summarised in Table 2. Reductions in functionality in the Middle and Low scenarios arise mainly from the reduced rate capability at various trigger levels, and the reduced performance of the track trigger and the L1 Muon trigger.

In the Reference scenario, the L0 and L1 triggers are designed to operate at rates up to 1 MHz and 400 kHz, respectively. In the Middle and Low scenarios the output rate capability of the L1 trigger is reduced to 200 kHz, primarily because of the limitations imposed by the readout electronics of the existing Muon spectrometer chambers that is not be upgraded in those scenarios.

The scope of the Level-1 Track Trigger (L1Track) naturally follows the coverage in η of the tracker system, finding tracks with $p_{\mathrm{T}} \geq$4 GeV in the Reference and Middle scenario, and $p_{\mathrm{T}} \geq$8 GeV in the Low scenario.

The design of the Muon L1 trigger system matches the upgraded configuration of the Muon spectrometer detectors as outlined in Section II.3.4.

The High-Level Trigger (HLT) system includes the upgraded Fast TracKer trigger (FTK++) and the EF processors. The FTK++ processor is specified for maximum rates of 100 kHz in the Reference scenario and 50 kHz otherwise, finding tracks with momenta with $p_{\mathrm{T}} \geq$1 GeV in the Reference and Middle scenarios, and $p_{\mathrm{T}} \geq$2 GeV in the Low scenario. The output rate of the EF processors are planned to be 10 kHz and 5 kHz in the Reference and in the Middle/Low scenarios, respectively.

II.3.2 Inner Tracker

In the Reference scenario (see Table 3) the Strip tracker is defined as in the LoI [1] document, and the Pixel tracker is similar to the one defined in the LoI with the addition of a very-forward extension to cover the pseudo-rapidity region up to $|\eta|$=4.0.
The Middle scenario foresees the removal of a Strip disk from each side of the end-cap Strip tracker, and the removal of the Stub layer from the barrel Strip tracker. The forward extension of the Pixel detector is reduced to provide coverage up to $|\eta|$<3.2.

Table 2. ATLAS TDAQ upgrade plans for the three scenarios considered [2].

Trigger and Data Acquisition	Scoping Scenarios Reference (275 MCHF)	Middle (235 MCHF)	Low (200 MCHF)
Level-0 Trigger System			
Central Trigger	✓	✓	✓
Calorimeter Trigger (e/γ)	$\|\eta\| < 4.0$	$\|\eta\| < 3.2$	$\|\eta\| < 2.5$
Muon Barrel Trigger	MDT everywhere RPC-BI Tile-μ	MDT (BM & BO only) Partial η coverage RPC-BI Tile-μ	MDT (BM & BO only) No RPC-BI Tile-μ
Muon End-cap Trigger	MDT everywhere	MDT (EE&EM only)	MDT (EE&EM only)
Level-1 Trigger System			
Output Rate [kHz]	400	200	200
Central Trigger	✓	✓	✓
Global Trigger	✓	✓	✓
Level-1 Track Trigger (*RoI based tracking*)	$p_T > 4$ GeV $\|\eta\| \leq 4.0$	$p_T > 4$ GeV $\|\eta\| \leq 3.2$	$p_T > 8$ GeV $\|\eta\| \leq 2.7$
High-Level Trigger			
FTK++ (*Full tracking*)	$p_T > 1$ GeV 100 kHz	$p_T > 1$ GeV 50 kHz	$p_T > 2$ GeV 50 kHz
Event Filter	10 kHz output	5 kHz	5 kHz
DAQ			
Detector Readout	✓ [400 kHz L1 rate]	✓ [200 kHz L1 rate]	✓ [200 kHz L1 rate]
DataFlow	✓ [400 kHz L1 rate]	✓ [200 kHz L1 rate]	✓ [200 kHz L1 rate]

The Low scenario in addition implies the removal of a complete Strip barrel layer (layer # 3), and the removal of the stereo modules from two additional Strip barrel layers (leaving only axial modules in layers #2 and #4). The very-forward Pixel system is completely dropped, so that the coverage is as in the LoI layout, i.e. $|\eta|$<2.7.
The configuration of the ITk detector is described in detail in Chapter IV. In particular, cross-section drawings in Figs. 6-9 visualise the layouts of the ITk detector for the three scoping scenarios.

Table 3. Upgrade plans of the ATLAS ITk and calorimeter systems for the three scenarios considered [2].

Detector System	Scoping Scenarios Reference (275 MCHF)	Middle (235 MCHF)	Low (200 MCHF)
Inner Tracker			
Pixel Detector	$\|\eta\| \leq 4.0$	$\|\eta\| \leq 3.2$	$\|\eta\| \leq 2.7$
Barrel Strip Detector	✓	✓ [No stub layer]	✓ [No stereo in layers #2,#4] [Remove layer #3] [No stub layer]
Endcap Strip Detector	✓	✓ [Remove 1 disk/side]	✓ [Remove 1 disk/side]
Calorimeters			
LAr Calorimeter Electronics	✓	✓	✓
Tile Calorimeter Electronics	✓	✓	✓
Forward Calorimeter	✓	✗	✗
High Granularity Precision Timing Detector	✓	✗	✗

II.3.3 Calorimeters

The ATLAS calorimetry uses liquid argon detector technology for the electromagnetic barrel and end-cap (EMB and EMEC) , the hadronic end-cap (HEC) and the forward (FCal) calorimeters, and scintillating Tiles for the hadronic barrel calorimeter. A cross-sectional view of the forward calorimetry in ATLAS is shown in Fig. 38.
The upgrade programme of the calorimeter system is summarised in Table 3. The Reference scenario includes a new sFCal, with higher transverse granularity for improved handling of the large fluctuations in the energy deposition due to the large pile-up expected during operations at the HL-LHC. The sFCal design includes 100 μm liquid argon gaps in the first sFCal1 module (with respect to the existing 250 μm in FCal1), an improved HV distribution network, and improved cooling, to cope with the large energy deposit expected in the detector because of the very high instantaneous luminosity. Large energy deposits could lead to space-charge effects from ion-buildup in the liquid argon gap, as well as to large reductions in the voltage on the electrodes, and finally to potential over-heating (even local boiling) in the liquid argon.

In case the FCal is not upgraded and cannot be properly operated under HL-LHC conditions, the addition of a MiniFCal detector in front of the existing FCal is being considered, as explained in detail in Section V.4.4. With the possible exception of a MiniFCal, no upgrade of the calorimeter detectors is foreseen in the Middle and Low scenarios.
The Reference scenario also includes a finely segmented precision timing detector placed in the existing volume of the Minimum Bias Trigger Scintillator and covering approximately the range 2.4 < $|\eta|$ < 4.3. This is the region for which the segmentation of the electromagnetic calorimeter is significantly reduced compared to the central region ($|\eta| < 2.5$), and where detector performance, e.g. electron resolution and pile-up jet rejection, will be degraded due to the large pile-up at the HL-LHC. Both fine transverse segmentation and precision time resolution would allow the identification and rejection of energy clusters produced by pile-up collisions.
The readout electronics of both the LAr and Tile calorimeters needs to be upgraded because of radiation tolerance limits, and because the on-detector front-end electronics cannot operate with the L0 and L1 trigger rates and latencies required for the Phase-II luminosities. As such, their upgrade is included in each of the three scenarios.
Similarly, the information from the last layer (D-layer) of the Tile calorimeter will be sent to the muon trigger for all three scenarios, as it provides complementary measurements important for the reduction of the trigger rate due to fake muons.

II.3.4 Muon spectrometer

The scope of the Muon upgrade focuses primarily on the improvement of the performance of the muon trigger:

- Finer granularity trigger based on MDT detectors to improve the sharpness of the transverse momentum thresholds at L1 or, even at L0 if allowed by the L0 system latency.
- The addition of new RPC detectors in the barrel ($|\eta| < 1$) to increase the coverage and the redundancy of the L0 system.
- Different options for the partial or complete replacement of the original on-chamber electronics for the MDTs are also considered.

The configuration of the Muon spectrometer after the proposed upgrade is shown in Fig. 47. The trigger electronics is upgraded in all three scenarios, in both the barrel and end-cap spectrometers. A replacement of the trigger chambers in the forward region $2.0 < |\eta| < 2.4$ is foreseen in all three scenarios to improve the trigger selectivity. In the Reference scenario the muon acceptance will be increased by the inclusion of a very forward muon tagger, attached to the NSW shielding disk and covering the region $2.6 < |\eta| < 4$.

II.3.4.1 Barrel detectors

In the Reference scenario, new RPC and small tube diameter MDT (sMDT) chambers are installed in the small sectors of the Barrel Inner layer (BI) region (BIS), while replacing the existing on-detector electronics on all the chambers. The present front-end electronics do not have sufficient throughput to handle the hit rates expected during the HL-LHC operating conditions, with the L0/L1 trigger parameters defined in Section II.3.1 and, more in detail, in Chapter III. The sMDTs are installed only in the location of the Barrel Inner Small chamber sectors (BIS), while RPCs are installed also in the Barrel Inner Large chamber sectors (BIL), on top of the existing MDT chambers (see Chapter VI and Fig. 47 for further details.) The upgrade of the on-detector electronics on both the “large” and “small” sectors of the BI region implies labour-intensive operations in the experimental hall during LS3, but

Table 4. Upgrade plans of the ATLAS Muon system for the three scenarios considered [2].

Muon Spectrometer	Scoping Scenarios Reference (275 MCHF)	Middle (235 MCHF)	Low (200 MCHF)
Barrel Detectors and Electronics			
RPC Trigger Electronics	✓	✓	✓
MDT Front-End and readout electronics (BI+BM+BO)	✓	✓ [BM+BO only]	✓ [BM+BO only]
RPC Inner layer in the whole layer	✓	✓ [in half layer only]	✗
Barrel Inner sMDT Detectors in the whole layer	✓	✓ [in half layer only]	✗
MDT L0 Trigger Electronics (BI +BM+BO)	✓	✓ [BI +BM only]	✓ [BI +BM only]
End-cap and Forward Muon Detectors and Electronics			
TGC Trigger Electronics	✓	✓	✓
MDT L0 Trigger and Front-End read-out electronics (EE+EM+EO)	✓	✓ [EE +EM only]	✓ [EE +EM only]
sTGC Detectors in Big Wheel Inner Ring	✓	✓	✓
Very-forward Muon tagger	✓	✗	✗

provides the ATLAS experiment with a robust L0 trigger based on RPCs, covering the acceptance holes in the current system, and significantly reduces the impact of the longevity issues (reduced gain) for the existing RPC chambers. It also provides a three-station L0 trigger based on MDTs with the best possible momentum selectivity, eliminating the limitations in the L1 trigger rate and latency coming from the present on-detector electronics.

In the Middle scenario the BI RPC and sMDT chambers are upgraded only for the more easily accessible half of the stations at larger pseudo-rapidity, where the rates are highest. The electronics of the existing BI MDT chambers that are not easily accessible, is not upgraded. Conversely, the upgrade plan includes the replacement of the electronics for all the Barrel Middle layer (BM) and Barrel Outer layer (BO) chambers.

The Low scenario is the bare minimum for the barrel spectrometer: it has the same acceptance holes as the present RPC trigger, with additional efficiency losses due to the ageing of the original RPC chambers. There would be no upgrade of the RPC and sMDT chambers in the BI region. In addition, the L0/L1 MDT trigger is available only in the BM and BO to provide at least some momentum selectivity based on a two-point measurement and to partially compensate for the degraded performance of the RPC chambers.

II.3.4.2 End-cap chambers

The replacement of the trigger chambers in the forward region $2.0 < |\eta| < 2.4$ with small Thin Gap Chamber (sTGC) chambers is foreseen in all three scenarios. This will improve the trigger selectivity in that region, which has the highest hit density and, therefore, is most vulnerable to ageing and pile-up effects.

In the Reference scenario the upgrade plans include the replacement of the MDT front-end readout and of the L0 trigger electronics of all the chambers, with the obvious exception of the NSW, and the installation of a very-forward tagger to take best advantage of the very-forward ITk tracking extension in this scenario. In the Middle and Low scenario no forward tagger is foreseen, while the MDT front-end readout and trigger electronics is upgraded only in the outer and middle end-cap stations (EO and EM).

Chapter III

Trigger and Data Acquisition System

III.1 Introduction

The ATLAS detector electronics and the TDAQ system were originally designed to operate at an initial "low" luminosity ($\mathcal{L} = 10^{33}\text{cm}^{-2}\text{s}^{-1}$) at low trigger thresholds, followed by a "high" luminosity phase ($\mathcal{L} = 10^{34}\text{cm}^{-2}\text{s}^{-1}$) with higher trigger thresholds. The detector electronics was designed to buffer data for a maximal latency of 2.5 μs and to be able to cope with a Level-1 trigger (L1) trigger rate of up to 100 kHz. The Read-Out Drivers (RODs) of the ATLAS detector components and the original TDAQ system, were designed to operate with an initial L1 trigger rate of 75 kHz with a possible upgrade, realised in preparation for Run 2, to 100 kHz for $\mathcal{L} = 10^{34}\text{cm}^{-2}\text{s}^{-1}$.

The successful physics programme of the ATLAS experiment during Run 1 of the LHC has shown that a strategy of using reasonably low single-electron and muon thresholds, coupled with a comprehensive trigger menu for hadronically-decaying tau leptons, missing-transverse-momentum triggers and jet triggers is very effective. It also demonstrated the advantages of designing a flexible system with fairly large contingencies to allow for new ideas.

The luminosity of the LHC is expected to increase after the Phase-I upgrade [12] to $\mathcal{L} \simeq 2-3\times 10^{34}\text{cm}^{-2}\text{s}^{-1}$ and to as much as $\mathcal{L} \simeq 7.5\times 10^{34}\text{cm}^{-2}\text{s}^{-1}$ after the Phase-II upgrade [1]. It is important to retain trigger capability for low single electron and muon thresholds, coupled with comprehensive tau and hadronic selections, after the Phase-II upgrade; significant improvements to the TDAQ system are needed to accomplish the physics goals of these upgrades. In the Phase-I upgrade, the triggers are being made more selective with the addition of the NSW [10] into the L1 muon trigger and a higher-granularity calorimeter trigger coupled with a new topological triggering capability (the latter already being available in Run 2). In the Phase-I upgrade the L1 latency and rate remain unchanged. The Phase-I upgrade also includes the FTK [11] that is used to do full tracking on all events accepted by the L1 trigger.

To accommodate the much larger step in luminosity to $\mathcal{L} \simeq 7.5\times 10^{34}\text{cm}^{-2}\text{s}^{-1}$ for the high-luminosity phase of the LHC, it is necessary to increase the maximum rate and latency of the trigger. In the Reference scenario the front-end electronics of all the existing ATLAS detector systems is replaced, to allow for a higher L1 trigger rate and a longer latency. The front-end electronics for systems installed in the Phase-I upgrade, such as the NSW, will not be replaced in the Phase-II upgrade.

The Phase-II two-level hardware trigger with an additional Level-0 (L0), is shown in Figure 2. In the Reference scenario the two-level hardware trigger is required by the NSW which can accommodate a maximum L1 rate of 400 kHz. The NSW was designed with the LoI scheme in mind[1]. Work is ongoing to determine if the NSW L1 rate capability can be raised to 1 MHz and the two-level system simplified. In the Middle and Low scenarios, the remaining MDT electronics can accommodate maximum L1 rates of only ~ 200 kHz and therefore require the two-level system.

To limit the size of buffers in the detector electronics, the L0 trigger decisions are required to have a latency of less than 6 μs and will be based on Muon and calorimeter triggers as described in Sections III.2.1 and III.2.2. The L1 trigger is based on Regions of Interest (RoIs) seeded by L0 triggers and on full calorimeter readout with a granularity higher than the one used at L0. As described in Section III.3.1, one component of the L1 trigger, the Level-1 Track Trigger (L1Track), will be based on tracks built from ITk hits and a second one, the Level-1 Global Trigger (L1Global),

[1] In preparation for the ATLAS Phase-II LoI [1] it was assumed that it would not be possible to replace all of the electronics associated with the monitored drift tubes (MDTs) that are used for the precision determination of muon momentum in the ATLAS muon spectrometer. This limitation is due to the difficulty in accessing the MDT chambers in the inner barrel region (BI). When used in a triggered mode, the legacy MDT electronics allows for a fairly long latency (in excess of 30 μs), but for the occupancies expected at HL-LHC the MDTs are limited in readout rate to approximately 200 kHz. To avoid the rate limit associated with the legacy MDT electronics, a L0 trigger is introduced into the design with an average rate of 1 MHz; the legacy MDT electronics is read out only after L1.

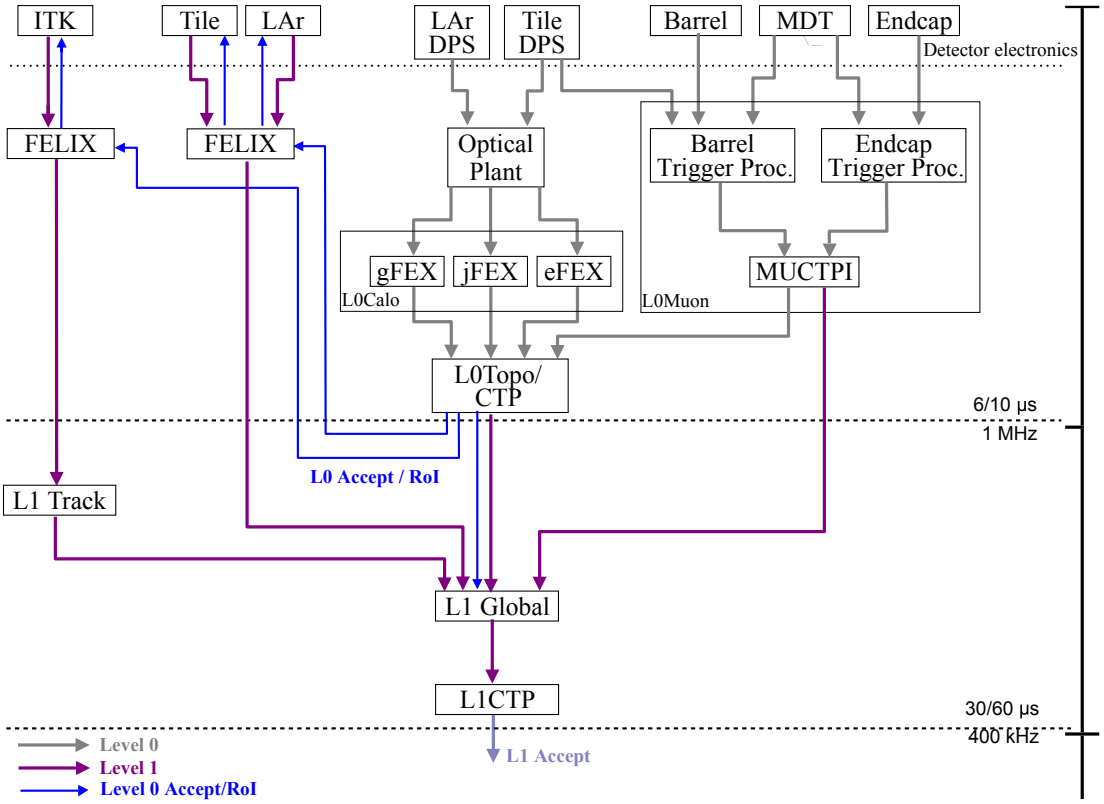

Figure 2. Schematic of the Phase-II ATLAS Trigger. For clarity, the FELIX readout of the trigger systems is not shown in the diagram. This readout can also provide input to L1Global. The Barrel Trigger Processor comprises the Barrel Sector Logic and the Barrel L0 MDT Trigger Processors. The End-cap Trigger processor comprises the NSW Trigger Processor, the End-cap Sector Logic and the End-cap MDT Trigger Processors.

described in Section III.3.2, will include detailed calorimetry information. L1Global will also have access to L0 muon trigger information. A schematic of the data flow for the proposed Phase-II trigger is shown in Figure 2. The L0 and L1 Central Trigger Processors (CTPs), described in Section III.4 and shown in the figure, collect the trigger elements from the respective components of the trigger systems, apply vetoes, dead time and pre-scales, and distribute the L0 and L1 Accept signals.

In order to have flexibility for future improvements, such as a single-level hardware trigger system, and to provide some contingency, any new electronics for the ATLAS experiment is required to be compatible with longer latencies, as given in Table 5. The detector readout is required to accommodate latencies of up to 10 μs at L0 and 60 μs at L1, and to to be compatible with average L0 rates of up to 1 MHz and average L1 rates of up to 400 kHz. Detectors buffer data during the L0 and L1 latencies, either on-detector or off-detector, as noted in Table 6. Off-detector buffering allows maximum flexibility for future changes to the trigger in the Reference scenario. In the Middle and Low scenarios, the current MDT system severely restricts this flexibility.

In all scenarios the L0 trigger rate has been increased with respect to the Phase-II LoI to increase the physics acceptance, especially for tau triggers. This is motivated in Section III.7. In addition, L0 and L1 detector latencies have been increased to allow flexibility in case the limitations from the legacy MDT system can be removed.

The Phase-II Data Acquisition (DAQ) system described in Section III.5 is designed to make maximal use of commercial networking and computing hardware. Data from the detectors will be

Table 5. Requirements for any newly constructed elements for ATLAS Phase-I and Phase-II. “Max. Trigger Req." refers to the requirement on the total latency of any trigger decision. Upgraded detectors and readout systems will need to be compliant with the latencies and rates indicated under the column “Min. Detector Req.”. L0 latency refers to the time difference between the triggered beam crossing and the arrival of the L0 Accept at the detector electronics. L1 latency refers to the time difference between the triggered beam crossing and the arrival of a L1 Accept at the detector electronics. L0 and L1 rates refer to the trigger rates, averaged over one turn of the LHC, at the highest instantaneous luminosities.

Specification	Latency	
	Max. Trigger Req.	Min. Detector Req.
L0 Latency	6 μs	10 μs
L1 Latency	30 μs	60 μs
L0 Rate		1 MHz
L1 Rate		400 kHz

transferred from the detector buffers to the software based Event Filter (EF) and event storage via the FELIX readout system (see Section III.5.1) that will convert detector data transport protocols such as Giga-Bit Transceiver project (GBT) to a commercial standard such as 40 or 100 Gigabit Ethernet or InfiniBand. The FELIX systems can also pass low-latency trigger data to L1 as shown in Figure 2.

III.2 Level-0 Triggers

L0 triggers will provide trigger decisions within a latency of 6μs. The major triggers at L0 will be based on muon and calorimeter data, as well as their combinations in the topological processors. After the Phase-II upgrade, the muon triggers will contain a new component from the MDT and will also make use of the NSW to be installed in Phase-I, as well as the existing RPC-based and TGC-based triggers. In the Reference scenario additional RPC coverage will be added to improve the efficiency of the barrel RPC triggers. The barrel and end-cap muon-trigger information will be merged in the Muon to CTP Interface (MuCTPI) described in Section III.4 The L0 calorimeter triggers will be largely based on the Phase-I L1 system, but will include improvements made possible by increased forward-detector granularity (in the Reference scenario) and from the improved Tile electronics (see Section: V.3).

III.2.1 Level-0 Muon Triggers

The first part of this section describes the L0 muon barrel triggers, which depend on RPCs for precision timing complemented by MDTs for precision momentum measurement. This is followed by a discussion of the L0 muon end-cap trigger which depends on the NSW, TGCs and MDTs, as well as the outer layer of the Tile barrel and extended barrel calorimeters and the forward-most RPC chambers in the inner barrel. The upgrades to the muon detector systems are described in more detail in Section VI.

Muon triggers in the barrel will be seeded by tracks in the RPC system. The new RPC electronics will perform all trigger coincidences off-detector. It is foreseen to use the coincidence of as few layers as possible in the RPC detector to provide maximal trigger efficiency.

In the Reference scenario the addition of a complete triplet of RPCs, positioned at the innermost layer of the muon spectrometer (BI layer), will make the barrel trigger system more robust against ageing effects in the existing RPCs and increase the acceptance. As a result, the product of muon

Table 6. All ATLAS data are buffered at the nominal beam crossing rate of 40 MHz. The second column of the table gives the location of initial buffering for the L0 latency. The third and fourth columns indicate, respectively, which data are readout to the L1 trigger processors (on a L0 Accept) and to the EF (on a L1 Accept). It should be noted that ITk is being constructed to allow either Region-of-Interest (RoI) based buffering or full readout at the L0 rate. In case of full readout of ITk after a L0 Accept, no additional readout is needed after L1.

System	Buffering	L0 Readout	L1 Readout
ITk	On-detector	RoI/Full	Full
LAr	Off-detector	RoI	Full
Tile	Off-detector	RoI	Full
MDT	Off-detector	None	Full
Legacy MDT	On-detector	None	Full
NSW	On-detector	None	Full
RPC	Off-detector	None	Full
Thin Gap Chamber (TGC)	Off-detector	None	Full

acceptance and efficiency in the barrel region will increase from approximately 65% (assuming the high voltage is reduced to prevent ageing of the existing RPCs) to approximately 95%. The new triplet will have almost complete angular coverage in the barrel region of the detector and can be combined with hits in the outer layer of the RPC to provide a trigger which is unaffected by the internal structural elements that reinforce the ATLAS barrel toroid coils. In the Middle scenario the new BI layer will only cover the high $|\eta|$ half of the barrel and the product of acceptance and efficiency will be limited to $\sim 80\%$.

In the end-caps, muon triggers will be provided by the NSW and the TGCs in the big wheel. The NSW trigger processor will provide both the $\eta-\phi$ position of the muon and the local polar angle β. This information can be compared with the $\eta-\phi$ position of the muon detected in the end-cap TGCs. In addition, the end-cap TGC can be used to make a second measurement of β, which is sensitive to the bending of the muon in the magnetic field of the end-cap toroid. The TGC value of β can be matched to the value of β from the NSW in the end-cap sector logic, making an effective cut on the muon momentum. This muon-momentum estimate can be further improved using the MDTs from the big wheel of the Muon Spectrometer.

The coincidence logic will also include an input from the outermost (D-layer) of the Tile calorimeter. The Phase-II Tile muon signals will be much improved over the ones used in Run 2 which are based on the “low-gain” amplifier output. The Tile muon signals are most useful in the region outside of the NSW coverage where they can be used as an added coincidence to reduce background $(1.0 < |\eta| < 1.3)$. The high sensitivity outputs can also be used to trigger on di- and tri-muon signatures (such as $\tau \rightarrow \mu\mu\mu$) that have several closely spaced muons.

The drift time of the ATLAS MDTs for hits furthest from the wire is approximately 1 μs, a factor of 40 longer than the time between consecutive bunch-crossings. The MDT hits can most effectively be included in the trigger when a Bunch Crossing IDentification (BCID) is provided by a coincidence of RPC, TGC and/or Tile hits. In the Reference scenario, all MDT hits in the barrel can be streamed off-detector to the shielded counting room, USA15, and track segments can be found based on a BCID and RoI from the RPC hits. In the Middle scenario it will not be possible to replace the electronics of all of the MDTs and it is unlikely that all of the MDT hits from the inner layer of the muon system

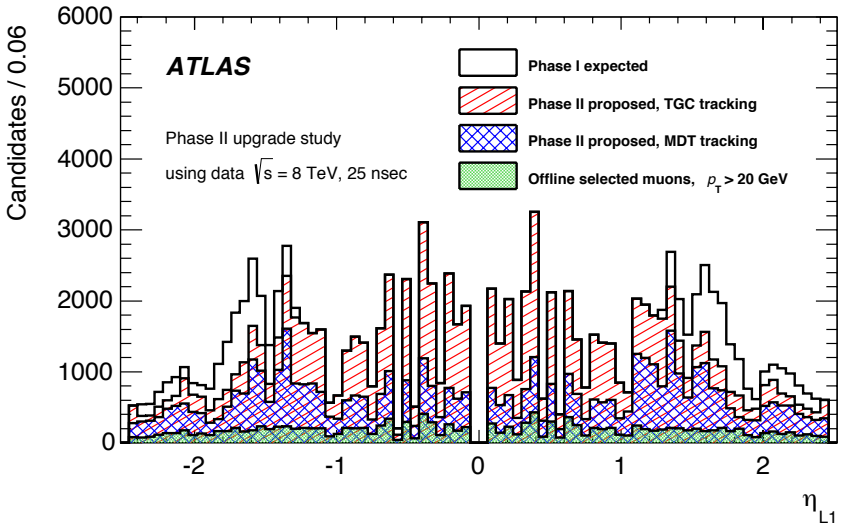

Figure 3. Expected rate reduction for muon triggers based on a measurement of the local polar angle, β, before and after the barrel and end-cap toroid. The red hatched area shows the effect of the TGC determination of β combined with the NSW. (The TGC and NSW systems do not affect the barrel triggers with $|\eta| < 1.3$). The blue hatched area shows the improvement after the MDT trigger is added. The plot is based on emulation of the NSW performance using the 2012 detector configuration of ATLAS.

can be used in the trigger. In all of the scenarios the end-cap MDT hits are available to the trigger processors.

In the Reference scenario the difference between the local polar angle, β in the inner and outer barrel MDT layers can be used to sharpen the momentum resolution allowing a tighter cut with minimal loss of efficiency, this will reduce the trigger rate by approximately 50%. In the end-cap region, the difference between the angle β in the NSW and in the big-wheel MDTs can similarly be used to provide an effective momentum cut as illustrated in Figure 3. The MDT hits will be processed using processors based on FPGAs coupled with Central Processing Units (CPUs). The MDT processor will deliver the trigger decision quickly enough so that the L0 trigger decision can be distributed within the required latency of 6 μs.

III.2.2 Level-0 calorimeter Triggers

The L0 calorimeter trigger will re-use the system installed as part of the Phase-I ATLAS upgrade that is outlined in the TDAQ Phase-I TDR [8]. In the Phase-I upgrade, triggers will be based on three feature extraction processors. The eFEX is designed to use the finest granularity available from the Phase-I upgrade of the LAr trigger electronics [9] with a size of $\Delta\eta \times \Delta\phi$ of 0.025×0.1 in the strips and main layer of the calorimeter, and a size of $\Delta\eta \times \Delta\phi$ of 0.1×0.1 for the pre-sampler, the last layer in the e.m. calorimeter and the hadronic calorimeters. The eFEX is used to identify electrons, photons and tau leptons with $|\eta| < 2.5$. The jFEX is based on a transverse granularity of $\Delta\eta \times \Delta\phi$ of 0.1×0.1 in the Tile calorimeters and in the LAr calorimeters in the region $|\eta| < 2.4$. In the remainder of the acceptance the trigger transverse granularity is almost the same as the full granularity used in the offline analysis. The jFEX is able to identify jets, as well as calculate contributions to global quantities such as E_T^{miss} in slices of η. The gFEX is based on transverse granularity of $\Delta\eta \times \Delta\phi$ of 0.2×0.2 and allows the entire event to be processed in a single module. For example, the gFEX is able to identify jets with $R = 1.0$.

In the Phase-II upgrade, the signals to the Feature EXtractor trigger processors (FEXs) will

continue to use the same LAr trigger electronics as in Phase-I. In Phase-I the Tile calorimeter input will use the Run 1/Run 2 legacy calorimeter trigger system. In Phase-II the Tile input will come from digitised signals described below in Section V.3 and will allow for more detailed longitudinal information to be distributed to the FEXs. These new inputs will require that a portion of the Phase-I Optical Plant be replaced. In addition the algorithmic firmware of the FEXs will require significant changes to adapt to the high pileup environment of the HL-LHC.

These calorimeter trigger objects as well as the muon trigger objects are processed by the topological processor that can be used to trigger on derived quantities such as the scalar sum of jet transverse energies (HT), the vector sum of jet transverse energies (missing HT), the invariant mass of di-electrons and di-photons, etc. After the Phase-II upgrade this topological processor will be used to seed L1 triggers as described in the next section. The trigger objects formed by the eFEX, jFEX and gFEX will also be transmitted to L1Global and will require an additional readout hardware system called L0Calo-to-L1Calo.

III.3 Level-1 Triggers

The L1 Phase-II trigger adds two new capabilities compared to the L0 system. The L1Track trigger processes L0 RoIs to search for ITk tracks with high transverse momentum. The L1Global uses full-granularity calorimetry for analysis of RoIs, and improved granularity (over L0) for the entire detector for jet finding and the reconstruction of quantities such as E_T^{miss}, HT and missing HT. FPGA-based clustering algorithms, which can be used to compress efficiently the data sent to the L1Global processor and provide the most accurate reconstruction of jet energies and other related quantities, are currently being studied in an R&D programme.

III.3.1 L1Track

The L1Track processor will use hits from the ITk strips and pixels to find tracks within RoIs which are seeded by the L0 calorimeter and muon triggers. In a first step, the hits will be clustered into "super-strips" for a subset of the strip and pixel layers. These super-strips are then processed by associative memory chips that search for matches to templates. To limit the number of patterns to be evaluated, the transverse momentum, p_{T}, of tracks used for the templates is restricted to $p_{\mathrm{T}} > 4$ GeV in the Reference and Middle scenarios. To implement L1Track for the full η-acceptance of the tracker (Reference Scenario) approximately 3.2 billion patterns are needed. This is reduced to approximately 2.6 billion patterns in the Middle scenario. In the Low scenario, an additional cost saving – at the price of degraded performance – can be achieved by reducing the number of patterns by a factor of two, which would only allow tracks with p_{T} above 8 GeV to be found. In the Low scenario approximately 1 billion patterns are needed. Valid patterns are then fed to a track-fitting step that uses the full granularity of the strip and pixel detectors, but not necessarily all of the strip and pixel layers.

The L1Track trigger has the largest impact on electron identification and on pileup rejection for multi-object events such as di-tau decays and multi-jet events. For electron identification the transverse momentum of the track can be matched to clusters from L1Global allowing selections based on both E/p and the difference in the position of the extrapolated track and calorimeter cluster to be made. The latter selection significantly benefits from the full granularity readout available at L1Global. The rejection for backgrounds to electrons with transverse momentum above 20 GeV is at least a factor of 5.

Multi-object events are generally dominated by combinatorial background from pileup. This background can be reduced by associating tracks to the objects and then requiring that the objects are

Table 7. Likely operating points for tracking based pileup rejection in different regions of the detector. The Reference scenario for L1Track has $p_{\mathrm{T}} > 4$ GeV and $|\eta| < 4.0$, the Middle scenario has $p_{\mathrm{T}} > 4$ GeV and $|\eta| < 3.2$ and the Low scenario has $p_{\mathrm{T}} > 8$ GeV and $|\eta| < 2.5$. It should be noted that the jet η ranges are narrower than the L1Track acceptance.

Track p_{T} cut	jet p_{T}	jet η range	Hard-scatter jets efficiency	Pile-up jets efficiency
> 1 GeV	20 - 30 GeV	$\|\eta\| < 2.4$	96%	25%
> 2 GeV	20 - 30 GeV	$\|\eta\| < 2.4$	87%	9%
> 4 GeV	50 - 70 GeV	$\|\eta\| < 2.4$	91%	2%
> 4 GeV	50 - 70 GeV	$2.4 < \|\eta\| < 3.2$	85%	4%
> 4 GeV	50 - 70 GeV	$3.2 < \|\eta\| < 3.8$	86 %	5%
> 8 GeV	50 - 70 GeV	$\|\eta\| < 2.4$	61.5%	0.7%

from the same primary vertex. In the Reference and Middle scenarios, tracks with $p_{\mathrm{T}} > 4$ GeV are fairly well matched to the jet and tau candidates that satisfy the L0 trigger.

In the Reference scenario, L1Track is deployed out to $|\eta| < 4.0$, in the Middle scenario $|\eta| < 3.2$ and in the Low scenario $|\eta| < 2.5$. The performance of L1Track on selecting hard-scatter jets and on rejecting pileup jets is shown separately for three ranges in η in Table 7. As can be seen from the table, the $p_{\mathrm{T}} > 8$ GeV limitation in the Low scenario leads to an efficiency of only 61% for hard scatter events, severely restricting the usefulness of the L1Track to remove the pileup contribution to multi-jet events. In the Low scenario it is likely that L1Track will be used only for electron and tau identification in the region $|\eta| < 2.5$. Therefore the tracker acceptance in the interval $2.5 < |\eta| < 2.7$ is not instrumented with L1Track in the Low scenario.

L1Track is being designed so that on average it can process data from about 10% of the ITk. The objects that need to be processed by L1Track can be customised to optimise the trigger selection.

It is currently foreseen to use nearly identical hardware for L1Track and for the hardware based EF tracker FTK++ (see Section III.6.1). The largest difference between the two systems is that L1Track must deliver track candidates to L1Global so that it can provide trigger flags to the CTP within the 30 μs L1 latency. In the L1Track system, the limited latency available requires that two copies of each pattern are needed. Work is ongoing to better understand the latency of the L1Track system; if a factor of two in patterns is not needed to meet the required latency, the p_{T} requirement could be reduced to $p_{\mathrm{T}} > 2$ GeV which would result in a large gain in efficiency for tagging hard-scatter jets.

ATLAS has also considered conceptual designs of a self-seeded track trigger that would run at the full beam crossing rate (40 MHz). These designs require doublets or triplets of silicon layers so that the first step of track finding can be done on the detector. To be useful, self-seeded track triggers would need to complete within the L0 latency. This is very challenging and precludes the use of pixel layers in track finding, limiting the z resolution of the tracks and preventing the system from being used at high η. Such designs are currently not compatible with the present ITk stave design favoured by ATLAS.

III.3.2 L1Global

The time-multiplexed L1Global trigger system receives input from the LAr and Tile calorimeters, from the L0 FEXs. from the L0 muons trigger processors and from L1Track. The full calorimeter information is available for selected RoIs and reduced data are available for the entire calorimeter. It is foreseen to transfer calorimeter data to the L1Global processor with a latency of approximately 1-2 μs after the L0 trigger decision. Unlike the L0 calorimeter FEX processors, the L1Global pro-

cessors will be time multiplexed. At a L0 Accept rate of 1 MHz a new event will arrive approximately every 1 μs and be assigned in a round-robin fashion to the next available processor. Each processor is busy with a given event for approximately 24 μs. During this interval, the data are transferred from the calorimeter readout to one of the processors and are subsequently processed. After calorimetry processing, tracks arrive from L1Track, a trigger decision is reached and it is forwarded to the L1 CTP.

In order to handle fluctuations in the event rate, approximately 40 processors will be needed. Calorimeter data are transferred from approximately 350 elements of the LAr and Tile back-end processors. To avoid unnecessary queueing five outputs for each element are foreseen. Time multiplexed events will be made available via aggregators that will collect L1 data from the calorimeters (see Sections V.2 and V.3).

Each L1Global processor will be designed with an input bandwidth of at least 0.8 Tb/s. This is not quite enough to read out the entire granularity of the LAr and Tile calorimeters in 1-2 μs, but it is sufficient to readout detector elements with energy significantly above the pileup noise. Using these reduced data L1Global could do jet finding, including some iterative jet finding such as the anti-k_{T} algorithm that is currently used in the Run 2 HLT trigger. After the jet finding is complete, the jets can be associated to tracks from L1Track and these tracks can be used to reject jets not associated with the primary vertex. It will also be possible for L1Global to apply almost the same jet-energy scale corrections as the offline analysis. This will increase the overlap between jets selected at the L1Global and those reconstructed in the EF and the offline.

In addition to the reduced data, full longitudinal and transverse granularity would be available for electrons, photons and decaying taus decaying in hadronic final states. Using the calorimeter data, the L1Global processors will calculate many of the quantities presently used for particle identification. After the calorimeter reconstruction is complete, the tracks can be used to improve background rejection for electrons and to improve the energy estimate for hadronically decaying taus. The improved calorimeter reconstruction in L1Global is needed to obtain the precision position matching needed to obtain the target electron rejection at L1. The evolving ATLAS likelihoods and Boosted Decision Tree (BDT) methods used for electron, photon and tau identification will be implemented in the L1Global processor.

In the L1Global processors It will also be possible to match tracks from L1Track with L0 muon triggers. It is expected that the MDT L0 muon system will have excellent momentum resolution and will be able to reject many of the low momentum muons that would otherwise pass the trigger p_{T} requirement. Almost all of the remaining low-p_{T} muons, for example, muon candidates that lack MDT hits or that are in low field regions of the acceptance, can be rejected by L1Global using tracks from L1Track. By only rejecting L0 muon candidates that are associated with tracks from L1Track, almost all low-p_{T} muons can be rejected without efficiency loss for high p_{T} muons.

In the case of multi-object triggers with electrons, muons and/or taus, L1Global can suppress combinatorial background from overlapping collisions by requiring the z coordinate of the objects near the beam spot are consistent with each other.

It is currently foreseen to implement L1Global using multiple high-performance FPGAs coupled with CPUs and possibly Graphics Processing Units (GPUs). The use of FPGAs allows data on more than one hundred fibres to be transferred simultaneously to the processor. Parts of the algorithm, such as cluster finding and the final step involving correlating tracking and calorimetry, will probably perform best if implemented in FPGAs. The FPGA part of the algorithms are likely to need only a small amount of the L1Global latency budget. Iterative procedures are likely to be accomplished using CPUs and/or GPUs and will require more of the latency budget.

The conceptual design of the L1Global system has evolved considerably since the Phase-I LoI. The design is largely the same in the three readout scenarios, as the system is dominated by the

large volume of data from the calorimeter.

III.4 Central Trigger Processors

The L0 CTP will collect trigger flags from the L0 Topological Processor and information from auxiliary triggers using specialised detectors. The L0 CTP will form combinations of the input information and also apply pre-scales and vetoes to triggers, control the overall and instantaneous trigger rate, introducing preventative dead time when required and issue the L0 Accept. The L0 CTP will ensure that detector buffers do not overflow by using leaky-bucket type algorithms as is presently done in the existing L1 CTP. It will also reject triggers whenever busy is asserted by any of the detector subsystems of ATLAS.

The L0 CTP will broadcast the accepted triggers to the topological processors which will in turn distribute the accepted RoIs to L1 systems. The merging of theRoIs from the topological processors and their translation into requests to read out individual tracking and calorimeter detector elements is currently costed as part of L1Global.

One component of the L0 CTP system is the L0 muon CTP interface (MuCTPI) that aggregates and merges the trigger information from the barrel muon and end-cap muon system before passing it on to the CTP and to the L1Global trigger.

The L0 CTP will be closely coupled to the L1 CTP. The L1 CTP collects trigger flags from the L1Global processors as well as any auxiliary triggers from the L0 CTP. After applying pre-scales and vetoes, the L1 CTP will issue L1 Accepts at a fixed latency from the originating beam crossing as is needed by legacy electronics.

The L0 and L1 CTP ensure that L1Track and L1Global do not overflow, monitoring the processor occupancy and if necessary introducing dead-time and suspending the generation of L0 Accepts until L1 capacity is available.

The L0 and L1 CTPs are foreseen to be located in the same Advanced Telecom Computing Architecture (ATCA) crate, possibly together with the L0 topological processors.

The scope of the L0 and L1 CTP systems is largely the same in all three scenarios.

III.5 Data Acquisition and Data-flow

The data acquisition system after the Phase-II upgrade of the ATLAS detector will be based on commercial components. Data from the detector readout will be transferred to the Front-End Link Interface eXchange (FELIX) system using either the GBT protocol or one of a few other similar protocols. In FELIX, the data are then transferred to a commercial network that will transport events to monitoring and calibration processors and also to the Event Filter (EF) where they can be processed using commodity computing hardware and custom track processors such as FTK++ described in Section III.6.1. A schematic diagram of this system is shown in Figure 4.

III.5.1 Detector Readout

The Phase-II FELIX system will be an evolution of the one that is being developed for the Phase-I upgrade [8]. In Phase-I this concerns the readout of the NSW, LAr Trigger Digitizer Board (LTDB), LAr Digital Processing System (LDPS), and the Phase-I L1Calo FEX system (that will become the L0Calo after the Phase-II upgrade).

The conceptual design of the FELIX system for Phase-II has not significantly changed since the ATLAS Phase-II LoI [1]. The FELIX system will use a commercial FPGA-based PCI Express (PCIe) card that handles data from the detectors that are then routed to a Network Interface Card (NIC)

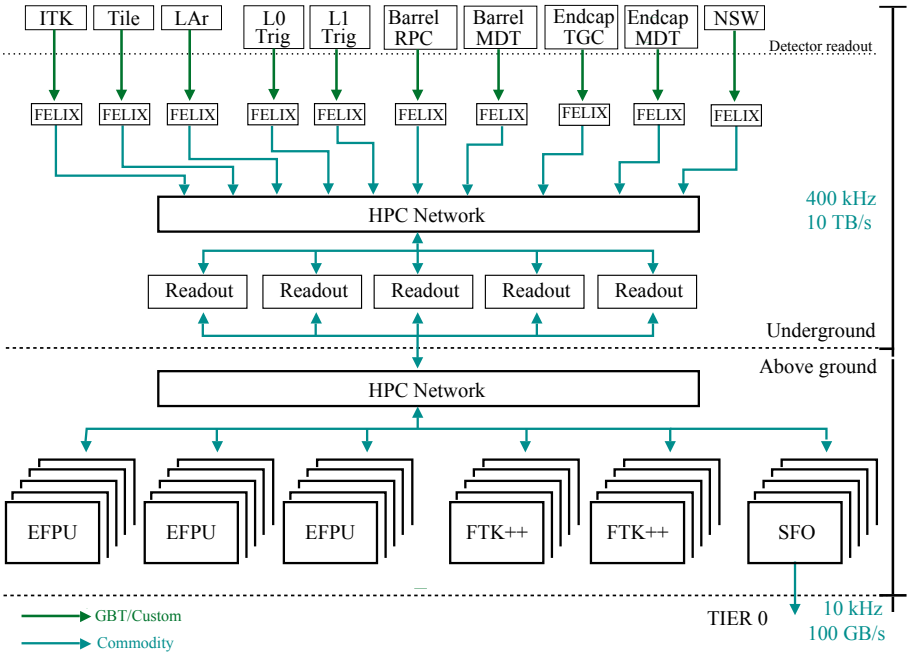

Figure 4. Overview of the Phase-II Data Acquisition and EF systems showing the flow of data from the detector readout to the EF computing farm.

which is attached to a commodity network switch. This commercial FPGA-based PCIe card will be re-specified for Phase-II to use more powerful FPGAs and to allow the use of higher-speed optical links. In addition, this card will be configured, as necessary, to send selected input data on low-latency links to the L1Track and L1Global processors (see Figure 2). The optimal path for data to be transferred from the detector readout to the L1 trigger sub-systems is currently under study. The FELIX system will also relay the Phase-II Timing, Trigger and Control system (TTC) information to the detector front end electronics. The TTC system will contain information about L0 and L1 Accepts as well as the Trigger Type that can be used for selective readout of parts of the detector.

The FELIX system also allows a powerful network of monitoring and calibration nodes to receive data from the detector electronics at high rates. These nodes will provide similar functionality to that of the Run 1 and Run 2 RODs.

The cost of the FELIX system is driven by the η coverage of the ITk detector and by the L1 readout rate.

III.5.2 Data-flow

A high-performance network is needed to transport, build and record the events from FELIX processors. This network will evolve from the system described in Ref. [8] to handle the needs of the larger events and higher rates. The ATLAS event size is expected to increase from the current size of ~ 1.5 MB to approximately ~ 5.0 MB at $\mathcal{L} \simeq 7.5 \times 10^{34} \mathrm{cm}^{-2}\mathrm{s}^{-1}$ due to high pileup and the increased number of channels in the ITk. In the Reference scenario, the network must accommodate a 400 kHz trigger rate, a factor of 4 larger than today.

The Data-flow system includes dedicated server nodes for event building. Fragments of events accepted by the L1 trigger will be routed to a given server node and the fragments will be assembled into events that are then routed to the EF, which is described below.

The Data-flow system also includes the data recording hardware called the Sub-Farm Output (SFO), which comprises the commodity hardware needed for recording and buffering the events selected by the EF. The SFO will record data at 10 kHz in the Reference Scenario and 5 kHz in the Middle and Low Scenarios.

III.6 Event Filter

The Event Filter (EF) is a large farm of commodity processors that runs selection algorithms designed to reduce the rate of events read out, from the L1 rate, 400 kHz in the Reference scenario and 200 kHz in the Middle and Low scenarios, to a lower one that can be permanently stored. The expected recording rate is 10 kHz in the Reference scenario and 5 kHz in the Middle and Low scenarios requiring that an average rejection factor of at least 40 is achieved in the EF.

Given the excellent performance expected of L1Track and L1Global, it will be difficult to obtain high rejection factors for single electrons and muons. For example, in Run 1 and Run 2, HLT electron selections gave a rejection of 200. It is expected that this rejection will be reduced by at least a factor of 10 to 20 after the Phase-I and Phase-II upgrade since many elements of the selection will have already been applied at L0 and L1. One element available in the Phase-II EF, but not at L1, is tracking in RoIs at low p_{T}, e.g. down to 1 GeV. These low p_{T} tracks can be used in tight isolation cuts that have minimal sensitivity to pileup by requiring that the reconstructed tracks come from the same primary vertex as the electron and muon candidates. After these tight isolation cuts it is expected that output rates for electrons with $p_{\mathrm{T}} > 22$ GeV and muons with $p_{\mathrm{T}} > 20$ GeV will be approximately 2.2 kHz each. For the Middle and Low scenarios, additional selections based on other high-p_{T} objects in the events, such as jets, are needed to reduce these rates to 1 kHz (each) and below. These additional EF-level selections will complicate physics analyses based on single-lepton triggers and could lead to larger systematic uncertainties.

Since the rejection with respect to L1 at the EF for isolated single electrons and muons is less than 40, the remaining selections will need to be tighter. For the majority of the hadronic menu and for lepton triggers which do not pass an isolation requirement, full-event tracking is required in order to reconstruct pile-up corrected quantities needed for the EF selection. In the Phase-I configuration of ATLAS, FTK is able to do full tracking on every event accepted by the EF. In Phase-II FTK++ (see Section III.6.1) will not be able to process every event. In the Reference scenario 100 kHz of the 400 kHz L1 rate will be processed with full tracking. In the Middle and Low scenarios, full tracking is limited to 50 kHz which significantly increases the thresholds for hadronic triggers and decreases the physics performance.

In all of the scenarios, the selection of events for recording to permanent storage from the hadronic menu will require intensive use of analysis level cuts based on kinematic quantities, such as invariant mass, and on jet-level measurements, such as b-tagging. These analysis-level cuts will rely on the high quality of the FTK++ tracks and on specialised tracking in specific regions of the detector done in the general purpose CPUs of the EF.

III.6.1 FTK++

FTK++ will be designed to find tracks in a similar way to the FTK processor that is currently being developed for the Phase-I upgrade. In contrast to L1Track, the FTK++ tracking processors are designed to find tracks in the entire ITk region and not just in RoIs. The longer latency and lower input rate for FTK++, allows tracks to be found down to lower transverse momenta. In the Reference scenario, FTK++ covers the angular range $|\eta| < 4.0$ and will include all ITk layers, with tracks available down to a p_{T} of 1 GeV. The η coverage of FTK++ follows the ITk coverage in the Middle and Low

scenarios. As with L1Track, in the lowest scenario, savings are obtained by raising the p_{T} threshold, in this case to 2 GeV, again giving reduced physics performance.

Many of the electronics modules in the FTK++ system will be common to the L1Track system. Some modifications will be needed for FTK++ since it is not required to process events in a fixed latency. In addition, FTK++ will be designed so that it can also be used to process simulated events during those times when services are available at Point-1 and the LHC is not operating.

Instrumenting the full tracker in the Reference scenario with $|\eta| < 4.0$ and for $p_{\mathrm{T}} > 1$ GeV requires that the FTK++ system contains approximately 13 billion patterns. Because sophisticated algorithms with very large rejection factors must be employed in the EF, FTK++ must have close to 100% tracking efficiency for low p_{T} tracks in jets. The requirements on L1Track are less stringent. As a consequence FTK++ requires more patterns than L1Track for a given angular and momentum range. On the other hand, if the FTK++ system operates at 100 kHz, only a single copy of each pattern is needed. The number of patterns needed for a given η and p_{T} range is similar for the two system.

Restricting the η coverage of the tracker in the Middle and Low scenarios reduces proportionally the costs of the FTK++ and L1Track. In the Low scenario, increasing the p_{T} cut from 1 to 2 GeV in FTK++ and from 4 to 8 GeV in L1Track reduces the cost by another factor of approximately two for both systems.

The proposed split, even in the Reference scenario, of the L1Track and FTK++ systems results in a considerable cost savings. Running FTK++ on entire events with a steady state rate of 1 MHz would require an additional factor of 10 in patterns and track-fitting resources. Thus, full-event tracking at the L1 rate is apparently cost prohibitive; it may be possible to improve the physics performance further by optimising the deployment of resources between L1Track and FTK++. Other improvements may be found during the course of the R&D programme that is described below in Section III.8.

III.7 Trigger Menus

In this section simplified illustrative trigger menus for the three scenarios are presented. The simplified menus contain the items that have been used in the physics studies presented in this document and cover most of the physics processes of interest at HL-LHC. The actual menus will be much more complex and will probably contain more than a thousand items with many supporting triggers that are needed for efficiency and performance studies.

An important feature of the menus is the reasonably low p_{T} thresholds for single-lepton triggers which are 22 GeV for electrons and 20 GeV for muons. As Run 1 experience has shown, these thresholds are low enough to trigger efficiently on leptons from SUSY and electroweak processes including Higgs boson decays. Another priority in the menu is the L0 triggers for hadronic decays of τ leptons which have been very important for our Run 1 studies of the Higgs boson. The hadronic menu contains several items with overlapping rates. These triggers make possible studies of fully hadronic processes such as $HH \to b\bar{b}b\bar{b}$ and are designed to maintain reasonable efficiency for challenging processes such as $ZH \to \nu\bar{\nu}b\bar{b}$.

The simplified illustrative menu for the Reference scenario is shown in Table 8. The L0 rates involving electrons, muons and taus have been estimated by scaling trigger rates from Run 1 ($\sqrt{s} = 8$ TeV and $\mu < 40$) to the expected conditions for HL-LHC ($\sqrt{s} = 14$ TeV and $\mu \simeq 200$). These extrapolations have been checked against the first Run 2 data ($\sqrt{s} = 13$ TeV and $\mu = 27$), but nevertheless have uncertainties of at least 10%. The hadronic rates are more difficult to estimate as the effects of pile-up on the observables are more complicated than for leptons and because the pile-up suppression techniques are rapidly evolving. These rates have been predicted using an improved version of the Monte Carlo simulation developed for Ref. [8].

The rejection factors used to predict the L1 rates in Table 8 are modest given that the efficiency loss at L1 is required to be minimal. Higher rejection factors could be obtained at the cost of decreased efficiency. The rejection factors are based on the studies similar to those performed for the ATLAS Phase-II LoI [1] which indicate that a factor of five rejection can be obtained for single electrons. Multi-object trigger rates are dominated by overlaps between different interactions occurring in the same bunch crossing. These overlapping interactions can be rejected effectively using L1Track at L1 by requiring that the longitudinal impact parameters of the tracks associated with objects are consistent with each other.

The rates at the EF for single objects are extrapolated from algorithms used in the Run 2 trigger. The hadronic rejection is assumed to be a factor 50 beyond what can be done at L1 and is crucially dependent on tracking from FTK++ over the full ITk acceptance. The EF hadronic rates given in the table include additional rejection, based on full-detector tracking from FTK++, that is used to further reject pileup and from analysis based algorithms such as b-tagging.

The totals in Table 8 include explicit overlap removal for the hadronic triggers and a fraction of supporting triggers that is similar to what was used during Run 1.

Table 8. Simplified illustrative menu for the Reference scenario. There are considerable overlaps in the rates, especially from the hadronic triggers. The totals also allow for pre-scaled supporting triggers which are not listed in the tables. * For hadronic items, the EF rates assume additional rejection from b-tagging and other event-level analysis algorithms. **Forward jets also include multi-jet triggers with lower thresholds and requirements on other quantities such as invariant mass.

Item	Offline p_{T} Threshold [GeV]	Offline $\lvert\eta\rvert$	L0 Rate [kHz]	L1 Rate [kHz]	EF Rate [kHz]
isolated Single e	22	< 2.5	200	40	2.20
forward e	35	$2.4 - 4.0$	40	8	0.23
single γ	120	< 2.4	66	33	0.27
single μ	20	< 2.4	40	40	2.20
di-γ	25	< 2.4	8	4	0.18
di-e	15	< 2.5	90	10	0.08
di-μ	11	< 2.4	20	20	0.25
$e-\mu$	15	< 2.4	65	10	0.08
single τ	150	< 2.5	20	10	0.13
di-τ	40,30	< 2.5	200	30	0.08
single jet	180	< 3.2	60	30	0.60*
fat jet	375	< 3.2	35	20	0.35*
four-jet	75	< 3.2	50	25	0.50*
H_{T}	500	< 3.2	60	30	0.60*
$E_{\mathrm{T}}^{\mathrm{miss}}$	200	< 4.9	50	25	0.50*
jet + $E_{\mathrm{T}}^{\mathrm{miss}}$	140,125	< 4.9	60	30	0.30*
forward jet**	180	3.2 - 4.9	30	15	0.30*
Total			~1000	~400	~10

Table 9 shows a comparison of the offline p_{T} thresholds, η coverage and efficiency for the three different scoping scenarios. The two largest effects on the menu from scoping changes inside the TDAQ system come from raising the p_{T} cutoff for tracks in L1Track from 4 to 8 GeV in the Low scenario and from changing the rate of full tracking provided by FTK++ from 100 kHz in the Reference scenario to 50 kHz in the Middle and Low scenarios. Since many low-momentum jets have no tracks above p_{T} of 8 GeV, L1Track has little pileup-rejection capability in the Low scenario.

The differences in muon efficiency are caused by the variation in coverage of the new layers of barrel muon chambers among the three scenarios.

Table 9. Simplified illustrative menus for the Reference, Middle and Low scenarios. The p_{T}cut refers to the typical offline cut which will be used with the trigger. In general, efficiency refers to the efficiency of the trigger selection with respect to the offline selection. For the electrons, the inefficiency is largely due to L1Track. In the case of muons, the efficiency refers only to the barrel muon efficiency. In the case of hadronic variables, such as jets, H_{T}, $E_{\mathrm{T}}^{\mathrm{miss}}$, etc. the efficiency refers to the efficiency at the threshold p_{T}. At higher $p_{\mathrm{T}}$the efficiency is expected to be 100%. ** Forward jets also include multi-jet triggers with lower thresholds and requirements on other quantities such as invariant mass.

item	Reference			Middle			Low		
	p_{T} Threshold [GeV]	$\lvert\eta\rvert$	Eff.	p_{T} Thr. Threshold [GeV]	$\lvert\eta\rvert$	Eff.	p_{T} Thr. Threshold [GeV]	$\lvert\eta\rvert$	Eff.
iso. Single e	22	< 2.5	95%	28	< 2.5	95%	28	< 2.5	91%
forward e	35	$2.5 - 4.0$	90%	40	$2.5 - 3.2$	90%	-	-	-
single γ	120	< 2.4	100%	120	< 2.4	100%	120	< 2.4	100%
single μ	20	< 2.4	95%	25	< 2.4	80%	25	< 2.4	65%
di-γ	25	< 2.4	100%	25	< 2.4	100%	25	< 2.4	100%
di-e	15	< 2.5	90%	15	< 2.5	90%	15	< 2.5	82%
di-μ	11	< 2.4	90%	15	< 2.4	80%	15	< 2.4	65%
$e - \mu$	15	< 2.4	90%	15	< 2.4	84%	15	< 2.4	70%
single τ	150	< 2.5	80%	150	< 2.5	80%	150	< 2.5	80%
di-τ	40,30	< 2.5	65%	50,40	< 2.5	65%	50,40	< 2.5	55%
single jet	180	< 3.2	90%	225	< 3.2	90%	275	< 3.2	90%
fat jet	375	< 3.2	90%	400	< 3.2	90%	450	< 3.2	90%
four-jet	75	< 3.2	90%	85	< 3.2	90%	90	< 3.2	90%
HT	500	< 3.2	90%	600	< 3.2	90%	750	< 3.2	90%
E_T^{miss}	200	< 4.9	90%	225	< 4.9	90%	250	< 4.9	90%
jet + E_T^{miss}	140,125	< 4.9	90%	150,175	< 4.9	90%	160,200	< 4.9	90%
forward jet**	180	3.2 - 4.9	90%	225	3.2 - 4.9	90%	275	3.2 - 4.9	90%

III.8 Areas where R&D is needed

The major topics driving the TDAQ R&D are summarised below. The list is not exhaustive, a detailed R&D plan is being developed in the context of the TDAQ Initial Design Review that will be completed in early 2016. It is expected that many of the questions associated with these topics will be closed in time for the TDAQ TDR in late 2017. For a few items, such as those associated with L1Track and FTK++, it may be necessary to define specific options for evaluation after the TDAQ TDR.

1. The L0 muon trigger system will have processors very much like the ones used in the NSW. R&D studies are needed in two areas:

   1.A An investigation of the best method to implement segment finding and fitting in the MDT trigger will be performed to be sure that the processing of the MDT data can complete within the latency requirement of the L0 trigger. Studies of how fitting can be most economically implemented will also be undertaken. MDT segment finding and fitting requires modest resources and smaller devices can be used than for the L1Global processor.

   1.B Studies of the best way to combine information from the NSW, TGC and RPC with MDT track segments will be performed. These studies will focus on finding a strategy to implement track fitting with low-end FPGAs.

2. The L1Track trigger and FTK++ track finder at the EF input are expected to be based around

Associative Memory (AM) ASICs as used in the Phase-I FTK. Four R&D topics for the L1 track trigger, FTK++ and the AM are listed below.

2.A An investigation of the parameters (pattern density, power consumption and bandwidth) needed in the upgraded AM ASIC will be made.

2.B Studies of alternative AM chip development paths that could simplify the overall design and increase AM ASIC flexibility will be undertaken. One idea is to integrate the AM chip with an FPGA in the same package. The issues to be considered include cost when in production and other practical challenges, such as the availability of the appropriate packaging technologies.

2.C The track-fitter performance available with the FPGAs to be used in Phase-II will be studied as a function of cost.

2.D Other issues related to the configuration of FTK++ and L1Track will be explored, including the network connectivity (e.g. 100GbE) and the cooling strategy. The power per board is driven by cooling capability. Increasing the power per board is potentially a way to decrease costs. This will allow the configuration of AM chips, FPGAs and local memory on the main FTK++/L1Track boards and their mezzanines to be optimised. In addition the number of different boards needed in the system will be minimised.

3. The L1Global processor and pre-processor are dependent on algorithms very much like what is currently used in HLT. R&D studies are needed in three areas.

3.A Studies of the best method to implement the needed physics algorithms using the combined tracking, calorimeter and information will be performed. The L1Global algorithms include electron and photon identification, tau identification, jet identification and the optimal reconstruction of missing-transverse momentum. Studies will be made to find the best hardware solutions, for example specialised FPGAs, GPUs and CPUs, that will allow these algorithms to execute in 10 to 20 μs.

3.B Network solutions that can be used to move data with low latency to the hardware executing the algorithms will be studied.

3.C The optimal distribution of the algorithms among processors will also be studied. For example, it may be most efficient to form topological clusters first, within the LAr and Tile system, and then transport composite objects to the L1Global processor. Alternatively, time multiplexing that allows for global processing of the events may be the most efficient. The optimal method will critically depend on available network bandwidth and latency, as well the capability of the prototype event processors and the firmware algorithms used to form the clusters.

4. The Central Trigger Processors will be adapted to the architecture of the Phase-II upgrade. The following R&D topic will be examined.

4.A The structure of the L0 and L1 CTPs will be studied to allow optimal communication among the processors. CTP R&D is already occurring in the course of Phase-I. An improved CTP has already been deployed for Run 2, but will need to be replaced to accommodate the Phase-II architecture. A new MuCTPI will be deployed after LS2 to accommodate new requirements from the NSW.

5. The following Detector Readout and DAQ Hardware R&D topics will be considered.

5.A The FELIX system will be studied to find a commercial system that provides the interface between GBT signals and the commercial networks, including the integration of the TTC.

5.B The optimal integration of the commercial hardware and software for the ATLAS DAQ system will be found, including the required in-house developed “glue”.

III.9 Prototyping and R & D plans

Many aspects of the Phase-II TDAQ upgrade are already being explored in the Phase-I upgrades that are currently ongoing.

Work is underway on the conceptual design of the MDT L0 trigger. This will require the fitting of MDT track segments within a time interval of approximately 1 μs. These algorithms are similar to those being used in the Phase-I NSW Trigger Processor, which has even tighter time constraints. The experience gained will help in designing the processors and algorithms for the MDT trigger.

The FTK++ Phase-II project is building on the FTK AM-based track-finding system for the Phase-I upgrade that should already be fully commissioned and working by the time of the TDAQ Phase-II TDR in Q4 of 2017.

The Phase-I FTK will do full tracking for the current ATLAS tracker and it will operate with a rate of 100 kHz. Initially the Phase-I FTK will work with pile-up of $\mu < 40$, but the hardware resources will be scaled up to work with larger pile-up levels if this is needed. Integration of this device into the ATLAS EF will help us to better understand how to effectively use fast tracking in physics triggers and what changes can be made for Phase-II.

Given the large increase in pile-up and the complexity of the ATLAS ITk in Phase-II, ATLAS has a vigorous R&D programme for the AM that will be needed by FTK++ and L1Track. The AM06 chip for FTK, which was recently submitted for production, is one of the first 65 nm projects in high-energy physics. The goal of the R&D programme will be to develop an AM design in the 28 nm technology to allow for L1Track and FTK++ systems that can store more than one billion patterns. The performance of FTK++ and L1Track depends strongly on the number of patterns. For example, doubling the number of patterns used in L1Track could allow the p_{T} range in the Reference scenario to be extended down to 2 GeV, greatly improving its pile-up rejection capabilities. This R&D programme should be well underway by the time of the TDAQ Phase-II TDR.

The Phase-I calorimeter trigger upgrade relies on state-of-the-art FPGAs and optical links. While the Phase-II Global trigger differs conceptually from the Phase-I upgrade, it relies on similar components. The TDAQ institutes are gaining valuable experience in the design and layout of very large systems with hundreds of very high-speed optical and electrical links interconnecting FPGAs. This experience will be very helpful in designing the Phase-II system. Many of the prototypes for the Phase-I upgrade will be completed by the time of the Phase-II TDAQ TDR.

III.10 Cost Estimate

The Work Breakdown Structure (WBS) for the Phase-II TDAQ project is shown in Table 10. Also given in the table are the expected CORE costs of the items in the three scenarios. The difference in costing between the three scenarios is largely driven by factors external to TDAQ. The cost of L1Track and FTK++ depend on the η coverage of the tracker. The allowed rate at L1 is driven by the limit imposed by the legacy MDT electronics that is retained in the Middle and Low scenarios. The two choices reflected in the costing table that are internal to TDAQ are (i) the rate of full tracking by FTK++ which is reduced from 100 kHz in the Reference scenario to 50 kHz in the Middle and Low

scenarios and (ii) the p_{T} threshold for tracking in L1Track (4 GeV in the Reference and Middle scenarios versus 8 GeV in the Low scenario) and FTK++ (1 GeV in the Reference and Middle scenarios versus 2 GeV in the Low scenario).

III.11 Cost risk analysis

The TDAQ costs fall into two categories, custom electronics and commodity computing.

The cost of the custom electronics is typically equally split between the cost of producing and mounting components on the Printed Circuit Board (PCB) and the cost of the FPGAs that are used on the boards. In general the board and FPGA costs are proportional to each other. In low-end systems, only a few layers are needed on the PCB. On high-end systems the PCB may contain as many as 30 layers and must be produced with advanced techniques. The cost basis of these systems is accurately known from pre-prototype and prototype production from the Phase-I upgrade. It has been assumed that the performance of top-end systems will continue to improve in the future as it has in the recent past and that prices will remain stable. Industry trends will be carefully monitored in the future and adjustments made to the design in order to preserve physics performance, should the current trends not continue.

In addition to FPGA costs, about 15% of the FTK++ and L1Track costs consist of costs for the AM chip production. This is a custom integrated circuit and the production will be done in the same way as has been done with FTK. Once the full-sized chip is developed a pilot run will be done to produce the first production chips. This will be followed by the series production of the remainder of the chips. A failure of the pilot run due to a design flaw would require additional Non Recurring Engineering (NRE) investment, which is about 5% of the total project cost for FTK++ and L1Track. Every effort will be made to ensure that the pilot run succeeds, including a lengthy and exhaustive review process. Another avenue to reduce the risk is to spread the NRE among as many users as possible. ATLAS and CMS collaborators are working closely together with the goal of finding an AM chip solution appropriate for both experiments.

The price and performance of commodity computing hardware continues to evolve at a steady rate. The model used to estimate the costs of the commodity computing assumes continued increases in performance for a fixed price as have been observed in the recent past. An important element of risk mitigation for computing is the careful design of software so that future trends can be followed. For example, the number of computing cores per server continues to increase at constant price while the unit price of memory is declining only slowly. ATLAS software is being redesigned as part of the Phase-I upgrade to allow parallel execution of algorithms, which in turn, will result in a decrease in the memory need per core. Careful monitoring of trends in commodity computing coupled with a vigorous software effort for Phase-II will allow the ATLAS experiment to mitigate problems caused by changes in commodity computing.

The CORE cost in Table 10 are denominated in 2014 CHF. Most of the custom electronics costs will be expended in the local currency of the collaborating institutes and will not be subject to exchange rate risk. The commodity computing and high-end FPGA costs are largely tied to the USD, here there is some exchange rate risk for collaborating institutes if their local currency changes with respect to the USD. Similarly the production and NRE costs of the AM chip will be tied to the USD and exchange rate risk exists if the local currency of the institutes fluctuates with respect to the USD or if the funds are pooled in a third currency for the production and NRE costs.

Table 10. WBS for the TDAQ Project for the three scenarios. The costs are converted to CHF using 2014 exchange rates.

WBS	Item	Reference Total Cost [kCHF]	Middle Differential Cost [kCHF]	Low Differential Cost [kCHF]
1	**TDAQ system**	**43,305**	**-11,417**	**-18,194**
1.1	**L0 Central**	**1,206**	**-**	**-**
1.1.1	L0CTP	720	-	-
1.1.2	MuCTPI	279	-	-
1.1.3	RoI Distributor	207	-	-
1.2	**L0 Calorimeter**	**695**	**-**	**-241**
1.2.1	FEX	499	-	-241
1.2.2	Topo. Proc.	142	-	-
1.2.3	Optical Plant	49	-	-
1.2.4	L0Calo-to-L1Calo	5	-	-
1.3	**L0 Muon Endcap**	**2,557**	**-110**	**-110**
1.3.1	TGC Sector Logic	1,777	-	-
1.3.2	End-cap MDT Trigger	780	-110	-110
1.4	**L0 Muon Barrel**	**1,320**	**-145**	**-171**
1.4.1	RPC Sector Logic	541	-35	-61
1.4.2	Barrel MDT Trigger	780	-110	-110
1.5	**L1 Central**	**1,933**	**-**	**-**
1.5.1	L1CTP	858	-	-
1.5.2	TTC	1,075	-	-
1.6	**L1Global**	**3,390**	**-**	**-**
1.6.1	Aggregator	843	-	-
1.6.2	Event Processor	2,546	-	-
1.7	**L1Track**	**4,191**	**-668**	**-2,494**
1.7.1	Processing	2,769	-422	-1,553
1.7.2	Second stage	1,422	-246	-940
1.8	**FTK++**	**13,035**	**-4,876**	**-9,561**
1.8.1	Processing	9,304	-3,437	-6,735
1.8.2	Second stage	3,731	-1,440	-2,826
1.9	**DAQ/EF**	**14,978**	**-5,616**	**-5,616**
1.9.1	Detector Readout	8,707	-961	-961
1.9.2	Dataflow	1,471	-905	-905
1.9.3	EF	4,800	-3,750	-3,750

III.12 Summary Schedule

The expected schedule for many of the items in the WBS of the TDAQ upgrade project is shown in Figure 5. After the TDAQ TDR, each of the major WBS components will develop preliminary designs and prepare the (Preliminary Design Reviews (PDRs)). Upon successful completion of each PDR the first prototype devices will be built. The Final Design Reviews (FDRs) will follow after successful construction of prototypes. When the FDR is completed successfully, the first module that will be able to be used in the experiment will be produced. Finally, a set of Production Readiness Reviews (PRRs) is scheduled to authorise the production of the modules and/or system for final construction. In some cases, especially for commodity hardware, the FDR and PRR can be combined. In other cases (for example, Detector Readout) a single PDR may be held for several systems.

The earliest items to be completed are the L0 CTP and L0 Calorimeter systems which are needed for the first detector commissioning. Experience from LS1 shows that approximately two years are needed to commission ATLAS after major changes.

Commodity hardware is delivered as needed. Detector readout hardware, such as FELIX, will be delivered as the detector system are installed. Other hardware, for example, some of the CPU servers in the EF, will be delivered during the first year of data taking. This allows the most performant machines to be purchased.

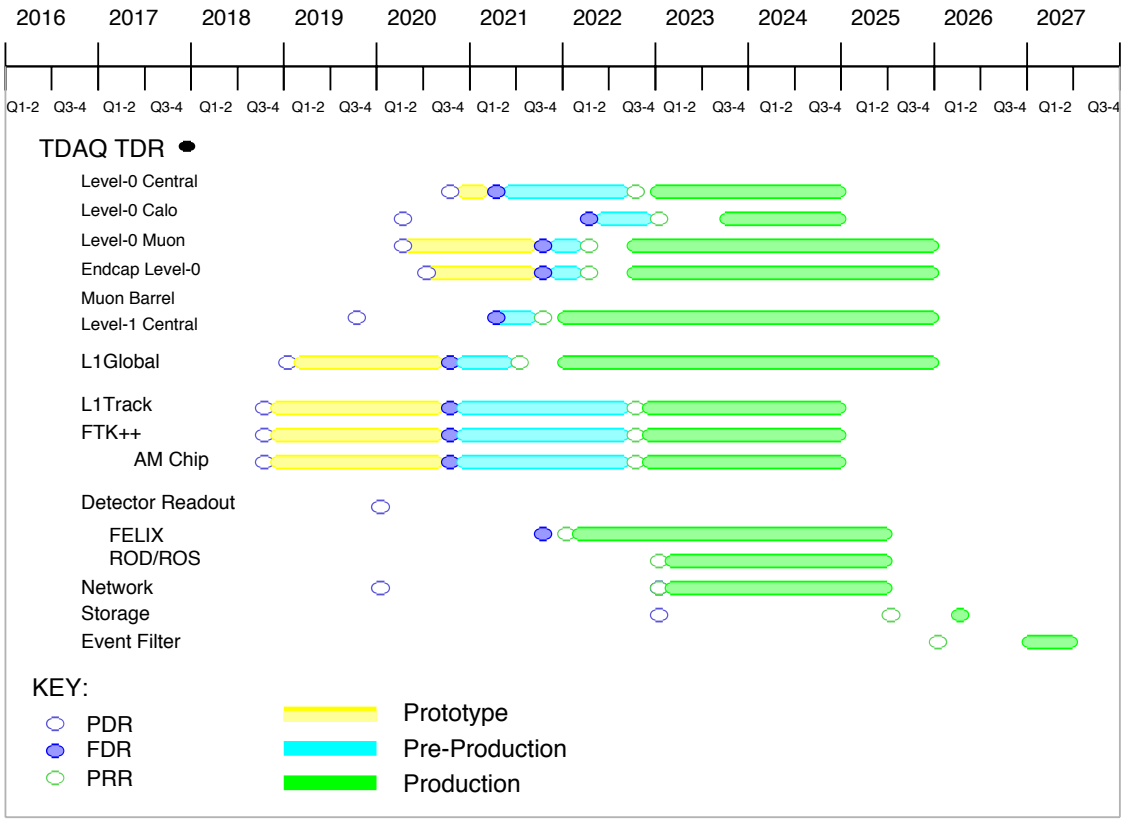

Figure 5. Expected schedule for major items in the TDAQ system. The coloured dots indicate the dates of the Technical Design Report (TDR), Preliminary Design Review (PDR), Final Design Review (FDR), and Production Readiness Review (PRR). The open black symbols show the production schedule for the final modules. No installation schedule is shown in the Gantt chart.

Chapter IV

Inner Tracker

IV.1 Introduction

The ITk for the Phase-II upgrade of ATLAS, as described in the LoI is an all-silicon tracker. It was designed to measure the transverse momentum and direction of isolated particles (in particular muons and electrons), to reconstruct the vertices of pile-up events and associate the vertex with the hard interaction. It is also able to identify secondary vertices in b-jets with high efficiency and purity, measure the tracks in the cores of high energy jets with high efficiency, provide good two-track resolution and ensure a low rate for reconstruction of fake tracks. It can identify the decay of tau leptons, including impact parameter information, and is also able to reconstruct the tracks associated with converted photons.

The LoI layout of the ITk forms the basis of the designs presented here for the Reference, Middle and Low scoping scenarios. A major change since 2012, when the LoI was written, is a much improved understanding [3, 4] of the importance for the HL-LHC physics programme of extending the tracking coverage well beyond $|\eta| = 2.7$, and matching this with improvements to other detector components at high $|\eta|$. In what follows, the LoI layout is described first, however for the reasons just outlined and detailed in Section XI.2, the Reference scenario layout includes additional pixel coverage to provide tracking to $|\eta| = 4.0$. This is the maximum coverage possible within the constraints of the current tracker volume in the z direction and a reasonable beam-pipe diameter. This Reference scenario tracker concept, with very forward coverage, is referred to here and elsewhere as the LoI-VF layout.

IV.1.1 Design, layout and differences with the existing tracker

The ITk will be immersed in the magnetic field from a 2 Tesla solenoid. The studies presented here use hybrid silicon pixel modules at the inner radii, surrounded by silicon micro-strip modules at larger radii. It is 6 m long (active length) and will fill all the available space in the detector cryostat out to a maximum active radius of 1,000 mm, including the space currently occupied by the straw-tube detector, the Transition Radiation Tracker (TRT). In the central (barrel) region there are four pixel layers followed by five strip layers (three with shorter strips and two with longer strips). To maintain the coverage and optimal performance in the transition region between the end of the barrel and largest radius of the end-cap there is also a short-stub barrel (radius 862 mm) of limited length in z. In this LoI layout, the coverage of the forward regions extends only up to $|\eta| = 2.7$ and is provided by a total of six pixel discs and seven strip discs. For an extended η-coverage more pixel discs are needed. The LoI layout has been optimised for coverage, and small gaps have been preserved between sub-detectors to allow for supports, services and insertion clearances.

The ITk has been designed to balance the tracking performance required for the Phase-II physics programme against the cost of construction. The required tracking performance builds on the lessons learnt during Run 1 and the performance of the ITk will be as good, and in most cases better, than the existing ID in an environment with significantly higher pile-up. For the Reference and Middle scenarios, the coverage of the ITk extends to higher values of η relative to the LoI layout, to maximise the physics potential at the HL-LHC. This region poses severe challenges to the design, construction, pattern recognition, track-reconstruction software and the robustness of the tracker to detector losses during operation in this very harsh environment. The LoI layout of the detector is shown in Fig. 6 and the resulting sensor areas and channel counts are shown in Table 11.

The design of the ITk takes advantage of new technology developed since the construction of the existing ID and its performance will be enhanced by a lower mass construction, reducing the effect of multiple scattering, photon conversions and hadronic interactions. The lower mass is achieved by a combination of several advances. More efficient multiplexed designs lead to fewer

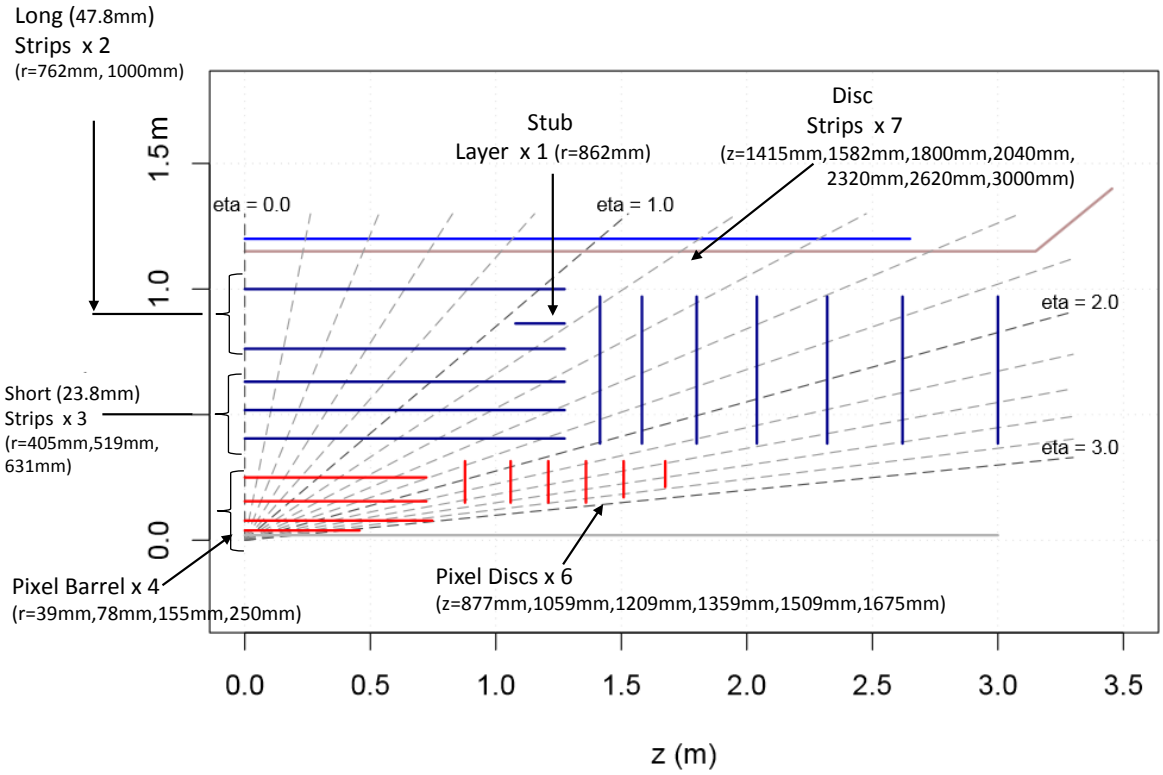

Figure 6. A cross-section of the ATLAS ITk tracker presented in the LoI showing the coverage of the pixel detector in red and strip detector in blue. The rapidity coverage extends up to $|\eta| = 2.7$ and is matched to the coverage of the muon system. The blue line outside the ITk volume represents the coil of the solenoid magnet.

Table 11. The surface area and channel count for different parts of the LoI layout configuration used for the performance and physics simulation of the Pixel and Strip detectors.

Detector	Silicon Area [m^2]	Channels [10^6]
Pixel barrel	5.1	445
Pixel end-cap	3.1	193
Pixel Total	8.2	638
Strip barrel	122	47
Strip end-cap	71	27
Strip total	193	74

cables for distributing HV and Low Voltage (LV) power to the detector modules. Higher performance cooling based on evaporative CO_2 technology allows the use of smaller diameter cooling pipes. The use of higher thermal performance carbon-composite materials and techniques, such as thermally-conducting carbon-foam and co-cured electro-mechanical assembly, lead to substantial mass reductions. Low-power, small feature size (65 nm and 130 nm) Complementary Metal-Oxide Semiconductor (CMOS) front-end electronics will be used. New readout technologies, combined with a new TDAQ architecture with much higher bandwidth than the present ID, allow the readout of large amounts of detector information in this very high pile-up environment while keeping mass low.

The ITk is designed for rapid installation and ease of access to take account of the activated environment which will be encountered close to the interaction point. The HL-LHC presents new challenges for the component and system reliability which are required to achieve the target lifetime for this complex detector. The ITk has much more stringent requirements on radiation tolerance than the existing ID and will have to employ more radiation-hard sensor technologies.

IV.2 Detector layout scenarios and rapidity coverage

As already mentioned in the introduction, work since the LoI has shown that the physics program is significantly enhanced with an increased pseudo-rapidity coverage with respect to the LoI layout. The Reference scenario therefore assumes an η-coverage to $|\eta| = 4.0$ as being the best compromise between the requirements of physics and constraints of space, material and services. The details of the best way to realise the extension are still an active area of investigation within the ITk community. The exact pseudo-rapidity cut-off must take into account the combined effects of: the decreased magnetic field at large z and small radius, the decreased lever-arm for tracks that originate in that region and the effects of increased material from the services that would be located in front of the calorimeter. In particular, additional material in this location must be carefully monitored, since it not only degrades the resolution of the forward calorimetry, but it also increases the flux of secondary particles into the forward regions of the ITk, which in turn increases the neutron fluence throughout the tracker cavity.

In preparation for the Strip and Pixel TDRs, a tracker layout task-force has been created, and has been reviewing the general requirements for the ITk layout and design, as well as looking at further optimisation of the Pixel and Strip layouts beyond the current LoI designs. Several variations are being examined, including detailed engineering considerations for the local and global supports, as well as the services. A wide range of performance and physics benchmarks are being used to evaluate these layouts, and the task-force is expected to report in early 2016. As a result of this work, the baseline ITk layout which will be described in detail in the ITk TDRs is expected to evolve from the present LoI designs discussed in this document. However, the overall cost for the ITk is not expected to change substantially in this process, although both cost and performance will be further optimised within the constraints imposed by the ITk requirements.

IV.2.1 Reference scenario layout

For the Reference tracker layout presented in this document the angular coverage provides full tracking capability to $|\eta| = 4.0$. This layout of the ITk system is shown in Fig. 7 and it is referred to here and elsewhere in the document as the LoI-VF layout. It has twelve pixel discs on each side of the detector to keep the number of space points on a track approximately constant up to $|\eta| = 4.0$. This detector layout can be considered as idealised, in the sense that it has not yet been optimised in terms of mechanical construction and maximum performance for a given silicon area, and the routing of services is very challenging, but the performance should depend mainly on the number

of space points and the segmentation, and so we have confidence that this layout provides a useful assessment of the relative performance variation between scenarios.

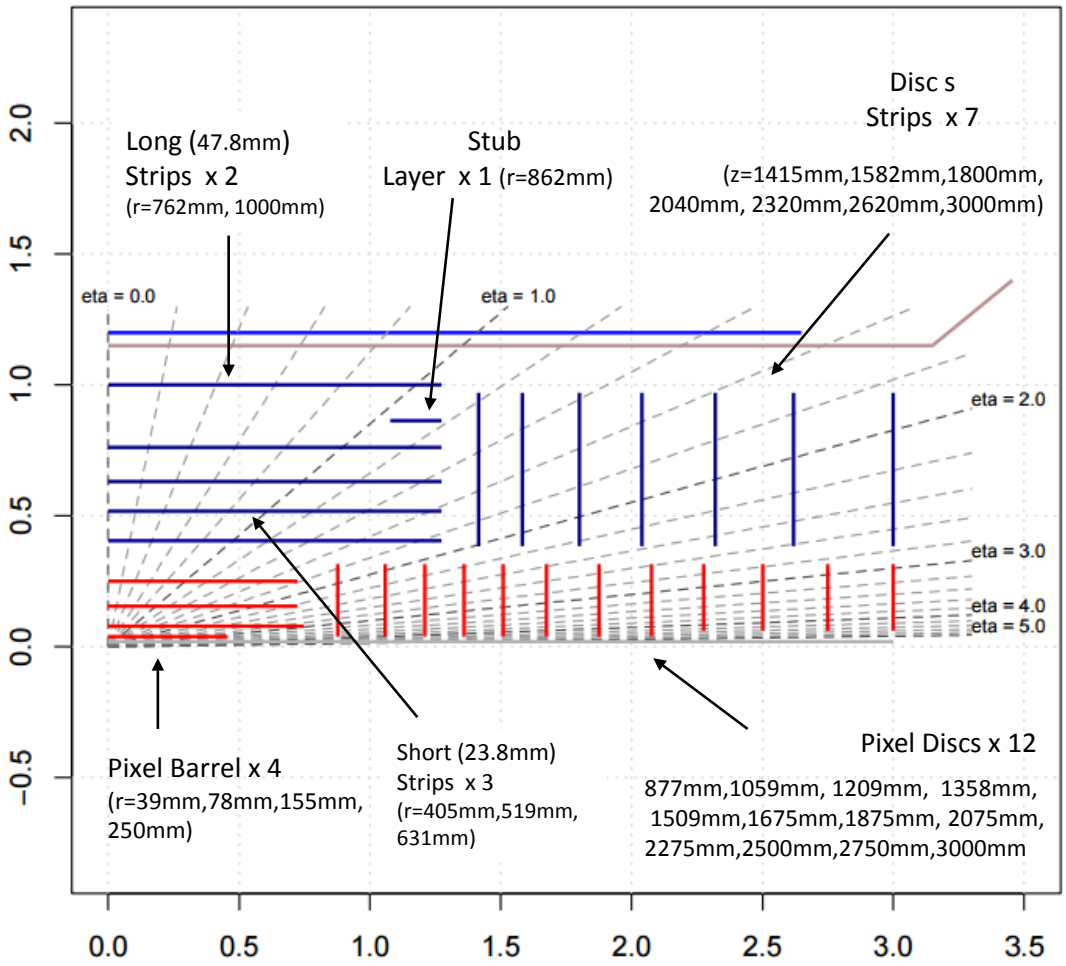

Figure 7. A cross-section of the LoI-VF layout showing the coverage of the pixel detector in red and the strip detector in blue. The pseudo-rapidity coverage extends up to $|\eta| = 4.0$. Blue and red lines represent strip and pixel layers, respectively. Horizontal and vertical lines represent barrel and end-cap layers, respectively. Lines of constant pseudo-rapidity are indicated. The blue line outside the ITk volume represents the coil of the solenoid magnet. This layout is used in the Reference scenario.

IV.2.2 Middle scenario layout

The layout of the ITk in the Middle scenario (shown in Fig. 8) introduces notable reductions compared to the Reference scenario. A pair of strip discs (i.e. the next to the last disc in z) and the stub layer are removed from the strip detector; and the η-range covered by the pixel discs is limited to 3.2. Due to the limitations of time for the preparation of this scoping document, no re-optimisation of the relative positions of the different detector elements has been attempted for this layout. The hit information (digitisation) from the regions which have been removed are not provided to the reconstruction software and are not used in the performance analysis. The material of the elements which have been removed, however, remains in the detector simulations. This layout explores a modest

reduction in the area of the Strip system at larger η-values to evaluate whether such reductions produce a non-negligible loss of performance. Similarly, the reduction in η-coverage provides sensitivity to the importance of the larger very forward tracking coverage provided in the Reference scenario.

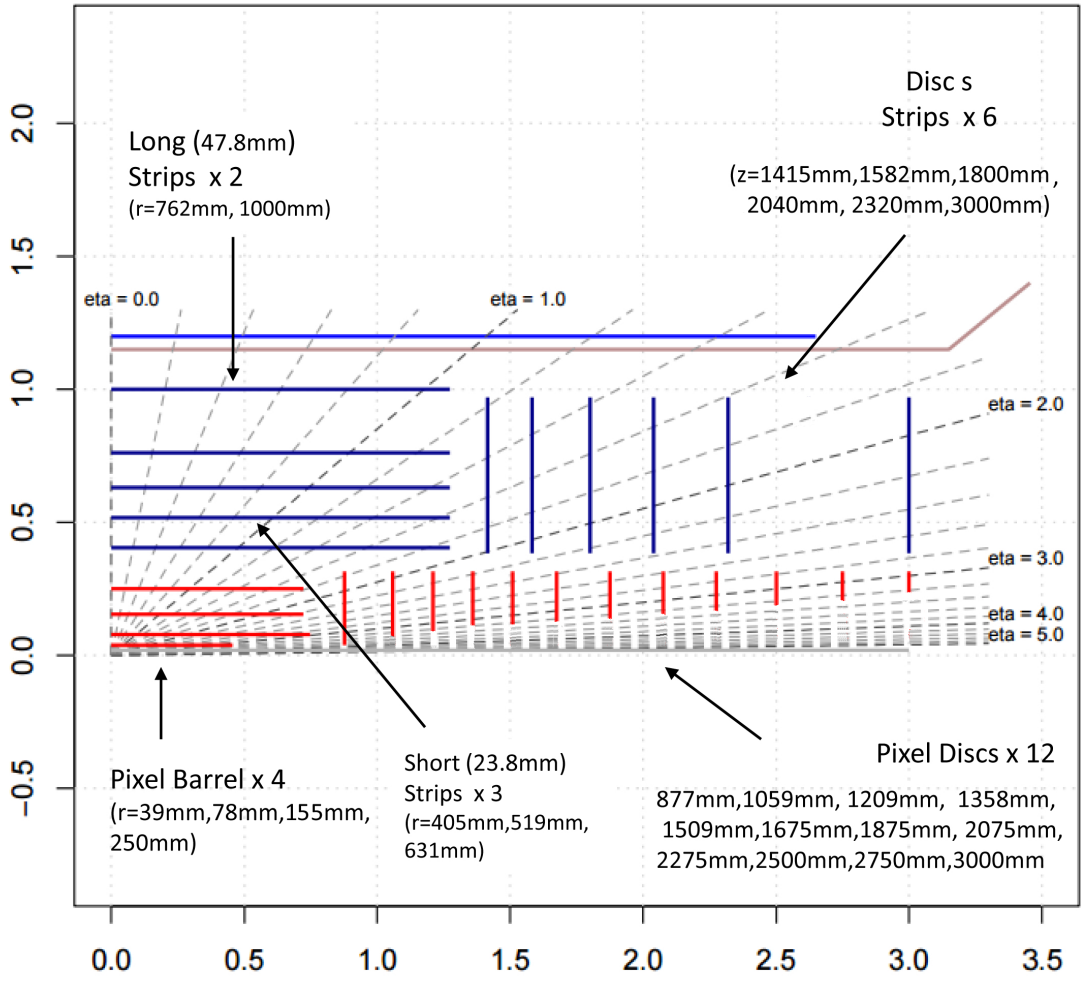

Figure 8. A cross-section of the Middle scenario layout, which is based on the LoI-VF layout. The pseudo-rapidity coverage extends up to $|\eta| = 3.2$. Blue and red lines represent strip and pixel layers, respectively. Horizontal and vertical lines represent barrel and end-cap layers, respectively. Lines of constant pseudo-rapidity are indicated. The blue line outside the ITk volume represents the coil of the solenoid magnet.

IV.2.3 Low scenario layout

In the Low scenario further reductions have to be made with respect to the Middle scenario. The tracker (pixel disc) η-coverage is further reduced to $|\eta| = 2.7$. The middle barrel of the strip system and one side of each of the double sided silicon strip modules on the two barrel layers which are adjacent to the middle layer, are also removed (see Fig. 9). The innermost and outermost strip barrel layers are left unchanged. Again, no attempt is made to re-optimise the module plane positions and the hit information (digitisation) from these regions is masked from the reconstruction software. The material for the elements which have been removed is still in the detector simulations. No z

information from the stereo layers is available from the two barrel layers where one side of the strip modules has been removed. For these modules the only measurement available is from the r-ϕ coordinate and the coarse segmentation of the strips in z. The changes (parts removed) from the LoI-VF (Reference) layout are shown in Table 12.

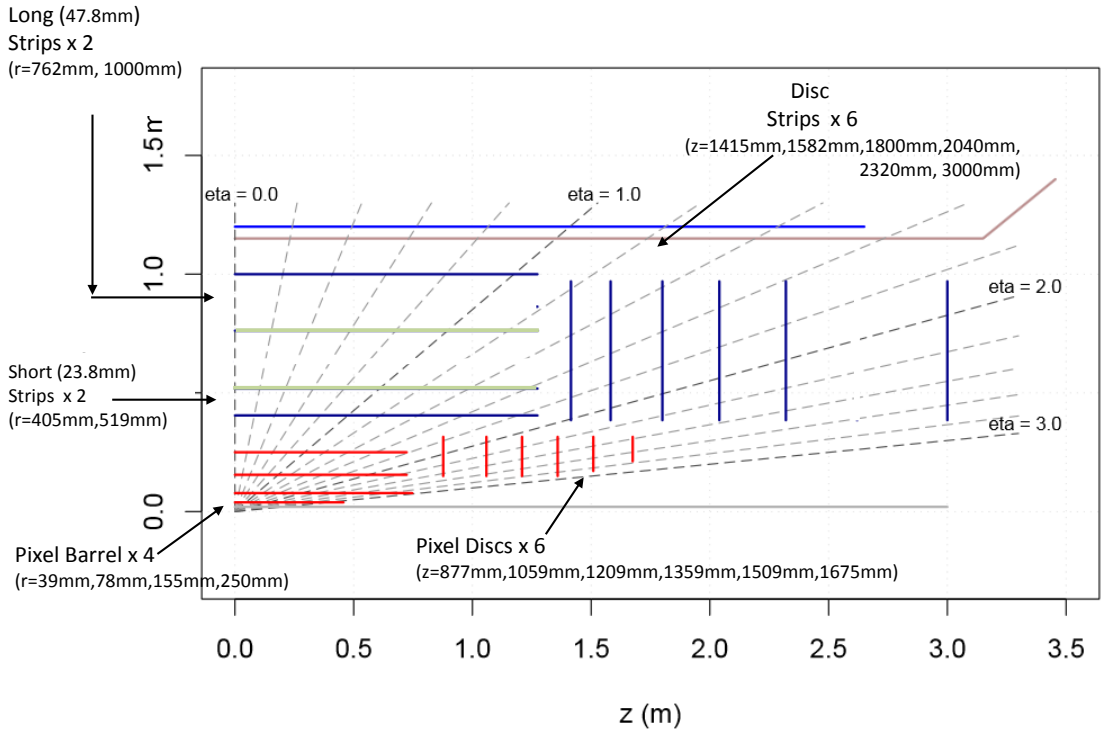

Figure 9. The Low scenario layout, which is based on the LoI layout. Dramatic cuts are made to the strip system removing measurements along the length of the track and the η-coverage range is limited to $|\eta| = 2.7$ by important reductions in the pixel system. The strip barrels shown in green are those where one side of the strip module has been removed. The blue line outside the ITk volume represents the coil of the solenoid magnet.

Table 12. The differences between the layouts for the Reference, Middle, and Low scenarios.

	Reference	Middle	Low
ITk strips - changes w.r.t. LoI layout			
Remove Barrel layer 3			✗
Remove 1 Disc set		✗	✗
Remove 2 stereo layers			✗
Remove stub		✗	✗
ITk η-coverage	4.0	3.2	2.7

This layout explores the performance impact of a very substantial reduction in the area of the Strip system in the barrel region, to evaluate the minimal number of large-radius measurements required for a successful ITk layout, as well as the performance degradation that results from such a reduction.

IV.3 The Pixel detector

This section summarises the technical design elements that the costing exercise and performance simulations are based on. On-going work either to bring these elements to maturity, or to further improve technology, or to innovate in order to reduce cost or increase performance, is covered in Section IV.6. The pixel detector design consists of a 4-layer barrel section and two end-caps, populated with silicon hybrid pixel modules held on carbon-composite support structures. The entire detector uses 4-chip modules (4 readout chips bump-bonded to a single silicon sensor tile) except for the innermost barrel layer where modules must be narrower in order to fit, and hence 2-chip modules are used. Significant technical progress has been made since the LoI on all fronts, but in most cases this progress has a minor impact on the results of this comparative study done with LoI technology. For example, progress on radiation hardness or control of Serial Powering (SP) modules, which is obviously important for building a working detector, has no impact on the performance simulations. On the other hand, reduction of mass and of pixel size relative to the LoI will lead to increased performance, but the variation in performance between the different scenarios will be insensitive to such changes. The use of a uniform module format across the entire detector makes cost estimation straightforward, as module cost is a major part of the overall CORE cost. Additionally, several other components scale with the number of modules, such as power supplies and many services. DAQ costs, including cables and fibres, scale with the number of measurement layers rather than the number of modules, as the data volume depends on angular coverage, not on surface area.

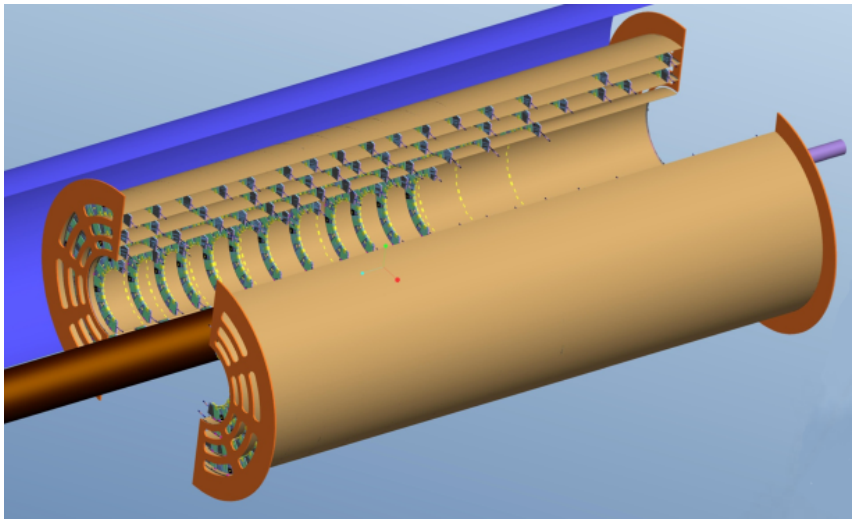

Figure 10. Ring layout end-cap design example. This is a mechanically-engineered buildable pixel end-cap layout that can achieve the same hit coverage as the functional flat disc layouts simulated in this study.

The pixel barrel design is unchanged in all 3 scenarios considered here, while the end-caps are very much larger in the reference layout than in the low scenario. The (LoI) end-cap design in this study is not a buildable design, but rather a functional layout: it provides a number of pixel hits with a realistic spatial distribution, with realistic hermeticity, and with a realistic material budget. Since the LoI, a buildable end-cap design has been developed and is being prototyped. This design uses rings held in shells rather than large radial extent flat discs. The ring design is very modular and flexible, and provides well defined control of services routing. Any η-coverage and number of measurements can therefore be accommodated with the ring end-cap design. The spatial distribution of hits can easily match the flat disc layout, but it can also be further optimised to reduce module count and

therefore cost. This optimisation was not included in the present study. Implementing it would not change the relative performance between the different scenarios, as the difference comes mainly from the η-coverage. A ring end-cap model with full η-coverage is shown in Fig. 10.

Even though the pixel barrel design is not varied here, it is worth pointing out that it is divided into an insertable 2-layer inner barrel, surrounded by a fixed outer barrel. For the reference design, the highest η (lower radius) rings in the end-caps will also form part of the insertable section. The insertable part is required in order to guarantee high performance for the entire 3000 fb^{-1}, as this may necessitate replacement of the inner layers due to radiation damage. Both front-end chip (Section IV.3.3) and sensor (Section IV.3.2) technologies have performance uncertainties at the radiation dose levels predicted for the innermost layer. At the 40 mm radius innermost layer the projected radiation dose for 3000 fb^{-1} is $\sim 1.4\times10^{16}$neq/cm^2 and 700 Mrad, while at the largest pixel radius (250 mm) the projection is $\sim 1.7\times10^{15}$neq/cm^2 and 85 Mrad. Chip and sensor designs must add safety factors to cover uncertainties in these projections. The safety factors vary from less than 1.5 at the innermost layer, where the luminosity to dose conversion has minimal contributions from secondaries and neutron albedo, to over 2 for the outer layer. There is no safety factor on the integrated luminosity because 3000 fb^{-1} defines the end of the run. The cost of a replacement inner barrel is not included in any of the scenarios presented.

IV.3.1 Pixel modules

For the LoI-VF layout used for all of the performance and physics studies described in Chapter XI, the pixel modules, and the associated ASICs and pixel sizes, are as described in this section. However, as discussed in Section IV.3.2 and Section IV.3.3, the final design is very likely to use the RD53 ASICs everywhere, with the corresponding 50 μm by 50 μm pixel size, and may use a module geometry which is optimized for those ASICs. This section describes the design used for all of the detailed simulations, where the 4-chip module dimensions are given by a 2 $\times$ 2 array of FE-I4 readout chips (FE-I4 is the readout chip used in the present inner layer of the ID, the IBL). Such 4-chip modules have an active area of 13.6 cm^2 in a footprint of 40.5 mm $\times$ 38 mm. The ITk pixel readout chip need not be exactly the same size as FE-I4, but as all prototyping is so far carried out with FE-I4 chips this is the baseline dimension. The design assumes 150 μm thick chips (as used in the IBL) bump-bonded to 150 μm thick sensors (50 μm thinner than IBL). The FE-I4 pixel size of 50 μm by 250 μm is used in the outer barrel layers, while inner layers have 25 μm by 150 μm pixels based on early readout chip demonstrators that showed this size was achievable. The end caps, on the other hand, use a 50 μm by 50 μm pixels size, which matches the RD53 development discussed in Section IV.3.3. Pixel size impacts physics performance to varying degrees, but is also an important system parameter that influences radiation tolerance, hit efficiency, and power consumption. Small pixels are important for tracking in dense jets, but for position resolution smaller pixels may or may not be better depending on the signal to noise, cluster size distributions, and reconstruction algorithms. A 4-bit precision pixel charge measurement is assumed. The three scenarios are investigated here using the LoI and LoI-VF layouts, checking for consistency of the results in the region $|\eta| < 2.7$, and the conclusions on relative performance are not affected by pixel size choices. Pixel size has no direct effect on cost.

As the module cost is dominant for the pixel system, a strong module prototyping program is very important. ATLAS institutes have purchased over 200 FE-I4 chip wafers for use in upgrade R&D (to be compared with 30 wafers used to build the IBL). FE-I4 4-chip modules have been produced using a variety of sensor prototypes at several bump-bonding vendors, with more still being explored. Examples of ITk pixel module development are shown in the Fig. 11. A substantial production exercise to assess rate and assembly quality is planned in the next year. The bump-bonding cost is

influenced by the thickness of the components, due to thermal bow effects requiring extra processing and handling for very thin silicon. Much R&D has gone into understanding what techniques are more effective to bump-bond thin chips and to qualify vendors to produce thin parts. All 3 scenarios assume that thin parts are used in the entire pixel detector.

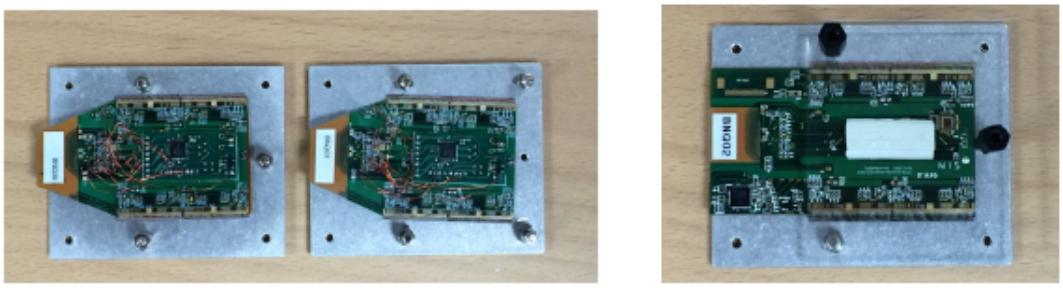

Figure 11. Quad modules for the SP stave: Left BNQ01/BNQ02 BNQ01 pseudo quad n-in-p sensor, BN102 pseudo quad n-in-p sensor. Right: BNQ00 digital module

IV.3.2 Sensors

With the exception of the inner barrel, all modules are assumed to use planar n-implant on p-bulk silicon sensors fabricated on 150 mm diameter wafers. As all these sensors are in areas of the detector that are not replaceable, they must survive 3000 fb^{-1}. This requirement at the highest dose areas of the outer pixels plus safety margin lead to the 150 μm thickness value. This thickness has been assumed everywhere for the present study. We take the end of life for planar sensors to be the point at which the power dissipated by the leakage current at full depletion voltage leads to thermal runaway. Actual catastrophic thermal runaway would never actually happen, as the leakage current is limited by series resistance and supply limits, but this gives an indication when proper depletion becomes impossible, leading to sharply lower efficiency or even inability to operate. This makes it clear that radiation tolerance is not only a sensor issue, but is intimately tied to the temperature that the cooling system can achieve and the thermal performance of the support structures and adhesives that couple the sensors to the cooling.

For illustration, Fig 12 shows, for given layer radius and support thermal performance, the evolution of the runaway point as well as the point at which the leakage current has a value of 10 nA per 50x50 μm^2 pixel (400 $\mu A/cm^2$), for 150 μm thick sensors. This study used the radiation dose after 3000 fb^{-1} plus safety margins, and a coolant temperature of -30°C. It does not include convection, only heat conduction, which is the main cooling mechanism. It should not be taken as a general result on sensor technology, as it is based on the parametrised performance of specific sensors under specific conditions, but it illustrates the importance of a system view of radiation tolerance. The plot shows that 150 μm thick planar sensors are well matched to the outer pixel conditions, but for the inner layers planar sensors should be thinner. Planar sensor power scales faster than linearly with thickness. The plot also includes 150 μm thick 3D sensors, which have suppressed thermal runaway due to their low depletion voltage, but they have higher leakage current which degrades readout chip performance. The value 10 nA per 50x50 μm^2 pixel was taken as indicative of significant degradation. The shaded region shows the limit of achievable thermal performance based on all prototyping to date. The expected variation of adhesive interfaces was included and the points show the worst case module at each radius. This plot shows that achieving 3000 fb^{-1} sensor radiation tolerance with high confidence is very challenging at the inner radii. The aim is to design for 3000 fb^{-1}, with

replaceable inner layers in lieu of a comfortable safety margin. Work is ongoing investigating thinner sensors, lower leakage designs, lower coolant temperature - perhaps as low as -35°C (a severe challenge for evaporative CO_2), higher thermal conductivity adhesives, and composite materials.

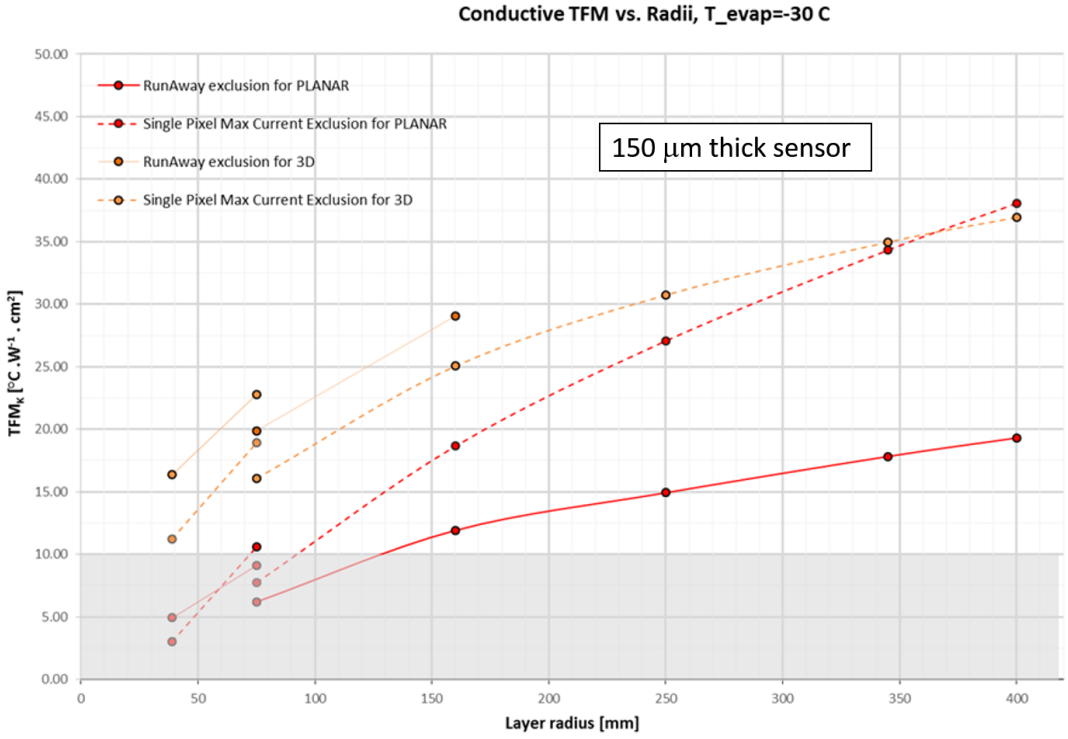

Figure 12. Evolution of the runaway point (solid) as well as the point at which leakage current equals 400 μA/cm^2) (dashed), vs. layer radius for different module support thermal performance figures of merit (TFM), after 3000 fb^{-1} plus dose safety margins, and a coolant temperature of -30°C. Predictions for 150 μm thick planar sensors are shown in red, and for 150 μm thick 3D sensors in yellow. Lines are "broken" for the low radius points because 2 cm wide sensors are assumed at low radius and 4 cm wide at higher radius, but always cooled by a single cooling pipe.

Sensor thickness does affect cost. For 150 mm diameter wafers there is a sharp difference between 320 μm or thicker sensors, and any lower thickness, because of thinning pre or post front side processing. We have assumed thinned sensors are used everywhere. Clearly radiation tolerance demands them at most radii, but perhaps at the highest radius some cost savings could be realised with thicker sensors. For the inner barrel we have assumed more expensive sensors, such as 3D, or thinner planar possibly with n-implants in n-bulk, which requires double-sided processing. The pixel barrel design assumes "flat loading" of modules, as in IBL, with modules placed edge-to-edge along a stave instead of shingled. This is a simple and cost-effective loading, but it requires sensors with relatively thin inactive edges to avoid acceptance gaps. Sensors have been prototyped with slim or active edges that are active to within 50 μm of the sensor edge. Current sensor prototyping is starting to produce sensors with 50 μm x 50 μm bump pitch to match RD53 prototypes, both for 3D and planar technologies.

IV.3.3 Pixel front-end ASIC

As already mentioned a large number of FE-I4 chip wafers (the readout chip used in the IBL) have been purchased for ITk module prototyping. However, the ITk will not use the FE-I4 chip anywhere. This is a change from the 2012 LoI, where use of FE-I4 was assumed for all but the inner layers. This was a conservative assumption, because at the time of the LoI there was not yet a well-defined design effort to produce a new chip, nor had a technology been chosen for a potential new chip. Since the LoI, the RD53 collaboration [13] has been formed and has made significant progress, and CERN has established a frame contract for the 65 nm CMOS technology that RD53 has chosen as its baseline. RD53 is a joint ATLAS-CMS activity, but in the end each collaboration may have its own variation of a production chip – this is not yet decided.

The ITk pixel readout chip is being developed by RD53 in a 65 nm feature-size bulk CMOS process. The radiation hardness of this process has been extensively investigated with the goal of reaching 1 Grad radiation tolerance. Based on the results, RD53 has so far produced design guidelines to achieve well-predicted performance after 500 Mrad, including analog simulation models. This makes it possible to design circuits that meet detailed specifications after 500 Mrad. RD53 has found that the same level of prediction is not equally feasible for 1 Grad, because beyond 500 Mrad there is too much variability in the resulting damage depending on the exact history of operation and temperature during irradiation and annealing. Devices designed with the 500 Mrad guidelines might still work well after 1 Grad, but the very same devices may fail if irradiated under different operating conditions. This current level of uncertainty reinforces the requirement to make the inner barrel insertable (note that this is a completely separate mechanism from sensor bulk damage). A significant mitigation factor for ASIC radiation damage has been found to be low temperature during exposure. This is fortunate since the pixel detector must be cold during operation, and radiation exposure happens during operation. Room temperature annealing is always beneficial, but the effect is modest.

Besides radiation tolerance, the ITk readout chip will have 5 times smaller pixels, yet with higher data rate per pixel than FE-I4. The 65nm feature size process makes it possible to meet these challenges, but the process alone is not enough – new design approaches are needed as well. The RD53 readout chip will be a mostly digital device, with of order 5×10^8 transistors, compared to 8×10^7 in FE-I4. The pixel amplifiers will be contained in 4-pixel *analog islands* embedded in a logic matrix. This provides more powerful connectivity than previously used, allowing for better data flow and digital signal distribution. However, this also exacerbates one of the main challenges of RD53, which is stable operation at very low threshold. FE-I4 modules have been reliably operated with thresholds as low as 1000 e^-, and the lower capacitance of pixels which are 5 times smaller should allow RD53 to reach even lower thresholds. Smaller pixels, thinner sensors, and high radiation damage actually require lower threshold operation – possibly as low as 600 e^-, to be determined by prototype efficiency measurements on the timescale of the TDR. But single pixel noise (which scales with capacitance) is not the only factor that controls the minimum stable threshold. Digital-analog feedback and fluctuations of ground and power within the chip inflate the lowest achievable threshold. The effect on local threshold of power fluctuations and digital activity has been measured in FE-I4 modules and provides important lessons for RD53 work. Consequently RD53 is exploring the design of a constant power chip, where power consumption is always the same regardless of activity. This is in fact very appropriate for a SP system, and even for the CO_2 cooling system, which is designed to handle the maximum power and operates with greater stability close to this operating point. Furthermore, maintaining optimal knowledge of the alignment of the mechanical support system when the power, and hence the temperature, remains constant will also be substantially simplified.

Finally there is the high data volume challenge. Simple scaling of the FE-I4 chip output band-

width of 160 Mb/s by the ratio of the number of pile-up interactions (200/40) times the ratio of the trigger rates (1 MHz/100 kHz) suggests that the ITk readout chip should have an output bandwidth of 8 Gb/s, and this is even before taking into account that smaller pixels will require more bits (greater address space), or that low-latency readout may require additional bandwidth. A larger inner radius than used for the IBL would be a mitigating factor. RD53 is developing a 5 Gb/s chip serial output, along with more efficient encoding than used by FE-I4, as well as on-chip data compression. The final bandwidth and number of output links per chip will be determined after further prototyping and simulation.

IV.3.4 Output Data Transmission

The chip serial output mentioned above will drive electrical cables from the modules to optical links placed at the ends of the solenoid surrounding the Inner Detector, as is currently the case for the Run 2 pixel detector. These cables must be low mass, radiation hard, and low enough loss for 5 Gb/s data transmission over 4-6 m. Development of candidate cables is in progress in close contact with RD53. RD53 will design the electrical data transmission chain with cable models supplied by this development. The optical links may be “passive” as in the present detector, in the sense that they simply translate electrical to optical signals without processing any bits, or active, combining multiple detector channels into higher bandwidth optical channels. The CERN Versatile Link [14] in “passthru” mode is a candidate for a passive link. Plans for an array version of the Versatile Link, capable of up to 10 Gb/s per fibre, would make for a compact optical conversion footprint. Placement of optical links outside the detector volume allows further time for their development and selection, and avoids the need for extremely radiation-tolerant optical components.

IV.3.5 Mechanics and Services

The mechanical support design is based on carbon-fibre composites and CO_2 evaporative cooling in titanium pipes. Significant improvements in materials and assembly techniques, coupled with the reduced size cooling pipes needed by CO_2, result in a large reduction of detector mass relative to the Run 1 pixel detector. Several of these improvements were already used in the IBL. Thermally-conductive carbon-foam allows effective heat transfer to the small cooling pipes with very low mass. Assuming 150 μm thickness chips and sensors, the mass of each layer in the central barrel or of each ring in the end-caps can be approximately 1% of a radiation length (X_o) for perpendicular incidence, excluding structures to support the layer. For comparison, the Run 1 detector mass was 2% for each layer, and 2.5% per layer when all support mechanics are included. In order to avoid the mass penalty from support structures in the central barrel, some proposed designs use high moment-of-inertia structures that can be end-supported. This can be done for example by coupling 2 layers as in the I-beam prototype of Fig. 13. The end-cap rings consist of symmetric sandwich structures (facing-foam-facing) with cooling pipe and electrical services (flex circuits) embedded in the centre (Fig. 14). Modules are loaded on both sides of a ring in an alternating pattern to achieve hermeticity, just as was done in the Run 1 pixel end-caps.

In the central barrel the modules will be held parallel to the beam-line, with no R-Z tilt, and in the end-caps they will be perpendicular to the beam-line, also with no tilts. At the ends of the barrel the option of tilting the modules is being investigated. This would reduce the number of modules needed in that region, without loss of acceptance, at the expense of more complex geometry and cabling. A photo of an "Alpine" prototype support, which holds modules in a tilted orientation by using thermally-conductive foam pedestals, is shown in Fig. 13. Recently, the studies concerning layouts with inclined sensors have been expanded, and a new possible design, named "SLIM", is

being considered. It is based on the concept of a straight, light linear support structure where pixel modules can be independently mounted at different angles with respect to the beam line. Preliminary studies indicates that very good thermal and mechanical performance can be obtained, and prototypes are being fabricated. For the conventional geometry where all barrel modules are axially oriented, rather than considering there to be too many modules at the barrel ends and trying to reduce the number of them, investigations are underway to evaluate how to take advantage of the added information that these modules provide. The added information comes in the form of very long clusters: a string of hit pixels in a row along the track direction (the very low thresholds proposed for the ITk-pixel system allow efficient detection of tracks traversing pixels in the 50 μm direction). With a fine granularity pixel detector, such long clusters can be exploited for pattern recognition and for increased track parameter resolution. The superior pattern recognition that long clusters provide might allow reducing the number of end-cap measurement planes instead of saving modules at the ends of the barrel through tilting.

The ITk pixel services in the detector volume will be dominated by the data cables. This is a big difference compared to the Run 1 detector. The greater data volume is one reason for this, but the main reasons are the reduction in cooling pipe size thanks to CO_2 cooling, and the reduction of power cables by approximately an order of magnitude by using SP distribution. The result is that the total services will be less per module than in the Run 1 detector. The services routing is being designed with conservative data cable sizes taken from commercially available twin-axial ribbons. All services are routed to higher radius than the modules they serve as soon as possible, which avoids the build-up of material along the beam pipe outside the active region. Thus is something that was not possible for the IBL, because the IBL was a retrofit, with the only available routing space along the beam pipe. As expected, services are most congested for the insertable inner barrel. A design option is being investigated where the inner barrel is split at z=0. This would greatly reduce insertion/extraction time (and therefore potential radiation exposure) because services would not need to be dressed/undressed to pass through the detector volume.

IV.4 The Strip detector

The strip detector of the ITk is situated just outside the pixel detector and contains more than 190 m^2 of n-in-p planar silicon-strip sensors tiled over the surface of five full length barrels in the central region and one stub-barrel (the three inner barrels use shorter strips, the two outer and the stub barrels use longer strips), and seven strip discs in each of the two forward regions. The basic detector unit is the module and modules are mounted onto staves in the central region or petals in the end-cap regions. Strip sensors are AC-coupled with n-type implants in a p-type float-zone silicon bulk (n^+-in-p Float Zone (FZ)). This type of sensor collects electrons and has no radiation-induced type inversion. The sensor target thickness is 300-320 μm . The current design of the barrel sensors foresees a size of 97.54 $\times$ 97.54 mm^2 to maximally utilise the area of a 6-inch (150 mm) wafer and reduce cost. There are 1,280 readout strips with a 75 μm pitch and a field-shaping strip at each side across a sensor. There are two variations of barrel sensors. One has four rows of shorter strips (23.820 mm) to be used on the three inner cylinders, and the other has two rows of longer strips (47.755 mm) for the outer two cylinders. The ABC130 chip is designed to read out two rows of strips. This choice matches the track density at HL-LHC giving low occupancy as well as low strip capacitance.

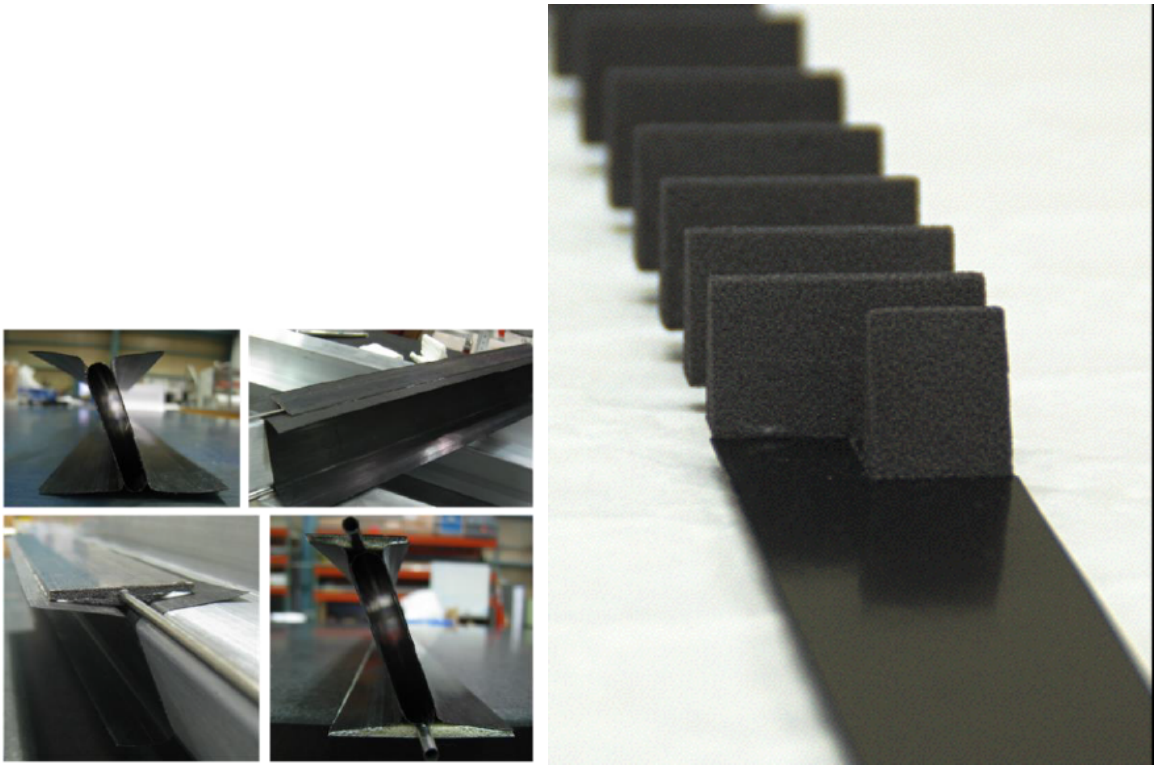

Figure 13. Photographs of a prototype I-beam support (left) and of an Alpine module support (right).

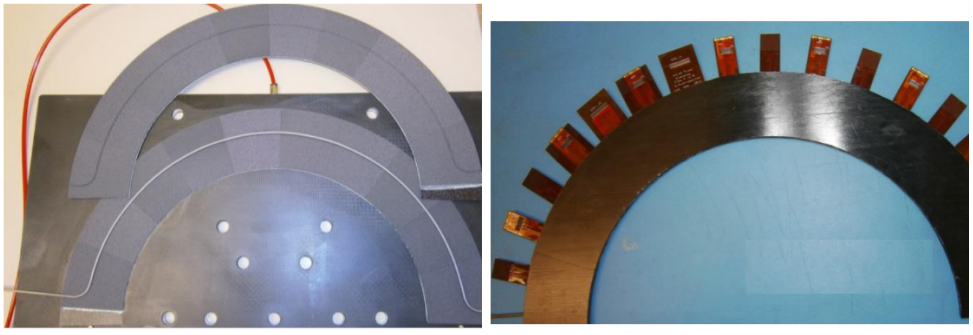

Figure 14. Photographs of a prototype end-cap ring during fabrication (left) and after, just before folding embedded flex cable tabs onto surfaces (right).

IV.4.1 Strip Sensors

One of the key requirements for the strip sensors is to be able to withstand the expected maximum fluence of $8.1 \times 10^{14}_{\text{neq}}$ cm^{-2} at a radius of 405 mm and to operate at up to 500 V. To allow for uncertainties in fluence calculations, a specification of $1.6 \times 10^{15}_{\text{neq}}$ cm^{-2} is imposed. Two generations of short strip sensors have been fabricated: ATLAS07 and ATLAS12. With the ATLAS07 sensors, the performance of the baseline sensor technology (n^+-in-p FZ with p-stop isolation) was shown to meet all specifications. The ATLAS12 series includes enhanced punch-through-protection structures at the end of strips for protecting the AC-coupling capacitors against very large local charge deposition, such as occurs in beam-splash events. There is also a smaller inactive edge space (450 μm) which reduces the dead region of the sensors, and a modification to the bond pad layout to match the ABC130 readout ASIC. Miniature sensors (1×1 cm^2) from both series are the subject of an extensive irradiation and testing program; these studies include a full suite of surface and bulk properties evaluation. As an example, Fig. 15 shows the charge collected after standard annealing of 80 minutes at 60 °C and at a bias voltage of 500 V after irradiation at six different facilities. A batch of 120 sensors with four rows of axial strips (ATLAS12A) is now available for the next round of module, stave, and petal prototyping using the 130 nm ASIC set. In addition, a batch of 45 sensors with two rows of axial and two rows of "stereo (40 mrad rotated)" strips (ATLAS12M) are available for prototyping a "stereo" sensor.

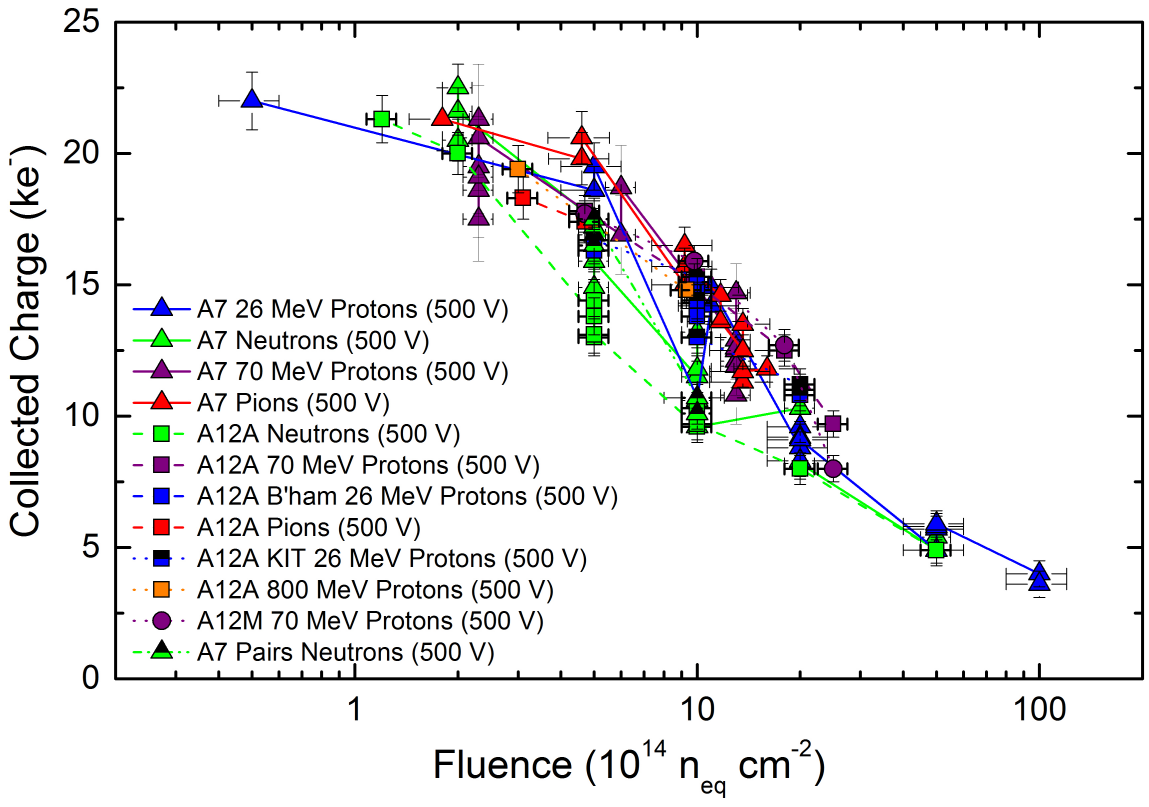

Figure 15. Collected signal charge at a bias voltage of 500 V for minimum-ionising particles as a function of the 1 MeV n_{eq/cm^2} fluence for various types of particles. A signal charge of $\sim 12{,}000e$ is observed at $1 \times 10^{15}_{\text{neq}}$ cm^{-2}.

IV.4.2 Modules and Readout ASICs

Prototype strip modules have already been produced for the strip barrel and end-cap with ASICs fabricated in both the 250 nm and the 130 nm IBM technology. The production of ABC250 has been thoroughly tested at multiple productions sites and a full-length prototype stave has been operated successfully. Modules have also been tested on the bench and in test-beams and the performance is seen to meet all requirements for the HL-LHC. The recent (2015) delivery of the strip Hybrid Controller Chip (HCC) ASIC has allowed the construction of the first barrel modules with the combination of 130 nm front-end chips read out with the new HCC. A barrel module with 10 ABC chips (2,560 channels) that has been read out at 160 Mb/s is shown in Fig. 16.

The development of the tooling for strip module production continues to progress and barrel and end-cap modules are now being routinely produced at multiple production sites. During the series production of strip modules, it is anticipated that approximately 15-20 strip-module production sites will be operating throughout the project.

Similarly, the production of the tooling for the construction of staves and petals is also well advanced. In Fig. 17, the tooling developed for the mounting of 13 short strip modules to carbon-fibre staves is shown. It is anticipated that two such sites will be needed to mount all of the barrel modules onto the staves. For the strip detector the baseline is to use the optical links being developed by the Versatile Link VL+ project [14], which aims to provide common systems for the ATLAS and CMS Phase-II upgrades. The associated chip-set is being developed by the CERN GBT team. This chip-set includes the lpGBTx ASIC, which is a proposed low power/higher speed version of the current Giga-Bit Transmitter (GBTx) ASIC. This takes data from individual module e-links, which can run at up to 320 Mb/s, and multiplexes them onto one high-speed serial output. This output drives the GBT Laser Driver (GBLD) ASIC which then drives a Vertical Cavity Surface-Emitting Laser (VCSEL). The Low Power GBT transmitter (lpGBTx) will be operated in “wide bus” mode for the data links which provides a user bandwidth of 8.86 Gb/s.

IV.5 Common ITk Items

IV.5.1 Readout

The readout electronics of the ITk system needs to meet the TDAQ trigger requirements, and supports both a full L0 1 MHz (latency 10 μs), and a 400 kHz L1 trigger readout mode. This places severe demands on the front-end design and the rate at which data is transmitted between the front-end electronics, the end of structure cards and optical transmitters used to send the data off-detector, where it is finally passed on for further processing. For a mean pile-up of 200 and at the smallest radius of the pixel detector, each of the front-end ASICs will be producing data at approximately 5Gb/s. Currently available optical transmitters are not sufficiently radiation tolerant to work at these radii. It is therefore necessary to transmit the data electronically over some distance (several meters) before it can be converted to optical signals for transmission off-detector. This electrical transmission should have a low bit error rate and must not introduce too much inactive material into the detector volume. There are several ongoing R&D efforts investigating several types of cables and configurations: Micro Twinax, Twisted Pair, and other solutions. One topic of research is clearly to reduce the material for the cables and hence the radiation length of the services. Initial results are encouraging, and rates exceeding 6 Gb/s have been demonstrated over 1 m low-mass twisted-pairs cables. Appropriate fast signal drivers tolerant of the high radiation levels need to be found or developed.

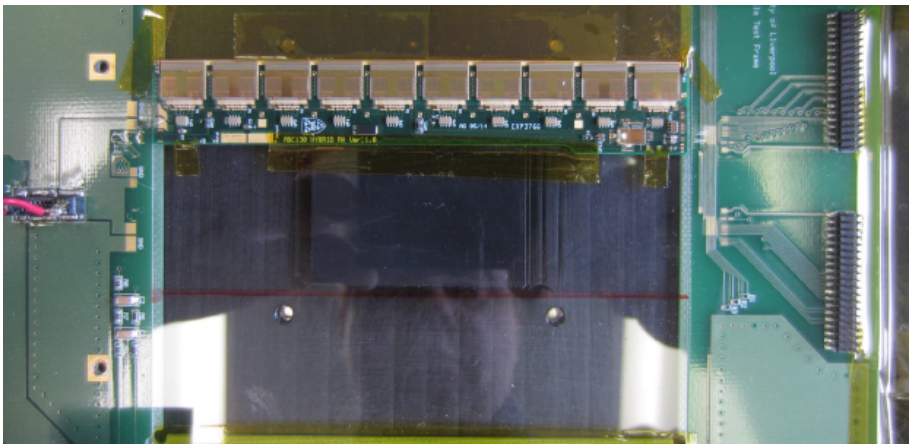

Figure 16. Photograph of the first strip barrel module with 10 IBM 130 nm ABC chips (2,560 channels) and the IBM 130 nm Hybrid Controller chip with a 80 MHz clock (160 Mb/s).

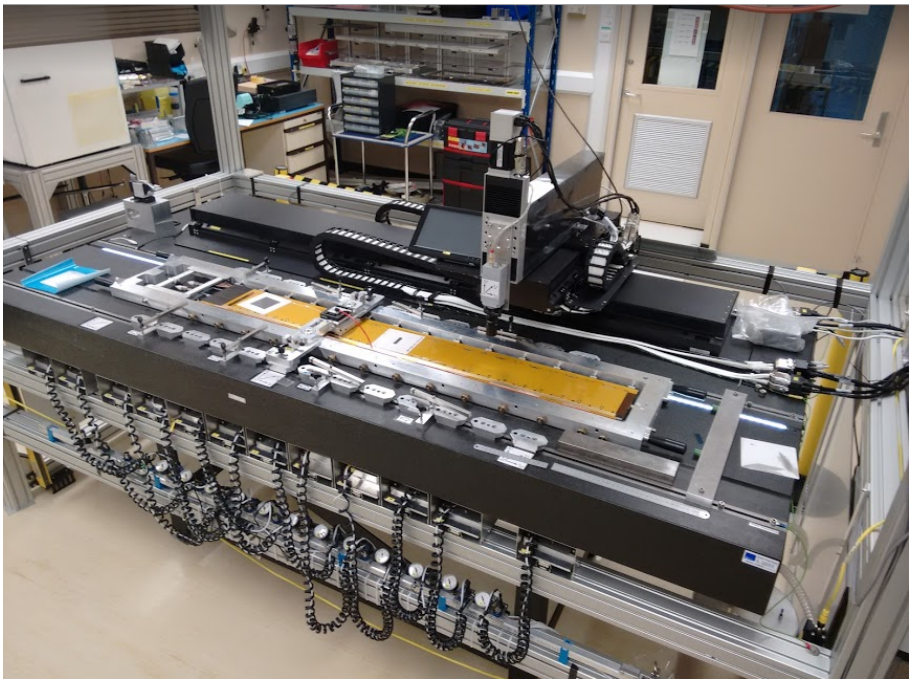

Figure 17. Strip module mounting: up to 13 modules, held in a construction frame, are glued in a row to make one side of a short-strip barrel stave. The completed modules (short or long strip) are glued and surveyed on one side and then turned over so another set of modules can be glued on the other side. The stave includes an embedded cooling tube in the middle of the structure and co-cured bus tapes on either side. The optical transmitters will be located on an EoS card.

IV.5.2 Powering scheme

The ITk represents a significant increase in channel count over the existing ID. There is a large increase in the number of detector modules in both the strip and pixel detectors (the strip detector increases from 4,088 to 20,000 modules; the pixel detector from 1,744 to 10,000 modules for the LoI and significantly more for the LoI-VF/Reference layout). It will not be possible to repeat the model used in the ID, where each module has its own independent high voltage and low voltage (HV, LV) supply. Such an approach would significantly increase the inactive material in the tracking volume and would impose severe space and routing constraints on the design of the detector. For the ITk, it is necessary for groups of modules to share the same LV and HV supplies. Low-voltage multiplexing for groups of modules can be achieved by either SP or point-of-load Direct Current to Direct Current (DC-DC) conversion. Based on the comparison of the electrical performance of full-length strip stave prototypes powered by SP and DC-DC conversion the strip community has already settled on DC-DC conversion for the LV-powering scheme. In the case of the strip detector the size of the LV power conversion package was not a serious constraint. For the pixel detector, the DC-DC conversion package is too large for serious consideration within the limited space available. For the pixel detector the FE-I4 chips already contain linear shunt regulators which can be operated in a SP mode. While powering studies in the pixels will continue, for calculations of service routing and material studies SP is assumed as the baseline. Studies are underway on HV multiplexing, that allows one HV supply for many modules but with switching of individual modules, so a single failure does not jeopardise the others. Prototypes using commercial small footprint Gallium Nitride (GaN), Silicon JFET, Silicon MOSFET, and Silicon Carbide (SiC) JFET devices are being evaluated in the strip community. These approaches are capable of switching voltages up to 1,700 V for the lifetime of the HL-LHC. These technologies are also now being actively explored by the pixel community. Such devices may benefit both communities and help to minimise the material in the detector volume.

IV.6 Ongoing R&D activities

For the ITk Pixel detector, some of the questions being addressed by the ongoing R&D activities include:

1. **Low-power high-resistivity planar sensors**: The design and production of low-power high-resistivity planar pixel sensors, able to withstand the radiation environment of the HL-LHC for the entire lifetime of the experiment.

2. **Large area detector**: Fabrication of the large area ($\geq$10 m^2) pixel detector in the time allowed by the ITk production schedule, in a way that is cost effective with a high yield and low risk, particularly in terms of establishing robust enough Quality Assurance (QA)/Quality Control (QC) procedures to be confident of the performance of all components in the intense radiation environment.

3. **Readout**: The best way to read out the large volumes of data and transfer them off the detector for downstream processing in a way that will not adversely affect detector operation or tracking performance.

4. **Powering schemes**: Develop and optimise LV powering schemes for the on-detector electronics and HV biasing distribution to the detector modules.

5. **Alternative sensor technologies**: Investigate alternative pixel-sensor technologies that could be developed on the timescale of the ITk production schedule that would:

- Significantly reduce the cost of modules
- be easier to manufacture
- provide reduced material

For the ITk Strip detector, some of the questions being addressed by the ongoing R&D activities include:

1. **Sensors**: The design, development and purchase of radiation-tolerant sensors in high volumes for staves (central region) and petals (end-cap) that will work for the lifetime of the experiment.

2. **Readout and data rates**: The best way to read out the data from the strip modules at the data rates required by the ATLAS trigger system. This needs to be done for the entire detector, both for 1 MHz L0 trigger rates, and for 400 kHz rates respecting the L0/L1 trigger architecture.

3. **Data bandwidth and aggregation**: The best way to aggregate the data on the detector for transmission off-detector with sufficient bandwidth required to keep up with the trigger rates.

4. **Module powering scheme**: The best way to supply ~20,000 detector modules with LV and HV. Individual supplies as used for the original ATLAS tracker are ruled out and modules must be powered in groups.

5. **Hybrid design optimisation**: Reduction of the number and cost of the different types of module hybrids. Aim to finish the design and demonstrate the required performance ahead of the TDR.

6. **Design optimisation of staves and petals**: Ensure that the design of the staves and petals is optimised for cost, ease of production, adequate data transmission and low mass ahead of the TDR.

7. **Alternative detector technologies**: Investigate alternate strip detector technologies that could be developed on the timescale of the ITk production which might offer benefits in terms of cost and/or performance.

8. **QA procedure optimisation**: Set up optimal sufficiently robust QA procedures to ensure required performance of all components in the intense HL-LHC radiation environment.

IV.7 R&D plans and time-line

An overview of the R&D deliverables needed to produce the TDRs in 2016 (ITk-Strips) and 2017 (ITk-Pixels) is given below.

For the Pixel detector the R&D deliverables are:

1. The development of sensor technologies including: thin standard planar (n-in-p) and 3D sensors with adequate radiation tolerance, minimum dead areas and minimised power dissipation at the radius of the innermost layers at the end-of-life. A qualified prototype is expected by end 2016 or beginning 2017.

2. The design of a front-end chip that is capable of reading out the pixel detector at the required trigger rates, tolerant of the extreme flux of radiation at smallest radius with low power and with high bandwidth. ATLAS ITk-pixel institutes are working within the RD53 collaboration [13] to

develop front-end architectures for both ATLAS and CMS. This will be realised in a 65 nm technology. For the readout chip a main R&D deliverable will be the fabrication of a large format prototype, called RD53A, to be submitted towards the end of 2016. This will be produced on full 12" wafers, suitable to exercise the bump-bonding assembly chain. The chip prototype cost is shared between the ATLAS and CMS collaborations.

3. A significant fraction of the cost, complexity and risk is the bump-bonding. As part of the preparation for the TDR, the ITk collaboration will work to qualify at least three bump-bonding vendors with an aggregate capability of 100-200 modules/week, which is required to complete the detector within the required schedule. For the qualification of bump-bonding vendors, the deliverable will be a quad-module trial production in 2016. Approximately 100 quad modules per vendor will be fabricated with the older FE-I4 chips available from the production of the IBL to minimise the overall cost.

4. While the on-detector front-end electronics generates digital electrical signals the data is transmitted off-detector optically. The transition from electrical to optical is not done on the detector module but as close as possible. The bandwidth requirements, required radiation tolerance of the transmitter, the location of the transmitters, the distance between the front-end chips and the transmission of the data between the front-end chips and the optical transmitters using the minimum amount of material in the active volume is a critical design issue that needs considerable development if it is not to adversely affect detector operation or tracking performance. For the data transmission from the front-end chips the deliverable will be the cable-qualification and full-scale prototype of candidate technologies by the end of 2016.

5. For the power distribution, qualified at system level, the deliverable will be a full-scale power distribution prototype for a stave. Initial prototypes will necessarily be based on FE-I4 chip modules.

6. One particularly promising and active area of research within the pixel community is that of CMOS sensors. This technology offers the possibility of low-cost, low-voltage commercial sensors with some of the front-end electronics embedded in the sensor itself. Before this technology could be used for HL-LHC it will be necessary to demonstrate both the radiation tolerance, required at the pixel detector radius, and a significant cost advantage with respect to more established technologies. For the development of CMOS smart sensors the deliverable will be a full-scale radiation-tolerant demonstrator module by the end of 2016.

For the Strip detector the R&D deliverables are:

1. The finalisation of the design and ongoing characterisation of planar n-in-p sensors for the barrel and end-cap modules. The purchase of sensors for the development of tooling used for module development and pre-production will continue up to the time of the TDR in late 2016.

2. The development of a radiation tolerant 256 channel front-end readout chip, called ABC-star, for the strip modules that will enable the entire strip tracker to be read out at either 1 MHz L0 trigger rate or at 400 kHz while respecting the new L0/L1 trigger architecture. This development relies on the years of experience gained in the current ATLAS Semi-Conductor Tracker and will be realised using the 130 nm process.

3. The development of the HCC that aggregates the data from the individual front-end chips and prepares them for transmission off-detector by optical transmitter. This chip will be realised in the radiation-tolerant 130 nm process. Limited production runs will be done of both front-end

and HCC chips to allow for the pre-production construction of modules, staves and petals. The first submission of pre-production chips will be in Q1 2016 and radiation tolerance and Single Event Upset (SEU) testing will continue up to and beyond the submission of the TDR.

4. How to supply the LV and HV to the front-end electronics is an active area of development. Developments in DC-DC converters are currently being assessed for the LV supply and HV switching for the detector bias. Demonstration of the viability of HV and LV powering schemes, specification of power supplies and understanding of the possible re-use of existing cables should be underway by Q4 2015.

5. The design of the hybrids for both the barrel staves and end-cap petals needs to be finalised for the new architecture that will enable the entire strip detector to be read out at 1 MHz. Hybrid designs and layout need to be complete and reviewed by Q1 2016. Final stave and petal power-boards and bus-tape designs will need to be completed and reviewed in 2016.

6. The ITk strip community is also actively engaged in studies of CMOS sensors. Because the strip detector has such a large area the cost saving and performance enhancements could be considerable.

IV.8 Cost estimates

The calculation of the CORE cost of the ITk is based on knowledge from the construction of the current Pixel and Semiconductor Tracker (SCT) systems, the IBL upgrade [ref] and other upgrade R&D projects, existing vendor pricing (for example for integrated circuits fabricated through CERN frame contracts), and extrapolations of commodity pricing (for example for FPGAs). The profile of the CORE spending has been updated to take into account the new LHC schedule in which LS3 begins in 2024. Items that are not supplied by institutes will necessarily be covered by a common fund. A new CORE costing has been prepared for this document and is part of the ongoing preparation for the TDRs. The profile of the current CORE costing is based on production plans but may need to be further modified in light of supplier's schedules. The CORE cost estimate for the ITk project is shown in Table 13. It is broken down into sections covering the pixel and strip specific elements, and the global elements, including off-detector electronics, global mechanics and services. There are still uncertainties that arise both in the production costs and also due to open questions in the design.

IV.8.1 Cost of Forward Pixels

The LoI-VF layout is idealised and it is not optimised for cost. It should be stressed that the cost of the end-cap pixels presented here is not based on the LoI-VF layout but on a more efficient ring design that is currently under consideration within the ITk Layout Task Force. The coverage of the ring option is the same as the LoI-VF and is achieved with a smaller area of silicon modules and less material.

IV.8.2 Pixel Staves and Discs

The pixel system is split into the inner radii (insertable) barrels and the outer radii barrels and forward discs. The inner radii barrels will be the most technologically challenging part of this system, but the area and hence cost are relatively small. The cost estimates have some uncertainties due to the final choice of sensor technology, the new front-end ASIC in 65 nm technology and the large bandwidth

Table 13. CORE cost estimates for the ITk project for the three scoping scenarios. The cost of the sensors for both strips and pixels includes the cost of the mask sets. The cost of the front-end electronics includes the cost of the front-end ASICs and mask sets and in the case of the pixel detector includes the interconnection of the sensor to the front-end chip. The "further electronics" category for the strip detector includes: the bare flex-circuits with passive components, bonding wire, EoS boards, the Versatile Link, the GBT and Power boards. The further electronics for the pixels includes on-detector DCS, on-detector cables and service panels to bring the services to the end of the tracker volume.

WBS	Item	Reference Total Cost [kCHF]	Middle Differential Cost [kCHF]	Low Differential Cost [kCHF]
2	**ITk system**	**120,422**	**-7,215**	**-23,598**
2.1	**PIXEL detector**	**32,187**	**-915**	**-4,798**
2.1.1	Sensors	7,008	-205	-1,148
2.1.2	FE Electronics	11,301	-314	-1,699
2.1.3	Further Electronics	4,298	-92	-564
2.1.4	Off-Detector Electronics	5,387	-156	-977
2.1.5	Mechanics	4,192	-148	-410
2.2	**STRIP detector**	**72,100**	**-6,300**	**-18,800**
2.2.1	Sensors	29,100	-2,300	-8,500
2.2.2	Front-End (FE) Electronics	3,600	-200	-800
2.2.3	Further Electronics	15,400	-1,500	-4,700
2.2.4	Off-Detector Electronics	9,600	-1,200	-2,100
2.2.5	Local Supports	6,600	-600	-1,300
2.2.6	Global Supports	7,800	-500	-1,400
2.3	**COMMON items**	**16,135**	**-**	**-**
2.3.1	Mechanics	12,760	-	-
2.3.2	Electronics	3,000	-	-
2.3.3	TTC Infrastructure	375	-	-

required for 1 MHz readout. The assembly of the relatively small number of modules could be achieved with current methods. The outer radii barrels and the forward rings are less technologically challenging but will require large scale production.

The principal areas that must be addressed as part of the preparation of the pixel TDR are the bump-bonding and the module loading. The bump-bonding large scale production is considered feasible by the vendors currently engaged in R&D, but achieving the required rate must be demonstrated. The community is working with a number of companies to qualify them for bump-bonding production to ensure robustness of the process and to minimise cost. A limited high-rate exercise should be carried out prior to the TDR. Module loading will be done in-house at institutes, not industrially, and high rate must be demonstrated for the TDR as part of the stave and sector design process.

The LoI costing for the pixels assumed that a revision of the FE-I4 chip, used for the IBL, would be used for the ITk outer barrel layers and forward discs. This was a conservative choice to meet the LoI installation schedule and did not depend on the uncertainty about the development of a new chip. With the current installation schedule, the establishment of a 65 nm frame contract by CERN, and the successful formation of the RD-53 collaboration, there is considerable confidence that the 65 nm readout chip under development by RD-53 will be available in time to be used everywhere, not just in the inner layers. This reduces cost and effort by avoiding a revision of FE-I4 and takes advantage of the higher performance that the 65 nm chip will provide, in particular for the 1MHz readout. The fabrication cost-per-chip in 65 nm is the same as for the current FE-I4. The sensor and ASIC costs include both the cost for the fabrication and the NRE mask costs, which, with some suppliers, are subject to a separate order. The hybrid costs include the production of the hybrids and the mounting of surface mount components, which will be done in industry. The costs for the materials used in mounting the ASICs, and wire-bonding them to the hybrids, which will be done in the institutes, are also included.

IV.8.3 Strip Staves and Petals

The sensor and ASIC costs include both the cost for the fabrication and the NRE mask costs, which with some suppliers are subject to a separate order. The hybrid costs include the production of the hybrids and the mounting of surface mount components, which will be done in industry. The costs of materials for the mounting of the ASICs (front-end electronics) and wire-bonding on to the hybrids, which will be done in the institutes, are also included. The costs of the local supports include the cost of the materials for: the carbon-fibre and carbon-foam, the titanium cooling pipes and the electrical bus-tapes. The staves will be constructed in the institutes, not in industry. The EoS costs includes all of the electronics and support cards at the end of the stave for receiving and transmitting data and handling HV and LV supplies. The principal areas that must be addressed as part of the preparation of the TDR are the production costs of hybrids and the costs of the bus-tapes. It has not been decided if these will be manufactured in industry or at the institutes. This decision will change the balance of CORE and non-CORE costs.

IV.8.4 Support Mechanics

The strip and pixel support mechanics costs (WBS 2.1.5 and 2.2.6) include the mechanics for supporting the strip and pixel staves, the strip petals and the pixel discs, and the internal services and Faraday cage shielding. The services cover electrical (HV and LV cables), plus the optical and cooling services from the EoS to Patch Panel #1 (PP1) and from PP1 to Patch Panel #2 (PP2). The common mechanics cost (WBS 2.3.1) includes the outer support cylinder and inner pixel-support tube.

Global DCS and alignment covers pressure sensors, NMR probes, environmental and radiation sensors and the global alignment system. The costing for the LoI layout is based on extrapolations from the original construction. Changes to both the detector layout and the readout architecture mean that there is still a considerable degree of uncertainty in the final cost.

IV.9 Cost Risks

IV.9.1 Pixels

The cost of the interconnection of the sensor to the front-end chip by bump-bonding represents about 30% of the cost of the pixel system. It is the key cost driver and is a significant source of uncertainty in the total cost of the pixel system. If it is possible to adopt CMOS sensors (only likely in the outer layers) it may be possible to glue the sensing element to the front-end chip and this could represent a significant cost saving for those modules. However, this technology has not been demonstrated to meet all of the requirements of the detector over its entire lifetime and it is not clear that the stringent mechanical tolerances, that would be a requirement of the gluing process, can be met with high yield and quality such that the process remains cost effective. This is an open area of investigation within the pixel community. Between the time of writing and the time of the pixel TDR there will be ongoing development of the interconnect process with the different bump-bonding sites available at the pixel institutes and the micro-electronics industry. There will also be a limited campaign of mini pixel-module productions with the different bump-bonding vendors to assess the unit cost, efficiency, quality and potential throughput in order to define the pixel-module production models.

IV.9.2 Strips

The cost of the sensors represents about 40% of the cost of the strip system in the reference detector. The values used for the purpose of calculation here are seen as representative and are taken from private communications between HPK Photonics (the vendor used to provide sensors for much of the prototyping) and ATLAS. The values are not taken from a quote. A better estimate is expected to be available closer to the time of the TDR. The cost of the mechanics for the strip system relies on scaling of values used for the construction of the existing inner detector. A range of such values exist depending on assumptions about the construction. Conservative values have been used in preparing the cost estimates and these will be refined in advance of the TDRs when the design is finalised and the construction processes and flow are understood.

IV.9.3 Common Items

The re-use of some of the services currently used in the ID is being explored and could save on the costs of the common items. This has been the subject of different studies within the ITk. It will not be possible to re-use the cooling tubes because of the increase in pressure in going from a fluorocarbon-based coolant (C_3F_8) to CO_2. For this reason we foresee new cooling pipes. It might be possible to re-use some of the electrical cables (HV and LV) that go from the service caverns to patch panels close to the detector. This can be achieved because of the increased use of HV multiplexing and LV SP and point-of-load DC-DC conversion. However, it is almost certain that the final connections between PP2 and the detector will need to be replaced with new carefully routed cables over relatively short runs of several metres. While multiplexing does offer benefits in terms of

minimising material in the tracker volume and unit cost it does bring with it a more significant risk of correlated losses of parts of the detector if one key element in the system fails.

IV.10 Schedule Summary

The ITk construction and installation schedule is based on the updated HL-LHC schedule presented in 2015. The ITk will be installed in LS3 which starts at the end of 2024 and is expected to last for 30 months with physics running starting in mid-2026. Before the installation of ITk into ATLAS, the Inner tracking Detector (ID) must be safely removed from the cryostat to the surface and handed over to Radiation Protection for consolidation, storage and eventual disposal. A complete and detailed schedule for the removal of the ID and installation of the ITk is not yet available and requires detailed planning with ATLAS Technical Coordination who must take into account the requirements of multiple sub-systems. Preparation is underway within the Inner Detector and ITk-mechanics groups to understand the details of the process and the associated time-line. The ITk detector will need to be available for installation into ATLAS in early 2025. The ITk is designed for rapid installation and ease of access while in the ATLAS cryostat. The combined operation of installation and service connection is currently assumed to take no more than six months. The community constructing the ITk detector have proposed a further requirement that the tracker should be available for commissioning on the surface at Point-1 one full year before it is required for installation. This requirement is based on the experience gained with the current tracker. This plan will provide substantial experience with connecting and commissioning the ITk detector on the surface, and thereby minimise exposure to radio-activation during or after installation (while commissioning), and also minimise the time required to achieve full operation of the ITk before physics data-taking. This goal implies that the construction and surface integration of the ITk for testing must be complete by late 2023. A Gantt chart showing a preliminary schedule of the ITk project during LS3 is presented in Fig. 18.

The schedule for the construction of the ITk is shown schematically in Fig. 19. The major milestones for the project including the TDRs, and the pixel and strip production periods, are visible. It should be noted that the integration of modules onto macro global-support structures will start around the end of 2020 (strips) and needs to be complete approximately three years later.

In parallel with the R&D activities related to the construction of the ITk, preparation has started to develop the procedures required for the removal of the current ID. Activities will encompass preparation of an ID Technical Decommissioning Report, outlining the procedures for the removal of the ID, taking into account the activated environment, collection and cataloguing of information and tools from the ID installation, and preparation of 1:1 mock-ups of the current ID and its services. It is anticipated that the Decommissioning Report will be developed and submitted in parallel with the ITk project TDRs, as these efforts will have considerable inter-dependencies and will share resources during LS3 and its preparation.

The TDR for the Strips is currently planned to be ready for submission in late 2016 and for the Pixels in late 2017. The later delivery of the pixel TDR will allow the pixel community to take full advantage of their shorter construction time to develop more optimal technical solutions.

In parallel with the preparation of the final designs, and as input for the TDR, market surveys will be launched with CERN procurement to identify potential suppliers for the major cost items. This will allow greater confidence in the accuracy of the prices for these items in the TDR. It is also important to qualify the potential suppliers for the long lead-time components before the final tendering process. A key difficulty for many components is that the requirements related to radiation hardness cannot be readily captured in QA procedures. This requires extensive prior R&D followed by written assurances that device processing will remain unchanged between the fabrication of pre-production devices built to final specifications, which have been through the full radiation qualification process,

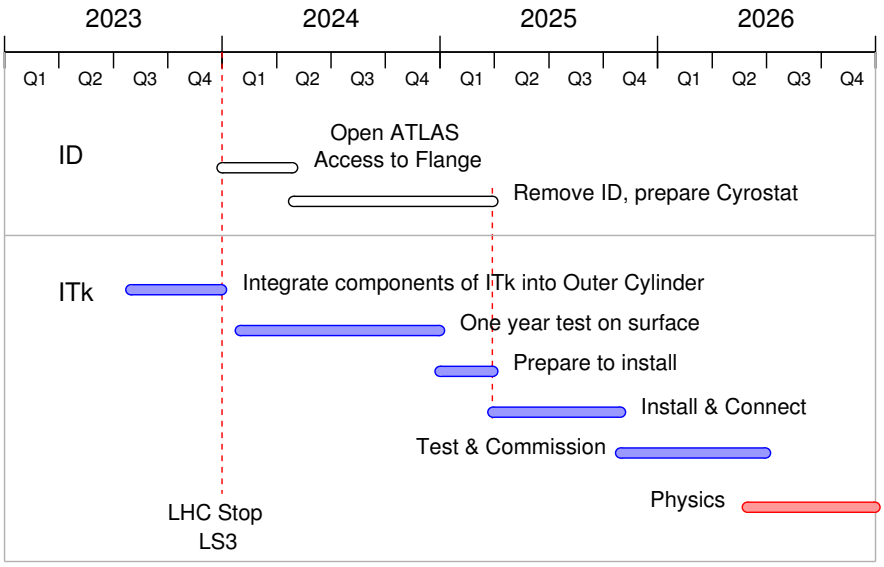

Figure 18. The schedule for the end of the construction of the ITk, the start of LS3, the removal of the current ATLAS ID and the installation, connection and commissioning of the ITk

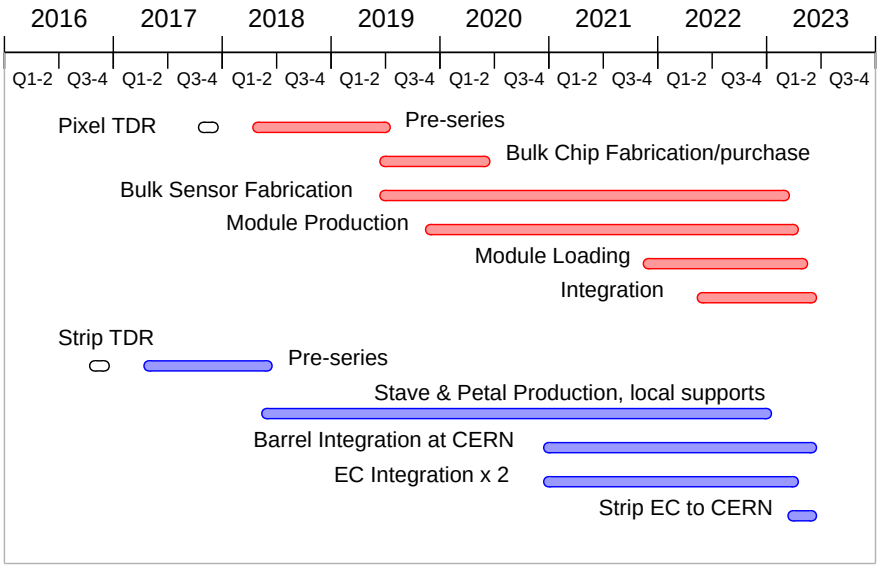

Figure 19. The schedules for the pixel and strip systems from the TDR into pre-production and then series production.

and the fabrication of the series production devices. A qualification phase, based on the early procurement of a sufficient number of devices, and the verification that they meet final specifications, is essential given the time-scales required for adequate irradiation and test-beam studies. In the past, CERN procurement has also needed assurances that resources would be available before launching the final tender process. Furthermore, for the SCT, there was a pre-series procurement for a small fraction of the order with a potential break-point in case problems were encountered either in terms of radiation tolerance in sample testing, QA difficulties, or delivery schedule issues. Another challenge is that some sensor suppliers require separate early procurement of masks and polished wafers to mitigate cash-flow problems.

Following previous procedures, after the TDR, the ITk will typically place contracts for a pre-series of about 5% of the total volume with pre-negotiated break points that enable the ITk Project Leader or representatives, to terminate the contracts if the parts do not meet the specifications. Pre-series modules also need to be built and tested to the final specifications including a limited irradiation campaign. These components are used to: qualify the vendor's production procedures and capabilities, ITk reception and QA procedures, streamline the component flow between sites including part-tracking, and to bring the production sites through site qualification to production readiness. Based on experience gained during the construction of the ID, we expect this process to be time consuming and we expect a slow ramp up to full production, in order to guarantee the highest quality of the large number of mass produced parts. This will be especially true for the ITk strips, where we anticipate a large number of production sites.

The pre-production phase covers both the qualification phase prior to the TDR and the pre-series phase after the TDR.

In the upper part of Fig. 19 we see that the ITk-pixel detector production plan starts in 2017 with pre-production. The fabrication of the next generation of pixel FE readout chip will start in 2018. The testing of these chips continues for the duration of the construction. Sensor fabrication starts with qualification and pre-series orders and continues over 2 years with module pre-production starting when the components are available. Stave and disc loading takes place in 2022. Integration and testing of the pixel package also takes place in 2022, continuing into early 2023. Integration of the pixels into the ITk takes place in 2023. In the lower part of Fig. 19 we see an outline of the production of the ITk-Strip Detector.

The fabrication of modules for both Strip Barrel and Strip End-Caps will be managed through different institutes. The mounting of the modules onto staves and petals will also happen at the institutes. The integration of the strip barrel will take place at CERN. The construction of the two strip end-caps will take place at DESY and Nikhef, and they will be shipped to CERN in 2023. The details of: the number of assembly sites for the construction of modules, staves, discs, rings and petals, component yields, storage requirements, the required rates of production and mounting, and the details of the component flow for both pixels and strips need to be worked out between the time of writing and the TDRs. However, significant production experience was gained in the construction of the ID and the IBL, lending confidence to the existing estimates for the ITk. These estimates have already shown that considerable automation and industrialisation will be part of the strip production.

For the construction of the pixels in the ID there were seven module assembly and testing sites to manufacture the components for the 1.7 m^2 area detector, and the production took just over two years. The ITk pixel detector will be more than 8 m^2 in area, and a similar institute-based production model will be used for the fabrication of the pixel modules. Based on the statements of interest so far, there are approximately 60 institutions who have expressed interest in working on the ITk-pixel detector and the same number who have expressed interest in working on the ITk-strip detector (some institutions work on both).

Chapter V

Calorimeters

V.1 Overview of the Calorimeter upgrades

The detectors of the ATLAS Calorimeter system, including the Liquid Argon (LAr) e.m. calorimeters, the Scintillating Tile hadronic barrel detectors (TileCal) and the Hadronic End-cap Calorimeter (HEC) maintain their required performance under HL-LHC conditions and therefore do not need replacement. In contrast to that, the performance of the LAr Forward Calorimeters (FCals) will be degraded by the high energy and particle density in the LAr detector elements under HL-LHC conditions. Therefore, the replacement of the FCal with a high-granularity sFCal is foreseen in the Reference scenario, as described below. Together with a new High Granuarity Timing Detector (HGTD), to be installed in front of the LAr Calorimeter end-caps, this will allow a mitigation of pile-up effects in the forward and end-cap regions. Moreover, the readout electronics of the LAr and Tile calorimeters will need to be exchanged due to limited radiation tolerance and the necessary upgrade of the ATLAS trigger to operate at higher rates and latencies (see Chapter III).

The LAr and Tile calorimeter electronics upgrades discussed in Sections V.2 and V.3, respectively, are mandatory and are part of all three scoping scenarios. The detector options discussed in Section V.4.2 (high-granularity sFCal) and in Section V.5 (HGTD) appear only in the Reference scenario.

The upgrade of the Tile and LAr readout electronics includes a replacement of the on-detector front-end electronics in a more radiation tolerant technology, of the optical links, of the off-detector signal processing units, as well as the powering systems and the interface modules to the TTC and DAQ systems of ATLAS. The new readout electronics will provide support for a more sophisticated detector signal processing optimised for high pile-up conditions.

The increased event pile-up is a challenge for precision calorimetry in general, and in particular in the forward and end-cap regions ($2.4 \leq |\eta| \leq 4.9$). In the FCal, the high energy and ionisation density will cause degraded signal pulse-shapes induced by HV sagging due to large currents across the protection resistors, as well as ion build-up effects in the LAr gaps. More importantly, the high energy density may make the FCal inoperable due to argon bubble formation (boiling). In the Reference scenario, a high-granularity sFCal with improved physics performance at high pile-up and with smaller LAr gaps, lower values of the HV protections resistors and active cooling to mitigate performance degradation is proposed to replace the current FCal. Furthermore, a HGTD to be installed in the end-cap region $2.4 \leq |\eta| \leq 4.3$ is proposed to measure the arrival time of charged particles in order to assign them to different collision vertices. This will provide additional active pile-up suppression in the reconstruction of energy flow in the equipped area. The expected improvements in performance are in particular relevant for physics processes with jets in the end-cap and forward regions, like vector-boson fusion and vector-boson scattering processes, and for physics signatures with missing transverse energy, as documented in Section XI.

In the Middle and Low cost scenarios, no upgrades of the detectors in the end-cap and forward region are foreseen, unless risks associated with the formation of argon bubbles (boiling) are evaluated to be too high, in which case the installation of a MiniFCal in front of the existing FCal becomes mandatory. Different sampling-detector technologies are under detailed investigation for use in the MiniFCal, with LAr/Cu, Si/Cu, and single-crystal diamond/Cu as active and passive materials, respectively. The installation of a MiniFCal will be also the preferred solution in the Reference cost scenario if there is a too high risk of argon bubble formation and if the risk analysis of the removal of the FCal and the installation of the sFCal indicates a non-negligible risk of failure.

In the following, the calorimeter components to be upgraded in preparation for the HL-LHC operation are presented, together with the required R&D programme and the procedures to select between the different technologies.

V.2 LAr Calorimeter Read-out Electronics

V.2.1 Incompatibility of the Current Readout Electronics with HL-LHC Design Requirements

The expected instantaneous and total luminosities at the HL-LHC and the new ATLAS trigger scheme correspond to operation conditions which are beyond the design specifications of the read-out electronics of the ATLAS Liquid Argon (LAr) calorimeter system.

In the current LAr readout system [15, 16], the detector signals are stored every 25 ns in analog pipelines on the FEBs which are installed on the detector in a radiation environment. Upon arrival of a L1 trigger accept signal, four samples are digitized for each channel at the bunch-crossing of interest and are sent via optical links to the back-end system. The depth of the analog pipelines, the speed of the optical transmission, and the processing power of the back-end electronics do not allow to go beyond trigger accept rates of 100 kHz. Therefore, the current electronics is incompatible with the future L0 and L1 trigger rates of 1 MHz and 400 kHz and latencies of $10\,\mu$s and $60\,\mu$s, respectively.

Within the Phase-I Upgrade in the LHC LS2 shutdown, the LAr trigger readout will already be equipped with additional electronics to provide finer granularity signals to the current L1 calorimeter trigger system [17]. This signal path will stay and is designed to serve as L0 trigger input in the HL-LHC phase. The L0 trigger in the HL-LHC phase will be based on calorimeter and muon spectrometer signals and will correspond to today's L1 trigger. The future L1 trigger will include also input from the ITk.

Moreover, the current front-end electronics has been qualified [18] for total radiation doses which correspond to a total luminosity of 1000 fb^{-1}, including safety factors accounting for uncertainties of the radiation background simulation and of the ASIC and Commercial Off-The-Shelf component (COTS) production processes. The luminosity to be collected during HL-LHC operation is therefore beyond the specifications of the current front-end electronics [19]. Exceptions are the LAr Trigger Digitizer Board (LTDB) that will be installed already during the Phase-I Upgrade [17] and the pre-amplifier systems of the HEC [20], which are installed inside the LAr end-cap cryostat. The LTDB components and the HEC pre-amplifier systems are designed to withstand HL-LHC equivalent radiation doses which is confirmed by dedicated irradiation studies [17, 21].

The future trigger and radiation tolerance requirements thus imply a full replacement of the current front-end and back-end readout system, with the exception of the Phase-I trigger readout components and the HEC pre-amplifier systems. The radiation tolerance requirements are summarized in Tab. 14 based on the current ATLAS detector geometry [19], and applying updated safety factors for the simulation of background levels. These have been measured and were found to be in good agreement with simulations [22]. The expected radiation levels will need to be further updated once the ATLAS detector options for the HL-LHC running are chosen.

V.2.2 Readout Architecture Studies and R&D for HL-LHC

The LAr readout electronics to be installed for the HL-LHC phase will implement radiation tolerant front-end electronics which performs the pre-amplification and shaping of the analog signals of all 183,000 LAr detector channels and an early analog-to-digital conversion without on-detector buffering of data. A high-bandwidth optical-link system will transfer the data at 200-400 Tb/s to a FPGA-based back-end system, where digital signal filtering, energy reconstruction, preparation of L1 trigger inputs and long-latency data buffering are performed. The replacement of the LAr readout electronics will allow an optimisation of the analog and digital signal processing in order to improve the trigger and physics input during high-luminosity operation and to mitigate pile-up effects.

Table 14. Radiation tolerance criteria of the LAr electronics for operation at HL-LHC for a total luminosity of $3000\ \mathrm{fb}^{-1}$, including safety factors for background estimation, given in brackets. For COTS, an additional safety factor of 4 is included in case of production in unknown multiple lots. Furthermore, the ATLAS policy specifies annealing tests that allow reducing the enhanced low dose rate safety-factor to 1, which currently is set to 1.5 for ASICs and 5 for COTS.

	TID [kGy]		NIEL [n_{eq}/cm^2]		SEE [h/cm^2]	
ASIC	0.75	(2.25)	2.0×10^{13}	(2)	3.8×10^{12}	(2)
COTS (multiple lots)	9.9	(30)	8.2×10^{13}	(8)	1.5×10^{13}	(8)
COTS (single-lot)	2.5	(7.5)	2.0×10^{13}	(2)	3.8×10^{12}	(2)
LVPS (EMB and EMEC)	0.58	(30)	9.2×10^{12}	(8)	2.4×10^{12}	(8)
LVPS (HEC)	0.17	(2.25)	4.7×10^{12}	(2)	2.7×10^{11}	(2)

The layout of the new LAr readout is sketched in Fig. 20. The future FEB-2 will amplify the detector signal, apply an analog shaping, digitize the signals with 40-80 MHz sampling frequency, serialize the data stream and send it out via fast optical links. The data from all 183,000 LAr channels are received by the back-end Pre-Processor system, where digital filters are applied for optimized energy calibration and pile-up suppression. Input signals for the ATLAS L1 trigger are produced compatible with a 1 MHz L0 trigger rate and a $60\ \mu s$ total latency requirement. At L1 accept, all data are sent to the ATLAS DAQ system. The DAQ and L1 trigger interface is foreseen to be the FELIX system (see Section III.5.1).

The FEB-2 boards will furthermore produce input signals to the LTDBs, which will have been installed on the detector during the LHC LS2 shutdown. These provide so-called Super-Cell transverse energy sums which are input to the L0 trigger in the HL-LHC phase. The L0 data are received in the USA15 counting room by the LAr Digital Processing Boards (LDPBs), also installed in LS2. The LDPBs calculate calibrated transverse energies for each Super-Cell and provide their correct bunch-crossing assignment at a rate of 40 MHz. The total latency of less than $1.2\ \mu s$ and the size of the off-detector data buffers are well within the requirements for the L0 trigger system.

The Phase-I trigger readout system contains several custom components that can be considered as evolutionary steps towards the Phase-II readout. The front-end LTDB is equipped with radiation tolerant Analog-to-Digital Converters (ADCs), serializers and optical links, while the LDPB is based on high-performance FPGAs with large data bandwidth (Altera Arria-10). A comparison of the achieved performance of the Phase-I system and the Phase-II requirements is shown in Tab. 15. For all Phase-I components the R&D is in the final stages and close to be certified for series production.

With the upgrade of the LAr front-end an optimisation of the readout system for HL-LHC conditions will be possible. In particular, an improved treatment of in-time and out-of-time pile-up effects is expected with the future analog and digital signal processing. Extensive studies are on-going to evaluate different pulse shaping and digital signal filtering strategies based on a detailed simulation of the full readout chain for highest pile-up scenarios of $\mu \simeq 200$ [23]. Figure 21 shows, as an example, the simulated response of a unipolar shaper designed in 180 nm technology and the effect of a unipolar shaping scheme on the signal baseline in ADC counts. A unipolar shaping would imply a reduction in power consumption compared to a bipolar shaping, and the preliminary simulation studies indicate that the baseline shift for the case of unipolar shaping is in the order of 100 ADC counts assuming a 12-bit ADC, even at highest pile-up of $\mu = 200$. If confirmed in more detailed studies, this would correspond to an increase in effective dynamic range that can be covered by the ADC.

In order to capture the expected range of deposited energies per LAr calorimeter cell, a dynamic range of 16-17 bits per channel is required. In the central LAr Calorimeter region the maximum input current per channel is about 10 mA and the noise should therefore not exceed 100 nA. Similar

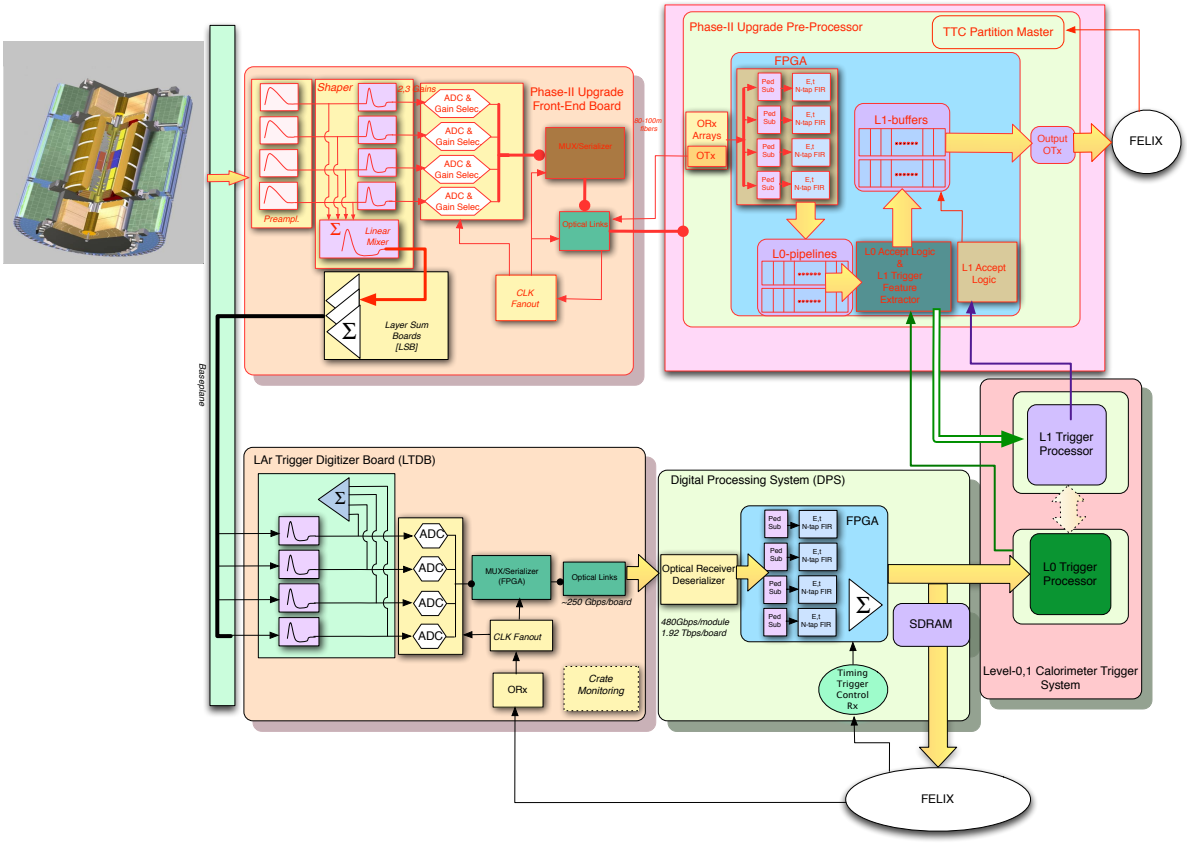

Figure 20. Architecture of the Phase-II readout system of the ATLAS LAr Calorimeters. The new Phase-II readout components are shown along the top row of the signal flow. The FEB-2 boards are amplifying and shaping the detector signals and digitize all data at 40-80 MHz. High-bandwidth optical data-transmission is used to send the data to the back-end system equipped with Pre-Processor boards, which are the interface to the L1 trigger and the ATLAS DAQ. The Super-Cell trigger readout, to be installed already during the Phase-I upgrade, is shown in the bottom half of the flow diagram. It will provide the input to the low-latency L0 trigger.

performance requirements hold for the other LAr Calorimeter areas. Cooling capabilities require the power per channel to be less than 50 mW. Furthermore, the serializer and optical transmitter should provide a data rate of at least 9 Gb/s per fibre excluding packaging and forward error corrections.

Custom ASICs in technologies with feature sizes between 65 nm and 180 nm are being developed to fulfill these requirements [24–26]. Pictures of prototype ADC chips developed within the Phase-I and Phase-II R&D processes are shown in Fig. 22, together with irradiation test results for one of the prototypes. All 12-bit ADC prototypes are confirmed to meet the Phase-II requirements in terms of radiation and power consumption. Commercial 12-bit ADCs were tested within the Phase-I R&D and found to fulfill the specifications [17]. Recent custom developments include triple-redundant layouts and an active correction of Single Event Effect (SEE) effects [24], schematically shown in Fig. 23, which further improves radiation robustness.

The goal of the further ASIC development is an integration of the pre-amplifier, shaper and ADC stages in a single chip in order to reduce the system complexity and power consumption. It also allows fewer supply voltages compared to the current system which will simplify the power distribution system. Early successful designs of pre-amplifier and shaper in SiGe BiCMOS technologies

Table 15. Comparison of parameters of the Phase-I trigger readout system, which is entering series production in 2016, with the Phase-II Pre-Processor System of the ATLAS LAr Calorimeters.

	Phase-I LAr Trigger Readout	Phase-II LAr Pre-Processor System
Number of channels	34,000	183,000
ADC bit precision	12	10-14
ADC sampling frequency	40 MHz	40-80 MHz
Optical-link speed	5.44 Gb/s	10 Gb/s
Total front-end rate	25.2 Tb/s	200-400 Tb/s
Data rate to L1 trigger	41.1 Tb/s (at 40 MHz)	20 Tb/s (at 1 MHz)
Data rate ATLAS DAQ (at 0.1-0.4 MHz)	100 Gb/s	7 Tb/s
Number of I/O fibres per FPGA	66	120
Input rate per FPGA	205 Gb/s	1200 Gb/s
Output rate per FPGA	270 Gb/s	75 Gb/s

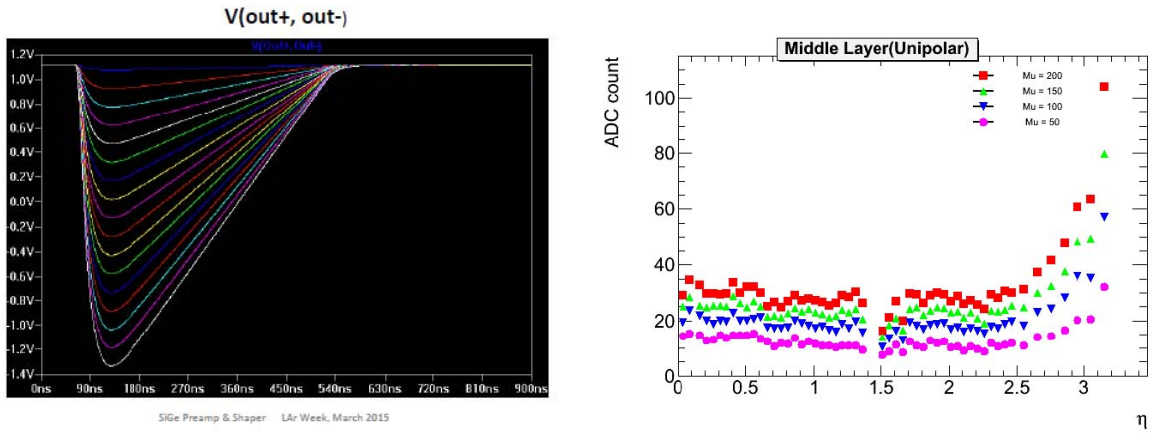

Figure 21. Left: Simulated pulse of a unipolar shaper in 180 nm technology. Right: Baseline shift in ADC counts due to signal pile-up determined for a mean number of events per LHC bunch-crossing, μ, between 50 and 200 for different pseudo-rapidity ranges in the middle layer of the LAr Calorimeters.

(IBM 8WL and IHP) achieved non-linearity and noise levels within the LAr requirements. Current design activities include 130-180 nm BiCMOS and 65 nm CMOS technologies with successful implementations of the pre-amplification and unipolar and bi-polar shaping stages for 14-bit and 10-bit signal range, respectively. In both technologies pipelined SAR ADCs up to 12 bit precision have been prototyped, and developments towards a 14-bit ADC in 65 nm technology are ongoing.

Since the dynamic range of the system extends to more than 16 bits, a single gain stage is not sufficient assuming the current radiation tolerant ADC developments. Design layouts and simulations are being performed, for example, for 2-gain systems with two 14-bit ADCs, which may also ease the detector calibration procedure compared to the current 3-gain readout. In order to avoid a gain selection at the radiation tolerant front-end, the output of all ADCs is foreseen to be sent to the back-end system, where the optimal gain selection can be applied digitally. This readout configuration, with two 14-bit ADCs per channel, is assumed as a baseline for the cost estimates of the LAr Calorimeter readout system (see Section V.2.5).

Each of the 1524 FEB-2 boards will send the data from up to 128 readout channels on about 16 fibre links with 9 Gb/s link speed, excluding data packaging and forward error correction. This

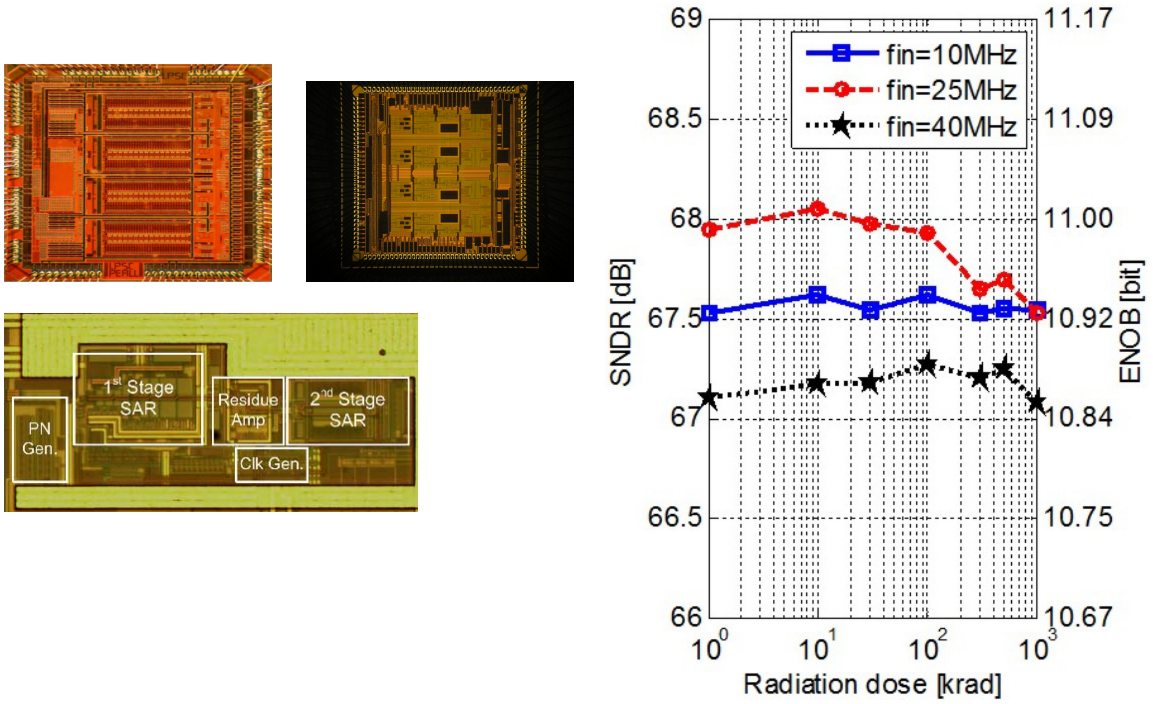

Figure 22. Left: Photographs of example test chips of a four-channel 12-bit 130 nm SAR ADC (top left) [26], of a four-channel 12-bit mixed SAR-pipeline 130 nm ADC (top right) [25], and a 2-stage 65 nm 12-bit SAR ADC (bottom) [24]. Right: SNDR measured for the prototype of a 65 nm 2-stage 12-bit SAR ADC after irradiation up to 1 kGy [24]. Similar results are obtained for the other 12-bit ADC prototypes [25, 26].

will allow a transmission of 2×14 bits per channel and bunch-crossing. Within the LAr community, a VCSEL array driver and transceiver module has been developed in 250 nm Silicon-on-Sapphire (SoS) technology and achieves 8 Gb/s [27], as demonstrated for a prototype in Fig. 24. For going beyond this link speed, a technology with smaller feature size is however necessary. The data transmission targets of the CERN-wide optical-link projects, Low Power GBT transmitter (lpGBT) [28] and Versatile Link PLUS (VL+) [14], are planned to meet the LAr rate requirements and will be designed in 65 nm technology. In both projects, the LAr development groups are closely involved. In case all front-end functionalities are laid out in the small 65 nm feature size, a further integration of all components into a complete FESOC is considered, as shown in Fig. 23. R&D work for such an option is on-going and it has interesting advantages: no I/O between the shaper and ADC reduces noise from parasitics, and no I/O between the ADC and serializer will substantially reduce the ADC power consumption.

An overall optimisation of the whole system is thus required, and is the subject of the current R&D of the ATLAS LAr community in order to select the optimal front-end solution, taking performance, feasibility and costs into account.

TTC signals furthermore need to be sent to each of the 1524 FEB-2 boards in the front-end crates. These signals are planned to be directly transmitted on fibre links using the FELIX infrastructure and to be decoded by the lpGBT chipset. This avoids the use of a dedicated controller board as a single point of failure and makes the design of a dedicated control ASIC unnecessary. The number of clock and control fibres per FEB-2 board will be at least 2, for redundancy, and at most 8, depending on the readout segmentation and the readout fibre mapping to the back-end system.

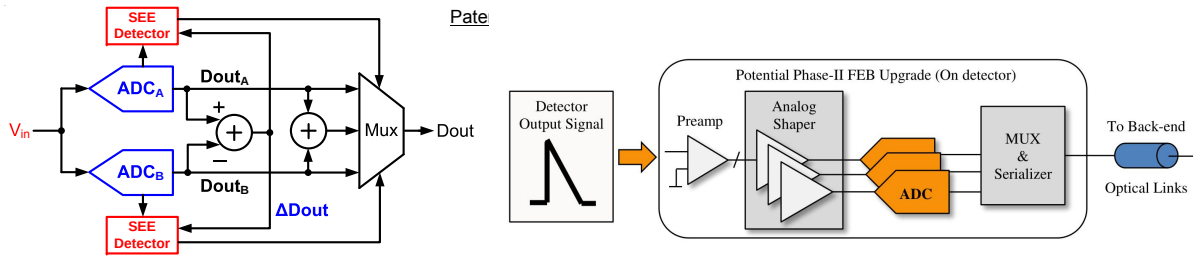

Figure 23. Left: Concept of split ADCs with SEE detection mechanism, which selects the ADC which is not hit by an ionising particle in case a difference between the two ADC outputs is observed [24]. Right: A FESOC will integrate the analog pre-amplification, shaping, the analog-to-digital conversion and the serializer and optical-link components in a single ASIC.

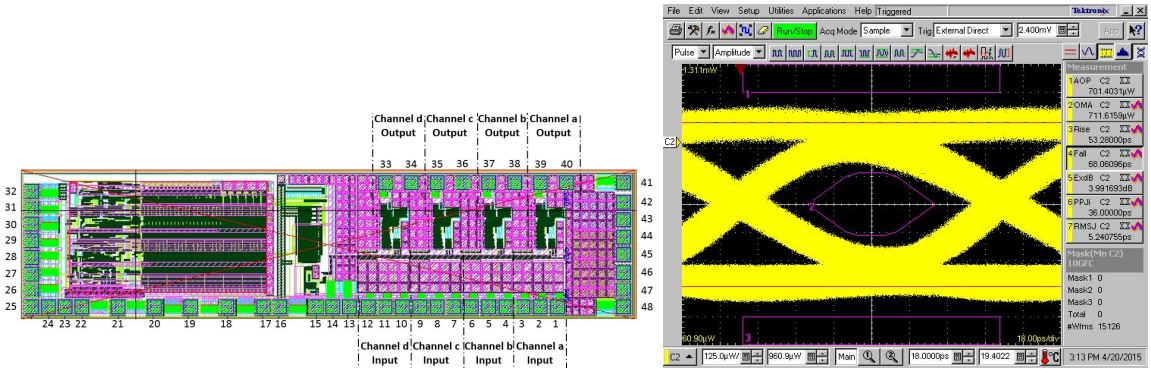

Figure 24. Left: Image of a prototype VCSEL array driver in 250 nm SoS technology for data transmission up to 8 Gb/s [27]. Right: Eye diagram taken with a prototype of the VCSEL array driver transmitting a pseudo-random binary sequence at 8 Gb/s.

The back-end system is planned to be composed of 60-120 LAr Pre-PRocessor (LPPR) units in ATCA format each equipped with 4 high-performance FPGAs either installed on Advanced Mezzanine Cards (AMCs) or directly on the PCB board. For the LAr readout, FPGA models with a large number of serial links (≥ 96) are foreseen such that about 1 Tb/s of data can be handled in each FPGA processing unit. The number of necessary processing boards depends mainly on the ADC sampling frequency which is at least 40 MHz. Higher frequencies of up to 80 MHz - with potentially higher out-of-time pile-up suppression capability - are considered.

A concentration of on average 4 FEB-2 data streams would already be feasible with the Phase-I LDPB [17] which is equipped with 4 processing FPGAs, similar to the LPPR module. A Phase-I demonstrator board for the LDPB module is shown in Fig. 25. A pre-prototype of the LDPB, composed of an ATCA main board and four AMC units, is being fabricated. From the trigger perspective, it would be ideal to process the detector signals from a trigger tower region of $\Delta\eta \times \Delta\phi = 0.2 \times 0.2$ with a single FPGA. This motivates the evaluation of modern FPGAs with a large number of transceivers (like ALTERA Arria 10 [29] or Xilinx Virtex Ultrascale [30]) for their application in the LPPR modules. In the baseline scenario, a data output of 28 bits per LAr Calorimeter channel at 40 MHz is assumed to be received by LPPR modules using 4 FPGAs each with 120 input links. The integration of large-scale FPGAs on the processing boards has challenging aspects, like the need for high-density Multi-Fiber Push On (MPO) connectors and efficient power dissipation, and is subject of the R&D programme which closely follows the technological advances of the respective commercial

components.

Each FPGA will decode the data stream, align and arrange the data from different channels in order to prepare the L1 trigger output. Advanced digital filtering methods will be applied to extract the energy and signal time in each calorimeter cell and to correct for out-of-time pile-up effects. Regional pile-up mitigation methods may furthermore suppress in-time pile-up contributions to the energy measurement. In this way, full granularity input is provided to the L1 trigger with best possible energy calibration and pile-up corrections. All calorimeter data are digitally available in the back-end FPGAs, which allows a straightforward implementation of circular buffering during the trigger latency periods with random access to the triggered event data. The total output rate per FPGA is in the order of 75 Gb/s, which does not take replication of data to the trigger system into account and which may increase depending on the details of the trigger information required. The energy reconstruction and trigger pre-processing algorithms are fully configurable in FPGA firmware and can be continuously adapted to the HL-LHC operating conditions.

The concentration of signals from large detector areas into one processing module requires the 16×1524 fibres arriving from the front-end to be re-mapped. Assuming that each such module can cover 24 fibre ribbons with 12 fibres each, a total of 85 re-mapping modules are needed. Optical power measurements and bit error rate tests will be performed to verify if the re-mapping modules can be passive or need active components.

The front-end system will be completed by a set of calibration boards, which inject signal pulses of programmable amplitude and well-known shape directly onto the calorimeter electrodes, except in the forward calorimeters (FCal) where the signals are sent to the FEB-2. The electronics calibration procedure is a key ingredient of the calorimeter calibration. Given the simplified powering scheme, new radiation tolerant ASICs need to be developed for the calibration boards and are foreseen to integrate all necessary functionalities in a single chip. The ASIC is planned to incorporate the Digital-to-Analog Converter (DAC) function, the pulser switch and the digital logic to select which channel to pulse and select the DAC value. The current and voltages delivered will be larger than in the currently installed LAr calibration boards in order to adapt to the expected dynamic range of the high-energy signals in the calorimeter layers, while keeping the injection resistors in the LAr cryostats unchanged. For this reason, Silicon-on-Insulator (SoI) technology is a probable choice for the calibration ASIC.

V.2.3 Low Voltage Powering Systems

The LAr front-end power distribution system and the HEC low-voltage power supplies will need to be replaced for reasons of radiation tolerance. Moreover, the ASIC technologies utilized on the future front-end and calibration boards will be more homogeneous in the required voltages than the current LAr readout system. This will allow a replacement of the Low Voltage Power Supplys (LVPSs) by a point-of-load power distribution system based on DC/DC converters implemented close to and even on the front-end boards. Research and development for radiation tolerant DC/DC converters functioning in a magnetic field environment as well as for main power converters is ongoing. Currently available DC/DC systems [31] will likely need further developments to meet the requirements on power density and space. Apart from the powering system for the main front-end components, the HEC LVPS need to be replaced, also for reasons of radiation tolerance. Here, the design can largely follow the design of the current HEC-LVPS since the cold readout electronics for the HEC will remain unchanged. Commercial power Metal-Oxide Semiconductor Field-Effect Transistors (MOSFETs) have already been qualified successfully for radiation tolerance, and other components are under study, like radiation tolerant FPGAs for control purposes.

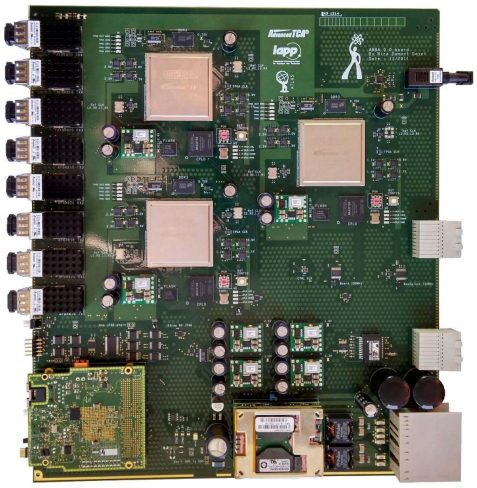

Figure 25. Left: Demonstrator board of the Phase-I LDPB module, which is equipped with 3 Altera Stratix-V FPGAs. This board is currently operated to read Super-Cell trigger data from a LAr barrel calorimeter region during LHC Run 2. The Phase-I LDPB can be considered as an evolutionary step towards the Phase-II LPPR board.

V.2.4 R&D Timeline and Technology Selection

The R&D for radiation tolerant custom ADCs has already been started in the context of the Phase-I upgrade of the LAr Calorimeter trigger readout and is now orienting towards HL-LHC requirements. Design studies of custom ASICs for the pre-amplifier and shaping stage are also ongoing. The R&D of the LAr Calorimeter group on low-power and high-bandwidth serializer and optical-link systems is fully integrated into the CERN-wide lpGBT and VL+ projects. The next generation of prototypes of the custom components for the front-end and calibration boards is foreseen for the years 2015-2016. All front-end prototype components will be routinely tested for their radiation tolerance. This will allow an Initial Design Review (IDR) with a detailed overview of the technologies in the second half of 2016.

The back-end Pre-Processor system is a direct evolution of the LAr LAr Digital Processing System (LDPS) developed for the Phase-I upgrade of the LAr Calorimeter trigger readout. The R&D prior to the IDR in 2016 will concentrate on evaluating commercial FPGA and optical-link systems which fulfill the high-bandwidth requirements and allow the necessary concentration of the data in the processing units. A system and signal processing optimisation will be performed using detailed simulations of the readout system and the expected physics.

Fully functioning prototypes of the front-end and back-end components are planned to be available by 2017, when a TDR is foreseen. At this time, the selection of the optimal readout concept and the technologies will be made. The aim is to finalize the design of the various ASIC components by 2019, build and test prototypes in 2020-2021 and run production in 2021-2022. Design of the front-end boards will proceed in parallel, using R&D and prototype components as they become available to advance as early as possible on component integration. Front-end and back-end board production will happen in 2023-2024, followed by installation.

V.2.5 Cost Estimates

Table 16 summarizes the estimated CORE costs for the upgrade of the LAr Calorimeter readout.

Table 16. CORE costs for the new LAr Calorimeter readout. *(Comment: LPPR and FELIX/TTC costs still in review.)*

WBS ID	Upgrade Item	All Cost Scenarios [kCHF]
3.1	**LAr Readout Electronics**	**31,394**
3.1.1	**LAr Front-end Electronics**	**20,427**
3.1.1.1	Front-end Boards (FEB-2)	9,743
3.1.1.2	Optical fibres and fibre plant	4,306
3.1.1.3	Front-end power distribution system	3,123
3.1.1.4	HEC LVPS	622
3.1.1.5	Calibration System	2,484
3.1.1.6	Shipping and Logistics	150
3.1.2	**LAr Back-end Electronics**	**10,967**
3.1.2.1	LAr Pre-processor Boards (LPPR)	10,212
3.1.2.2	Transition modules	122
3.1.2.3	ATCA shelves	66
3.1.2.4	ATCA switches	76
3.1.2.5	Server PC	22
3.1.2.6	Controller PC	8
3.1.2.7	FELIX/TTC System	460

V.2.5.1 Cost Drivers and Cost Risk Analysis

The cost estimates of the front-end and back-end components are based on cost inquiries for the production or purchase of the main components and on the experience from the preparation of the Phase-I Upgrade production. The main cost risks are caused by the following items:

- The price development of high-performance FPGAs and MPO connectors is uncertain. The FPGA costs represent a large fraction (about 60%) of the LPPR production costs.
- An increase of the baseline readout frequency from 40 MHz to 80 MHz would have direct impact on the number of LPPR boards required, on the number of optical data-transfer links and on the size of the optical re-mapping plant. Doubling the sampling frequency without reduction of the number of transferred bits per channel will basically double the cost for the back-end system. R&D is on-going to establish if the improvements due to the 80 MHz readout scheme justify such an investment or if the increased data volume can be compensated by a reduction in bits per channel.
- The re-mapping modules for the optical data-transfer fibres are assumed to be constructed of passive optical components. If R&D suggests active optical re-mapping this will lead to a cost increase.
- The costs for front-end powering are based on the costs of the current low-voltage power distribution system. A cost variation is possible if the ongoing R&D shows that a different powering scheme is required.

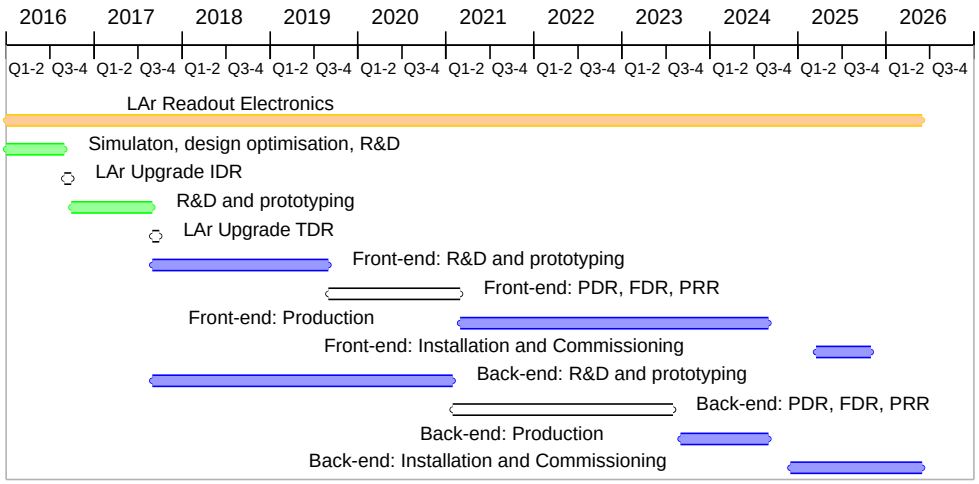

Figure 26. Overview of the time-line and milestones for the main system components of the front-end and back-end systems of the LAr readout electronics upgrade.

V.2.6 Schedule and Milestone Summary

As pointed out in Section V.2.4, there will be a combined IDR and TDR for the LAr calorimeter upgrade in the second half of 2016 and 2017, respectively. For the main front-end and back-end components a graphical schedule overview is shown in Fig. 26. The milestones for the different readout components are arranged according on the length of the estimated production time. Therefore, the production of front-end elements like the power distribution systems can start later than the production of the main front-end components, like the FEB-2 boards, which will leave more time to optimize their design.

V.3 Tile Calorimeter Electronics

The Tile Calorimeter [32, 33] measures the remaining $\sim$ 30% of hadronic energy after the LAr calorimeter [34]. It is a barrel-like structure of iron-scintillator wedges, with 64 wedges covering the azimuthal angle range; the structure of one of these wedges is shown in Figure 27. Each scintillator tile is read out via wavelength shifting fibre from two sides, leading to an intrinsic redundancy in the energy measurements. The photo-tubes and front-end electronics are at a radius of approximately 4 m from the beam-line, housed in 3 m-long mechanical structures referred to as drawers, which provide alignment of the Photomultiplier Tubes (PMTs) with the fibres; the drawers also facilitate cooling of the electronics.

The HL-LHC environment presents several challenges for the Tile calorimeter. The ambient cavern radiation can lead to SEU effects in some components, for which error correction techniques and redundant systems will be required. In some cases, the integrated radiation dose can lead to permanent component failure. A second major challenge is in dealing with the high occupancy, particularly out-of-time pile-up from previous crossings. A third challenge is to make the new readout system compatible with the new trigger scheme with the 1MHz L0 rate. To cope with these challenges, all on-detector and back-end electronics are to be replaced, as well as the mechanical

structure that houses them. Several options for the front-end shaping and HV control are discussed, and the strategies for down-selecting are described.

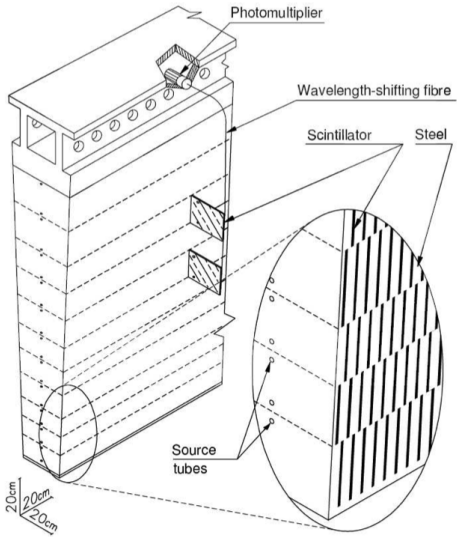

Figure 27. Tile Calorimeter structure showing iron wedge structure, scintillators, PMTs, and the girder housing the electronics drawers.

V.3.1 Electronics Overview and HL-LHC Challenges

The front-end electronics of the Run 1 Tile system is based on a so-called 3-in-1 amplifier/shaper card [35]. The signal chain is shown in Fig. 28. Signals are digitised using 10-bit ADCs on a digitiser board, and two gain ranges are used to cover the necessary 16 bit dynamic range. The system also sends analog signals over a 70 m run to the off-detector trigger processor (these cables introduce approximately 350 MeV of noise), and includes drivers for charge-injection and Cs source slow integration calibrations. Signals are buffered and later sent off-detector via optical fibres to a ROD when a trigger is received.

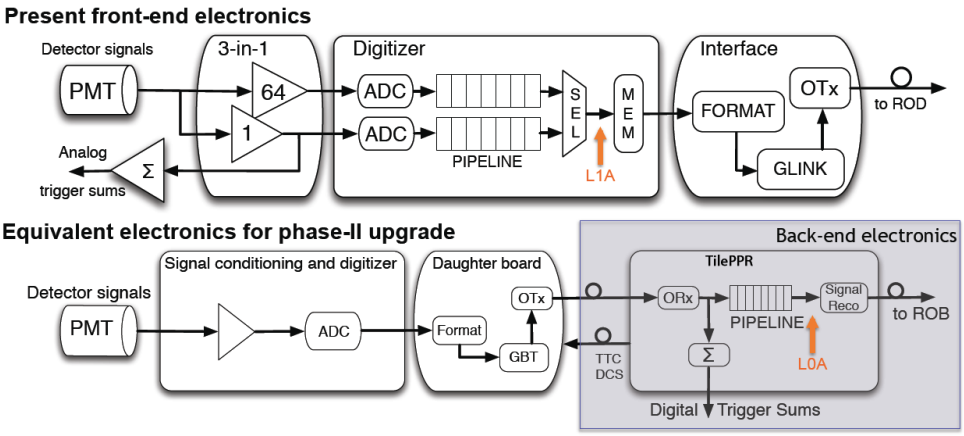

Figure 28. Signal flow in the current system (top) and in the proposed Phase-II system (bottom).

The Tile calorimeter drawers are inserted in the iron structure, thus the radiation tolerance requirements are significantly lower than for the systems closer to the beam pipe and in the forward areas. The largest dose happens at the ends of the barrels; this is where the low voltage power supplies are mounted. SEU effects have been observed during Run 1 in an older version of the LVPS but have been eliminated with a revised version using more radiation tolerant controllers.

The current electronics will not survive the doses expected by the time of HL-LHC, and SEU events will be more frequent. The high pile-up might overwhelm the 50 ns FWHM time constant shaper, and the high event rates require a more intelligent trigger with better energy resolution. For these reasons it is necessary to redesign the Tile electronics. Additionally, many replacement components of the current electronics are no longer available. The new design addresses several problems of the current system, for example reducing the large number of interconnects and adding redundant LVPS feeds, to name but two. Additionally, the smallest independent module size has been reduced in the new design so that a worst case single point failure (currently causing some dead regions of $\Delta\eta \times \Delta\phi \approx 0.8 \times 0.1$) will affect only 1/8 of a current barrel module's channels with a loss of only 1/2 the light yield from any cell.

V.3.2 Electronics for HL-LHC

For HL-LHC running, both the front-end electronics [36] and the trigger/DAQ pre-processors Tile Calorimeter Pre-Processors (TilePPRs) [37] have been redesigned, and all COTS components have undergone a program of extensive radiation testing with ionising radiation (Co^{60}), protons at a medical facility, and neutrons from a reactor. Additional redundancy is introduced in the signal processing and LVPS chains. The most dramatic change is to send the data from all Tile cells off-detector by high-speed fibre optic links. The new signal chain is shown in Fig. 28. The 3-in-1 amplifier/shaper card of the current system will be replaced by one of three alternatives under study. A Motherboard (MB) routes the high-speed signals to a Daughter-board (DB) [38], and the MB also distributes LV and handles slow controls. Since all data is sent off-detector for each event, there is no longer a need for analog fast trigger lines since the L0 tower trigger can be formed at the back-end pre-processor using the digital cell data.

It is possible that the current front-end shaping will not be optimal for the high pile-up environment. In order to study this, as well as test all the new electronics, a "hybrid demonstrator" prototype has been constructed. This device is an exact prototype of the Phase-II drawer, but with the addition of backwards-compatible analog trigger cables so that it can be used in the current detector. Recent tests of a demonstrator has obtained performance superior to that of the current system and has permitted more accurate costing and design of mechanical tooling. A Charge-injection-Scan (CiS) from the demonstrator, shown in Fig. 29, shows linearity of 0.5 parts per mil, an order of magnitude better than the current system.

To facilitate easier extraction and replacement for repair, particularly considering the high radiation doses, the mechanical drawer system will be replaced with shorter "mini-drawers" supporting 12 PMTs (the current drawers support 24 PMTs). Prototypes for these mini-drawers have been manufactured for the hybrid demonstrator as shown in Fig. 30.

The LVPS system consists of +10 V feeder supplies located at the ends of the barrels, as shown in Fig. 31. Point of load regulators (POLs) are used on the MB and DB to supply the needed voltages. Each MB and DB is functionally separated into halves, with each half processing the photo-tubes from one side of the wedge. Each half has a separate LV feed that could power both halves (by means of a diode OR) of a mini-drawer if one feed fails.

The DB controls all communication with the back-end electronics. The Daughter-board (DB) also receives slow control commands from the TilePPR and routes it to the Motherboard (MB). Each half

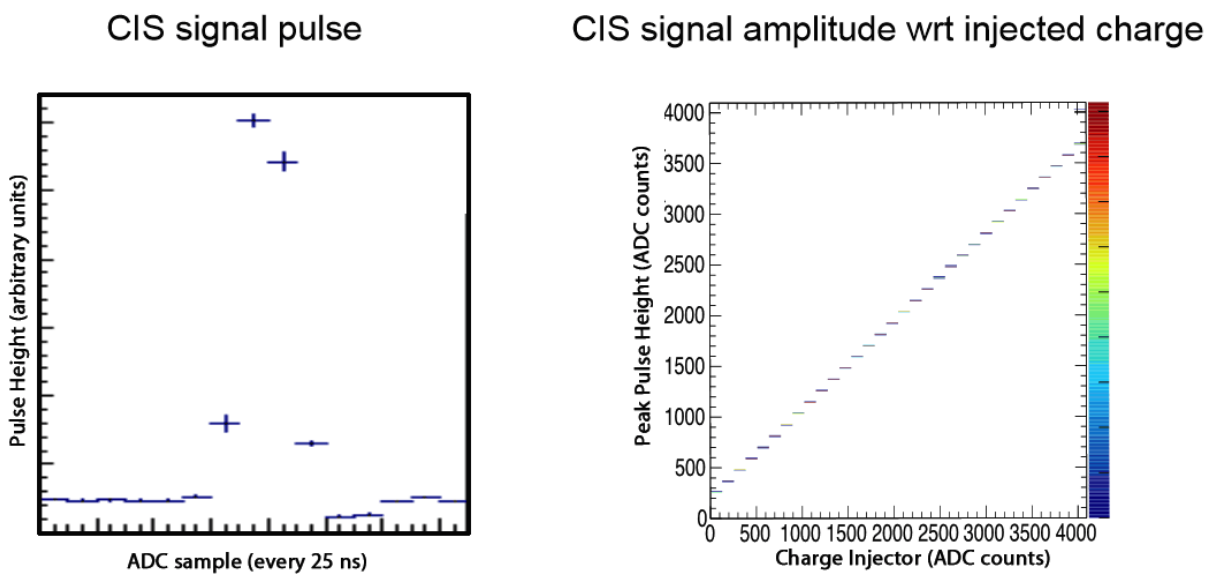

Figure 29. (*left*) One CiS pulse shape. (*right*) Pulse height versus CiS pulse amplitude.

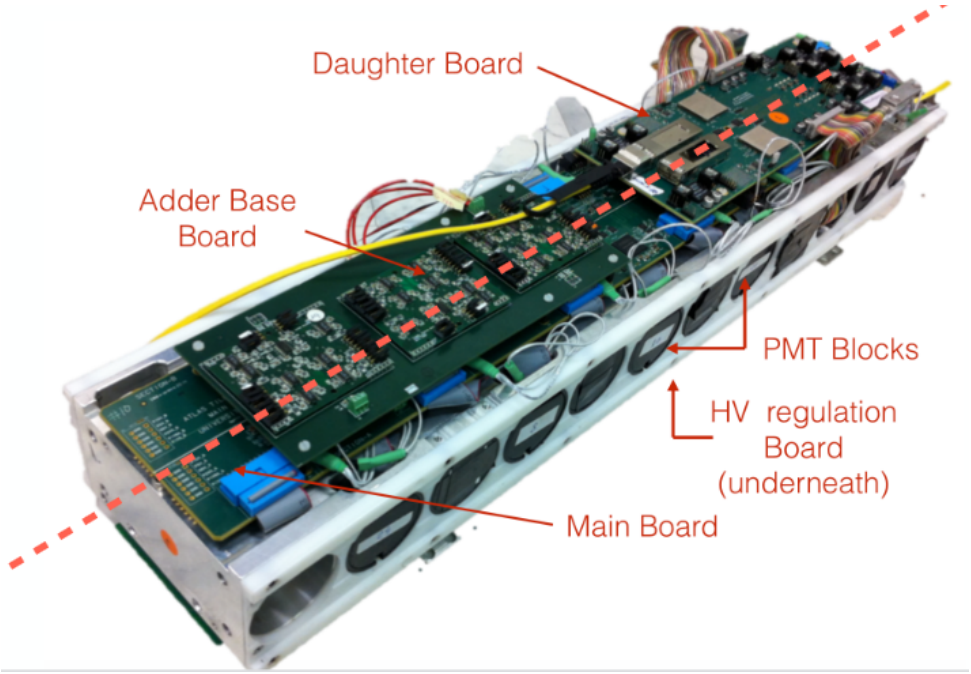

Figure 30. One new mini-drawer used in the demonstrator; the analog trigger adder card will not be present in the Phase-II system.

DB is controlled by a Kintex-7 FPGA, as shown in Fig. 32. The MB sends the digitised signals from the PMTs to the FPGAs on the DB by means of a 400-pin SAEF connector; the FPGA then sends the data to the back-end electronics by means of optical fibres.

A modulator-based [39] Quad Small Form-Factor Pluggable (QSFP) optical module is used to drive the fibres at 4.8 Gbps upload- and 10.24 Gbps download speeds. While the CERN GBT [40]

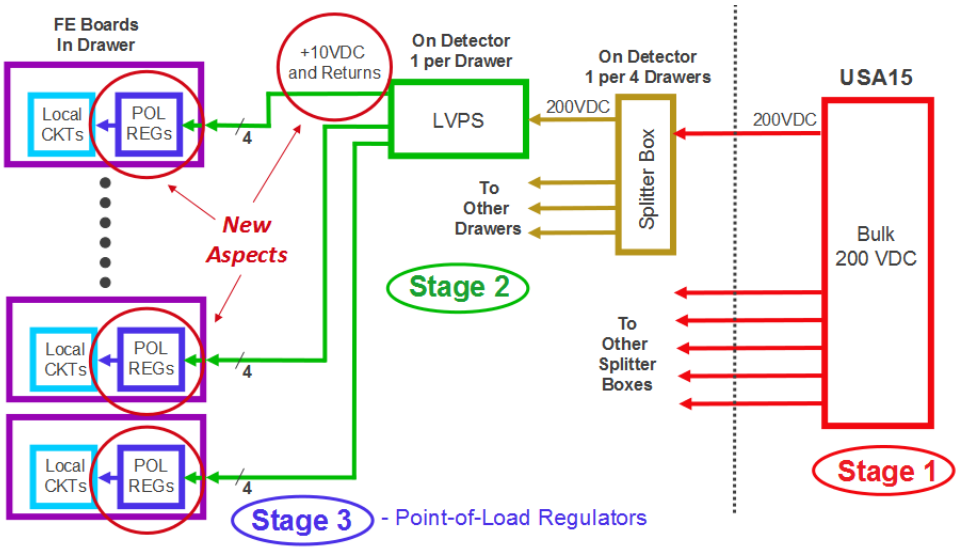

Figure 31. Power distribution scheme.

protocol is programmed in the FPGA to handle error correction of the data stream, the only GBT product employed in the system is the GBTx ASIC which generates a stable TTC beam clock; it is also used to remotely re-flash the firmware when necessary. All other communication with the back-end TilePPR is accomplished in the Xilinx "GTX" layer of the Kintex7 FPGA. Commercial optical modulators instead of versatile-link driver/receivers have been chosen for cost-effectiveness, small PCB footprint, and the demonstrated radiation hardness of this technology. Modulators also permit the possibility of sending the data at higher rates in the future.

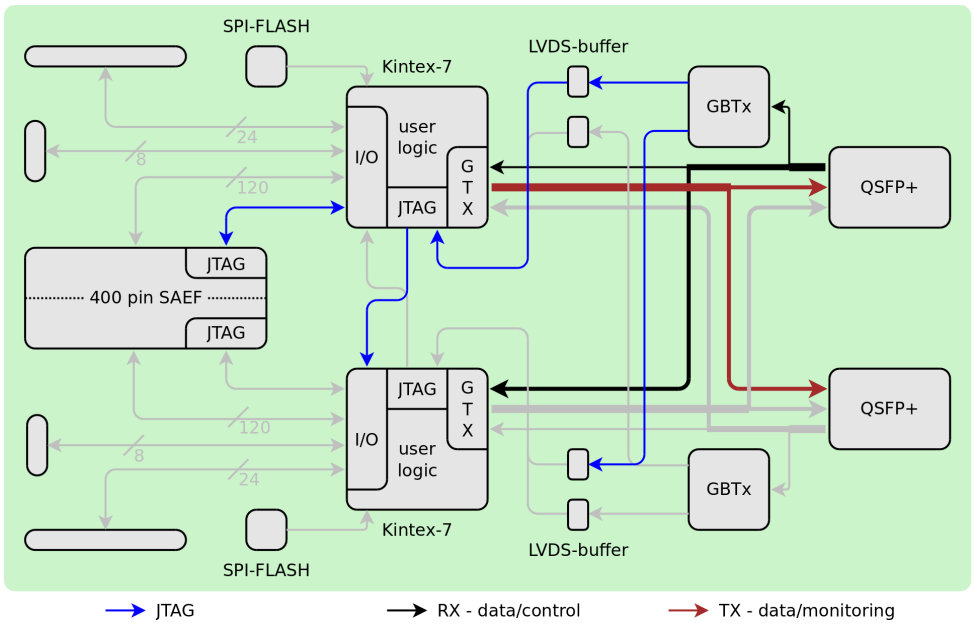

Figure 32. Signal flow in the Daughter Board (version 3).

Three alternatives are being studied to replace the amplifier/shaper card. One possibility is

simply to redesign the 3-in-1 with new discrete COTS components. With this card, the 12-bit digitisation must reside on the MB. The other alternatives are custom ASICs shown in Fig. 33. It is possible that the small feature sizes (65 or 130 nm) could be very radiation tolerant, and that the noise might be lower, particularly if the ADC is incorporated in the ASIC. With the lower voltage used in these technologies, it will be necessary to have more than two gain ranges. The "Charge Integrator and Encoder" ASIC (QIE) [41] alternative has a 7-bit ADC and 4 gain ranges; it also has time-stamping. The "All-in-One" front-end is based on the Front-end for Atlas TilecAL Integrated Circuit (IC) (FATALIC) [42] ASIC, and makes use of the current-conveyor concept. A radiation-hard ADC is incorporated into the FATALIC chip, which uses 3 12-bit gain ranges.

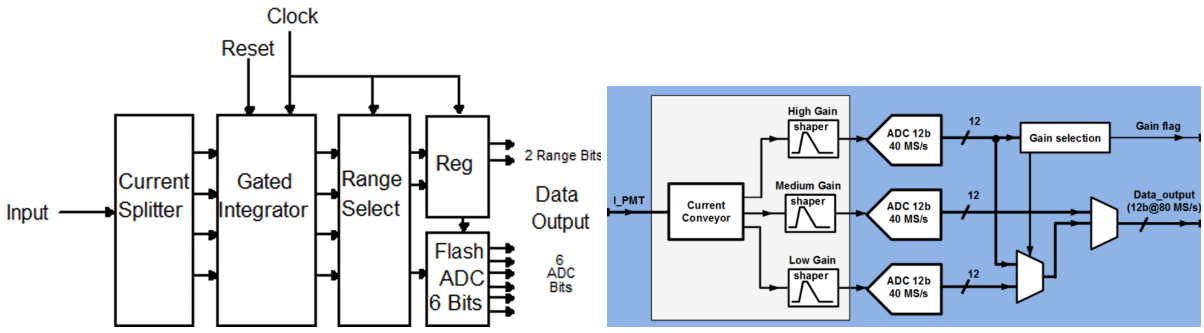

Figure 33. (*left*) QIE signal flow. (*right*) FATALIC basic circuit.

The new read-out scheme using high bandwidth links places much higher demands on the TilePPR than in the current system. The signal flow of the TilePPR is shown in Fig. 34. The TilePPR is responsible for receiving and routing data received from the drawers, sending trigger tower signals to the trigger, receiving and transmitting slow controls to the drawer, and establishing the system (currently TTC) timing to synchronise the readout stream with the DAQ. This system uses Virtex-7 and Kintex-7 FPGAs and QSFP optical transceivers.

High voltage supply and monitoring of the Photomultiplier tubes is also done in the mini-drawers. Currently two alternative systems are under study. In one case, HV from a single HV feed to the mini-drawer is adjusted for each PMT by a controller card similar to those on the current system. This card communicates with slow controls via the DB. The alternate system under study has the HV distribution off-detector, with 12 HV cables running to each mini-drawer.

V.3.3 R&D for Phase-II Upgrades

The focus of the Tile Calorimeter upgrade activity is replacement of electronics and improvement in the associated electronics housing. The Phase-II upgrade plans for the Tile Calorimeter include the following new items for which R&D is being carried out:

- On-detector mechanics
  - Mini-Drawers (shorter than in the legacy system) housing the electronics and tooling
- On-detector electronics:
  - Front-end boards and Main-Boards (3 options)
  - “Active” PMT (photomultiplier tube) voltage dividers
  - Daughter-Boards (with radiation tolerant FPGAs)

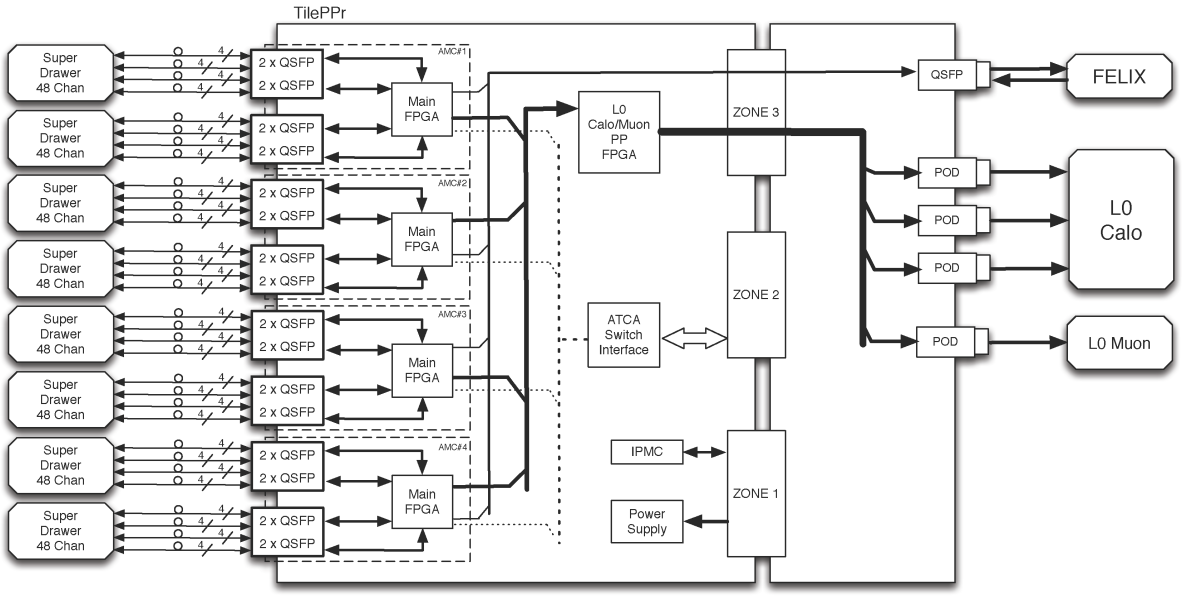

Figure 34. TilePPR data flow.

  - Low Voltage Power Supplies
  - High Voltage system (2 options, one with off-detector regulation per PMT)

- Off-detector electronics
  - Development of TilePPR , including trigger pre-processing

- Optics in the gap/crack area
  - Radiation resistant scintillators

The scintillator slabs located in the gap area between the barrel and end-cap calorimeters, used to correct for the energy lost in the pseudo-rapidity region between 1.0 and 1.6, will need to be replaced with more radiation resistant material. Studies of properties of new types of scintillators and fibres and tests under HL-LHC radiation doses are ongoing. The response of the four scintillators slabs in each phi-wedge in this region between the calorimeters, degraded by 2% to at most 12% in the innermost radius during Run 1.

There are ongoing investigations of the possibility to use multi-anode PMTs to read parts of a fibre bundle that correspond to sub-sections of a readout cell using the individual pixels of the photo-detector. The merits of improving the longitudinal and transverse granularity are under evaluation, based on studies of jet resolution of jets, jet substructure, and muon identification in the last layer. In parallel, an important study of the response drifts of the current PMTs as experienced during collisions in Run 1 is ongoing, with the aim to understand the source and to predict the behaviour with the light exposure expected under HL-LHC conditions.

The IDR for the Tile Calorimeter Phase-II upgrade is tentatively scheduled for the third quarter of 2016, and the submission of the TDR to the LHCC is foreseen in the third quarter of 2017. The principal issues to be understood prior to the TDR are:

- On-detector mechanics

  - Optimal design of handling tools and services on the basis of the anticipated opening and access scenarios for Phase-II.

- On-detector electronics
  - Robustness against radiation.
  - Reliability (power and data transmission and stability).
  - Best strategy for pile-up robustness.

Front-end and back-end prototype versions will be tested in the TileCal integration facility with ATLAS TDAQ and test-benches as they become available. Laser and Cs calibration systems are available. In addition, several test-beam runs in 2015 and 2016 are planned in order to record a library of PMT signals for different Tile cells and to characterise the performance of the different amplifier/shaper and HV control alternatives.

Concerning the mechanics, realistic exercises to emulate the access conditions in the cavern are also planned. In order to get operating experience under field conditions, a hybrid demonstrator version of the upgraded system has been developed so that it is completely compatible with the present system. One demonstrator super-drawer (composed of 4 mini-drawers) will be ready and commissioned on the surface around the end of 2015 and can be ready for insertion in ATLAS from then on, most probably during the 2016/17 end of year technical stop.

The major R&D deliverables required before TDR submission are the construction of prototypes, performance evaluation and comparison of the alternative options in realistic environments (i.e. with particles in test-beam runs), as well as long-term tests in the TileCal integration facility. Testing of the radiation tolerance to HL-LHC doses is already well advanced, with many components already partially and a few even fully qualified. This program of measurements of TID failure due to proton, neutron, and ionising fluence, SEE, and NIEL are ongoing and have led to a number of Tile Internal Notes [43–47].

The following intermediate milestones are defined in the global schedule in order to allow monitoring of the progress and permit timely corrective actions. For on-detector electronics, prototypes of the 3 FE options should be built and tested by mid-2016. A prototype of the TilePPR should be available before mid-2016. The R&D for active HV Dividers is essentially complete, with further testing and performance evaluation to be conducted in the near future. Prototypes of the 2 alternative HV systems should be available by end of 2015. Test beam measurements should begin 2015Q4 and be completed by 2016Q4. The decisions for which FEB and HV options to employ should be made by 2017Q2. Complete radiation qualification of all subsystems should be completed by 2018Q2. We note that two subsystems are essentially complete: the on-detector LVPS prototypes are available and being tested, and mini-drawer prototypes are ready and have passed tests; tools and services should be validated by mid-2016. Components for the prototypes will be purchased between mid-2015 and the end of 2016. It is assumed that sufficient effort and R&D funds are available among the participating institutes.

V.3.4 Strategy for Selecting Final FEB, HV Options

The goal is to decide on the best options for the front-end amplifier/shapers and HV control by the time of the TDR in late 2017. A list of essential evaluations includes:

- Long-term full system functionality test in an ATLAS-like DAQ and DCS slice, with noise measurements and stability in a dedicated setup at CERN.

- Testing for robustness against pile-up and for overall signal reconstruction performance with simulated signals and calibration data on dedicated surface setups.
- Performance evaluation with test-beam particles (electrons, muons, pions of high intensity) and beam-simulated pile-up.

The selection will be based on best performance as assessed through simulation and measurements by prototypes in test beams. The three front-end options do not differ dramatically in cost, and employ rather different pulse shaping and gain ranges. Measurement of their performance in electron, proton, and pion beams of varying intensity should establish which technology handles pile-up the best.

Similarly, the two alternative HV control systems do not differ significantly in cost. Tests using the prototype drawer are underway to measure the noise introduced by the two systems and their stability. Work is also underway to design and compare monitoring of HV in the two systems.

V.3.5 Cost Estimates, Cost Drivers and Risks

An initial CORE costing estimate of the Tile Calorimeter Phase-II upgrade was done in 2012. This was revised in recent months in light of actual expenditures for the "demonstrator" prototype. Furthermore, future production-phase cost estimates have been obtained from suppliers of some of the more expensive components. The costs are shown in Table 17 for four select configurations of the system using the three amplifier/shaper cards and two HV control options. In the table, "internal" HV option refers to the system where the adjustment and monitoring of each PMT voltage is done on the mini-drawer using a controller similar to that used in the current Tile Calorimeter system, while "external" refers to an alternative where the source of each PMT voltage is supplied from off-detector. The final configuration choice for the upgrade will be based on evaluation of the performance using simulation and prototypes.

Table 17. Tile Calorimeter Phase-II CORE costs.

WBS	Item	Base Cost [kCHF]	Option 1 [kCHF]	Option 2 [kCHF]	Option 3 [kCHF]
FE option:		3in1	3in1	QIE	AllInOne
HV option:		internal	external	internal	internal
Tile:		**8,580**	**8,785**	**8,987**	**8,619**
4.1	**Drawer Mechanics**				
4.1.1	Mini-drawers	1,229	1,229	1,229	1,229
4.1.2	Tools/Mechanics	60	60	60	60
4.2	**On-detector Electronics**				
4.2.1	PMT Dividers	173	173	173	173
4.2.2	FE Boards	716	716	1,852	873
4.2.3	Main Boards	987	988	258	869
4.2.4	Daughter Boards	1,561	1,561	1,561	1,561
4.2.5	LVPS System	987	987	987	987
4.2.6	HV System	768	973	768	768
4.3	**Off-detector Electronics**				
4.3.1	TilePPR	1,098	1,098	1,098	1,098
4.4	**Infrastructure**				
4.4.1	Services	1,001	1,001	1,001	1,001

The four alternative configurations shown are similar in total cost. The main cost drivers are the larger FPGAs on the DB and TilePPR, the complex PCB (14, 16 layer) for the DB and some MB versions, the ATCA crate system, and the optical fiber system. Because of the recent construction of a demonstrator, there is a high level of confidence in the cost projection for a full scale system. The costing shown here includes quotes for future PCB assembly and cost of FPGAs in production quantities in FY2017. For some of the services such as fiberoptic cables and ATCA crates which will be common to many systems, organized bulk purchasing by CERN could lower the cost significantly, but this has not been assumed in the cost estimate.

V.3.6 Summary Schedule and Milestones

The Gannt chart for production of the Tile Calorimeter electronics is shown in Fig. 35. The production process involves three broad stages: pre-production, production, and assembly. For pre-production there will be procurement of small quantities of most components except where larger volume purchasing is cost effective. The pre-production units will be assembled, "burned-in" at elevated temperature for a period of weeks, followed by a final radiation qualification of the units to qualify batch components. The production phase will consist of PCB manufacture and assembly, followed by burn-in and testing. Subsystem units will be sent to CERN for assembly. All FE components except for the FEBs and the HV dividers will start being mounted on the mini-drawers prior to the LS3 access. The PMT blocks will be recovered from the detector in the beginning of LS3, then assembled with the new FE electronics and inserted in the mini-drawers. The assembled modules will then be tested with a dedicated test-bench for all readout and calibration functionality.

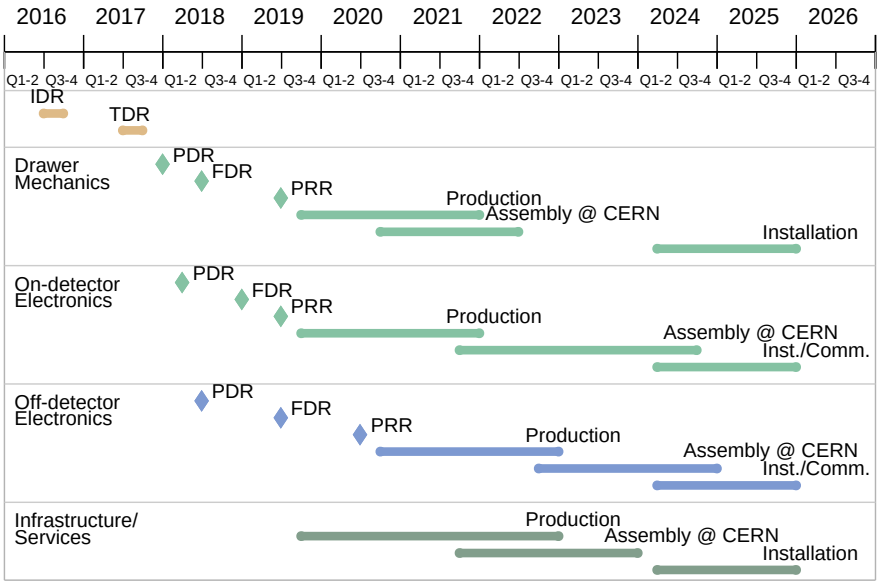

Figure 35. Top-summary schedule and milestones of the Tile Electronics upgrade project.

V.4 Forward Calorimetry

V.4.1 Performance of the LAr FCal at HL-LHC luminosities

The main function of the ATLAS forward calorimeter (FCal) is to provide hermiticity, contributing to good resolution on missing transverse energy, and to provide for efficient tagging of forward jets, for instance from vector-boson fusion or vector-boson scattering processes. The existing ATLAS forward calorimeter was designed to operate at instantaneous luminosities up to the maximum proposed for the nominal LHC experimental programme, $10^{34}\text{cm}^{-2}\text{s}^{-1}$. Even for this luminosity, the harsh environment near the LHC beam-line, where the FCal is located, means that the LAr gaps must be much smaller than in the other ATLAS LAr calorimeters, in order to avoid problems related to ion build-up, which would distort the electric field in the gap and thus degrade the response. At the instantaneous luminosity proposed for the HL-LHC, these gaps, as small as 269μm in the FCal module closest to the interaction point, are no longer small enough to avoid this problem. The higher luminosity also results in a larger current draw, leading to voltage drops across current-limiting protection resistors that are located inside the end-cap cryostat. This exacerbates the ion build-up problem by further reducing the field in the gap. The combined effects of ion build-up and HV sagging would cause distortions of the physics pulse shapes in the high-$|\eta|$ region, as discussed further below. A final possible complication at the HL-LHC is that the increased beam heating of the FCal modules may lead to boiling of the liquid argon. Simulation studies and mock-up measurements intended to address this question are in progress.

If it cannot be established that the LAr will not boil, then some upgrade of the forward region will be required. If not, the option of doing no upgrade remains open, though the effects described above may result in performance losses in this region. Fast simulation studies indicate these issues are important for the population of the tails of the missing E_{T} distribution (in particular from events with no real missing E_{T}) and for forward-jet tagging, which is important for VBF and VBS processes.

In the LAr end-cap integration process, the FCal is inserted into the bore of the end-cap after the installation of the large cold cover, with which it overlaps slightly, as is visible in Fig. 36. While this is bolted into position on both sides of the cryostat, it was also welded into position on both sides. These welds will need to be cut if it is to be replaced. The right-hand photo in Fig. 36 shows the FCal in position for the final insertion. At this point in the process the cables from the FCal modules to the summing boards had been connected. The input connectors on the summing board are at the low-radius end, while the outputs, which connect to cables going to the feed-through, are at the high-radius end. Since the large cold cover will not be removed, the output connectors are inaccessible. Radio-protection issues make it impractical to unfasten the input connectors (which can really only be done by hand) so is not possible to re-cable the existing FCal.

The two upgrade scenarios being investigated are the construction of a replacement FCal, referred to as the sFCal, and the use of a small calorimeter, dubbed the MiniFCal, in front of the existing FCal. The sFCal would be similar in design to the existing forward calorimeter but would employ smaller LAr gaps, and lower-value protection resistors, to counter the problems associated with the higher ionisation load, as well as liquid nitrogen cooling loops to address any issues related to LAr boiling. FCal-style electrodes with smaller LAr gaps have been investigated in high-intensity proton beam-tests and shown to operate normally up to instantaneous luminosities in excess of those planned for the HL-LHC [48]. This is illustrated in Fig. 37 which also shows the expected combined effects of ion-buildup and HV sag in the high-$|\eta|$ region on the nominally triangular FCal physics pulses, for a range of instantaneous luminosities. In the MiniFCal scenario, a small calorimeter located just in front of the high-$|\eta|$ portion of the existing FCal would be used to reduce the flux in this region to levels at which the FCal can operate normally. Both scenarios have been previously

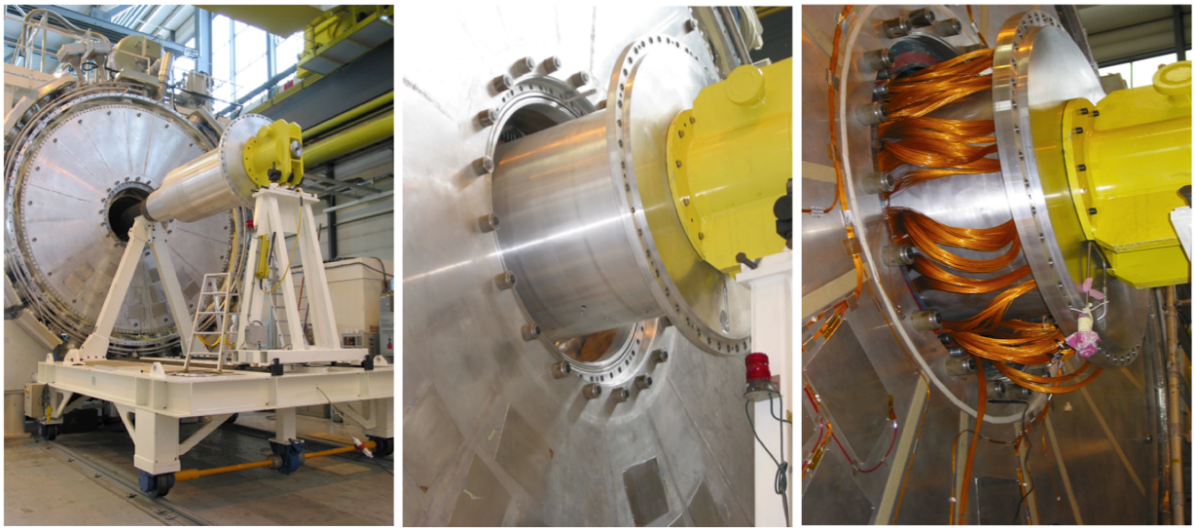

Figure 36. Installation of the ATLAS forward calorimeter. The left and middle pictures show two stages during a test insertion of the FCal cold vessel into the bore of the end-cap cryostat. The image on the right shows the final stage of real FCal insertion. The visible cables come from the calorimeter modules and are connected (by hand) to the input connectors of the summing boards, which are located at the low-radius end of each board (see Fig. 39).

Table 18. Numbers of electrodes, interconnects and readout channels for the ATLAS FCal. For the high-granularity sFCal, the number of readout channels could be increased to the number of interconnects by removing a signal summing stage that is currently done on board in the cold volume of the end-cap cryostat.

	Electrodes	Interconnects	Channels
FCal1	12,260	3066	1008
FCal2	10,200	1700	500
FCal3	8,224	914	254

discussed in the ATLAS Phase-II LoI [1] and the updated detector concepts are described below.

V.4.2 The high-granularity sFCal

Of the proposed upgrade scenarios, the only scenario in which the current performance in the forward region could be maintained or improved is the sFCal scenario. Proposed improvements would come from an increase in the readout granularity in this region, with a consequent improvement in the η and ϕ resolutions for clusters of calorimeter cells, an increased visibility of jet substructure and a reduced pile-up contribution per cell, which will help with pile-up mitigation strategies. Larger improvements in performance are expected in the case where this high-granularity sFCal overlaps in η with the coverage of an extended tracker.

On each side of ATLAS, the existing FCal comprises three modules with the properties shown in Tab. 18. The module closest to the interaction point, the FCal1 (see Fig. 38), is a copper/LAr device with 12,260 cylindrical electrodes oriented in the direction of the LHC beams.

Groups of four electrodes are ganged together with interconnect boards on the module readout face to produce the smallest readout unit, called a tube group. For most of the module, four such

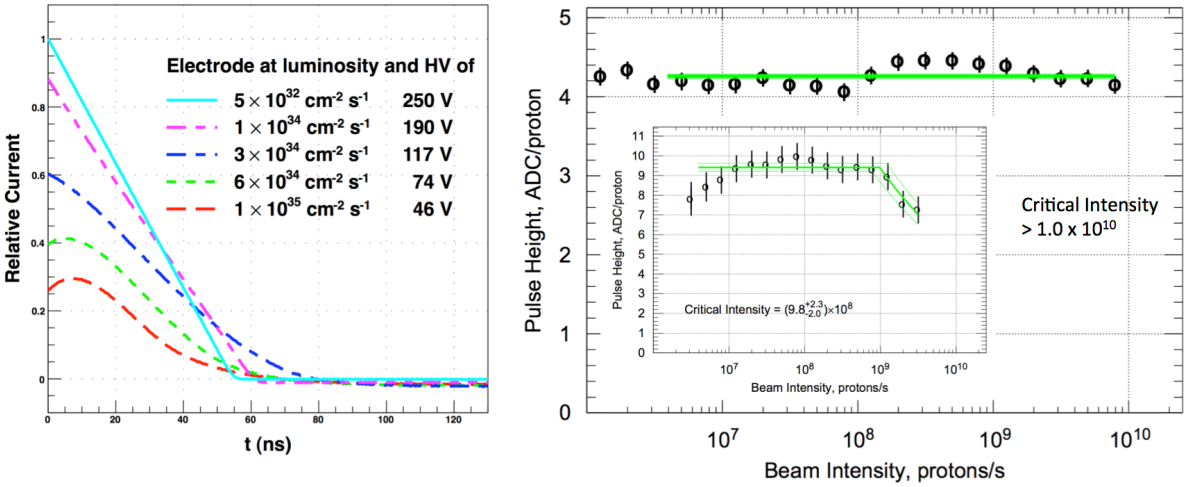

Figure 37. FCal pulse degradation at high-luminosities. The plot on the left shows the results of a simulation of the combined effects of ion-buildup and HV sagging on the nominally triangular physics pulse for an FCal1 channel at $|\eta| > 4.5$ with the regular (269 μm) LAr gaps, for a range of instantaneous luminosities. The plot on the right shows the results of high-intensity proton beam-test result of FCal-style electrodes. Narrow-gap (119 μm) electrodes show a constant response (per proton) up to very high intensities, well in excess of those expected at the HL-LHC. The inset plot shows that the nominal (269 μm gap) electrodes have a response that begins to fall off above a critical beam intensity (corresponding to an instantaneous luminosity just above $10^{34}\text{cm}^{-2}\text{s}^{-1}$.)

tube groups have their signals summed on a transformer located on boards mounted to the rear face of the HEC, so inside the end-cap cryostat cold volume. These form the *summed* readout channels. This is illustrated in Fig. 39. In the inner (high $|\eta|$) region of the detector, and to a lesser extent at the outer periphery, some channels are formed from a single tube group. These channels are referred to as *unsummed*. The second and third modules (the FCal2 and FCal3) have a similar electrode structure, but are made primarily of tungsten. The FCal2 employs gaps of 375μm and gangs together six electrodes per interconnect board; for the FCal3 the gap size is 500μm and there are nine electrodes per interconnect. As in the FCal1, summed channels in the FCal2 and FCal3 are formed from the signals of four tube groups.

The baseline design for the sFCal modules is similar to that of the current FCal but employs narrower LAr gaps of about 100, 200 and 300 μm, in the FCal 1, 2 and 3, respectively. An increase in the readout granularity can be easily implemented (without changes to the module design) by removing the signal summing which is done for most of the channels. This reduces the size of most of the readout cells by a factor of four. This could be done for all three modules. However, due to the large increase in the number of cables and of Front-End Crate (FEC) slots required, this is planned only for the front (sFCal1) module.

The LAr calorimeter subsystems employ pre-amplifiers located off-detector on the FEB-2, with the exception of the HEC, which uses cold GaAs pre-amplifiers located on boards mounted at the outer periphery of the HEC wheels, inside the cold volume of each LAr end-cap cryostat. Studies of the radiation hardness of the HEC pre-amplifier systems show that they will survive the total dose expected for the HL-LHC programme [21]. For this reason, the decision was taken to not remove the large cold cover of the end-cap cryostat. As a consequence the FCal summing boards, which are mounted to the rear face of the HEC, will be inaccessible, as will the cold side of the existing FCal feed-through. Therefore, the HV distribution for the sFCal (and the signal summing, where used) would need be done on a new set of boards. Design studies show that these can be mounted on the

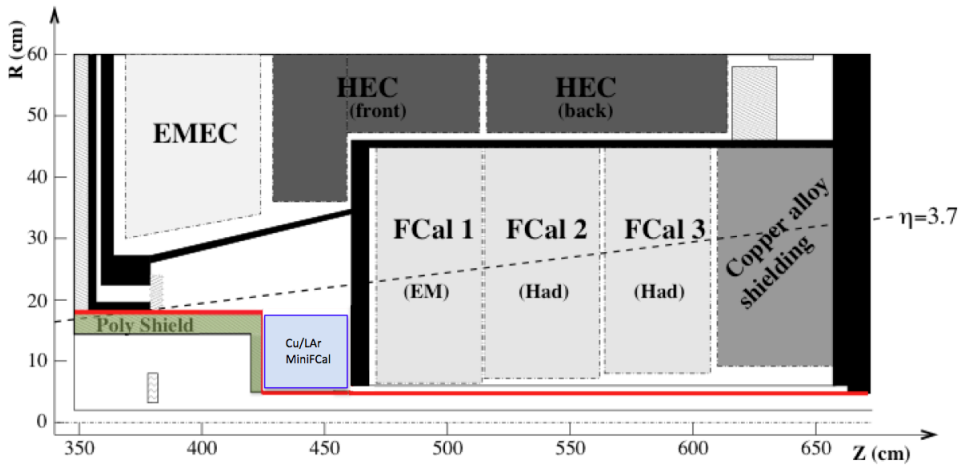

Figure 38. Cross-sectional view of the end-cap cryostat showing the positions of the currently installed FCal modules. These are planned to be replaced by a new sFCal detector. Also indicated is the proposed location of an alternative LAr MiniFCal module (blue) behind a shortened wide portion of the warm tube (red line).

rear face of a shortened shielding plug located behind the sFCal3 module, as shown for the current FCal in Fig. 38. The signal cables would then need to be routed to the FEB-2 boards. Currently, the proposal is to route these in the volume between the end-cap cryostat cold and warm covers. This would require a slight increase (in z) in the end-cap envelope.

If a high-granularity sFCal is built, there will be an associated increase in the number of signal cables required as well as in the number of FEB-2 boards. This would require the use of the other half of the existing FCal FEC which is currently used by the cryogenics group. It would also require the construction of a new feed-through, to service the additional half-crate. The relevant region is visible in the photo on the right of Fig. 39, where the feed-through and pedestal for the FCal FEC appear in the highlighted region.

For the high-granularity sFCal, there is the additional complication that the cold side of the existing feed-through (which would be needed) will be inaccessible, so would remain connected to the cables from the old FCal (which need to be cut and abandoned when the FCal is removed). Detailed design studies are being performed to optimise the new cabling to be routed through the warm space between the cold and warm covers and to be connected inside this feed-through, requiring that this be cut. The engineering studies include a full analysis of the FCal extraction and sFCal insertion procedures in order determine possible risks of damaging or deteriorating the performance of the new sFCal detectors or of the detectors installed in the same cryostat.

The geometry of the high-granularity sFCal and the associated conditions (pulse shapes, etc.) have been implemented in the ATLAS simulation infrastructure. Figure 40 shows event displays for a single electron (upper plots) and a single jet (lower plots) simulated for the FCal (left) and the high-granularity sFCal (right). In each case the display shows the deposited energy in the cells defined by the FCal or sFCal granularity, for the same simulated event. The effect of the (factor of four) improvement in the readout granularity is evident in both plots. Results of performance studies based on this simulation are presented in Chapter XI.

V.4.3 The MiniFCal

In the event that the possibility of LAr boiling cannot be excluded, an upgrade of the forward region will be required. If the sFCal option is not selected, the MiniFCal can provide a solution to the

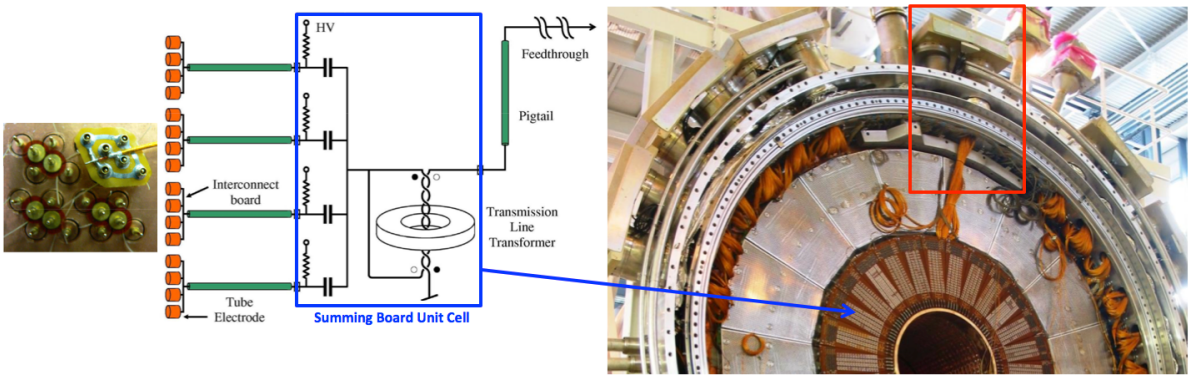

Figure 39. This figure illustrates the summing of signals for the FCal1. On the left is a schematic of how the signals from four groups of electrodes are summed on boards located on the rear face of the HEC (seen on the right). Also visible on the right (highlighted) is the FCal signal feed-through serving the half-crate that is currently used for the FCal front-end electronics. The HV distribution is also performed on the summing boards, which carry the current-limiting protection resistors referred to in the text.

problems described above, by reducing the flux into the high-$|\eta|$ region of the FCal to levels at which it can operate normally.

The initial MiniFCal concept was for a warm copper/pCVD-diamond sampling calorimeter that would fit within the existing warm tube, thus minimising the intervention needed on each end-cap cryostat. However, radiation testing of the diamond sensors indicated that they would likely not survive the accumulated dose at the HL-LHC [49]. The current design is for a copper/LAr device based on the same 100 μm electrodes planned for the first (e.m) module of the sFCal. This is described below, followed by a discussion of a more recent proposal for a warm MiniFCal.

V.4.3.1 The LAr MiniFCal option

The liquid argon MiniFCal would be located in the vacuum space of the "forward cone" region just in front of the cold bulkhead that is directly in front of the FCal1 module, as illustrated in Fig. 38, in its own cryostat that would hang off the back of a modified (shortened) warm tube, via a thermal break. A schematic view of this concept is provided in Fig. 41. The location minimises the lever-arm to the FCal for particles that are scattered in the MiniFCal. This distinguishes this design from the one proposed in Section V.4.3.2 where a warm semiconductor-based MiniFCal is situated near the front of the end-cap cryostat. Radiation simulations of the LAr MiniFCal indicate that its presence in front of the FCal would not result in significant increases to the radiation doses to neighbouring detectors, including albedo back into the volume of the inner tracker.

The services for the LAr device (LAr, LN_2 cooling loops, cabling) would be provided via a service conduit at $\phi = 90^\circ$, which will introduce an asymmetry in the response. Other engineering challenges, especially related to the cooling, are being addressed.

A full (Athena-based) simulation of this scenario has been developed, in order to establish the combined performance of the HEC/EMEC+FCal/MiniFCal and, in particular, to investigate the effect of the conduit material on the response.

V.4.3.2 The warm MiniFCal option

A warm MiniFCal is also being considered as alternative to the LAr MiniFCal option described in Section V.4.3.1. The sampling structure is composed of Si-detector layers as active material alter-

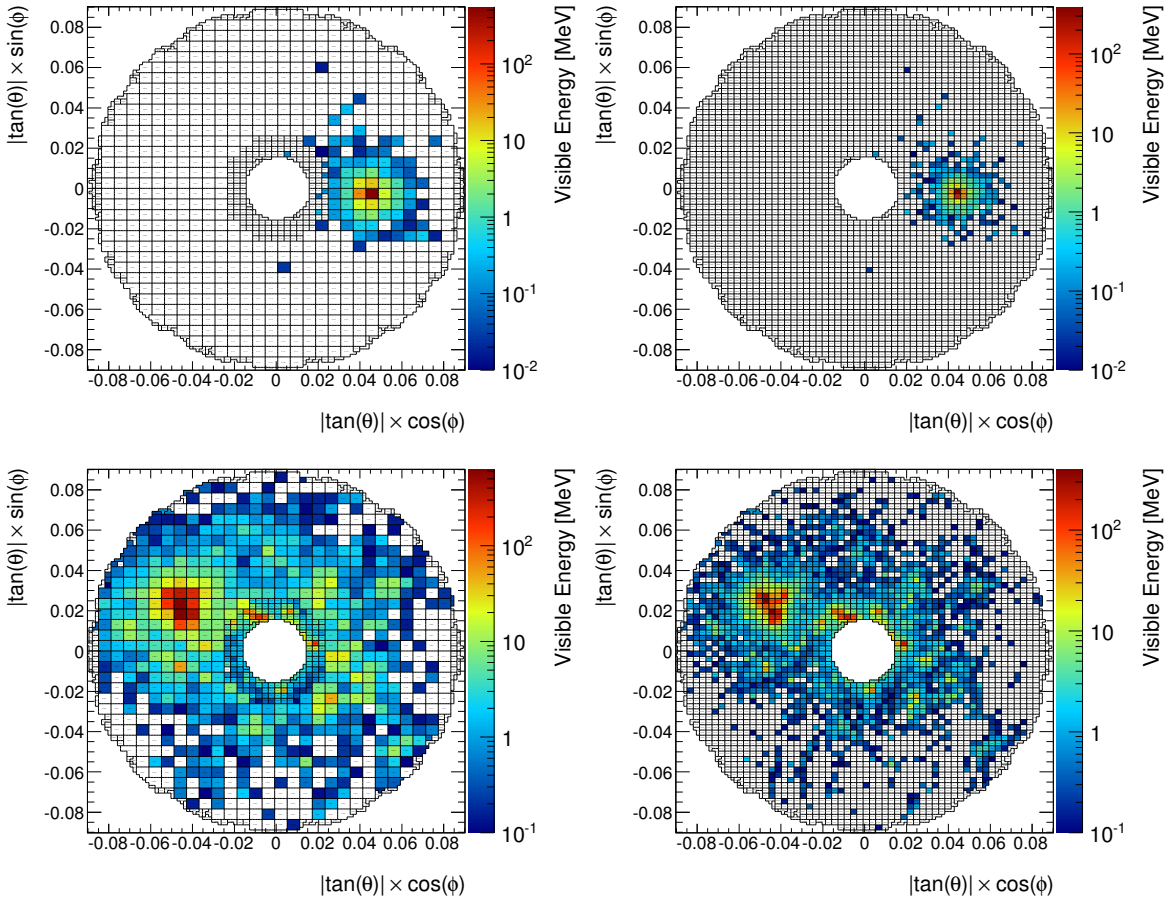

Figure 40. Event displays for the same single electron (upper plots) and the same single jet (lower plots), in the FCal1 (left) and the high-granularity sFCal1 (right).

nating with copper or tungsten layers as absorbers. Two possible locations are under investigation: at the front of the cryostat warm tube or at the rear (where the LAr version would sit). The radial extent of such a detector would be $50\ \text{mm} < R < 170\ \text{mm}$, equivalent to $3.7 < |\eta| < 4.9$, providing the coverage required to address possible LAr boiling issues. However, the location at the front of the end-cap may result in the possibility of shower spreading between the MiniFCal and the FCal, and provide a lever-arm for particles scattering in the MiniFCal. A dedicated performance simulation of this proposal is therefore required, in addition to the simulations used for radiation studies, which are discussed below.

Although the initial pCVD/Cu sampling MiniFCal concept has turned out not to be viable [49], R&D is continuing on an improved version using single-crystal diamond detectors, which is considered as an alternative to silicon-based sensors.

Also under consideration is an integrated silicon-based detector deployed for both the end-cap High-Granularity Timing Detector described in Section V.5 and the forward region. The use of a single technology for these two detectors would enable an integrated solution without an additional transition region.

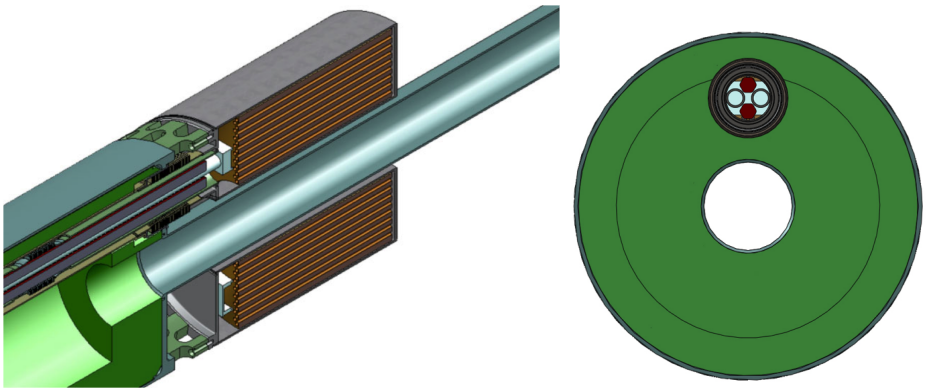

Figure 41. Schematic view of the LAr MiniFCal: (left) a cut-away side view of the module and associated infrastructure. The thermal break between the LAr MiniFCal cryostat is visible, as is the service conduit. The JM moderator material (tube + plug) is shown in green; (right) an end-on view (from the IP side) showing the JM moderator and the location and composition of the service conduit.

V.4.4 Timeline and Decision Path

In the Reference scenario, a high granularity sFCal is planned to replace the FCal. This decision is driven by performance considerations: the sFCal is the detector that guarantees the best performance in the region $3.2 < |\eta| < 4.9$.

In case a detailed risk analysis will conclude in the upcoming months that the replacement procedures in ATLAS will contain elements of severe risks to the other LAr detectors in the same cryostat or to the personnel involved in the operations, the MiniFCal options will be considered. A review of the necessary information required for the decision process is foreseen around mid 2016. For the case of the MiniFCal option, a decision path is in the process of being defined to establish which of the MiniFCal technologies is best suited.

For the Middle and Low scenarios, no replacement of the FCal is foreseen. However, in the event the probability of argon bubble formation evaluated at the highest HL-LHC luminosity is found to be significantly high, the same decision making process aforementioned will be used to establish the detector technology to be deployed for the MiniFCal.

In case the high-granularity sFCal is being built, the IDR is foreseen for the second half of 2016, shortly followed by the TDR in 2017. This will allow a construction time of 6 years, with a final assembly, integration and testing at CERN in 2021-2024. The sFCal installation is foreseen in 2024/2025.

Also for the MiniFCals, IDR and TDR are foreseen in 2016 and 2017, respectively. For the MiniFCal options the construction time is estimated to be 2 years, followed by assembly and integration at CERN in 2023/2024 and installation in 2024/25.

V.4.5 Cost Estimates

Table 19 summarizes the CORE costs and spending profile for the construction and installation of a high-granularity sFCal which is part of the Reference scenario. Costs for opening and closing of the end-cap cryostats and for the required sFCal cryogenics are considered to be part of the upgrade infrastructure and installation and are listed in Section VIII.

A MiniFCal will only be installed if a high-granularity sFCal will not be implemented and only under well-defined conditions (see Section V.4.4). Costs for the LAr/Cu and Si/Cu MiniFCal options are listed. Like for the sFCal, costs for cryogenics of the LAr/Cu MiniFCal are considered to be part

Table 19. CORE costs for the LAr Calorimeter upgrades in the forward region. Costs for a MiniFCal are only due if a high-granularity sFCal will not be implemented and only under well-defined conditions (see Section V.4.4).

WBS ID	Upgrade Item	Reference [kCHF]	Middle [kCHF]	Low [kCHF]
3.2	**High-granularity sFCal**	**10,033**		
3.2.1	sFCal1	1,381		
3.2.2	sFCal2	2,567		
3.2.3	sFCal3	2,480		
3.2.4	Cold cable harnesses	995		
3.2.5	Plug	115		
3.2.6	Cooling loops	28		
3.2.7	Cryostat modification	399		
3.2.8	Structural tube, cone, bulkhead	118		
3.2.9	Feedthroughs and signal cables	778		
3.2.10	Front-end and back-end electronics	771		
3.2.11	Detector support and tooling	402		
3.4	**LAr/Cu MiniFCal**			**907**
3.4.1	Detector and Cryostat			125
3.4.2	Warm tube, Moderator, Insertion			330
3.4.3	Electronics and HVPS			285
3.4.4	Module 0			167
3.5	**Si/Cu MiniFCal**			**3,573**
3.5.1	Cu absorbers			30
3.5.2	Sensors and on-detector electronics			1,001
3.5.3	Front-end readout			713
3.5.4	Back-end readout			1750
3.5.5	Services			80

of the upgrade infrastructure and installation and are listed in Section VIII. Costs for a single-crystal diamond/Cu MiniFCal are not given, since these are dominated by the custom developed sensors, which are still in early R&D phase and for which series production costs are yet unknown.

V.4.5.1 Cost Drivers and Cost Risk Analysis

The costs listed for the LAr sFCal and LAr MiniFCal are based on experience from the construction of the original FCal, updated with recent cost inquiries for the various detector materials and additional components, like cryogenics and electronics. For the warm MiniFCal, Si sensor costs were estimated from recent production campaigns, e.g. for the ATLAS IBL detector. Main cost items for the high-granularity sFCal are the detectors themselves, followed by the readout electronics and cryostat modifications. The LAr MiniFCal is in general not cost intensive, while the sensor and readout costs are driving the budget of a Warm MiniFCal.

Cost uncertainties are identified for the sFCal to be:

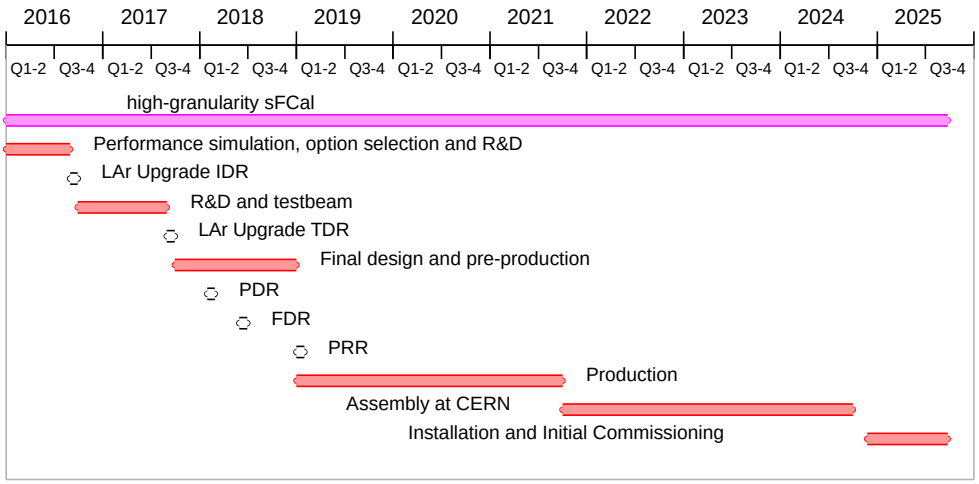

Figure 42. Overview of the time-line and milestones for the implementation of the high-granularity sFCal.

- the market price development for copper and tungsten material and machining
- costs for the feedthroughs, for which the design is still under study
- tooling and cryostat modification, in particular if radiation protection measures require automated procedures
- disposal costs of the current FCal

In case a MiniFCal needs to be installed, the main cost risks are:

- for a LAr MiniFCal: the copper market price, the costs for additional radiation protection measures, and the service conduit for LAr/LN_2/cabling;
- for a Warm MiniFCal: the sensor costs including their yet to define technology, and the number of readout channels.

V.4.6 Schedule and Milestone Summary

All LAr Upgrade elements are planned to provide a combined LAr Calorimeter IDR and TDR in 2016 and 2017, respectively. An overview of the subsequent milestones, production and installation periods for the high-granularity sFCal is presented in Fig. 42. The optional MiniFCal schedule is shown in Fig. 43.

V.5 High Granuarity Timing Detector (HGTD)

The Liquid Argon electromagnetic (e.m.) calorimeter was designed to have rather fine granularity in the first sampling layer over much of its acceptance, motivated by the possibility of measuring the pointing of photons coming from the primary vertex and the capability of rejecting π^0's with E_{T} up to around 50 GeV or more.

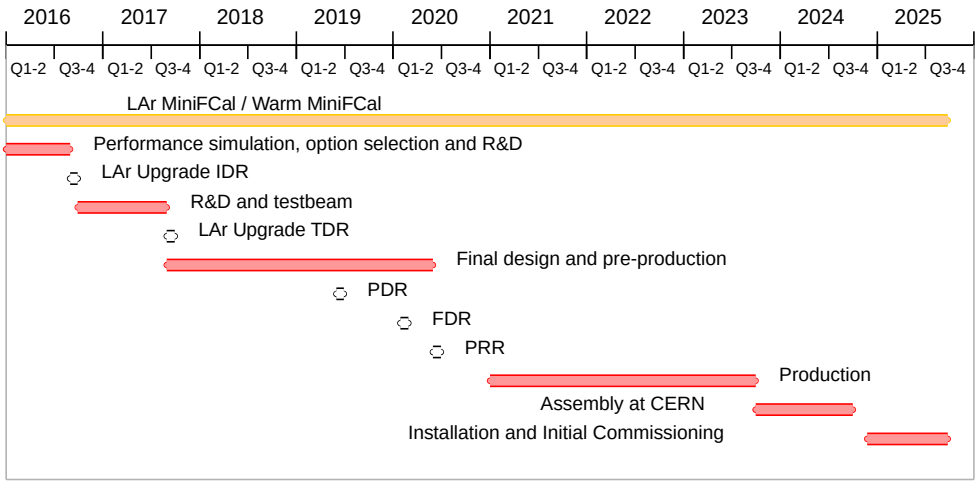

Figure 43. Overview of the time-line and milestones for the MiniFCal option that is only chosen under certain conditions (see Section V.4.4).

Simulation studies made at the time of the original construction concluded that precision physics measurements could not be extended much beyond $|\eta| = 2.5$. For this reason and to reduce the total cost of the readout electronics, it was decided to design the end-cap e.m. calorimeter's inner wheel with coarser granularity readout cells and with only two longitudinal segmentations, instead of the three used elsewhere. This yields no significant energy resolution degradation at nominal luminosity. However, the pile-up conditions expected at the HL-LHC will significantly degrade the calorimeter performance in the region $|\eta| > 2.5$. This is caused mainly by the increase of the total noise in individual readout channels. Fig. 44 shows the expected total noise energy (electronic + pile-up) of the individual calorimeter cells at different pseudo-rapidities, for $\mu \simeq 30$ and $\mu \simeq 200$. Moving from the lower to the higher pile-up scenarios, significant increases are evident, in particular in the first sampling of the inner wheel of the e.m. end-cap and in the forward calorimeters.

Instrumenting this region with high-granularity detectors having an intrinsic time resolution of the order of a few tens of pico-seconds is being considered as a way to mitigate these pile-up effects (see Section XI.2.7). Precision timing would allow the association of clusters in the calorimeter to a small area of the luminous region around the primary vertex, and a combination of timing and precision position information would enable ATLAS to develop algorithms for local pile-up subtraction on an event-by-event basis in the reconstruction of topological clusters and jet constituents, as shown in Section XI.

V.5.1 HGTD in the gap between the LAr barrel and end-cap cryostats

The gap between the barrel and end-cap cryostat will be occupied by the ITk services, the ITk end-plate, and a poly-boron shield, as shown in Fig. 45.

The distance between the ID end-plate (z=3458 mm) and the end-cap cryostat walls (z = 3548 mm) is $\Delta z = 90$ mm.

A reconfiguration of the region is possible considering that the minimum bias trigger scintillators needs to be replaced for operations at the HL-LHC. Under investigation is the possibility of installing

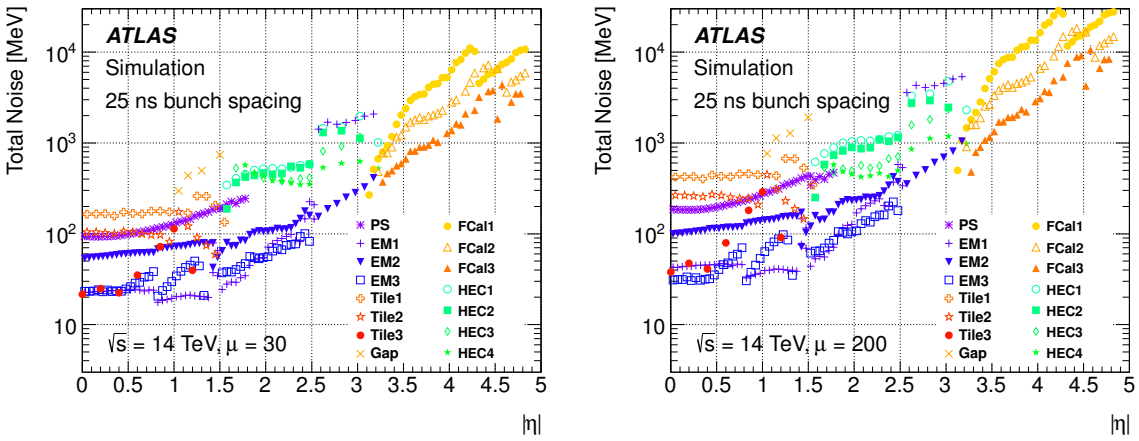

Figure 44. Calorimeter cell noise (electronic + pile-up) in the different longitudinal layers and at different pseudo-rapidities (η), for $\mu \simeq 30$ [left] and $\mu \simeq 200$ [right].

a new detector with high granularity and excellent time resolution, fitting within an envelope of $\Delta z = 60 - 70$ mm and extending radially between $R = 90 - 600$ mm, corresponding to $2.4 < |\eta| < 4.3$. A further extension to $|\eta| \simeq 5$, equivalent to a coverage down to $R \simeq 50$ mm, is also considered, but requires additional engineering and performance studies.

Also under consideration is an integrated silicon-based detector deployed in both the end-cap and forward regions. The use of a single technology for these two detectors would enable an integrated solution without an additional transition region.

V.5.2 Detector technologies under investigation

Different technologies are considered for an optimised performance in the region under consideration: Multi-Channel Plate (MCP)-based detectors, single-crystal or poly-crystalline diamonds, and different silicon-based detectors in different technologies.

A silicon-based option would benefit from synergistic R&D with the tracker community and with the technology chosen by the CMS collaboration, for their Phase-II e.m. end-cap calorimeter upgrade, and with the developments by the CALICE collaboration for the Si-W based ECAL calorimeter [50]. In the end-cap region 4-5 layers of silicon-detectors could be deployed in the volume described in Section V.5.1. Optionally, the active layers could be interleaved with W-absorbers to configure the detector as a pre-shower device (3-4 X_0) allowing for the conversion of photons and π^0's. In the forward region a MiniFCal could be designed as a fully absorbing e.m. calorimeter with up to 30 X_0 in 180 mm. Detailed simulation studies of both scenarios are needed to prove there is no impact on the performance of the LAr calorimeters sub-systems.

The NA62 collaboration [51] has reported a resolution of 260 ps of their GigaTracKer sensors, readout by TDCpix ASICs, exposed on a beam-test. Furthermore, recent developments in Low-Gain Avalanche Detector (LGAD) [52] and High Voltage CMOS (HV-CMOS) sensors (e.g. see Ref. [53]) make these technologies interesting for this application, achieving time resolution of the order of 100 ps on small scale prototypes: the timing resolution is essentially determined by the Signal-to-Noise ratio (S/N) for MIP-like signals. In the case of LGADs S/N is boosted by adding a low-amplification layer in the silicon bulk structure, and in the case of HV-CMOS sensors, by dimensioning the pixel/pad to collect significant ionisation charges from an e.m. shower, while keeping the pixel capacitance and the electronics noise as low as achievable.

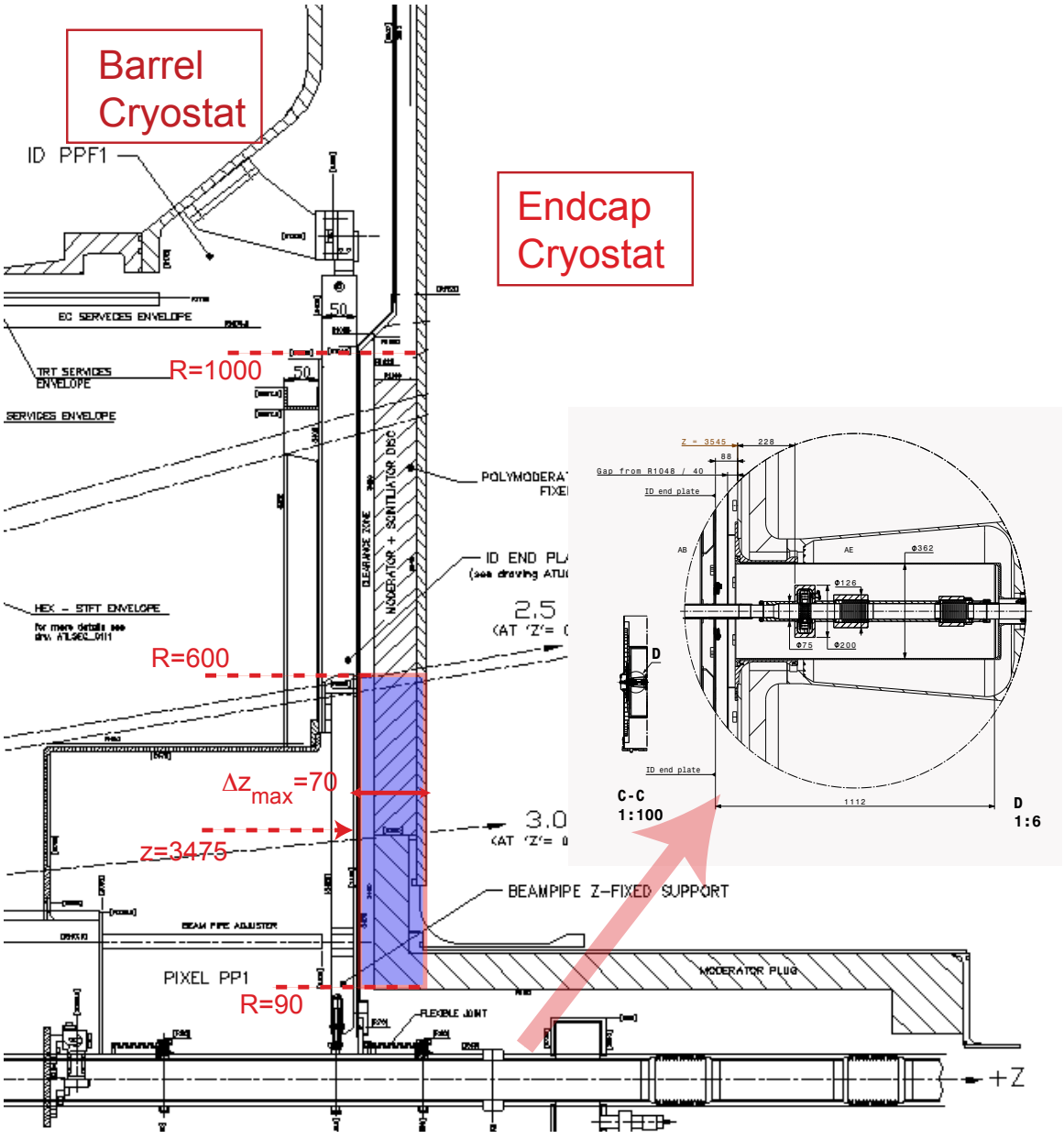

Figure 45. Cross-section of the ATLAS experiment and transition between the barrel and end-cap cryostats.

Table 20. CORE costs for a High-Granularity Timing Detector in the Reference cost scenario. No Timing Detector is being planned for the Middle and Low cost scenarios.

WBS ID	Upgrade Item	Reference [kCHF]
3.3	**HGTD**	**4,558**
3.3.1	Sensors and on-detector active electronics	1,921
3.3.2	Front-end readout	1,988
3.3.3	Back-end readout	450
3.3.4	Services	200

V.5.3 Time-line

In the upcoming years, intense simulation studies and R&D is required to optimise the performance of the HGTD and to develop the best sensor technology for this application, including test-beam campaigns. An combined IDR of the LAr calorimeter upgrade is envisaged for 2016 followed by a TDR in 2017. After finalising the design, the construction time is estimated to be 2 years, with final assembly and integration at CERN in 2023/2024. Installation is scheduled for the second half of 2025.

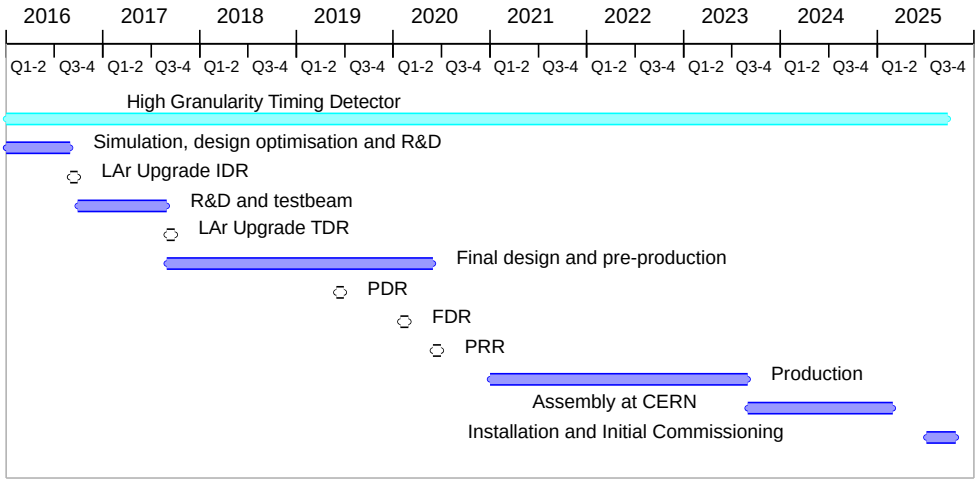

Figure 46. Overview of the time-line and milestones for the implementation of the HGTD.

V.5.4 Cost Estimates

Table 20 summarises the CORE costs for the construction and installation of a HGTD in the LAr Calorimeter end-cap region. The cost estimates are based on LGAD sensor technology and assume that $9\ \mathrm{m}^2$ of active detector area are equipped with a sensor granularity of $5 \times 5\ \mathrm{mm}^2$.

V.5.4.1 Cost Drivers and Cost Risk Analysis

The sensor and front-end readout costs are the main cost items of the HGTD. The cost uncertainties are therefore concerning

- the optimal sensor technology and the involved costs, which are currently based on LGAD detectors;
- the number of readout channels in the front-end and back-end in order to match the sensor granularity with the optimal performance.

V.5.5 Schedule and Milestones Summary

The R&D, production and installation schedule of the HGTD is summarised in Fig. 46, together with reporting and review milestones. The HGTD upgrade will be integral part of the overall LAr Phase-II IDR and TDR, planned for 2016 and 2017, respectively.

Chapter VI

Muon Spectrometer

VI.1 Introduction

A schematic drawing of the ATLAS muon spectrometer Muon Spectrometer (MS) including the proposed and planned upgrades is shown in Fig. 47. It consists of three large air-core superconducting toroidal magnet systems (two end-caps and one barrel) providing a field of approximately 0.5 T. The deflection of the muon trajectories in the magnetic field is measured via hits in three layers of precision drift tube (MDT) chambers for $|\eta| < 2$ and two layers of MDT chambers in combination with one layer of cathode strip chambers (CSC) in the innermost end-cap wheels of the muon spectrometer, for $2.0 \leq |\eta| < 2.7$. Three layers of resistive plate chambers (RPC) in the barrel ($|\eta| < 1.05$) and three layers of thin gap chambers (TGC) in the end-caps ($1.05 < |\eta| < 2.4$) provide the muon trigger and also measure the muon trajectory in the non-bending plane of the spectrometer magnets. The inner, middle, and outer layers of the barrel and end-caps are usually labeled BI, BM, BO and EI, EM, EO. The EI disks are also called the small wheels, the EM disks the Big Wheels. In 2019-2020 the Small Wheels will be replaced by new Small Wheels (NSWs) using small strip TGC (sTGC) and MicroMegas chambers for triggering and precision tracking.

In the present ATLAS detector the MS provides a level-1 (L1) hardware muon trigger which is based on hit coincidences within different RPC or TGC detector layers inside programmed geometrical windows which define the muon p_{T}. The high-level trigger (HLT) performs a software confirmation of the L1 muon trigger, by using refined p_{T} measurements from the precision chambers.

The HL-LHC luminosity upgrade requires a substantial performance increase in elements of the muon spectrometer system. This is true for the muon precision tracking as well as for the triggering system. The Monitored Drift Tube (MDT) precision tracking chambers will have to maintain excellent spatial resolution and tracking efficiency in a high hit rate environment caused by γ conversions and neutron reactions. The MDT read-out system must cope with the higher occupancies and an increased L1 trigger rate, which will be well beyond the present limit of 100 kHz.

The trigger system, on the other hand, will have to maintain a high level of efficiency for finding high-p_{T} tracks while keeping the rate of fake triggers low. Figure 48 shows the extrapolation of the L1 muon trigger rate measured in LHC Run 1 to the HL-LHC luminosity of $7{\times}10^{34}$ cm^{-2}s^{-1} for a muon spectrometer with the NSW. The muon trigger rate is about 50 kHz for a p_{T}threshold of 20 GeV, and is dominated by triggers in the end-cap region ($|\eta|$ >1.05).

The new ATLAS L0/L1 trigger system will impose new requirements on the trigger read-out systems as well as on the precision chambers as discussed in Sections VI.2 and VI.3.

The present MDT read-out electronics cannot cope with a trigger rate of 400 kHz in the muon spectrometer regions with the highest background rates. To overcome this limitation, the current read-out electronics cards would have to be replaced with improved ones. This is possible for most of the chambers, but access is difficult for chambers located mostly inside the toroid coils. Installation of the replacement electronics would require a major intervention to move the chambers out of the toroid. Replacing the electronics cards on the MDT chambers would provide another improvement of the quality of the muon trigger: upgrading the read-out electronics will allow the precision coordinates of the MDT to be used at L0 or L1 to sharpen the turn-on curves of the high-p_{T} trigger, significantly reducing the number of low-p_{T} muons passing the trigger selection. This requires the development of new MDT read-out electronics to allow the MDT coordinates to be made available to the trigger logic within the L0 latency. According to simulation, sharpening of the high-p_{T} threshold would reduce the fake muon trigger rate by up to a factor 4, which makes this concept an attractive option for the trigger system upgrade in phase II.

The performance of the existing MDT chambers together with the new EI stations, upgraded in LS2, is expected to be sufficient for operation at the HL-LHC. Only the MDT read-out electronics will have to be adapted to the new trigger scheme and to the increased hit rates.

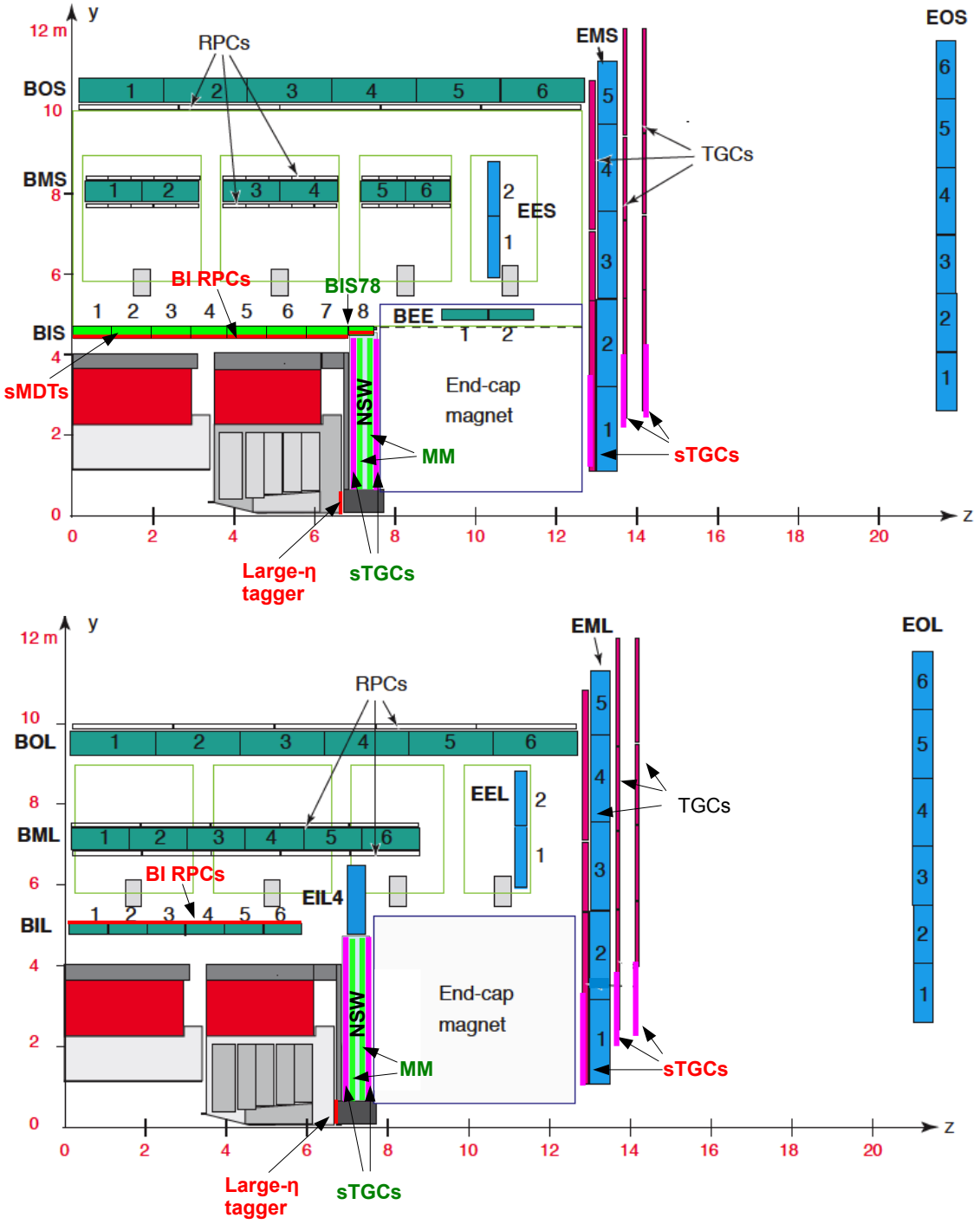

Figure 47. Drawings of the ATLAS Muon Spectrometer with the new chambers proposed for installation in the Phase-II upgrade (red text: BI RPCs, sMDTs, sTGCs, Large-η tagger), those to be installed during LS2 (green text: Micromegas and sTGCs in the new small wheel and RPCs and sMDTs on BIS78), and those that will be kept unchanged from the Run 1 layout (black text). The green (blue) chambers indicated as BMS/BML, BOS/BOL, BEE (EIL, EES/EEL, EMS/EML, EOS/EML) are MDTs. The upper panel shows the R-Z view of one of the azimuthal sectors that contain the barrel toroid coils ("small" sector), the lower panel shows a sector between the barrel toroid coils ("large" sector).

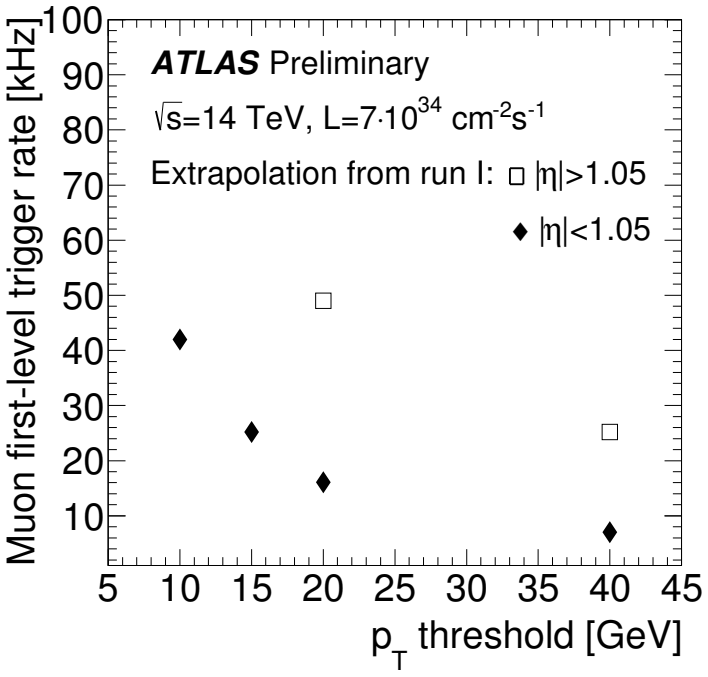

Figure 48. Extrapolation of the L1 muon trigger rate measured in Run 1 of the LHC to an HL-LHC luminosity of 7×10^{34} cm^{-2}s^{-1} for a muon spectrometer with the new small wheel.

The present read-out system and trigger electronics of the chambers in the barrel (RPC) and in the end-caps (TGC) will not be able to cope with the new L0/L1 trigger scheme, as the present electronics is designed for maximum latencies of 3.2 μs (TGC) and 6.4 μs (RPC), and for trigger rates only up to 100 kHz. Consequently, the whole read-out electronics chain will have to be replaced, offering the opportunity to rebuild the read-out chain for improved performance with modern technologies.

Another important aspect for the upgrade of the trigger electronics is the need to improve the selectivity for high-p_{T}tracks, which calls for an improved space resolution in the bending direction (η). The spatial resolution is presently limited by features of the construction of the trigger chambers, such as the width of the pick-up strips in the RPC and the modularity of wire-ganging in the TGC, which could only be changed by replacing all of the trigger chambers. The present read-out electronics of both trigger chamber systems does not supply information on the signal pulse height and therefore charge interpolation cannot be used to refine the position measurement.

The RPCs of the ATLAS muon spectrometer were designed for 10 years of operation at the LHC and for an integrated charge of up to 0.3 C cm^{-2}, which corresponds to about 10 years at a counting rate of $100\,\mathrm{Hz/cm^2}$. In order to ensure safe operation of the RPCs at the higher particle rates expected at the HL-LHC (of the order of $300\,\mathrm{Hz/cm^2}$), the chamber performance will be reduced in order to respect the original design limits on currents and integrated charge. This can be achieved by reducing the gas gain through lowering the operating voltages of the chambers. In the areas of highest background, the gas gain will have to be reduced to such low levels that hit inefficiencies down to 45% will be encountered. To maintain good trigger efficiency, new RPCs with increased rate capability will be installed in the inner layer of the barrel muon spectrometer. The installation of these chambers also makes it possible to close most of the acceptance holes of the present barrel muon trigger, which amount to more than 20% of the $\eta-\phi$ coverage for $|\eta|<1.05$.

The main sources of fake muon triggers in the end-caps are charged particle tracks not originating from the main pp interaction point. In order to increase the angular resolution of the muon trigger at large pseudo-rapidity ($|\eta| \simeq 2.4$), new high resolution TGC chambers will replace the present TGC chambers in the inner ring of the Big Wheel, improving the rejection of these non-pointing tracks. A further rejection of these tracks will be achieved by the MDT trigger.

The extension of the inner tracker pseudo-rapidity coverage to $|\eta|$=4.0 opens up the opportunity to identify muons at large values of $|\eta|$. The installation of micro-pattern gaseous or silicon pixel detectors between the end-cap calorimeters and the shielding discs in front of the NSW in the region 2.7< $|\eta|$ <4.0 will make it possible to tag inner detector tracks as muons in this pseudo-rapidity region.

In addition to the above improvements, it will also be necessary to replace the low-voltage and high-voltage power supplies to ensure safe operation of the muon spectrometer at the HL-LHC through the operational period extending to 2035.

VI.2 Upgrade of the MDT read-out electronics

VI.2.1 Reference scenario

At local hit rates above 500 Hz/cm^2, the MDT chambers start to lose spatial resolution and efficiency due to the build-up of space charge in the gas volume, leading to drift field fluctuations and reduced gas gain, see Refs. [34], [54] and [55]. Hit rate extrapolations from recent measurements indicate that the existing MDT chambers with their 30 mm diameter drift tubes can safely operate in most of the muon spectrometer throughout the HL-LHC operating period, as the hit rates will remain significantly below the 500 Hz/cm^2 limit. Higher rates only occur in the inner part of the EI station (small wheel), which will be addressed by the installation of the NSW in LS2.

In the present trigger system the L1 trigger arrives at the MDT front-end electronics with a latency of about 2.6 μs after the corresponding beam crossing, and the hit data need to be stored in the buffers of the Time-to-Digital Converter (TDC) during this period. After LS3, the L1 trigger processor will send out two distinct triggers, L0 and L1, after a latency of 6 and 30 μs respectively. Longer latencies imply an increased residence time of the data in the buffers and thus higher buffer occupancies. If the average occupancies grow too high, the buffers will overflow, resulting in data loss.

The MDT read-out electronics will also have to handle the increased trigger rates. This means higher data rates to be transferred from the front-end cards to the Chamber Service Module (CSM) and from there to the off-detector electronics in USA15. The read-out bandwidth between the front-end cards and the CSM is limited to 80 Mbit/s, and the buffer sizes inside the current TDC chips on the front-end cards do not allow operation at a 400 kHz L1 rate and above 30 μs latency in the chambers of the Big Wheel, in the middle and outer layer of the barrel and in some of the chambers in the inner barrel layer. Reliable operation is, however, possible everywhere in the barrel apart from the middle MDT chambers in the region of $|\eta|$ around 0.8 if one reduces the L1 trigger rate to 200 kHz.

The replacement of the front-end read-out electronics will be a major issue during LS3. Possible intervention scenarios have been investigated. The conclusion of these studies is that the electronics replacement is manageable within a time interval of 1.5 to 2.5 years depending on the size and organization of the work force. Several teams will have to work in parallel for the full duration of LS3 in order to replace the MDT front-end electronics on all chambers. The manpower required for replacing the front-end electronics on BI chambers is particularly high because chambers will have to be removed from the detector and re-installed, and other chambers and access structures will have to be moved out of the way for this operation.

To fully exploit the rate capabilities of the MDT drift tubes at L1 trigger rates beyond 200 kHz and L1 latencies beyond 30 μs, the present TDC chips have to be replaced by new ones with larger buffers. This requires new front-end cards with the new TDC chips and new Amplifier-Shaper Discriminator ASICs (ASDs) with the same functionality as the present ASICs. In addition to the new front-end cards the CSMs and RODs will also have to be adapted to the new read-out architecture, the Giga-Bit Optical Link (GOL) being replaced by the GBT [56] and the presently used TTC system by a more complex and flexible trigger distribution system.

VI.2.2 Reduced scenarios

The Middle and Low scenarios foresee the replacement of the MDT electronics only on some of the chambers. In the barrel the electronics of the middle (BM) and outer (BO) chambers, which are easier to access than the inner ones (BI), will be replaced. In the end-caps the front-end cards are accessible both in the EM and EO stations. The unkown longevity of the present electronics favours the replacement of the entire elctronics. However, as the present electronics is capable of the background counting rates in the EO stations, the electronics will be replaced only in the EM stations in the Middle and Low scenarios. In this way there will still be the possibility to have an MDT trigger (see VI.6) with a two-station measurement (BM-BO in barrel and NSW-EM in the end-caps), saving the large fraction of manpower needed to replace the front-end electronics on BI chambers. As the L1 trigger rate foreseen for the Low and Middle scenarios is limited to 200 kHz, it will still be possible to operate part of the chambers with the legacy electronics by using a specific variant of the new CSM.

VI.2.3 R&D activities and plans

The R&D program for the new MDT read-out electronics has already started with the successful design of a new ASD ASIC in 130 nm CMOS technology. Figure 49 shows a picture of this prototype ASD ASIC on the test board. Two options for the new TDC chips are being investigated, an FPGA-based TDC and an ASIC in 130 nm CMOS technology. Prototypes for both options are expected for 2016. Prototypes of new CSMs and new RODs are expected on a similar time scale.

VI.3 Upgrade of the muon trigger electronics

The current read-out system for the trigger chambers, both in the barrel and the end-caps, is incompatible with the new L0/L1 read-out scheme planned for the operation of the ATLAS detector at the HL-LHC. The whole trigger and read-out chain of the trigger chambers will therefore have to be upgraded.

VI.3.1 Upgrade of the muon barrel RPC trigger electronics

The barrel trigger electronics will be replaced in all three scenarios, since the current electronics is not able to satisfy the latency and trigger request rate foreseen for Phase-II [1]. The RPC front-end electronics do not need to be updated. The current PAD boards, located on-detector and used to read the RPC front-end data and to execute the trigger algorithm, will be replaced with new Data Collector Transmitter (DCT) boards, which will zero-suppress the front-end data and send it to the new Sector Logic (SL) boards located in USA15, as shown in Fig. 50. The SL boards will collect RPC data belonging to one trigger sector and execute the L0 trigger algorithm. The SL will also host the L1 read-out pipelines and send read-out data to the FELIX system each time a L1 is received.

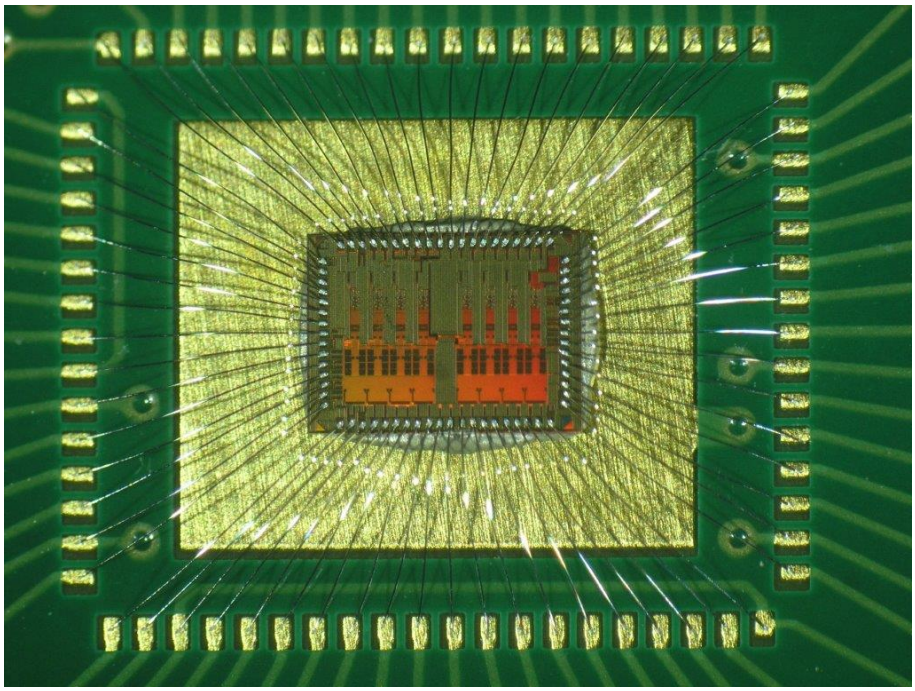

Figure 49. Prototype of the ASD MDT read-out chip on the ASIC test board.

Furthermore the SL will provide to the MDT L0 trigger processors the seed needed to perform the MDT tracking logic.

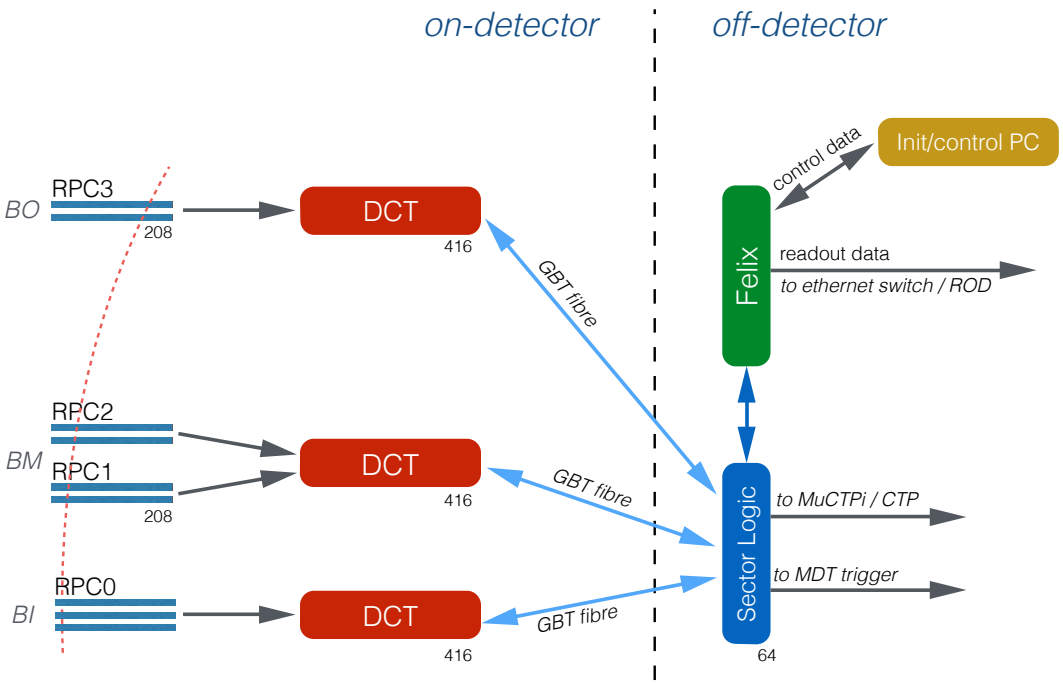

Figure 50. RPC L0 trigger schema for Phase-II

The numbers of DCT boxes in the barrel will be 1248, 1040, 832 respectively for the Reference, Middle, Low scenario, while the number of SL will be 64 in all scenarios.

VI.3.2 Upgrade of the muon end-cap TGC trigger electronics

The muon L1 trigger in the end-caps is generated by TGCswhich determine the deflection of tracks in the magnetic field of the end-cap toroid by measuring the track angle behind the magnet in three TGC layers in the Big Wheel [34]. The deviation of this angle from the direction of a straight line to the nominal position of the IP is used as a measure of the muon momentum.

The analysis of Run 1 LHC data revealed that one of the major sources of fake triggers is tracks which do not come from the primary vertex. To veto those triggers, a precise measurement of the track angle *before* the magnet is needed in addition. A new type of TGC with high space resolution will be installed in the EI station already for the Phase-I upgrade as part of the NSW. These new trigger chambers will measure the angle θ of the track w.r.t. to the beam line with 1 mrad accuracy. Tracks with a significant angular deviation from a straight line through the primary vertex will be discarded. A straight line fit through TGC hits in the Big Wheel provides the direction of flight with 3 mrad precision. This makes it possible to measure the muon deflection angle $\Delta\theta$, as the difference of the measured directions of flight in the small and Big Wheel with 3 mrad resolution allowing a reduction of the end-cap trigger rate by about 25%.

The new L0/L1 trigger scheme will require a complete replacement of the TGC read-out electronics chain, with the possible exception of the ASD preamplifier. This will allow the implementation of a new architecture for the read-out, where most of the logic functions will be moved from the experimental cavern to the low-radiation zone in USA15. Thus FPGAs can be used for L0 trigger formation as well as for data processing and transmission, providing a much greater level of flexibility. The new end-cap muon trigger requires the development of new on-detector electronics in 130 nm CMOS technology and a radiation tolerant flash-based FPGA for the data transmission to USA15.

VI.3.3 R&D activities and plans

The new RPC on-detector electronics is in part being developed for the BIS78 chambers to be installed during LS2. The chambers will consists of sMDT chambers for precision tracking and thin RPCs for triggering. Demonstrators of the RPC on-detector trigger boxes are planned for the year 2016. For the end-cap trigger, the on-going R&D is addressing the following topics: viability and radiation tolerance of flash-based FPGAs (as component of new on-detector boards) to be done in 2015-16; design and segmentation of trigger/read-out boards; overall optimisation of trigger logic.

VI.4 Upgrade of the RPC and MDT Chambers in the Barrel

VI.4.1 Reference scenario

The present barrel muon L1 trigger is based on three layers of RPC chambers, two in the middle stations and one in the outer stations, as shown in Fig. 47. Each chamber consists of two sensitive gas layers, each read out by orthogonal η and ϕ strips. The trigger for single high-p_T muons is issued when hits are found in coincidence in all three stations in both η and ϕ views. The system has high selectivity and performed reliably during Run 1 [57]. The system does suffer from limited redundancy, in the sense that any efficiency loss in one of the three layers results in an efficiency loss in the final trigger. The three-layer requirement also limits the trigger acceptance to the regions

with full coverage of all the three layers, which corresponds to only about 78% for $|\eta| < 1.05$. The main sources of acceptance losses are the gaps in the middle layer of RPC chambers for the barrel toroid ribs and the hole for the calorimeter services around $\eta = 0$.

The ATLAS RPC chambers have been certified for 10 years of operation at LHC and for an integrated charge up to 0.3 C/cm^2, corresponding to 10 years at a counting rate of 100 Hz/cm^2 [58]. At the HL-LHC luminosity, the expected rates for the chambers in the middle layer (Fig. 51) will reach up to 340 Hz/cm^2. The RPC system will run for 25 years instead of 10. The integrated dose in this time span exceeds the design specifications by a factor three. Experience in irradiation tests and

Sector	RPC unit Id. along Z direction																			Average
Φ Id.	-6.2	-6.1	-5.0	-4.0	-3.2	-3.1	-2.2	-2.1	-1.2	-1.1	1.1	1.2	2.1	2.2	3.1	3.2	4.0	5.0	6.1	6.2	
01.01	342	280	301	225	145	114	128	101		61	61	71	113	122	127	136	214	276	269	285	180
01.02	293	281	303	218	159	133	129	143		76	71	75	127	143	140	148	215	295	278	297	188
2	168	204	188	138	109	90	77	63	55	56	45	48	61	79	94	104	140	207	196	152	115
03.01	297	296	281	198	148	128	119	119	68	67	65	71	131	125	114	125	207	329	268	290	177
03.02	300	243	277	210	151	129	155	122	85	75	75	70	122	127	152	132	207	315	243	299	179
4	112	166	158	151	101	83	65	77	41	53	46	41	73	68	92	108	160	196	175	112	101
05.01	171	173	263	138	105	102	140	127	68	60	60	69	124	177	102	137	185	290	173	171	149
05.02	227	198	237	158	109	105	136	143	77	61	63	71	111	136	108	141	200	267	255	282	159
6	175	186	208	163	105	95	90	95	77	59	52	59	84	81	106	124	189	200	227	167	131
07.01	305	263	288	191	154	129	131	114		76	78		122	139	124	148	185	261	268	305	183
07.02	327	258	216	203	141	112	129	108		74	77		105	114	112	152	184	278	276	279	175
8	146	196	195	161	103	85	80	70	50	57	54	54	67	74	85	108	168	196	194	156	118
09.01	319	246	301	206	155	117	149	119		46	64		106	134	124	135	197	283	262	297	181
09.02	347	258	287	205	143	95	107	103		58	67		99	112	95	137	188	285	265	292	174
10	174	201	207	147	99	86	68	71	46	43	41	50	64	69	80	103	148	193	201	170	115
11.01	308	244	237	157	97	84	81	87		40	43		83	94	92	94	148	227	215	278	132
11.02	196	193	157	105	78	66	55	57		33	31		50	62	58	71	98	151	160	185	98
12						80	81	66	51	36	36	51	75	87	80						64
13.01	291	278	253		140	102	96	84	43	41	47	50	87	95	99	123		249	263	319	149
13.02	299	264	262		104	97	105	86	49	48	50	56	93	103	97	110		252	227	294	146
14						142	68	64	52	41	40	49	63	68	136						76
15.01	196	221	148	113	76	71	67	49		38	36		50	59	86	87	104	156	173	196	104
15.02	183	159	246	164	116	98	103	75		44	43		75	106	112	107	158	248	159	183	133
16	173	214	216	173	108	89	54	75	56	59	50	50	77	54	87	103	177	209	208	154	124
Average	229	223	234	167	118	101	96	88	56	52	51	56	86	97	103	118	171	240	221	221	137

Figure 51. RPC hit rates measured in Run 1 middle stations extrapolated to $\mathcal{L} = 7.5 \times 10^{34}$ cm^{-2}s^{-1}. The plot shows rates in Hz/cm^2 as a function of the ϕ sector and of the station number along Z.

in ATLAS operation shows that the RPC chambers can be maintained in good working conditions, without increase of the ohmic resistance and without significant deterioration of the performance, if they are operated below a certain current density limit and if sufficient gas flow with controlled humidity is provided. Stable conditions can be achieved in the present system if the yearly integrated charge is kept below 30 mC/cm^2/yr. This is considered to be a reasonably safe working point that can provide stable performance for approximately 10 years in the HL-LHC phase. To keep the current density within the stable operation limit, it will be necessary to reduce the voltage applied to the RPC chambers, which will in turn correspond to a reduction of the hit efficiency. A study has been performed to define a safe high voltage setting for the chambers and the corresponding efficiencies, based on measurements of detector currents and efficiencies as a function of HV and hit rate. The result is that the hit efficiency will be reduced by approximately 5% in the chambers at small η and by up to 45% in the chambers with the highest rates in the middle layer at $|\eta| \simeq 1$. To simulate realistic efficiency scenarios for the HL-LHC the efficiency reductions have been applied to the average efficiency of 95% measured during Run 1, which includes the effects of possible disconnected chambers due to gas distribution problems, dead read-out or HV channels etc.

A new layer of RPC chambers in the inner barrel stations of the Muon Spectrometer will increase the system redundancy and recover the overall efficiency of the trigger system if the hit efficiency in the old chambers is reduced to allow safe operation. Moreover it will close the present acceptance holes. Recently developed low noise amplifiers allow a substantial increase in the rate capability

of the RPCs by providing detection of signals with a factor ten less charge delivered in the gas with respect to the present RPCs [59]. The lower charge delivered by each avalanche allows the operation at lower currents for the same hit rate, reducing the ageing of the chambers with respect to the ATLAS RPCs. It is therefore proposed to use a triplet of new chambers with gas gap width of 1 mm (compared to 2 mm of the current RPCs) and with new high-sensitivity front-end electronics. Similar chambers have already been tested in the framework of studies for the NSW upgrade and will be used in the upgrade of the BIS78 chambers foreseen for installation in 2018 [60].

Tests of RPCs with new FE electronics demonstrated a rate capability well beyond the hit rates expected at HL-LHC in the BI area. Figure 52 shows the rate capability of a 1+1 mm doublet RPC equipped with a fast charge amplifier built in Silicon BJT technology. First prototypes of new generation FE ASICs based on SiGe technology have been produced in spring 2015 and are currently under test. Figure 53 shows the output signal from a prototype of the new SiGe FE ASIC, as measured in initial laboratory tests. An r.m.s noise much lower than 1000 electrons has been achieved without any optimisation, which is already more than sufficient for operation of the new ATLAS RPCs.

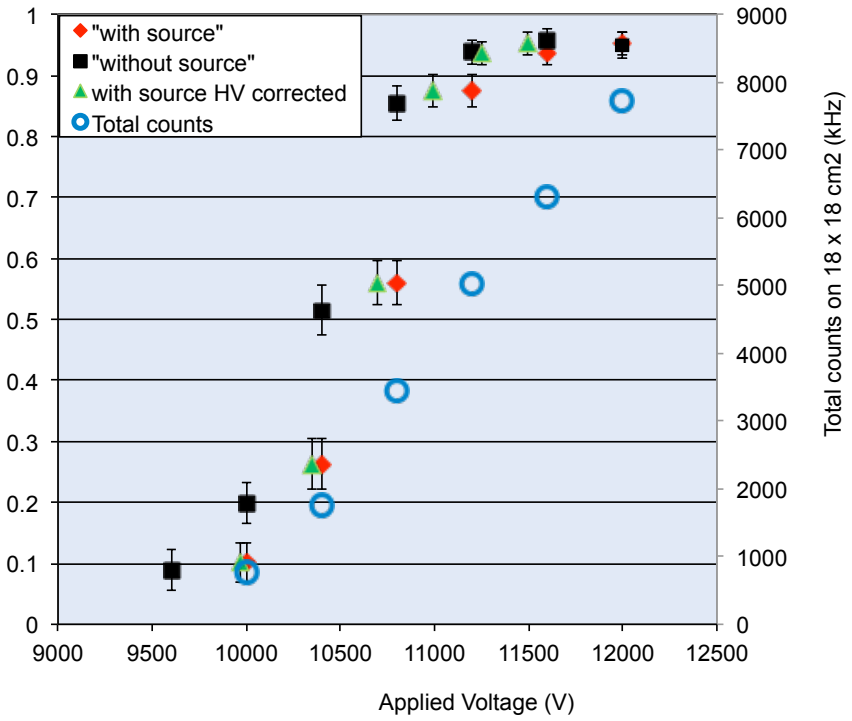

Figure 52. Efficiency as a function of applied voltage for a 1+1 mm doublet RPC equipped with a fast charge preamplifier. The efficiency curve is shown with and without irradiation with a γ-ray source, corresponding to a hit rate of approximately 12 kHz/cm^2. The chamber counting rate is also shown. The triangles represent the efficiency "with source" as a function of the actual voltage applied to the gas gap, after correction for the ohmic drop on the resistive plates. The chamber counting rate is also shown.

The space availability and possible installation procedures for the RPCs on the BI chambers have been studied in detail. For the "large sectors" between the barrel toroid coils, the RPCs can be installed on top of the existing MDT chambers. In the "small sectors", which correspond to the coils of the barrel toroid magnet, there are instead serious space limitations. The installation

Figure 53. The input (upper and middle panel) and the output (lower panel) signal from the new high-sensitivity SiGe front-end amplifier ASIC for the RPC. The plots are taken with an oscilloscope at 200 MHz, time scale is 10 ns/division. The injected input pulse of 7 fC (0.4 mV with ~ 2 ns duration) is not visible in the upper panel because it is hidden in the noise. The middle panel shows the input signal in “average mode”, i.e. averaged over many pulses to allow the observation of the small signal above the noise level. The lower panel shows the output of the FE chip.

of new RPC chambers in the inner layer requires the replacement of the present MDT chambers in the "small sectors", with new chambers made of small MDT tubes (sMDT) of 15 mm diameter (compared to the 30 mm of standard ATLAS MDTs). Such sMDTs have been tested and qualified in the past years [61, 62] and will be installed in several locations in the Muon Spectrometer in the winter shutdowns during Run 2 and during LS2. While the need for space is the driving factor, as a byproduct the new sMDT chambers will also provide higher rate capability. The performance of the system has been studied using simulations. Considering the reduced efficiency of the present RPC chambers due to reduced gas gain, the present RPC trigger would have a total efficiency in the barrel region of approximately 65%. With the addition of the inner layer of new RPCs and requiring a coincidence of 3/4 RPC layers, plus a coincidence of the inner and outer layer in the acceptance holes of the middle layers, the total efficiency in the barrel trigger will be close to 95%.

In addition, the excellent timing resolution of the new RPCs in the BI chambers can be exploited to improve the time-of-flight performance of the RPC system and thus the ATLAS capability to search for long-lived massive particles.

VI.4.2 Reduced scenarios

The Middle scenario foresees the installation of the inner RPC layer and the new sMDT in the small sectors only in the stations 4 to 6, corresponding to $|\eta| > 0.6$, where the old RPC chambers suffer from the highest background. With this option the estimated total barrel trigger efficiency will be approximately 80% instead of 95%. The Low scenario does not contain any upgrade of the RPC chambers and sMDT chambers, thus limiting the performance to that of the present RPC trigger (total efficiency of approximately 65%).

VI.4.3 R&D activities and plans

Current R&D is focusing on: the definition of the interfaces between front-end and trigger electronics and between the different systems in the electronics cavern USA15; the design and validation of new RPC front-end electronics; the characterisation of new RPC gas gaps and read-out electrodes; the performance and long-term viability of a new eco-friendly gas mixture [63]; mechanical and electrical integration of the RPC and sMDT in the small available space and for low-noise operation of the RPCs. The following R&D deliverable are foreseen to be completed before the end of 2016: the FE electronics prototype, the prototype of the new Faraday cage, the beam tests of small-size prototypes, and the long-term ageing tests using a new eco-friendly gas mixture at the GIF++ at CERN. Most of the R&D for the new RPC chambers is in common with the Phase-I BIS78 project.

VI.5 Upgrade of the TGC chambers in the inner ring of the Big Wheel

VI.5.1 Reference scenario

There are two main sources of fake muons in the muon end-cap trigger: tracks arising from backgrounds not pointing to the primary vertex and low-p_{T} muons due to insufficient sharpness of the high-p_{T} trigger turn-on curve. The first type of fakes will be addressed by the installation of the NSW during LS2. The second type of fakes are due to insufficient spatial resolution in the η-coordinate of the TGCs in the Big Wheels. This is of particular importance at large pseudo-rapidities ($|\eta| \sim 2.4$). To overcome this weakness it is proposed to replace the TGCs in the inner ring of the Big Wheel with small-strip TGCs of the new type which are also used in the NSW.

In the outer part of the Big Wheel, however, such a possibility does not seem realistic given the large number of chambers that would need to be replaced. Therefore, the only way to sharpen the trigger threshold in the outer part would be through the use of MDT coordinates for a better determination of the deflection angle, see Section VI.6.

VI.5.2 Reduced scenarios

The same upgrade plan as in the Reference scenario is foreseen in the Middle and Low scenarios for the sTGC detectors in the Big Wheel (BW) inner ring.

VI.5.3 R&D activities and plans

New sTGC chambers have already been tested and certified to fulfil the HL-LHC rate capability and ageing requirements in the context of the Phase-I NSW upgrade.

VI.6 Integration of MDT chambers in the trigger system

The transverse momentum spectrum of muons produced in pp collisions at the LHC and HL-LHC is steeply falling with increasing p_{T} as illustrated in Fig. 54 where the contributions to the inclusive muon cross section are shown as a function of p_{T} . To be sensitive to electroweak physics processes a single muon threshold as low as 20 GeV is desirable. Because of the very steep rise of the inclusive muon cross section at transverse momenta below 20 GeV, the muon trigger rate depends strongly on the muon trigger's momentum resolution at $p_{\mathrm{T}} \leq 20$ GeV. Due to the moderate spatial resolutions of the RPC and TGC trigger chambers, the L1 20 GeV muon trigger accepts muons down to p_{T} =10 GeV so that the muon trigger rate is dominated by the huge rate of muons with $p_{\mathrm{T}} \in$ [10,20] GeV.

In following paragraphs, the use of the MDT precision coordinates in the trigger decision will be demonstrated to sharpen the L0 muon trigger turn-on curve.

VI.6.1 Reference scenario

In the present architecture, trigger and precision chambers operate independently. The information of both chamber systems is read out separately, and the precise tracking information of the MDT is currently only used at the HLT, where the majority of trigger candidates are then discarded.

To apply the same effective method of trigger rate reduction already during the formation of L0 or L1, the precise MDT track coordinates must be fed directly to the trigger logic. This can be done quickly enough to be used to refine the p_{T} measurement within the L0 latency of 6μs. It can be implemented by introducing a second, *fast* read-out path, parallel to the existing one into the MDT read-out architecture as illustrated in Fig. 55. This fast read-out will have to continuously send MDT hit data to USA15 in order to make the accurate MDT coordinates available to the trigger logic at a fixed time interval after the corresponding beam crossing. [65, 66]

To simplify the drift time measurement for the fast read-out, the clock frequency of 1.28 GHz, used internally by the TDC, corresponding to a Least Significant Bit (LSB) value of 0.78 ns, can be relaxed to 40 MHz (or 80 MHz) for a fast, coarse, drift time measurement. With the average drift velocity of 20 μm/ns in the MDT tubes, the corresponding LSB of the position measurement is 0.5 mm (or 0.25 mm). This low-precision space resolution of the MDT is still more than an order of magnitude better than what is available from the trigger chambers, namely $\sim$3 cm strip width in

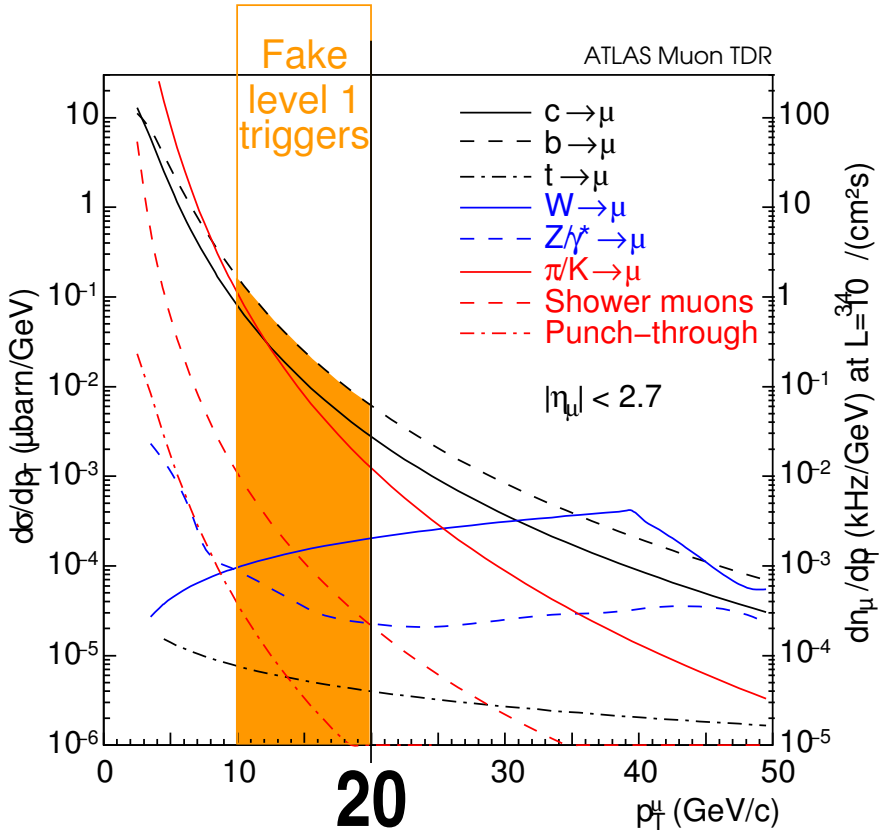

Figure 54. Contributions to the inclusive muon cross section as a function of the muon p_{T} [64]. The area shaded in orange indicates the span of transverse momenta of sub-threshold muons passing the present ATLAS first level 20 GeV muon trigger.

the barrel (RPC) and 1–6 cm η-segmentation in the end-caps (TGC). Consequently, a significant improvement of the p_{T} measurement accuracy can be achieved in all regions of the spectrometer.

In order to facilitate the reconstruction of track segments in the MDT chambers, the RPC and TGC track segments are used as inputs to the MDT segment reconstruction. MDT track segments can be used in two ways to improve the momentum resolution at trigger level. In the first approach the muon momentum is computed from the muon deflection angle which is taken as the difference of the muon directions of flight in two chambers of a trigger tower. In the second approach the track position in the three chambers of a trigger tower are used to compute the track sagitta as a measurement of the muon momentum. The fractional sagitta resolution is significantly higher than the fractional deflection angle resolution. As a consequence a better p_{T} resolution is achieved with the three-point sagitta method than with the deflection angle method.

Figure 56 shows a comparison of the 20 GeV L0 MDT trigger turn-on curves for the deflection angle and the three-point sagitta methods with the RPC and TGC L0 trigger turn-on curve. The use of the MDT data increases the selectivity of the muon trigger, in particular with the three-point sagitta method.

A reduction of the muon trigger rate by a factor 2 is expected over the whole acceptance of the muon trigger when using the deflection angle method. The three-point sagitta method would reduce the trigger rate by a factor 4.

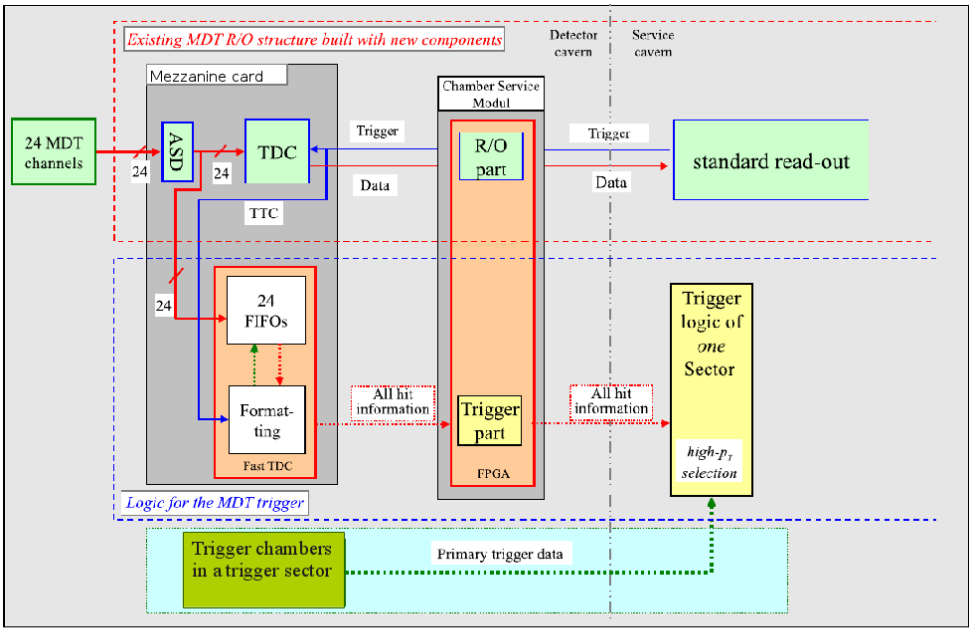

ASD: Amplifier Shaper Discriminator
TDC: Time to Digital Converter
FIFO: Buffer (first in first out)

Figure 55. Schematic drawing of the two MDT read-out paths: the upper block (red dashed line) shows the path of the standard read-out data while the lower block (blue dashed line) shows the fast path to be used for the MDT trigger.

VI.6.2 Reduced scenarios

The Middle and Low scenarios include the replacement of the MDT trigger electronics only for part of the system (BM-BO stations in the barrel, EM stations in the end-caps) thus making possible only a trigger based on the deflection angle.

VI.6.3 R&D activities and plans

A demonstrator of the basic principle of the fast read-out was successfully operated in the Gamma Irradiation Facility (GIF) at CERN in 2014 [67]. The next version of the demonstrator implementing all aspects of the fast read-out will be tested in the GIF++ in summer 2015. The next R&D steps are the implementation of a fast track reconstruction algorithm using a hybrid device including both an FPGA and an ARM Cortex A9 processor. A full system test in a muon beam with a magnet would then take place in the GIF++ in 2016.

VI.7 Muon tagger for high η

VI.7.1 Reference scenario

The planned extension of the ATLAS inner tracker to pseudo-rapidities between 2.5 and 4.0 makes it interesting to identify muons in this large pseudo-rapidity interval. For the interval $2.7 < |\eta| < 4.0$ we propose to instrument the region between the end-cap calorimeter and the JD shielding disc with position sensitive detectors to allow the tagging of inner detector tracks as muons. Simulation

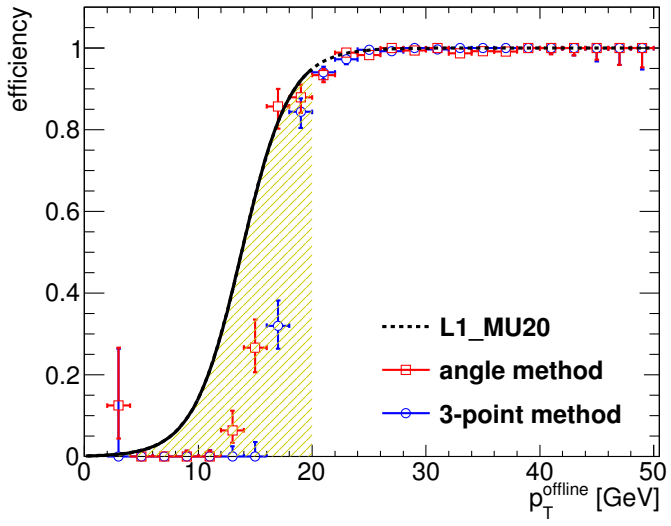

Figure 56. MDT muon trigger turn-on curves for a two-station (squares) and three-station (circles) trigger compared with the RPC L0 muon turn-on curve (solid line) in simulated data. The figure shows the results obtained for a barrel "large" sector.

studies show that the background of charged particles produced in the area of the muon tagging chamber is the main reason for muon mis-identification. These studies also show that a detector with 5 planes with a granularity of about 0.5 mm provides sufficient angular resolution to minimise the mis-identification probability. Because of the high radiation background either micro-pattern gaseous detectors or silicon pixel detectors (with pixel sizes of about 0.5×0.5 mm^2) have to be used in this detector region.

VI.7.2 Reduced scenarios

The high-η tagger is not present in the Middle and Low scenarios. This will limit the capability to identify muons to $|\eta| < 2.7$ instead of $|\eta| < 4.0$.

VI.7.3 R&D activities and plans

Micro-pattern or silicon pixel detectors are both capable of coping with the background environment at large pseudo-rapidities. The R&D therefore focuses on the design of compact detectors that can fit into the small available space in the forward region.

VI.8 Replacement of power supplies

The MDTs, RPCs and TGCs are equipped with low-voltage and high-voltage power systems belonging to the EASY3000 family by CAEN, plus the corresponding monitoring and control units. These components are installed in the cavern, and are not guaranteed to survive the radiation doses expected during the HL-LHC period. They have been tested in radiation and B-field environments compatible with 10 years of LHC operation, taking into account suitable safety factors. Even considering that the original safety factors can be reduced based on the good agreement between

measured and simulated radiation levels, the total ionising dose integrated in the tests corresponds to only about half of the that expected during the HL-LHC lifetime.

The design of the EASY3000 electronics took place during the years 2000 to 2005. This means that the continuing procurement of some key components, like PWM, EEPROM, opto-couplers and micro-controllers for maintenance or repairs is becoming critical. CAEN signed a contract with CERN for the maintenance of these power supplies up to the year 2018, and probably it could be extended up to the end of Run 3, but the component obsolescence will make the maintenance of the existing electronics up to 2035 very problematic.

Table 21. WBS for the Muon Spectrometer for the three costing scenarios.

WBS	Item	Reference Total Cost [kCHF]	Middle Differential Cost [kCHF]	Low Differential Cost [kCHF]
5	**Muon system**	**34,084**	**-8,782**	**-12,791**
5.1	**MDT**	**7,692**	**-2,071**	**-3,162**
5.1.1	sMDT detector	2,022	-1,011	-2,022
5.1.2	sMDT installation basket	20	-	-20
5.1.3	Mezzanine cards	4,000	-1,000	-1,000
5.1.4	CSM cards	1,650	-	-
5.2	**RPC**	**7,989**	**-2,318**	**-4,787**
5.2.1	Detectors	3,034	-1,517	-3,034
5.2.2	Installation mock-up	50	-	-50
5.2.3	Installation tooling	100	-	-100
5.2.4	On-detector electronics (DCT)	4,805	-801	-1,603
5.3	**TGC**	**4,436**	**-**	**-**
5.3.1	On-detector electronics (PS)	2,136	-	-
5.3.2	sTGC on BW inner ring	2,300	-	-
5.4	**High η-tagger**	**3,500**	**-3,500**	**-3,500**
5.4.1	Detector	1,100	-1,100	-1,100
5.4.2	FE electronics	1,500	-1,500	-1,500
5.4.3	Services+infrastructure	900	-900	-900
5.5	**Power System**	**10,467**	**-893**	**-1,342**
5.5.1	MDT	2,770	-	-
5.5.2	RPC	4,227	-893	-1,342
5.5.3	TGC	3,470	-	-

The above considerations indicate that the power supply system needs to be replaced in order to guarantee the reliable operation of the MS throughout the HL-LHC operating period. While the power system is by far the largest component of the muon system infrastructure where longevity is a concern, it is not the only one. There are other cases, for instance the optical alignment systems and the Embedded Local Monitor Boards (ELMBs), where a priori no upgrades will be required but lifetime extrapolations are difficult. These replacements would normally be considered as Maintenance and Operations (M&O) expenses, but are flagged in the context of the Phase-II upgrade project, as their cost may significantly exceed what is currently available in the Muon system M&O budgets.

VI.9 Costs

Table 21 summarises the CORE costs for the upgrade of the Muon System and the differences between the Reference scenario and the reduced ones.

VI.9.1 Cost drivers and risk analysis

The cost estimates for detectors - sMDT and RPC - are based on recent productions or projects of sMDT chambers and RPCs: the sMDT and RPC elevator chambers installed in LS1 to close acceptance holes due to the elevator shafts in sector 13 of the ATLAS muon barrel, the BMG project of sMDT chambers foreseen to be installed in sectors 12/14 in the 2016/17 extended shutdown, and the BIS78 project of sMDT+RPC stations replacing all of the BIS7 and BIS8 MDT chambers where currently no trigger coverage is available. These estimates are considered to be reasonably solid and accurate.

Cost estimates for read-out and trigger electronics, on the other hand, are based on conceptual designs only, and thus have significant uncertainties. Some details of the read-out architecture are still under discussion, and final choices may have an effect both on the cost of the electronics and on the cost of services (fibres, power cables). Final choices of components (ASIC, FPGA) have not been made either. These cost estimates are rather uncertain at this point.

A large fraction of the muon upgrade cost is the upgrade of the power system. A conceptual layout of a future power system is in preparation at this point. It is unclear whether the current architecture with mainframes in the main underground electronics cavern (USA15) controlling HV and LV boards in the underground experimental cavern (UX15) supplied with 48V power from the underground service area (US15) would be maintained or not. Given that other experiments face similar challenges and considering the high cost of such systems it seems natural that next-generation power systems should be developed in coordination with CMS, and together with potential vendors. The cost estimate presented here is based on the list price of the components in the current system, which is not necessarily going to have much similarity to the new system. At this early stage this is the best estimate that can be provided, but it may be very inaccurate.

VI.10 Schedule and milestones

An upgrade design with sufficient detail to start the process of ATLAS IDR will be available in the second quarter on 2016. The TDR with a detailed description of the project is expected for the second quarter of 2017.

The preliminary schedule for R&D, production, installation and commissioning of the new muon detectors is shown in Fig. 57. The schedules for the on-detector electronics and for the services (cables, fibres, gas pipes, crates, power supplies) are also shown.

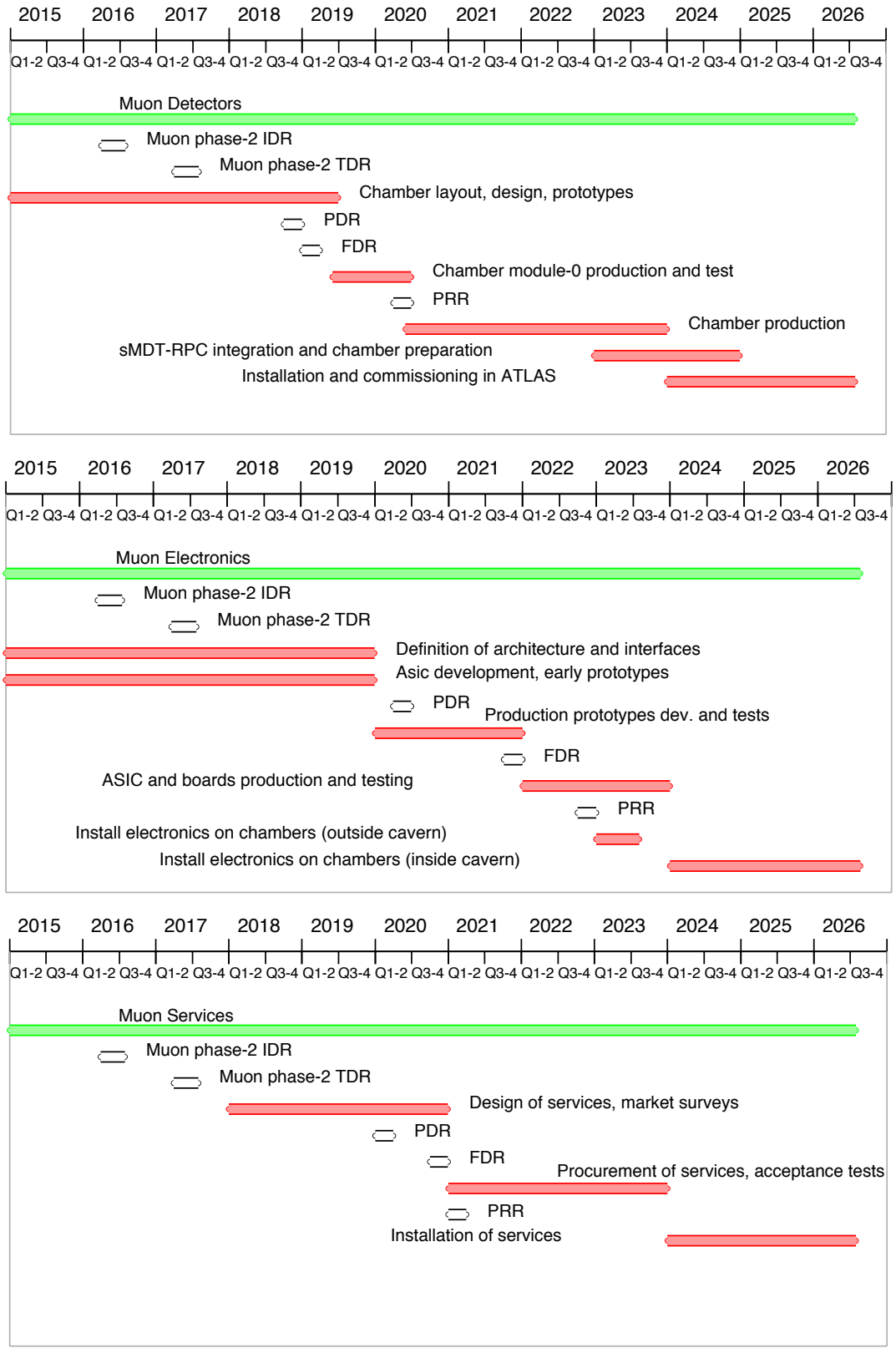

Figure 57. Preliminary schedule for R&D, production, installation and commissioning of the new muon detectors (upper panel), the new on-detector electronics (middle panel), and the services (lower panel).

Chapter VII

Forward Detectors

VII.1 Introduction

This chapter discusses possible upgrades to the existing forward detectors for the Phase-II period. These detectors are deployed along the LHC beam line as shown in Fig. 58. The current forward detectors include LUminosity Cherenkov Integrating Detector (LUCID), which instruments the region just beyond pseudo-rapidity 5.0, and measures quantities proportional to the instantaneous luminosity. There is also the Zero-Degree Calorimeter (ZDC) which is used to tag neutral energy flow in the very forward region, particularly in Heavy Ion running. Finally, there is the ATLAS Forward Physics (AFP) detector, the Forward Proton detector that should be installed in ATLAS during Run 2, to tag very forward protons to select diffractive or quasi-diffractive interactions. The Absolute Luminosity For ATLAS (ALFA) detector, which belongs also to the forward region, is planned to run until the start of LS2 when it will have provided the measurement of the total pp cross section at the updated LHC energy. Although it could be useful to have vertical Roman Pots (RP) running with AFP, at the moment there are no plans to continue to work with ALFA after LS2 and beyond. Studies are proceeding to understand whether any of these detectors should be upgraded for Phase-II running - further discussions with the accelerator are critical in order to understand any limitations or restrictions arising from the location of machine elements, or the HL-LHC optics, which could significantly affect the feasibility or detailed design of the forward detectors. In the following the case for each forward detector option for phase-II will be briefly discussed..

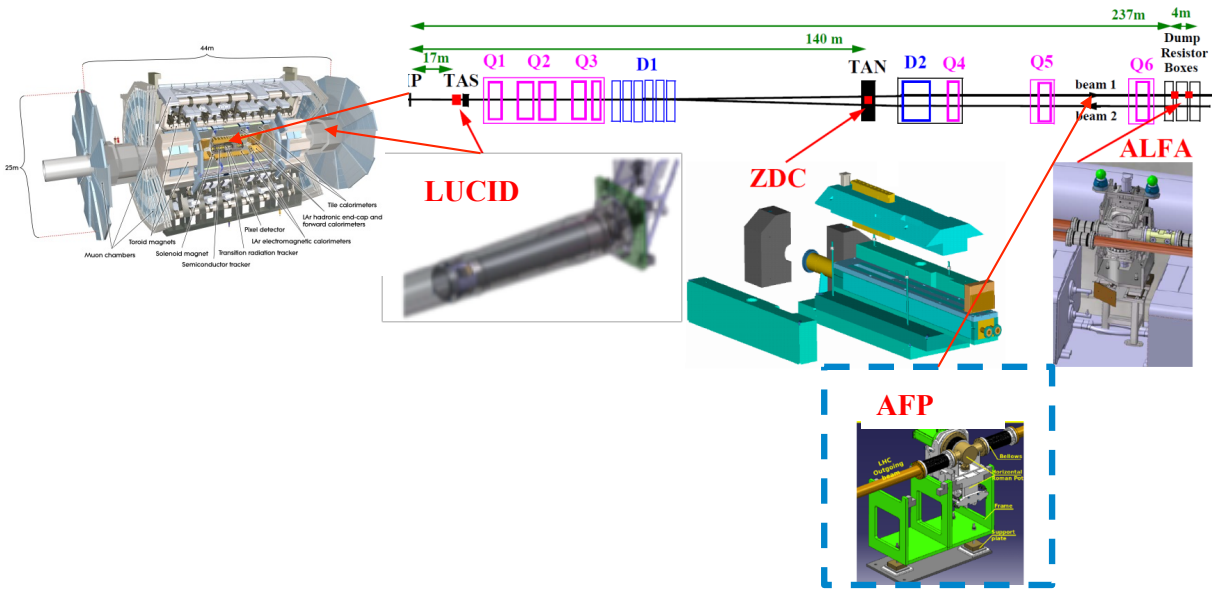

Figure 58. The ATLAS Forward detectors how they are deployed around the LHC beam pipe. The ATLAS Phase-I upgrade project is still not installed.

VII.2 AFP

AFP is a forward proton spectrometer consisting of two arms at about 210 m from the ATLAS IP. The purpose of the spectrometer is to tag and measure diffracted protons that remain close to the LHC beam line. Each AFP arm contains two Roman pot stations, at 205 m and 217 m, with tracking detectors placed in each pot and a compact time-of-flight detector in the station at 217 m. The

Roman pot beam interface allows the positioning of the detectors to about 2 mm from the proton beam during running and to retract the detectors during injection or beam dump.

AFP is an ATLAS Phase-I upgrade project and will be fully installed during the LHC shutdown in Winter 2016/2017. The initial physics program is the study of diffractive processes in special low-luminosity runs. Because diffractive processes generally have high cross sections, significant diffractive physics results can be obtained with a few weeks of special runs in the LHC Run 2 period. Amongst those are the study of the soft events, known as the underlying event in hard scattering processes; studies of diffractive production of W and Z bosons; the study of the soft and hard Pomeron and its structure in terms of quarks and gluons; and tests of the Balitskii-Fadin-Kuraev-Lipatov (BFKL) mechanism. Of particular interest is the Double Pomeron Exchange process, which features two forward protons and a pair of centrally produced jets. The measurement of this process marks the beginning of studies of hard central diffraction which eventually will lead to the need for higher luminosity. Ultimately, if AFP running at standard luminosity is demonstrably safe and has been approved, the tagging of forward protons at standard luminosity enables exciting new studies of central exclusive production (CEP) and of anomalous quartic gauge boson couplings, a possible harbinger of new physics. In the latter case, the high proton pile-up background in the detector can be greatly suppressed by exploiting the capability to measure the vertex with a precision of about $2\,\mathrm{mm}$ thanks to the excellent time resolution of $10\,\mathrm{ps}$ achievable with the timing detector.

If AFP has been demonstrated to run safely and without negative impact on standard LHC operations during Phase-I, the possibility to upgrade AFP for Phase-II will be considered in light of operating experience and physics results obtained. The possibility to upgrade depends not only on the detector design, but more importantly on the LHC machine design for the high luminosity phase. At the time of writing of this document, the HL-LHC design and operating conditions are still incompletely known and it is unclear if the new machine lattice will allow the use of horizontal Roman pots positioned within a few mm of the beam. High-luminosity running conditions, like luminosity levelling, could also prevent stable data taking with AFP. Given all these elements, a clear plan for AFP in Phase-II cannot be elaborated at this moment.

VII.3 ZDC

The ZDC detector has been designed to measure neutral particles (primarily neutrons) in heavy ion data taking runs, providing a L1 trigger to ATLAS and additional measurements of important parameters like the collision reaction plane and the event centrality. During Run 1 the detector was initially used also to measure neutral pions in pp collisions and to provide a luminosity measurement. The quartz rods which comprise the active calorimeter components were found to be less radiation hard than required for exposure to high intensity pp operation. Thus, it was decided to refurbish the detector after the 2011 proton run and to subsequently use it only during Heavy Ion runs, and low luminosity pp running. The quartz rods were replaced by new ones in 2012 and the detector was ready for the proton-Lead data taking which took place at the end of Run 1. The data taking was successful, providing a reliable L1 trigger and forward neutral energy for ATLAS, although it was realised during the run that again the calorimeter active elements were starting to be damaged by the high neutron flux from the fragmentation of the nucleus in the high rate proton-nucleus data, and the photomultiplier gain had to be increased several times to compensate for the overall factor 2–4 loss of signal from the quartz rods. During LS1, the ZDC institutes decided to reorganise their limited manpower and to investigate the possibility to upgrade the ZDC, and install this upgrade 2-3 years from now. In the meantime, the present plan foresees the use of the Run 1 version of the detector until an upgraded design is finalised and a new detector is built. The ZDC detector is designed to be positioned within the TAN absorber in front of the LHC beam separation dipole D2, and the

plans of the accelerator community for the replacement of this element for phase-II are not known at present. The design of the new TAN for Phase-II will be a fundamental constraint, which must be known before even starting the design of an upgraded detector. The second important unknown to be clarified is whether there will be a Heavy Ion program at the LHC during Phase-II. If such a program appears likely for Run 4, the ZDC institutes will be interested in developing a radiation-hard detector upgrade for use during this period.

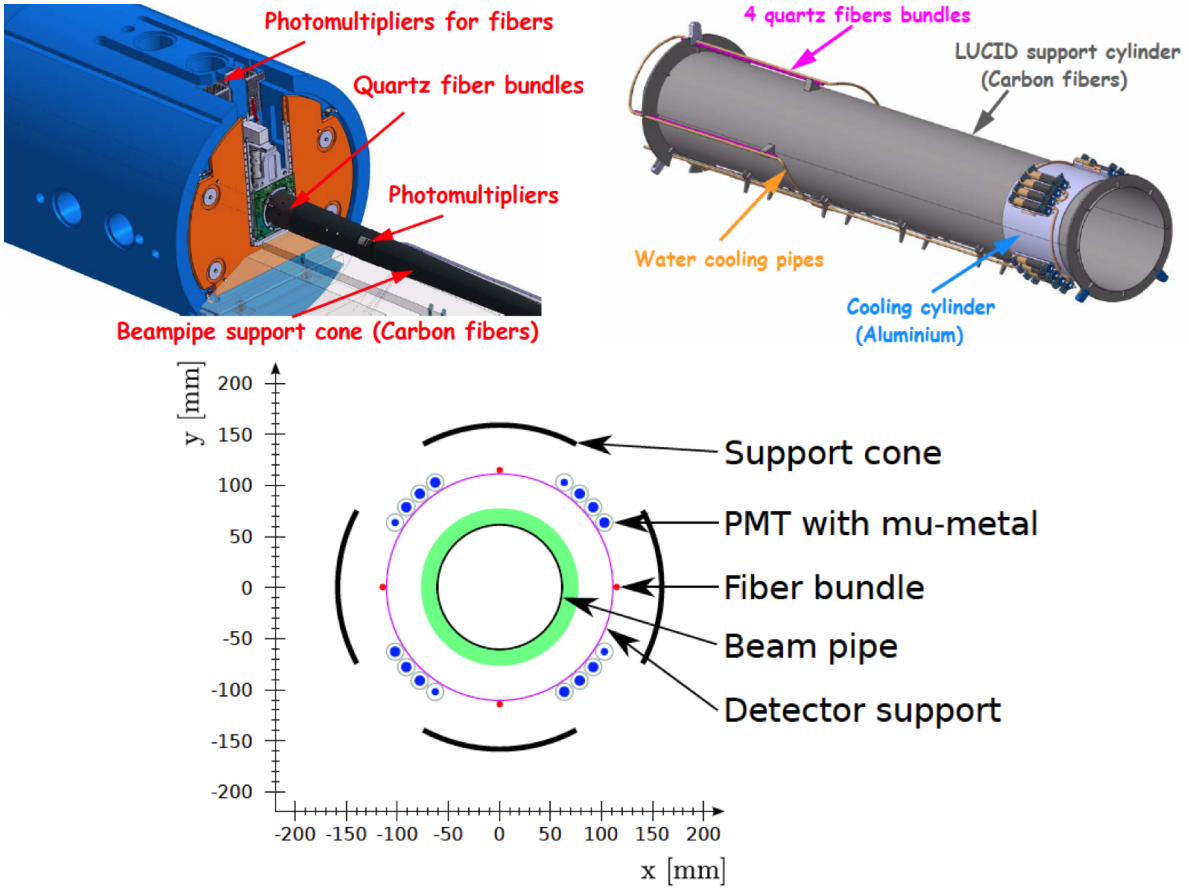

Figure 59. *Top left:* The location of the Run 2 LUCID detector in the ATLAS experiment. *Top right:* More details about the detector, the carbon fibre supporting cylinder and the cooling system. *Bottom:* Cross-sectional view of the detector.

VII.4 LUCID

The present LUCID geometry is shown in Fig. 59. It consists of two detectors, placed around the beam pipe symmetrically at about $17\ \mathrm{m}$ from the ATLAS IP. Each detector is formed by 16 PMT grouped by four and deployed in the ATLAS TAS shield region, as shown in the upper part of Fig. 59. The detecting medium is the quartz window of the PMT itself, which acts as a Cerenkov radiator. There are also 4 channels for which the radiator is a bundle of quartz fibres. These fibres are readout by PMT (one per bundle) placed on top of the ATLAS shielding (see the upper and middle part of Fig. 59). This readout method has already been tested successfully for the old LUCID, and has the advantage that the readout PMT sit in an area with a low level of radiation. The detector is placed

around the LHC beam pipe in a supporting carbon fibre cylinder as shown in the middle part of Fig. 59, and inserted in the carbon fibre beam pipe supporting cone. All the 20 readout PMT are inserted in mu-metal cylinder in order to shield them from stray magnetic fields. Details about the cross sectional view of the detector are shown in the lower part of Fig. 59.

The beam pipe is in aluminium and the support cone is made of carbon fibres. Since the detector must withstand the high temperature reached by the beam pipe during the bake-out phase, a suitable cooling system for the LUCID detector has been provided.

The LUCID detector is actually composed of three different detectors (see Fig. 60). The main

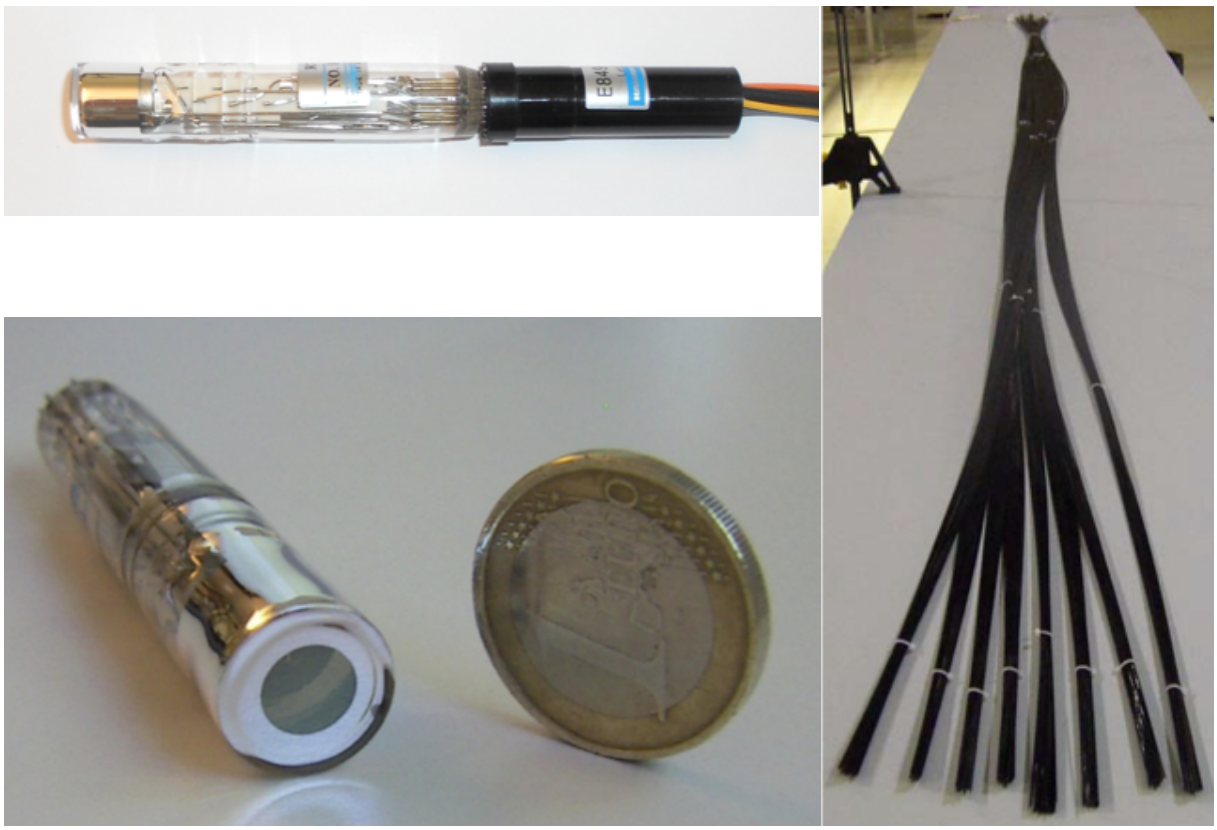

Figure 60. *Top Left:* Hamamatsu R760 PMT with quartz window of $10\,\mathrm{mm}$ diameter. *Bottom Left:* Hamamatsu R760 PMT modified to have a quartz window of $7\,\mathrm{mm}$ diameter. *Right:* Bundles of fibres used in the Run 2 LUCID detector.

detection scheme is to measure the light produced by charged particles above the Cerenkov threshold crossing the windows of Hamamatsu R760 PMTs (see upper part of Fig. 60). One of the main design criteria was to keep the detector acceptance low because of the increased occupancy in Run 2. For this purpose, a Hamamatsu R760 PMT has been produced with a sensitive window reduced from $10\,\mathrm{mm}$ to $7\,\mathrm{mm}$ which will significantly reduce the measured rate. This modification, which was specifically provided for LUCID, was produced by Hamamatsu by aluminising the PMT photo-cathode area.

An alternative readout method, already commissioned during Run 1, consists of measuring Cerenkov photons produced in bundles of long quartz fibres (Fig. 60, lower part) readout by R760 PMTs placed far from the beam pipe, where the radiation level is reduced.

As far as the fibre readout is concerned, the Cerenkov light produced in the quartz fibres is guided by the fibres themselves to the R760 PMT placed in an area with low radiation level. There

are 4 bundles of fibres per side used for this purpose. The fibres are routed along the beam-pipe by aluminium pipes.

The ATLAS experiment will surely need luminosity monitors for the Phase-II period of operation. At the time of this document there is no detector design available. It is however likely that one of the ATLAS luminosity monitoring techniques for Phase-II will rely on some modified version of the present LUCID detector. The present Run 2 LUCID can be considered already as an R&D project for a Phase-II detector in itself. Of the three detection techniques implemented, the most promising as a baseline for Phase-II is certainly the one in which the Cerenkov light produced in the quartz fibres is guided by the fibres themselves to the R760 readout PMT placed in an area with low radiation level. This version must be fully commissioned in the next years and, if proven to work in a reliable way, it is certainly the most appealing detection scheme since it decouples the heavily irradiated Cerenkov light detector, based on in very radiation hard quartz fibres from the readout devices, which can be placed in an area with low radiation level. The main item that must be commissioned in Run 2 in order to validate this detection scheme is the completely new LUCROD (LUCid ReadOut Device) card which performs, among other functions, the integral by bunch of the detected current, so providing the total delivered charge per bunch which is proportional to the instantaneous luminosity. This readout scheme is in principle free of the non-linearity of other commonly used signals over threshold counting algorithms, but depends critically on the detector stability. The monitoring of the fibres readout stability during Run 2 will therefore be crucial to validate the detection scheme based on quartz fibres.

One of the main challenges to be understood and solved is the new positioning of the LHC VAX which is shown in Fig. 61. In the left part of this figure the present position of the VAX and in the right part its proposed position after LS3 are shown. The reason for this displacement is to reduce the need for people to enter a high radiation area in case some of the VAX equipment fails. The consequence is that the new positioning will conflict with the present location of LUCID. Both the cable routing and detector position will be affected by this change. It appears that the new constraint imposed on the LUCID location in Phase-II will not represent an insurmountable problem and that solutions will be found.

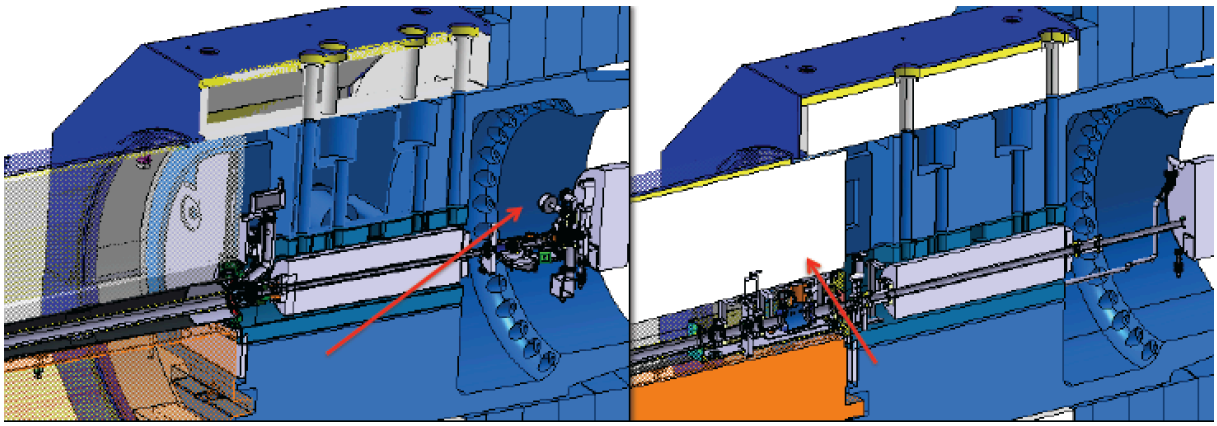

Figure 61. The TAS collimator area where the LUCID detector is deployed.The red arrows point to the VAX equipment on the ATLAS experiment side. *Left:* VAX position until LS3. *Right:* VAX position after LS3.

Table 22. Summary of the costs of the existing ATLAS forward detectors, and the relevant physics goals for the Phase-II forward detectors.

Detector	Cost Estimate (kCHF)	Physics Goals
AFP	1,000	Hard Diffraction, CEP
ZDC	800	Heavy Ions runs
LUCID	500	Luminosity

VII.5 Summary

There are several questions associated with the installation and operation of Forward detectors during the high luminosity phase-II period, which make it difficult to extrapolate to a reliable cost estimate based on an existing design for these detectors. As the answers to these questions appear during the next few years, it will become clear whether or not design solutions for the AFP, ZDC, or LUCID detectors during Phase-II are possible or not. This will allow more detailed studies of the physics potential for each option to be performed, and a decision reached as to whether or not ATLAS wants to include them in the Phase-II upgrade program. For reference, the costs of the existing versions of these detectors, based on past experience, are summarised in Table 22.

Chapter VIII

Infrastructure and Installation

VIII.1 Introduction

This chapter provides an initial analysis of the different areas of the Phase-II upgrade activities, that don't naturally fit inside a given sub-system community, and therefore should be considered as part of a common infrastructure contribution to the upgrade. These contributions involve significant, specialized technical responsibilities where the engineering and technical manpower in the ATLAS Technical Coordination (TC) team are particularly well-qualified to take on the leading roles. In addition, TC has formal responsibility for the installation and integration of all the activities in UX15 and in the related service caverns, including the installation and integration of the ATLAS detector sub-systems and of the common infrastracture. This work spans both the preparation period and the installation and commissioning period. In the former, studies of the mechanical interference between the systems will be done. Installation procedures will be prepared as well as an integrated schedule for all the activities with dependencies and interferences. In addition, an assessment of the radiological hazards related to each installation activity is being planned. For the installation and commissioning, TC is responsible for organising the installation tasks, and for providing engineering and technical manpower. It provides safe access to the detectors and will provide adequate shielding for the workers in activated areas. Moreover, TC is responsible for organising the relevant activities to integrate all of the upgraded detector systems, together with the existing systems, in the ATLAS read-out and Detector Control scheme. One particularly important duty of the TC team is to insure that all the common infrastructure will operate properly during the extended period of Phase-II running, and will cope with the more challenging requirements due to much higher luminosity. In particular it is a TC responsibility to assess and provide for new needs in terms of cooling (both for the electronics racks and for the experimental cavern), electrical power and electrical power distribution, control technical networks, detector safety systems, and for safety in general. Another important responsibility for the TC is to provide adequate laboratory and storage space to allow the construction and integration activities for all the different subsystems to proceed efficiently.

In parallel with the upgrade-related activities, TC is also responsible for the standard operations that are normally performed during yearly machine shut downs. These include: opening and closing the detector, standard maintenance of the subsystems, yearly maintenance of cooling and power systems (e.g. UPS) etc. All these activities are planned to be funded using different sources, given their difference in nature:

- All the standard maintenance and shut down activities, as well as infrastructure maintenance, intended to maintain the performance of a subsystem or of a common system, should be funded using the standard M&O A budget.
- Consolidation of infrastructure as well as laboratory and storage space could be funded using the CERN consolidation budget as a host lab responsibility
- All upgrade activities, and specifically all the activities intended to provide new functionality and better performance at higher luminosity, should be funded by an upgrade common fund under the responsibility of the Technical coordinator and Resource coordinator.

The remainder of the chapter is structured in sections that cover the following topics: (i) estimates of the radiation environment expected in LS3 and preliminary studies on safety and radio-protection requirements, (ii) detailed discussions of the opening and closing activities and the overall shutdown schedule, (iii) descriptions of the most relevant tasks related to integration, installation, and to common infrastructure for Phase-II, (iv) an estimate of the correspinding upgrade CORE costs to support infrastructure and integration activities.

VIII.2 Safety and Radio-protection

One of the challenges ATLAS needs to address for LS3 and for the subsequent access periods is the detector activation. In particular, all material included in the operational zone (radius < 1.5m) will be confronted with such a problem. As a non-exhaustive list, the beam pipe, the TAS collimator, the various shielding elements, the Inner tracking Detector (ID) and the End-Cap Calorimeters will all be highly activated and any work performed in their vicinity will need to be analysed and optimised according to the ALARA principle.

To achieve this goal ATLAS has organized an "ALARA team" starting in Run 1 working in close collaboration with the CERN DGS-RP group to perform simulations and to define dose maps, consistent with every standard configuration of the ATLAS detector. The radiation maps will be used as the basis to asssess and develop intervention procedures.

VIII.2.1 Radiation simulations

The radiation calculations needed to assess the activation and the residual doses for each interesting zone, where large maintenance or installation works are envisaged, are done using the FLUKA [68, 69] transport code. The results of calculations performed using the Run 1 geometry, have been cross checked with measurements, and generally show good agreement except for a small number of specific places where differencse as large as a factor of two to three are found. Those differences are attributed to specific changes in the geometry or in the material used in the real detector.

These results give confidence in the extrapolations for LS2 and LS3, where the geometry is known and specifically for the inner part of the detector which will remain unchanged until LS3. On the other hand, a rather large uncertainty is still present on the layout, materials and services for the upgraded detector which in turn will translate into a larger safety factor to be applied to the simulation results for LS4 and onwards.

Figure 1 in Chapter II (from Ref. [5]) represents the latest HL-LHC schedule beyond LS1, updated accordingly to the MTP 2016-2020, and presented at the last CERN Council session in June [6]. The operational parameters for the accelerator complex and a detailed profile of the delivered luminosity are described in the HL-LHC Preliminary Design Report [70], released at the end of 2014. ATLAS TC calculations of the expected activation doses and the classification of the radioactive zoning are based on the luminosity profile presented at the 2014 ECFA workshop (see Ref. [71]), which is roughly consistent with the profile assumed in [70]. The relevant figures of merit are the integrated luminosity of approximately 310 $fb^{-1}$and 1100-1300 fb^{-1}delivered to the experiments by LS3 and LS4 respectively (i.e. a factor of three to four increase). The shape of the radioactive waste zone and the doses at different cooling times for LS3 and LS4 are shown in Figs. 62-63 (as calculated using the geometry of Run 2). In LS3 the work close to the ID plate, after a period of 40 days for the cool down, and at a distance of 40 cm from the ID end plate will entail a dose of about 30 μS/h while after removing the old inner detector, and in the same position with respect to the IP, this dose will increase to 130 μS/h. During LS4 (after about three years of HL-LHC running) these figures will increase by about a factor four.

Table 23. The luminosity profile assumed for radiation modelling up to the end of HL-LHC (from Ref. [71]).

Year of LHC Operation	Peak / levelled luminosity [$cm^{-2}s^{-1}$]		Integrated luminosity [fb^{-1}]	
≤2012	0.8E+34		30	
LS1		**sum:**	**30**	**30**
2015	0.5E+34		20	
2016	1.5E+34		46	
2017	1.5E+34		36	
2018 (1/2 y)	1.5E+34		24	
LS2			**156**	**156**
2020 (3/8 y)	1.5E+34		15	
2020 (5/8 y)	2.0E+34		25	
2021	2.0E+34		55	
2022	2.0E+34		55	
LS3			**306**	**306**
2025 (1/4 y)	5.0E+34	7.5E+34	63	75
2026	5.0E+34	7.5E+34	250	300
2027	5.0E+34	7.5E+34	250	300
2028	5.0E+34	7.5E+34	250	300
LS4			**1119**	**1281**
2030	5.0E+34	7.5E+34	250	300
2031	5.0E+34	7.5E+34	250	300
2032	5.0E+34	7.5E+34	250	300
LS5			**1869**	**2181**
2034	5.0E+34	7.5E+34	250	300
2035	5.0E+34	7.5E+34	250	300
2036	5.0E+34	7.5E+34	250	300
LS6			**2619**	**3081**
2038	5.0E+34	7.5E+34	250	300
2039	5.0E+34	7.5E+34	250	300
2040	-	7.5E+34	**3119**	300
LS7				**3981**

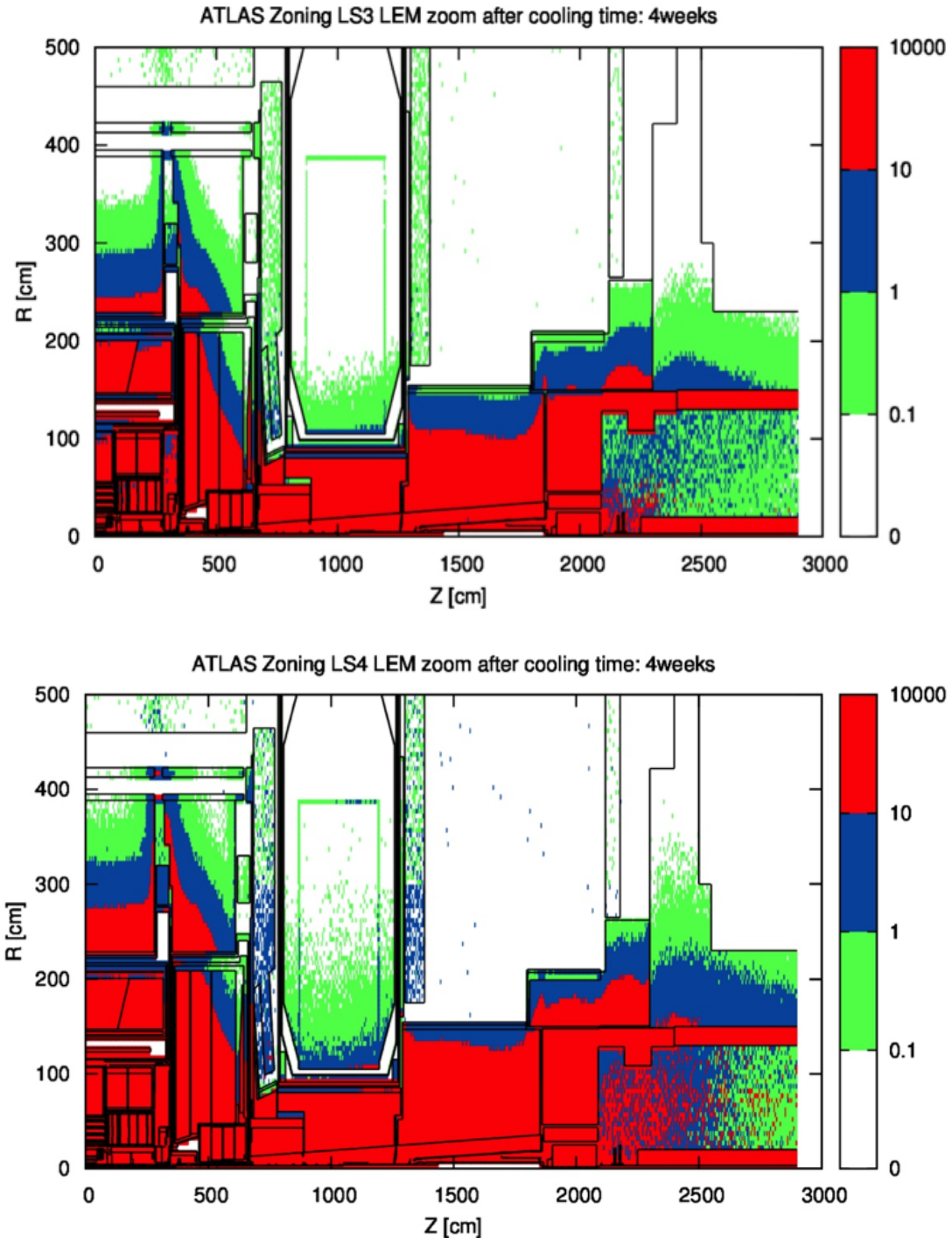

Figure 62. ATLAS radioactive material zoning after four weeks of cool down during LS3 (top) and LS4 (bottom). All regions with value of the vertical axis (color scale) above 1 are considered to be radioactive waste regions

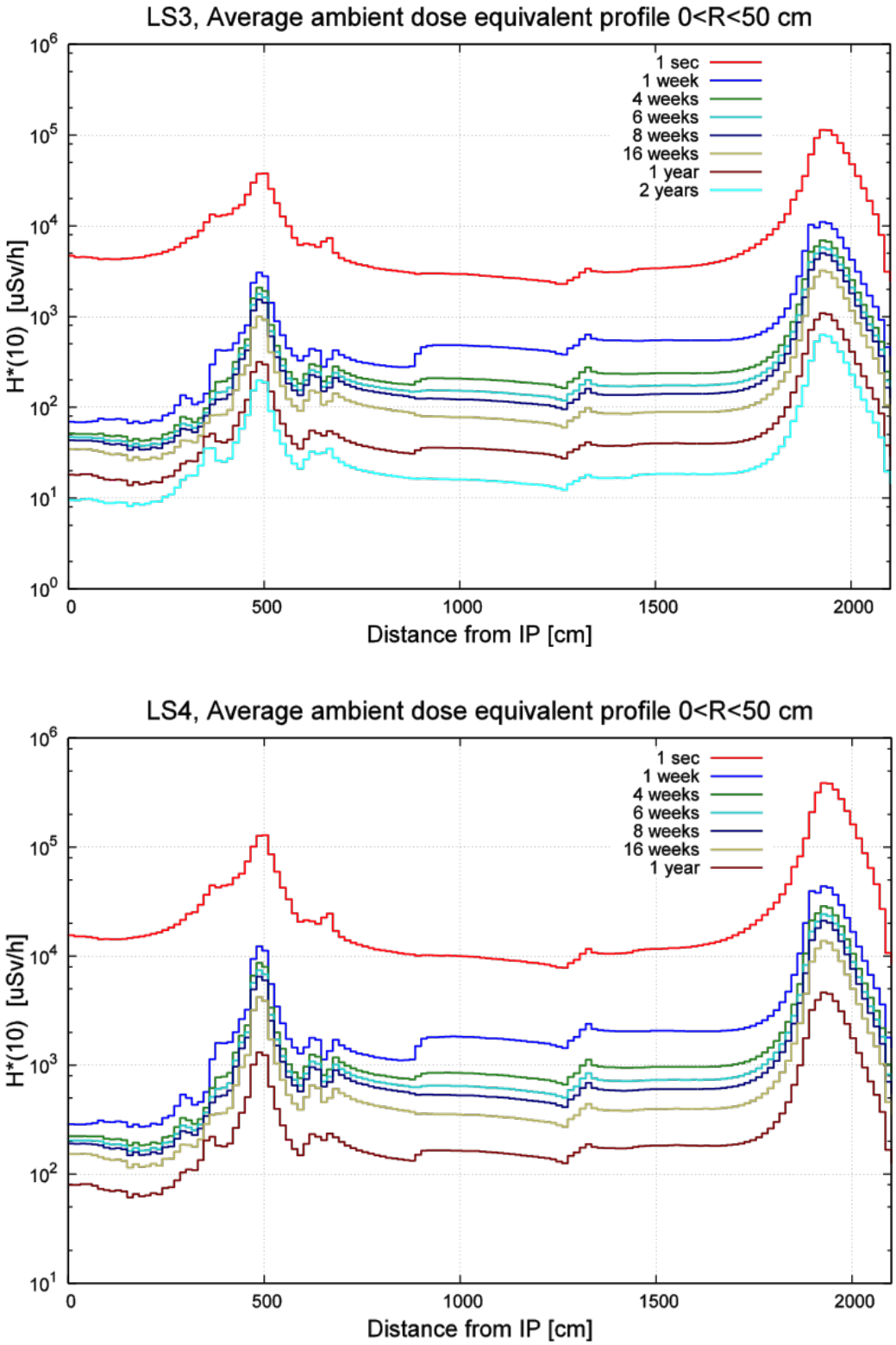

Figure 63. Residual radioactivity levels, at a radius of less than 50 cm from the beam line, for different cool down times in LS3 (top) and LS4 (bottom). The X axis is the distance along the beam line from the IP

VIII.2.2 Radiation protection requirements

CERN rules on radiation protection impose a maximal dose exposure of 6 mSv/year and 2 mSv/month for professional workers in a controlled area. However more constraining objectives are being defined CERN-wide, as radiation protection guidelines:

- The personnel dose should not exceed 3 mSv/year (12 consecutive months)
- The personnel dose should not exceed 250 μSv/week
- The design of new equipment should include a requirement about installation and maintenance to limit individual dose at 2 mSv/year

During LS3, there will be many different situations to consider, to date the most concerning are:

1. **Opening of the experiment.**
   The procedure for opening the ATLAS detector already takes into account the ALARA principle. The engineering procedures will be optimised to minimise the radiation exposure of the people involved in this activity. The intervention crew is trained specifically for this activity using in particular the experience of the previous long shutdowns (LS1 and LS2).

2. **Decommissioning of the Inner Detector.**
   The beam pipes will be removed but the un-cabling procedure for the ID, where people will be working in front of the barrel for several weeks or even months, requires very specific planning and care. Prior to LS3, it is planned to rehearse the procedure using a mock-up specifically built for use in a surface building. Depending on the dose budget that will be calculated prior to any intervention, rotation of personnel and even remote handling equipment may be used. Provisional shielding may be installed as well, but it is not yet clear what impact it would have on the decommissioning activities, by potentially extending the required time and complicating the tasks due to the need to work around the shielding. Once the services are removed, the extraction process for the ID will begin, using dedicated tooling whose design will fully integrate whatever shielding is required to meet the radiation protection requirement.

3. **Opening of the LAr end-cap cryostats.**
   In addition to the concern expressed above, this operation requires mechanical interventions on welds and structures and therefore one additional problem is the potential contamination of the entire working area. Ongoing preliminary studies are based on the use of temporary shielding, procedure optimisation and special tooling.

4. **TAS removal.**
   The removal of the TAS in the underground experimental cavern (UX15) deeply involves ATLAS TC, despite the fact that it is not a direct ATLAS responsibility. Early in the study, the requirement of radiation protection is integrated into the planning and remotely actuated tooling is considered.

5. **Activities on the inner radius of the Big Wheels.**
   The use of temporary shielding installed in front of the TAS and in front of the JTT shielding provides a comfortable solution. Such shielding has been manufactured and tested successfully during LS1.

For all cases, a full ALARA procedure needs to be established and the work packages need to be validated and approved by the CERN ALARA committee. A nuclear waste zone is established by

CERN DGS-RP. All material exiting this perimeter must be considered a priori as radioactive and go through a special radio-protection procedure which includes storage in a dedicated buffer zone and traceability for the entire life-cycle.

VIII.2.3 Radiation protection equipment

In addition to the technical measures foreseen to limit personal exposure, that have been described in the previous Section, the monitoring, in real time, of the radiation dose is at last a very efficient way to protect workers. Firstly, ATLAS plans to enlarge the use of operational dosimeters, secondly the experiment is committed, through the EDUSAFE [72] programme, to the development of advanced tools like gamma imaging camera or supervisory systems based on augmented reality. These systems allow for real-time feedback on actual dose rates in a given working area and real time imaging of potential hot spots. Therefore, they provide the possibility of dynamic optimisation of the work plans and techniques to minimise the actual dose acquired, and to create confidence in the workers that important measures to protect them have been taken.

VIII.3 Layout and configurations

The ATLAS cavern (UX15) will be accessible for about 30 months starting in December 2023. During this period, the ATLAS detector will be opened to allow for a series of modifications and improvements to the detector.

The mechanical operations required by the Phase-II upgrade are mainly driven by the insertion of the ITk. However, several other projects require a dedicated configuration of the experimental cavern, as detailed at the beginning of Section VIII.4.

To arrive to the main configuration (“Large Opening”), which allows for the extraction of the current ID, the forward shielding, which consists of 10 parts with a total weight of 836 tons, and both Muon Small Wheel (SW) are moved to the surface. The beam-pipes are vented and moved to the surface as well. The end-cap Toroids are moved into their garage position beside the beam axis. The end-cap calorimeters are moved by about 11.5 m longitudinally, just in front of the TAS Collimator (see figure 64). A set of dedicated platforms, which allow for work and operations to be performed under good conditions in front of the barrel calorimeter front face, are installed and dedicated scaffolding is erected as required.

The plan is to arrive at this main working configuration after 10 weeks of activity, working partially in 2 shifts. For safety reasons, all other activities in UX15 are very limited and strictly controlled during this period.

This configuration is suitable for the extraction of the ID and for the installation of the ITk, but it gives no possibility to access the front-end electronics of the calorimeter end-caps or the Tile calorimeter drawers. Later movement of the end-cap calorimeters needs to be performed to reach a situation as shown in figure 65.

All these opening operations are not new and have been exercised on several occasions: for the LS1 shutdown it has been done on one end of the experiment to remove the Pixel detector and reinstall the Pixel detector and the new IBL detector, for LS2 it will be performed on both ends to install the New Small Wheels. By LS3 ATLAS Technical Coordination will have acquired considerable experience with these operations.

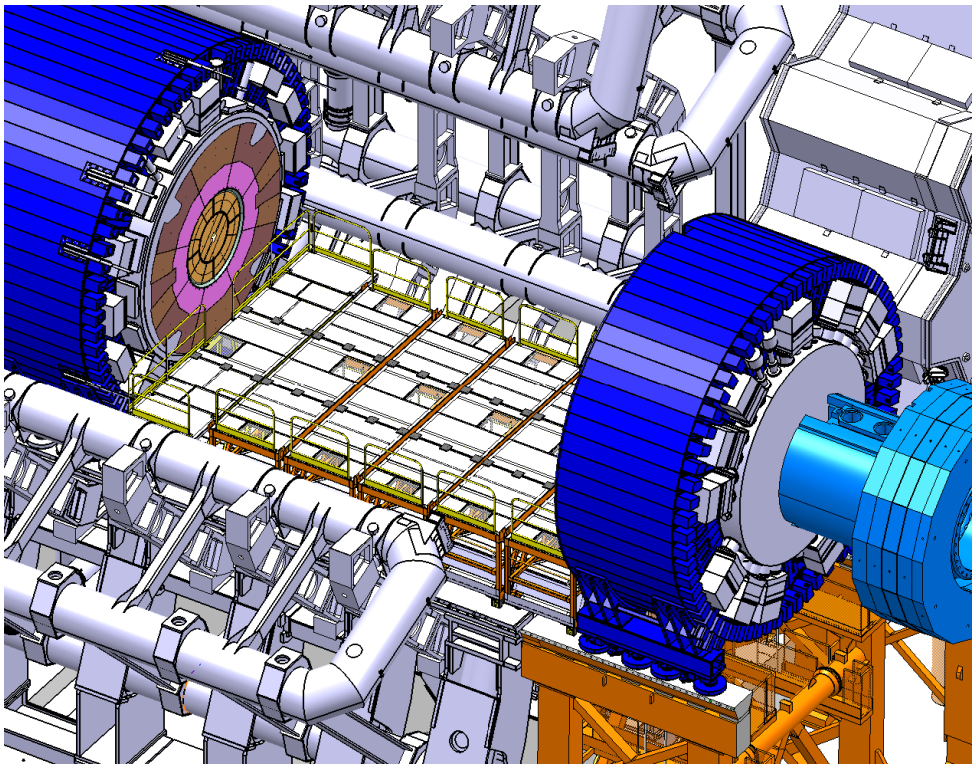

Figure 64. Large Opening configuration during the LS3 shutdown, with both small wheels lifted to the surface and dedicated flooring installed for ID activities

VIII.4 Installation schedule

A long shutdown (LS3), starting on 2024, is planned to allow the detectors and the accelerator to prepare for the conditions that will be encountered during the HL-LHC data taking period, which starts in 2026 with the aim of delivering an integrated luminosity of 3000 fb^{-1} over ten years.

Besides the opening and closing of the experiment, there are six activities, out of the many presented in this document, which largely determine the underground work organisation and the critical path for the schedule. They are:

- The removal of the current ID and the installation of the new ITk,
- The replacement of the read-out electronics for the MDT tracking system and the addition of new RPC chambers in the Barrel area,
- The upgrade of the Calorimeter front-end electronics and the installation of the new Tile drawers,
- The upgrade of the (TGC trigger electronics located in the Big Wheel region, and the replacement of the TGCs located in the inner ring of the Big Wheels),
- The replacement of the current FCal with the high granularity sFCal,
- The replacement of the TAS collimator with the new TAXS collimator.

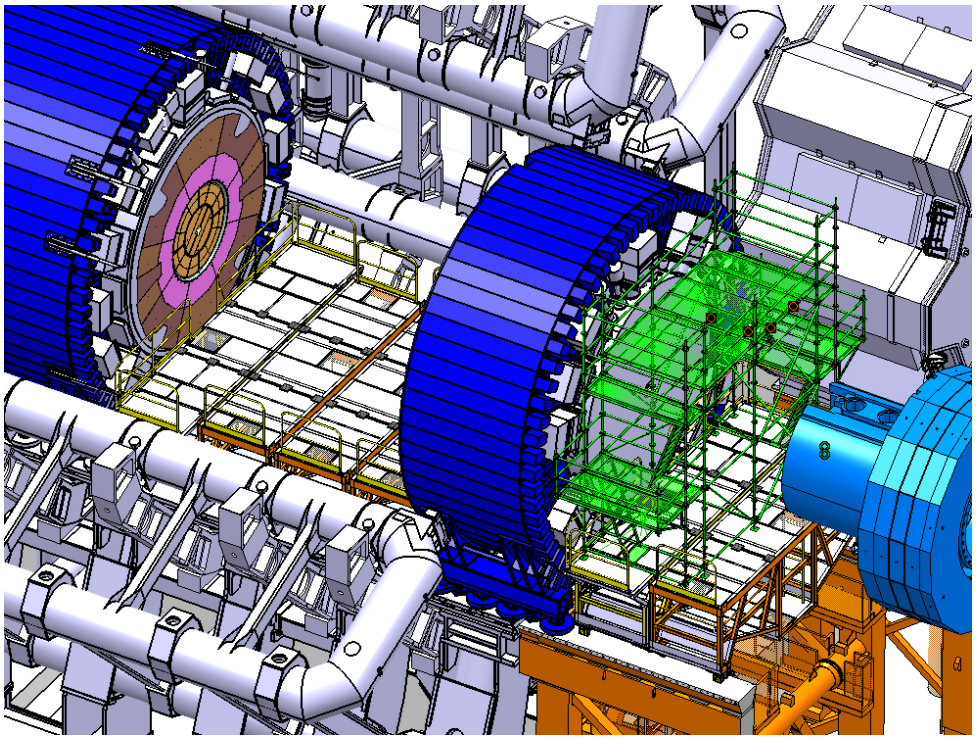

Figure 65. End-cap calorimeter moved to the intermediate position, suitable for access to the front-end electronics and Tile drawers

VIII.4.1 Schedule assumptions

- Activities in UX15 are minimised as much as possible, firstly to limit personal exposure to radiation, secondly because both the yearly technical stops and LS1 have shown that the efficiency of the underground work is much less than that which can be expected in a more friendly environment (difficult access, co-activity in a small area, etc).
- Maintenance and consolidation activities, which are not described in this document, are not taken into account at the present stage of initial planning. Based on LS1 experience, these activities will require significant time and resources. However they will not define the critical path of LS3 and will be incorporated into the schedule in a more detailed future version.
- Every component to be installed in the ATLAS detector is fully tested and qualified beforehand. The production and integration plan of the new upgraded systems should be such that they are available on the surface at least 2 months before the installation time.
- Opening and closing operations are foreseen to be partially carried out using two shifts. This organisation, set up in ATLAS Technical Coordination since 2010, is demanding in terms of human resources but has proven to be extremely efficient.
- The calendar is made on the basis of 5 working days per week, 8 hours/day. This assumption leaves some margin to accelerate the schedule if needed by adding additional manpower for double shifts and/or longer working weeks.

VIII.4.2 Overall sequence of the installation process

The installation schedule is built from an analysis of the activities to be performed by the various systems, taking into account the specific constraints of each of them in terms of the estimated duration, access requirements, and other activities taking place in parallel. A summary of these activities and constraints is presented below.

The existing ID is removed from the pit and brought to the surface for storage in a dedicated buffer zone at CERN for an initial radioactivity cool-down period until it can be decommissioned and/or disposed of. Before lifting it to the surface, all services must be disconnected. The removal of the ID has high priority at the beginning of the shutdown period over all other activities. After the removal of the existing detector, the floor is given to the removal and refurbishing of the necessary services (pipes, fibres and cables).

To allow enough time for the refurbishing work, the newly built ITk is lowered into position approximately nine months after the beginning of the shutdown. In parallel with the ID removal, and the installation of the ITk and the routing of the related services, the work for the Muon Barrel can start. It is foreseen to last up to 22 months depending on the specific upgrade options chosen, the available resources, and the work organisation. Indeed, replacing the MDT front-end electronics (mezzanine cards and CSM) on the BI chambers, and installing RPC chambers on top of them, is expected be a very difficult and time-consuming task.

There is insufficient space in the small sectors (BIS chambers) to add RPC chambers on top of the existing MDT. Therefore, the BIS MDT chambers are replaced by sMDT chambers with tubes of half the diameter of standard MDTs, thus creating the required space for the RPC. The old BIS MDT chambers are removed from the detector and then the new BIS sMDT chambers, integrated with the new RPC in a single package, and with the new front-end electronics assembled on them, are installed.

In large sectors (BIL chambers) some space has to be recovered in order to install the new RPC chambers. Indeed many services (cables, gas pipes, electronics) are mounted on the outer surface of the BIL MDT chambers and various access platforms currently prevent RPC installation. All these components have to be displaced in order to make room for the RPC chambers. Two different scenarios are currently being studied: (1) Temporarily removing the BIL chambers from ATLAS makes replacing the front-end electronics and re-routing services very easy; however many other MDT chambers (EIL4, BML4-6, EES1-2) as well as many access structures will have to be moved or removed in order to make way for the BIL. (2) Leaving the BIL in place avoids all these operations but replacing the MDT front-end electronics on BIL chambers in situ is very difficult due to the very limited space between the MDT tube endpoints and the barrel toroid coils. In both scenarios the RPCs would be installed separately from the MDTs on dedicated rails.

To fit the activity inside the available time, two technical teams are required to work in parallel, and the detailed sequence has to be flexible enough to cope with the ITk installation. As soon as the Large Opening configuration is achieved, the work on the calorimeters could also start. However, in order to limit co-activity, the interventions on each system, LAr and Tile, require an optimised organisation.

The LAr front-end electronics installation is scheduled to take three months per cryostat face (barrel A, barrel C, end cap A, end cap C, best installed sequentially). The barrel cryostat work is assumed to happen first, in parallel with ID un-cabling. Some interruption in the process is foreseen to perform mechanical removal of the ID. Scaffolding needs to be provided to access the crates safely. It is planned to work with two teams of experts (from the LAr community) in parallel who have to perform the following work:

- Removal of all services.

- Removal of the tower builder boards or the tower driver boards in the front-end crates.
- Exchange of the front-end electronics boards and calibration boards.
- Exchange of the on-detector low-voltage power supplies.
- Re-connection of the new services: fibres, cooling, power (it is assumed that the new services are installed before the campaign on each side starts).

The installation of new LAr electronics for the end-caps is scheduled much later, after the installation of the sFCal is completed.

For each part of the LAr calorimeter, the commissioning starts immediately after installation, full certification is expected to last several months. It is therefore very important to foresee the possibility to provide access to each side after commissioning is finished.

As for the Tile calorimeter, the best sequence would be:

1. Extract all the 256 super-drawers in order to recover the PMT blocks (they will be re-used in Run 4 with phase-II electronics).
2. Finish the assembly of the drawers on the surface adding the re-worked PMT blocks and testing them.
3. Move the assembled/tested drawers and insert them into the detector.

This scenario would require that the four regions of the tile calorimeter (LBA, LBC, EBA, EBC) are accessible at the same time for a long period which is very constraining. It is actually planned that this sequence is applied to each region sequentially. The end-cap calorimeters will be moved back to their intermediate open position (figure 65) about 3 months after the ITk is positioned inside the Barrel Calorimeter. This is assumed to be enough time to allow the most intense cabling work and ITk services installation to happen without disturbance and in optimal access conditions. From that time, the interventions planned on the LAr end-cap cryostats (sFCal or MiniFCal) can start and are expected to last about 5 months on each side. Replacing the Forward Calorimeter requires opening the cold vessel of the endcap cryostat. This is a challenging operation that entails weld cutting then re-welding of the cold vessel bulkhead, and some feed through modification. Protection against the high radiation dose and possible contamination inside the cryostat are relevant concerns, and related mitigation measures are expected to be time consuming. At the end of this period, the cool down of the cryostats will be launched. The replacement of the LAr electronics on the end cap calorimeters is scheduled in parallel with this cool down.

The closing process starts at the very beginning of 2026, as it is mandatory in order to access and work in the forward region. Such a scenario makes it possible to maintain access to the calorimeters for about 2 months after the full installation of the new systems. Once the detectors of the Barrel region will be back in run position, the priority is given to the TAS replacement with TAXS. It is a crucial step before which it is not possible to fully install the ATLAS beam pipes. The current estimated duration is 2 months, but this must still be confirmed. The bake-out of the beam pipe is planned just after the TAXS installation. The replacement of the MDT electronics on the Muon Big Wheel (BW) and End-cap Outer layer (EO) chambers is expected to last four months. The operation requires the opening of the BW, allowing access to the Large and Small Chambers electronics using a specifically designed basket hanging from the crane. The very last major intervention before the closing of the cavern is the replacement of the TGC trigger electronics. Although a fraction of the work can be anticipated, a large part of the work requires the BW to be in running position, and, therefore, the ATLAS detector can be completely closed. This activity requires a total of about three months, distributed in several steps, and can be done with several teams in parallel. After the end of this activity the cavern will be closed.

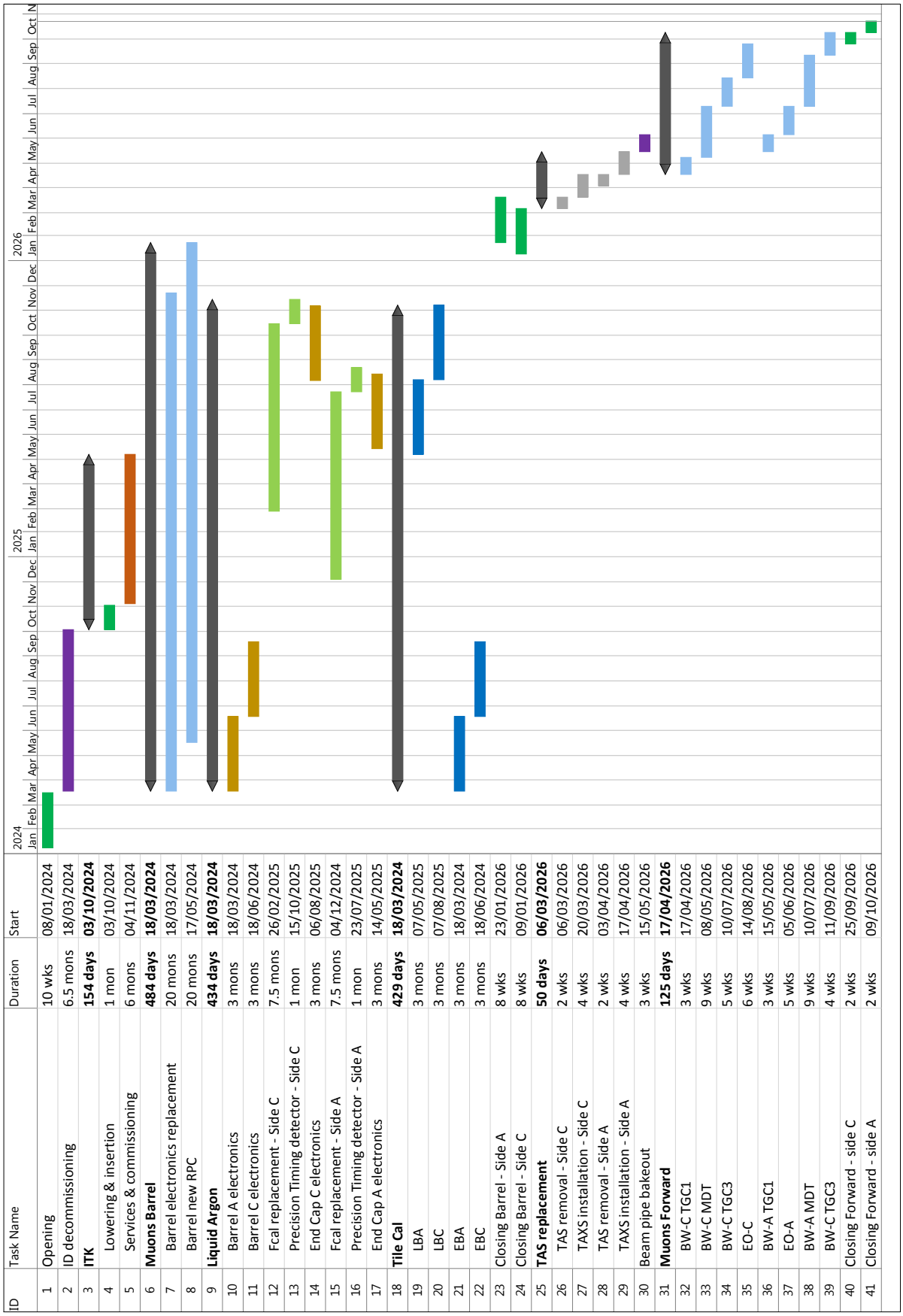

ID	Task Name	Duration	Start
1	Opening	10 wks	08/01/2024
2	ID decommissioning	6.5 mons	18/03/2024
3	**ITK**	**154 days**	**03/10/2024**
4	Lowering & insertion	1 mon	03/10/2024
5	Services & commissioning	6 mons	04/11/2024
6	**Muons Barrel**	**484 days**	**18/03/2024**
7	Barrel electronics replacement	20 mons	18/03/2024
8	Barrel new RPC	20 mons	17/05/2024
9	**Liquid Argon**	**434 days**	**18/03/2024**
10	Barrel A electronics	3 mons	18/03/2024
11	Barrel C electronics	3 mons	18/06/2024
12	Fcal replacement - Side C	7.5 mons	26/02/2025
13	Precision Timing detector - Side C	1 mon	15/10/2025
14	End Cap C electronics	3 mons	06/08/2025
15	Fcal replacement - Side A	7.5 mons	04/12/2024
16	Precision Timing detector - Side A	1 mon	23/07/2025
17	End Cap A electronics	3 mons	14/05/2025
18	**Tile Cal**	**429 days**	**18/03/2024**
19	LBA	3 mons	07/05/2025
20	LBC	3 mons	07/08/2025
21	EBA	3 mons	18/03/2024
22	EBC	3 mons	18/06/2024
23	Closing Barrel - Side A	8 wks	23/01/2026
24	Closing Barrel - Side C	8 wks	09/01/2026
25	**TAS replacement**	**50 days**	**06/03/2026**
26	TAS removal - Side C	2 wks	06/03/2026
27	TAXS installation - Side C	4 wks	20/03/2026
28	TAS removal - Side A	2 wks	03/04/2026
29	TAXS installation - Side A	4 wks	17/04/2026
30	Beam pipe bakeout	3 wks	15/05/2026
31	**Muons Forward**	**125 days**	**17/04/2026**
32	BW-C TGC1	3 wks	17/04/2026
33	BW-C MDT	9 wks	08/05/2026
34	BW-C TGC3	5 wks	10/07/2026
35	EO-C	6 wks	14/08/2026
36	BW-A TGC1	3 wks	15/05/2026
37	EO-A	5 wks	05/06/2026
38	BW-A MDT	9 wks	10/07/2026
39	BW-C TGC3	4 wks	11/09/2026
40	Closing Forward - side C	2 wks	25/09/2026
41	Closing Forward - side A	2 wks	09/10/2026

Figure 66. Overview of the LS3 installation schedule

VIII.4.3 Schedule details

Figure 66 shows an overview of the master schedule for LS3 based on the previous description. It is clear that all operations are very concentrated in time and that the schedule will be very challenging. This preliminary version is longer than the expected duration of LS3 by four months. Moreover, even if in the overview schedule there is provision for some contingencies (double shifts and longer working weeks as stated before), several conflicts in resources and co-activities are likely to slow down the work flow. The schedule shown in Fig. 66 is related to the Reference scope scenario. It is clear that it is the most constraining from the point of view of the installation process, the Middle and Low scenarios would result in a somewhat less challenging installation schedule.

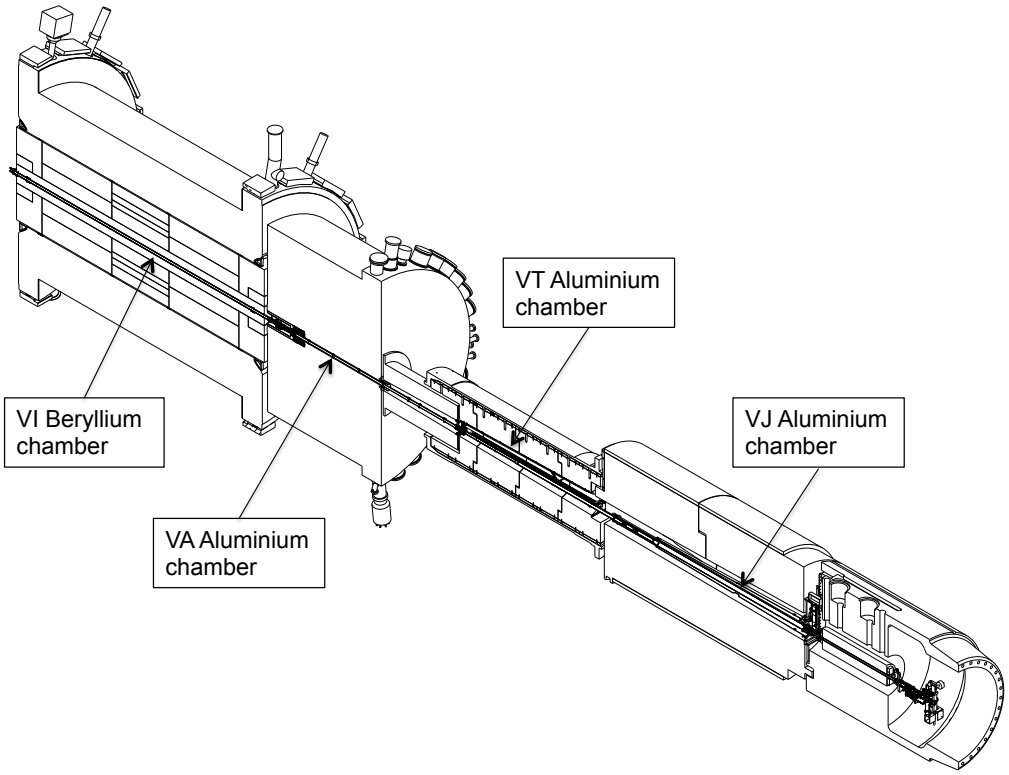

Figure 67. Pictorial view of the beam pipe sections in ATLAS

VIII.5 Beam-pipe

The ATLAS beam pipe consists of 7 vacuum chambers shown in Fig. 67. During LS1, all of these chambers have been replaced with new ones.

The central part, made of Beryllium, has been changed in order to match the smaller radius required for the addition of the IBL inside the Pixel detector. The six other chambers, originally made of stainless steel, have been replaced with Aluminium ones in order to minimise activation

and background during operation. Whether these vacuum chambers can continue to be used for Phase-II depends on various parameters:

- Depending on the aperture of the HL-LHC machine and on the design of the ITk inner layer, a new geometry for the central vacuum chamber, VI, may be specified and require replacement of the current VI beam-pipe.
- The beam-pipe inside the calorimeter (VA) should not be changed, except in the option where a LAr MiniFCal is installed. Indeed, the current position of the bellows is not compatible with the ATLAS specification for detector coverage for that scenario. A partial modification of the VA would therefore be mandatory.
- The outer part (VJ), ending at the TAS region, will still be suitable for ATLAS after LS3. Nevertheless, the on-going study, made at the request of CERN TE department, to move the VAX from the LHC tunnel side to the experiment side, would make it necessary to replace the two VJ chambers. Although this potential replacement is not under ATLAS responsibility, the consequences are significant for the opening scenario of the experiment and some forward shielding components may have to be modified or replaced.
- Finally, there is currently no option under consideration which would require that the beam-pipe inside the endcap toroids, the VT chamber, would need to be replaced.

The specifications for the possible new VI and VA beam-pipes need to be defined together with the detector systems (ITk and LAr respectively).

VIII.6 Installation common tools

During the original construction of ATLAS, TC was responsible for the mechanical installation of various components of each detector, in strong collaboration with the corresponding detector subsystem community. The sharing of responsibilities depends on the activities to be carried out in the cavern and on the availability of the most competent personnel. This policy will be pursued for the Phase-II upgrade through the main activities below.

Moreover, all the access platforms and scaffolding are part of the common tools. It is the responsibility of the Technical Support team to provide safe access tools to the detector sub-systems. Inside the Toroid area, all scaffolding is made of aluminium to minimise the weight of material to be carried to this particularly narrow environment. Regarding the number of activities that will run in parallel during LS3, the number of scaffolding requests is expected to be high and will have to be carefully included in the planning.

VIII.6.1 ITk mechanical installation

TC engineers coordinate the working group on the ITk mechanical installation. Several work packages have been defined that entail definition and development of the procedures, design, procurement and commissioning of the various installation tools: the lifting frame, the rotating table, the insertion cradle, the interfaces with Barrel Cryostat, and the support platforms. The manufacture of an accurate mock-up and the coordination of the training and rehearsal work are part of the work package definition. Figure 68 illustrates the ongoing study of the lowering sequence.

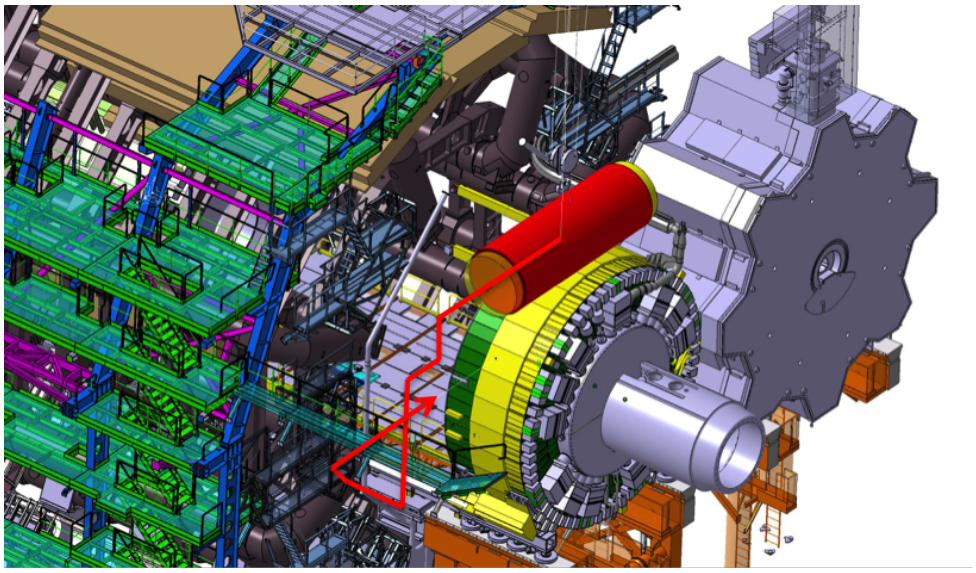

Figure 68. The lowering of such a large detector than ITk into the Toroid area will not be straightforward. Two options are currently considered for the lowering path of ITk, either from the top or from the side of the experiment. The red arrow in the picture above shows what the travel of ITk could be when it enters the Toroid area by the US15 side. Some specific temporary platforms (not shown here) will be designed to give access during the process..

VIII.6.2 Cryostat opening and closing

Whatever option is selected for the upgrade of the LAr end-cap calorimeters will require warming up and opening the endcap cryostat. In case the MiniFCal option is chosen, the installation operation mainly consists of replacing the Inner Warm Tube with a new one that supports the MiniFCal. A new cryogenics and detector service line has to be installed and a full cryogenics system has to be developed, in collaboration with CERN TE-CRG group, in order to supply the new cold vessel housing for the MiniFCal.

For the sFCal option, the extraction of the FCal requires opening the cold vessel of the cryostat. This is a challenging operation on a system which has been closed since 2004, more than 20 years earlier than the Phase-II upgrade. Some cutting of welds will be necessary on activated parts of the cryostat, adding complex safety issues to the technical concerns. The radiation dose budget is being assessed, in particular to define at which steps automated tooling or welding machines might be required.

ATLAS TC is leading the relevant engineering studies, including the risk analysis, in close collaboration with the LAr community.

VIII.6.3 Movement and installation of Barrel Muon chambers

The TC project office is responsible for the study of the mechanical installation of the new RPCs from the feasibility stage to the actual intervention on site. The responsibilities would include providing temporary access to the relevant working areas, the modification of any existing permanent gangways which might be in conflict with the new chambers, and the installation of tooling compatible with the geometry of every sector in the Barrel region. It is a huge project both before and during LS3 as the installation procedure is estimated to require about 2 years.

VIII.7 Point-1 Infrastructures

Point-1 infrastructure is one of the most significant “common tools” for the ATLAS experiment. As such it is under the supervision and the responsibility of TC.

The installation of new detectors for the Phase-II upgrade will entail new needs concerning electrical power supplies, cooling and ventilation capabilities, cabling, and rack cooling. Such improvements are not included in the maintenance program foreseen to prevent natural equipment obsolescence through the years.

Although the current status of the new or upgraded systems does not allow an exhaustive and detailed description of the impact on the common infrastructure, several items have been identified that require significant modifications.

VIII.7.1 Upgrade of electrical network

The electrical power distribution for both the normal 10 min UPS and Diesel backed-up UPS needs to be upgraded. The first improvement is required to support the new power supplies for ITk and more powerful ATCA crates for back-end electronics and triggering; the second improvement is required to support the new cooling systems for ITk.

For the 10 min UPS, the addition of a fourth 500kVA module to the three existing ones may be considered, although the procurement of this unit would have to be made while the modules of that type are still on the market. Making the upgrade on this earlier timescale (around LS2) would avoid the need for replacing the whole existing UPS system in SX1 with a new one, provided that the expected lifetime of the upgraded UPS would be sufficient for the completion of the HL-LHC programme.

For the diesel back-up generator in SDX1 that feeds main underground electronics cavern (USA15) equipment, a new UPS is foreseen, as it is no longer possible to upgrade the existing one, which is already 10 years old.

Moreover, the installation of the thermo-siphon cooling equipment during LS1 consumed all of the existing reserve capacity in the existing diesel supply. This situation is acceptable for Run 2 and Run 3, as there is not any new requirement foreseen. Nevertheless, the new UPS, to be installed in SDX1 during LS3, needs to have a more powerful diesel UPS and it is also expected that there may be additional requests, for instance for the detector services.

VIII.7.2 Upgrade of rack cooling

The Phase-II upgrade programme is dominated by the introduction of new off-detector electronics, which will use the latest technologies to increase the bandwidth and processing capabilities of these systems. In addition, the VME-based systems installed for Run 1 are now moving towards obsolescence. It is expected that, as part of the electronics upgrade for Phase-II, the current VME crates will be replaced with much more powerful ATCA shelves, to provide both the backplane bandwidths, processing interconnections, and higher power capabilities that will be required by the Phase-II electronics.

The cooling capabilities of the present rack systems are not optimal for use with ATCA shelves, and a more detailed evaluation is required to understand an upgrade path for these rack systems. Extensive studies and simulations are on-going to identify potential bottlenecks and airflow resistance sources. Mechanical improvements on the rack to optimise the cooling performance are also being considered.

Preliminary tests were carried out using vertical and horizontal air cooling and the results are now under evaluation, considering the pros and cons of both solutions. The augmented power dissipation of ATCA boards is likely to create cooling problems if the power dissipation per rack is within the range 10-15 kW. The procurement and installation of additional cooling on a non-negligible number of racks is therefore included in the Phase-II planning.

VIII.7.3 Cabling

Cabling activities are expected to be extremely demanding in LS3. A few systems require a very significant refurbishment of their services. Indeed the volume of cabling activities in LS3 is expected to be comparable to the activities during the initial construction and installation of ATLAS. Moreover, in some cases additional difficulties need to be faced, due to the presence of old cables that are impossible to remove from their current location. This will require evaluating new cable routing strategies, and the installation of new cable trays, in a very densely packed environment.

A preliminary list of cabling activities is given below:

- Removal of the existing ID cables and the later installation of new ITk cables.
- Replacement of LAr Front-End electronics and refurbishment of the cabling.
- Installation of new RPC chambers and corresponding installation of new cables.
- Installation of new cables and fibre optics for the read-out of the new Muon Trigger system.

Moreover, during LS1 it was seen that the cabling activities linked to many small activities on different sub-detectors were very substantial, and due to the complex working environment, the amount of manpower needed to perform this work was not negligible.

In LS3 a large cabling team with experienced coordination will be essential to perform this delicate work. The peak activity is expected to be in the second half of the long shutdown.

VIII.7.4 Cooling and ventilation

The cooling and ventilation plant for the ATLAS experiment is now able to provide about sixty thousand cubic meters per hour of cooled air in the UX15 cavern and it is believed that the cooling power is sufficient also for the running period after LS3. During the period prior to LS3, there are plans for a major upgrade in the controls of the cooling and ventilation plant, and standard maintenance of the full plant. The plant itself is believed to be able to remain operational for the full HL-LHC lifetime if properly maintained during the end-of-year technical stops. It is believed that no major upgrades are needed to the majority of the pumps and motors. Nevertheless, already now there are concerns about the temperature gradients present in the cavern. In particular the higher sectors of the RPC system are exposed to a temperature higher than the desired one, and continuous efforts are made during long shut downs to mitigate this problem. It is therefore mandatory to make new engineering studies on the cold air distribution in the experimental cavern in order to be ready to improve it during LS3. In particular a large redefinition of the air ducts is foreseen. The cooling power for USA15 on the other hand may need to be increased to cope with the larger power demands from the detector read-out and electronics. At present the operational margin is about 20%, which may not be sufficient to cope with the requests after LS3.

VIII.7.5 Network and software

To support the necessary increase of computing and networking capabilities required by the trigger and DAQ systems, two interventions may be needed. First, SDX1 may require consolidation of the floor as well as enhancement of the electrical power distribution network to support more computing racks. Second, civil engineering work may be required to provide services (power, network connectivity and cooling water) to an area where pre-built computing containers would be installed.

VIII.7.6 DCS

New network infrastructure (switches, routers and cables) would need to be purchased, installed and cabled to separate the DCS network from the standard ATLAS control network, and to enhance the availability and stability of the DCS system.

All of the centrally managed ELMB installed in the cavern and counting rooms, for detector control and monitoring, are planned to be replaced with the upgraded ELMB (ELMB++) devices, designed to comply with the enhanced requirements of the LHC upgrade phases (e.g. providing improved radiation tolerance).

VIII.8 Assembly buildings and storage space

The assessment of the surface facilities that are required to perform the integration of the various systems at CERN is still on-going. However, it is already known that the space currently allocated to ATLAS in various buildings on the Meyrin site and at Point-1 will not match the requirements for Phase-I and Phase-II (there are some significant overlaps).

VIII.8.1 Assembly and integration

Building 2175 (SR1) was used for the integration of the present ID, and is planned to be used for the integration of the ITk. The clean environment and most of the service infrastructure are already available. However some space needs to be kept during the full lifetime of the current ID to provide work areas in case un-expected and urgent work might be needed. The full space in this building cannot be allocated for ITk integration. An extension of the building is being considered and several options are under study. This extension needs to be equipped with services suitable to perform the full commissioning of the ITk detector on the surface, in particular significant upgrades of the cooling and gas systems are foreseen.

The clean room in Building 180 is planned to be assigned to either Pixels or Strips for integration activities. In either case, a significant refurbishment of this building will be required, including the improvement of ventilation and lighting, the installation of new racks, plus a new cooling system and a new gas system.

In parallel, the assembly hall in Building 180 needs to be organised for preparatory work on detector installation and procedure rehearsal. Several mock-ups are planned to be installed there at the beginning of the upgrade project to anticipate problems and optimise the procedures according to the ALARA concept. Among them:

- A dummy Barrel cryostat inner bore to provide the possibility of exercising the ITk installation, including services installation,
- A mechanical mock-up of the endcap calorimeter for the commissioning of the extraction and insertion tooling of the Forward calorimeter,

- A mock-up of the environment surrounding some of the Barrel Inner Muon chambers may be built to practise the insertion of new RPCs or the replacement of on-detector muon electronics.

VIII.8.2 Workshop

As far as mechanics is concerned, all these activities of prototyping require a very effective and flexible workshop. Indeed, tooling commissioning and procedure optimisation imply adjustment and modifications that can be requested at short notice. In this context, the close collaboration between ATLAS TC and the PH-DT group in the mechanical workshop of building 108 is of utmost importance.

Nevertheless, many of the machines are old (some are inherited from LEP experiments) and quite difficult to keep maintained and in conformity with safety regulations. To keep the workshop at an acceptable level of performance over the next 10 years requires a steady investment in equipment.

VIII.8.3 Storage

During ATLAS construction and installation, a large number of dedicated tools have been developed for several purposes: system integration and installation in the experimental cavern, but also supports for test beam and cold test for the LAr calorimeter. The tent B609 has been built at the beginning of the 2000s to store all this equipment. Since that time, many other items of tooling and specialised equipment have been developed and manufactured to improve the opening and closing process, as well as the access to detectors. Storage of all this critical tooling has become a challenging issue. Since the end of LS1, a campaign of re-organisation of the storage building (B609) is progressing. Despite this action, and the effort to throw away what is no longer needed, the need for a second storage location, preferably at Point-1, is more and more evident. A solution is still to be invited and proposed, but the additional equipment that is foreseen to be manufactured and used during LS3 will certainly require a new storage location.

VIII.9 Cost Estimates

In this section the total CORE cost of the installation and Technical Coordination activities related to the Phase-II upgrade is presented. In the CORE costs, all the upgrade-related activities explained earlier are included, on the other hand the costs associated with standard M&O A activities are not included, as for example opening/closing of the ATLAS detector or costs associated with additional shielding to be placed on top of the shafts. Also, the costs associated with the enlargements of experimental areas and buildings (e.g. SR1) are considered to be a host lab responsibility and not counted in the CORE table.

The main CORE cost drivers are the common infrastructure, which includes the upgrade of the electrical power distribution, cooling and ventilation (including the primary source for the detector cooling), technical network infrastructure, and access infrastructure. The safety cost estimate is of primary importance for the augmented risks due to the radiological hazards occurring during LS3 and beyond. The largest part of the cost estimates for this area are devoted to the development and production of remote handling equipment. The costs of additional manpower needed during LS3 are also important, and they are mainly linked to the installation of the new muon read-out electronics and chambers, to the decommissioning of the present ID, and to the large amount of cabling that will be required for the new detectors. The costs of new beam-pipes for ITk, and for the LAr sections (VI

and VA), are also considered to be part of the CORE costs. Overall, a total cost for the Reference detector scenario of 17.4 MCHF is foreseen for the common (infrastructural) activities as show in Table 24, corresponding to 6.4% of the total cost of the Reference detector.

Table 24. CORE Cost estimates of the Common Items to Level-2 in the WBS structure for the three scoping scenarios.

WBS	Item	Reference Total Cost [kCHF]	Middle Differential Cost [kCHF]	Low Differential Cost [kCHF]
7.	**Integration & Installation**	**17,417**	**-1,557**	**-2,977**
7.1	ATLAS Opening/closing	405	-	-
7.2	Safety	3,505	-	-
7.3	Muon spectrometer	1,900	-480	-1,900
7.4	Common Infrastructure	7,768	-	-
7.5	ITk	425	-	-
7.6	LAr sFCal	1,767	-1,767	-1,767
7.7	LAr MiniFCal	-	+429	+429
7.8	Forward Detector	120	-	-
7.9	ID Decommissioning	560	-	-
7.11	Beam-pipes	967	+261	+261

Chapter IX

Summary of Cost and Schedule

This chapter provides a summary of the overall CORE cost for the Phase-II upgrade, as well as the top-level milestones, and the required profile of funding needed to meet the schedule goals of the Phase-II upgrade project. The inputs to these top-level summaries are presented in the preceding chapters on the individual components of the upgrade.

The chapter contains brief overviews of the methods used to estimate the approximate total CORE project cost, the required manpower, the schedules for the individual components, and the required funding profile. It provides a high-level summary of the information, while the detailed information necessary for a meaningful review will be provided separately to the LHCC and UCG, in the form of multi-tab spreadsheets for each of the upgrade systems described in Chapters III–VIII (detailed information for the Forward system is not provided). The detailed cost information is provided separately for each scenario, although much of it is very similar for the different scenarios. In general, rigorous cost estimates are not possible before the TDR stage of each project, because many of the design details, or in some cases even different technical options, have not been finalised. In addition, there is no detailed assignment of which institute is responsible for each task, which means that only coarse manpower planning can be carried out. In the cost and manpower estimates given here, only approximate details of the production strategy are known, and rather generic models must be used, rather than site-specific and funding-agency specific estimates that will be made as part of the Technical Design Report (TDR) and the subsequent Memorandum Of Understanding (MOU) process.

IX.1 CORE Project Costs for each Scenario

The CORE costs for the Phase-II upgrade are estimated in 2014 CHF (averaging over the calendar year), but to the extent that it is feasible at this stage of the project, all costs are estimated in their local currencies. Then, they are converted to the reference CHF using scale factors which can be rapidly modified to allow updated cost projections accounting for changes in inflation and exchange rates across the relevant currencies. For the Scoping Document, they have been frozen to the values: USD/CHF = 0.92, EUR/CHF = 1.21, YEN/CHF = 0.0087, matching our 2014 assumption. The CORE cost also includes the so-called “module-0” components. These are pre-production components, produced using the final production tooling and manpower, which are required to meet the specifications and to provide the functionality necessary to be installed into the experiment. However, it does not include the cost for generic infrastructure, R&D programs, spare components, or prototypes with partial functionality. The costing period only begins once the relevant TDRs have been approved and the Memoranda Of Understanding have been signed by the relevant responsible individuals. In addition, although the CORE cost itself does not contain any contingency, our cost estimate does contain “quality flags”, which identify the type of information used as the basis of the estimate. Here, we follow a widely used convention with five different quality levels. The lowest level of uncertainty (1) corresponds to items with recent vendor quotes or standard prices, the next level of uncertainty (2) represents estimates based on recent purchases of similar components, the third level of uncertainty (3) represents an engineering design where all of the sub-components are known, the next level of uncertainty (4) is based on estimates from a conceptual design or scaled from a similar system, while the final, lowest quality estimate, is based on a rough estimate without any detailed design. This allows explorations of the robustness of the overall cost based on the fractions of that cost which are associated with different quality flags. In general, the CORE methodology treats essentially all deliverables as “in-kind” contributions, where the CORE value is intended to provide a universal metric for comparing contributions across funding agencies. The real costs will in general include components that are dependent on geographical and local economic issues, and each funding agency, working with the physicists they support, must establish this real cost for their

in-kind contributions, along with some reasonable estimate of the uncertainty or contingency the funding agency might require to provide their deliverables under a reasonable range of assumptions about cost risks. This methodology provides a framework for the 44 funding agencies of ATLAS to support construction of the Phase-II upgrade, which proved to be successful for managing the initial construction of the ATLAS detector.

The cost estimates here are based on a preliminary WBS for each project, which is expected to evolve as the designs mature and the project moves into the TDR phase.

Table 25 represents the top-level summary of the CORE costs in the Reference scenario for each detector system upgrade. The WBS organisation has been expanded to Level-2 so that the individual large sub-components are visible. The table also includes the differential costs for the Middle and Low scenarios. The relative contributions of each of the major detector system upgrades to the total ATLAS CORE costs are shown in Fig. 69.

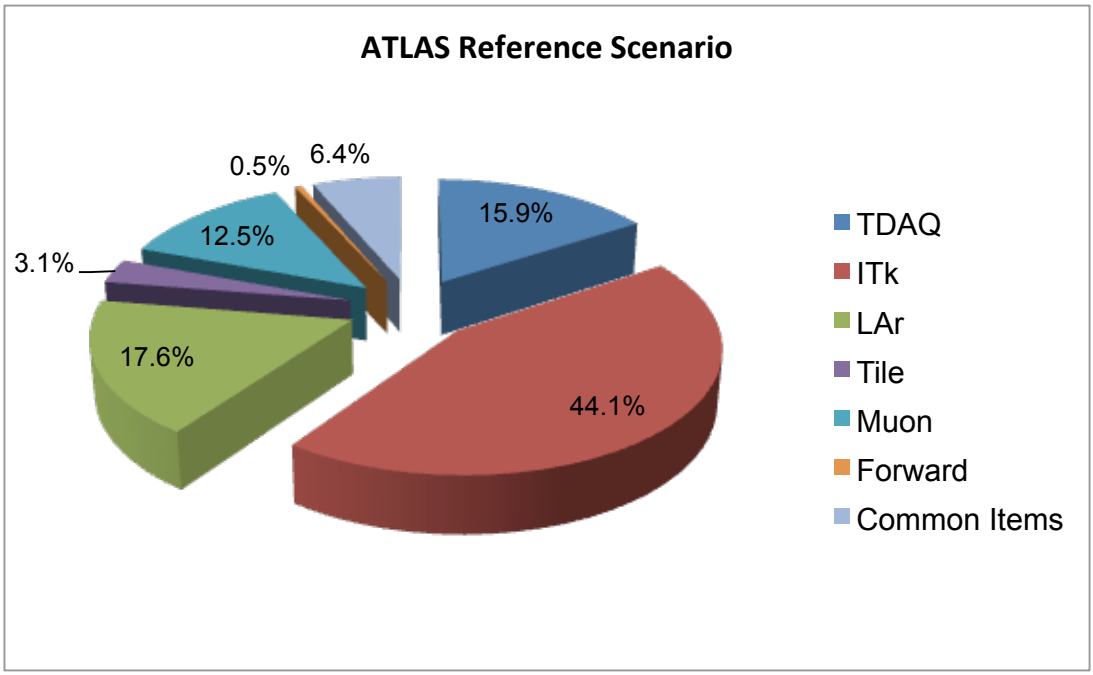

Figure 69. The relative contributions of each of the major detector system upgrades to the total ATLAS CORE costs (as a fraction of the total ATLAS upgrade cost) in the Reference scenario.

IX.2 Required Manpower

Manpower estimates are divided into several different categories: “academic” (e.g. physicists), “engineers” (mechanical, electrical, and software), and “technical manpower” (mainly technicians) Costs for many of these labor categories depend on location. Work in the early stages of the Phase-II projects will be done mainly at the relevant ATLAS institutes. However, later work involving integration, is often performed at larger institutes with shared manpower, which is generally more expensive. Final integration and subsequent installation is performed at CERN with attendant dislocation costs for institute personnel who travel to the lab. With the present very preliminary model for how and where different components may be produced, only rather generic assumptions are made. Estimates of the manpower required in each category were performed by the individual projects,

Table 25. Top-level summary of the CORE cost estimates for the Phase-II ATLAS upgrades by detector subsystems (expanded to Level-2 in the WBS).

WBS	Detector system	Reference Detector Total Cost [MCHF]	Middle Scenario Differential Cost [MHCF]	Low Scenario Differential Cost [MCHF]
	ATLAS	**271.04**	**-42.55**	**-71.16**
1.	TDAQ	43.31	-11.41	-18.19
1.1	L0 Central Trigger	1.21	-	-
1.2	L0 Calorimeter Trigger	0.70	-	-0.24
1.3	L0 End-cap Muon	2.56	-0.11	-0.11
1.4	L0 Barrel Muon	1.32	-0.14	-0.17
1.5	L1 Central Trigger	1.93	-	-
1.6	L1 Global Trigger	3.39	-	-
1.7	L1 Track	4.19	-0.67	-2.49
1.8	FTK++	13.03	-4.88	-9.56
1.9	DAQ/Event Filter	14.98	-5.62	-5.62
2.	ITk	120.36	-7.2	-23.6
2.1	Pixel	32.19	-0.9	-4.8
2.2	Strip	72.10	-6.3	-18.8
2.3	Common Items	16.08	-	-
3.	LAr	45.98	-13.60	-13.60
3.1	Read-out electronics	31.39	-	-
3.2	sFCal	10.03	-10.03	-10.03
3.3	HGTD	4.56	-4.56	-4.56
3.4	LAr MiniFCal		*+0.91*	
3.5	Si-based MiniFCal		*+3.57*	
4.	Tile	8.58	-	-
5.	Muon	34.08	-8.78	-12.79
5.1	MDT	7.69	-2.07	-3.16
5.2	RPC	7.99	-2.32	-4.79
5.3	TGC	4.44	-	-
5.4	High-Eta Tagger	3.50	-3.50	-3.50
5.5	Power System	10.47	-0.89	-1.34
6.	Forward	1.30	-	-
7.	Integration & Installation	17.42	-1.56	-2.98

correcting for the overlap period where both the Phase-I and the Phase-II upgrades will be active. The required manpower is tabulated in FTE-years.

Finally, each project also carried out an estimate of the available manpower in their communities, working through the individual Institute Boards for the projects. A cross-check has been established, as part of the construction of the "money matrix", by discussing with all of the National Contact Physicists to assess the available manpower for each upgrade project in each national community. These estimates are very preliminary, and in many cases the national communities are still early in their planning process for their detailed roles in the Phase-II upgrade programme. This process has been very useful, and will continue as commitments develop during the TDR preparation period, however it is still too early to reach any global conclusions as to whether the available manpower matches the required manpower throughout the Phase-II upgrade projects. Detailed information on the required manpower has been provided in the confidential spreadsheets delivered to the LHCC/UCG.

IX.3 Schedule and Milestones

The majority of the schedule is identical for each scenario. For this reason, the milestone figures included in this document generally refer to the Reference scenario. The major milestones in each project of the upgrade generally show the progression of the different components of the project through the basic stages of design, prototyping, pre-production leading to the module-0 prototypes which contain all of the functionality required to be installed in the experiment, series production, assembly and integration, and finally installation and commissioning. This process only starts once a given project has passed through the Initial Design Review (IDR) and Technical Design Report (TDR) stages, and the MOU agreements with each funding agency have been signed, making the necessary resources available to each project. This process is described in more detail in Chapter X. Once the project is defined and reviewed, then the design process for each component proceeds, following the standard sequence of steps through to the finalisation of each component design. The standard milestones for every major component include a Preliminary Design Review (PDR), when the design has reached a level of maturity where first complete prototypes could be built based on the preliminary design. After enough prototypes have been built to arrive at a design which meets all of the requirements for production (a first ‘’module-0" prototype), then a Final Design Review (FDR) is organised. The PDR and FDR are fundamentally technical reviews. Once a component has passed the FDR stage, preparations for the series production need to be carried out, including qualification of multiple production sites to produce components that meet specifications. This process includes the organisation of all the necessary equipment and technical manpower, as well as planning documentation. Once this process is complete, and the different sites are ready to begin series production, the Production Readiness Review (PRR) is carried out, and must be successfully completed before series production of components begins. Further, more specialised, reviews may be inserted into this sequence as needed, but these three standardised reviews represent the major milestones used to track the progress of the components of the project, and are therefore tracked in all of the milestone/schedule figures in the present document.

A Gantt-like chart with the most important milestones and tasks for each of the ATLAS Phase-II upgrade projects is shown in Fig. 70.

IX.4 Required Funding Profile

Each project has developed a detailed schedule for the pre-production, production, and integration phases. This is combined with the cost estimate, to give a spending profile for each project. These profiles are then combined to give the overall funding profile for the Phase-II upgrade, as shown in

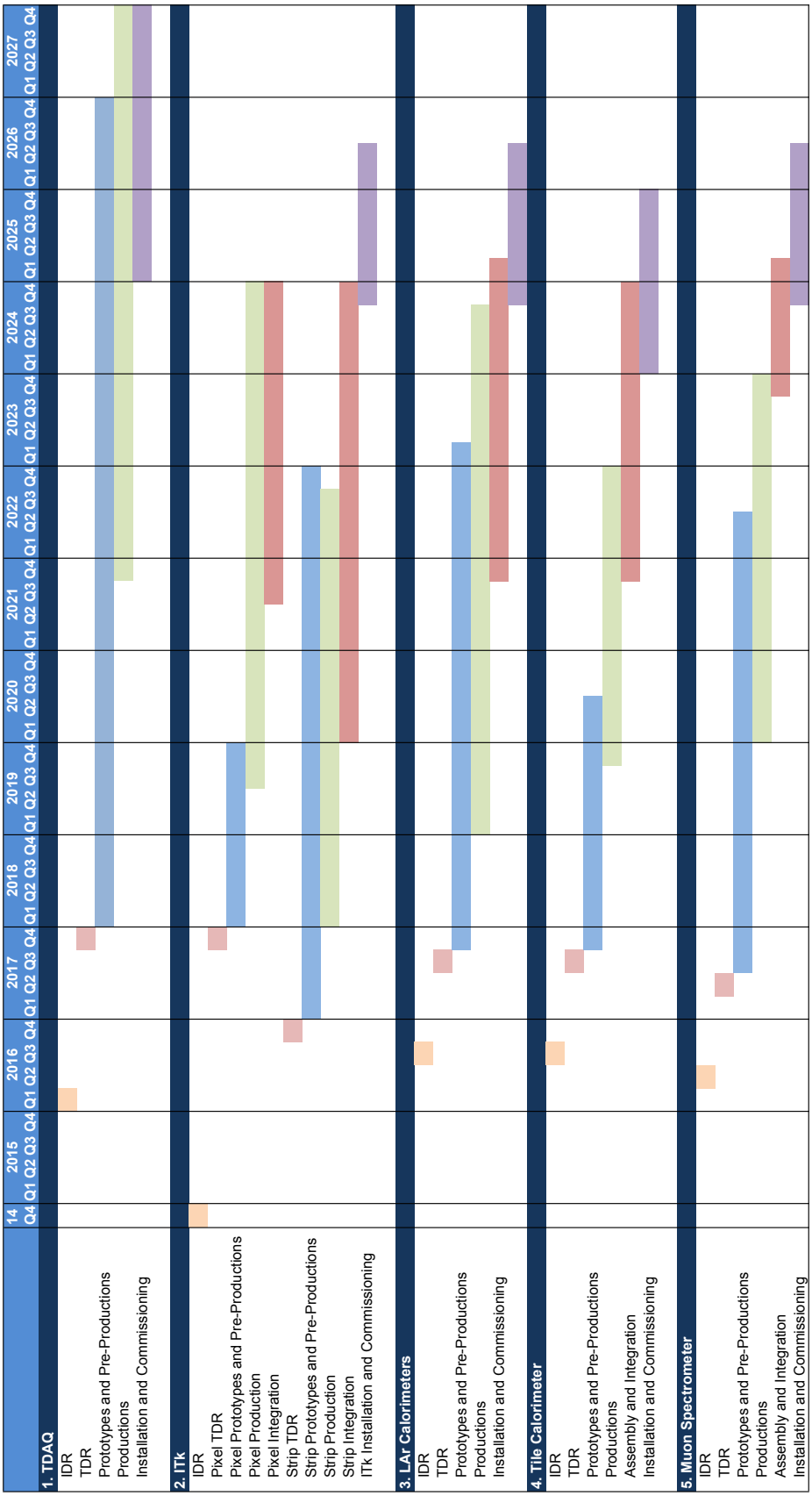

Figure 70. Top-level summary of the milestones and time-line of the ATLAS Phase-II upgrade projects.

Fig. 71 for the Reference scenario. This profile is initially dominated by the need to rapidly make large procurements for the ITk Strip project once the corresponding TDR has been approved, in order to begin the complex module production, which is followed by the similar process for the ITk Pixel project. The LAr and Muon projects then begin to ramp up as the large-scale spending for the ITk slowly ramps down. For the TDAQ upgrade, spending increases toward the end of the construction period to allow its largely commodity electronics to be purchased as late as possible, taking maximum advantage of cost savings and performance gains from industry.

At the time of the TDR for each sub-system, the individual project profiles will be understood in greater detail, and reviewed to optimise the distribution of the required resources, wherever this is possible without major perturbations in the overall schedule.

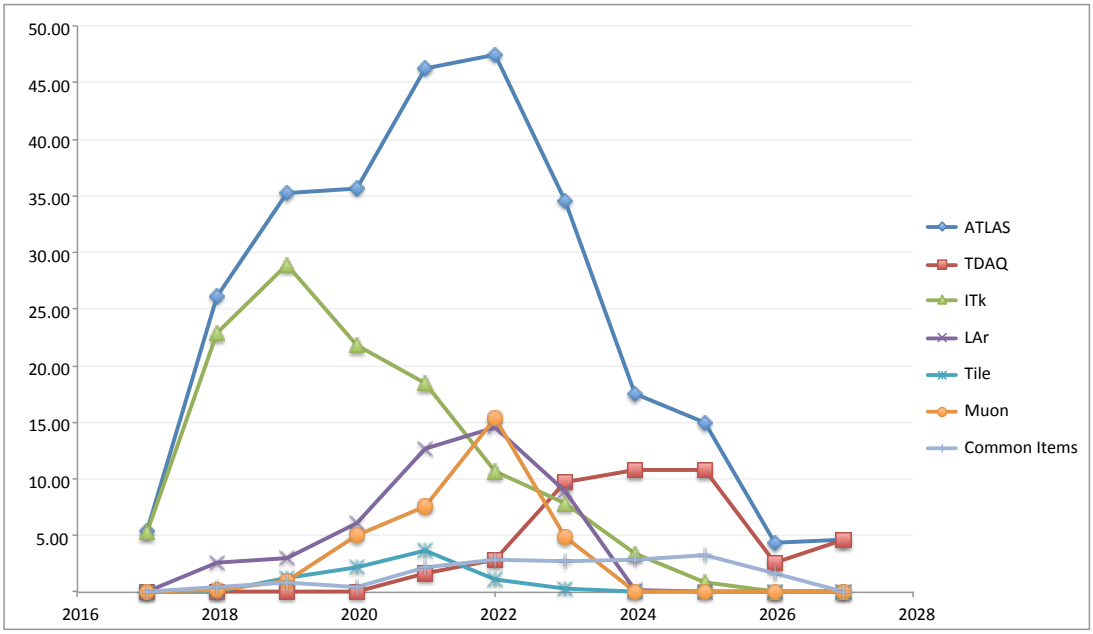

Figure 71. Spending profile of the detector systems and of the overall ATLAS upgrade in the Reference scenario.

Chapter X

Project Management Plan

X.1 Project Organisation

A simplified view of the ATLAS Upgrade organisation is provided in the organisation chart in Fig. 72. The upgrade activities and overall strategies are coordinated by the Upgrade Coordinator (Upgreade Coordinator), who is elected by the Collaboration Board with a renewable two-year appointment. The Upgrade Coordinator is a member of the Executive Board (EB), and participates in ATLAS management meetings with the Spokesperson, the Deputy Spokespersons, Technical Coordinator and Resource Coordinator as required by the Spokesperson. The Upgrade Coordinator chairs the Upgrade Steering Committee (USC), the committee which is formally responsible for the oversight of the entire Upgrade programme. The USC operates in close collaboration with the Technical Coordinator (TC) and the TC Project Office, which links to the technical coordination and operation of the entire experiment. Members of the USC at the time of writing include the ATLAS management team, the Detector sub-system Project Leaders (PLs), the Upgrade Project Leaders (UPLs) for the Phase-I and Phase-II projects (only the ITk Phase-II project has reached the stage where it has a formal PL), as well as members of the Upgrade Project Office, the Upgrade Physics Conveners and the Upgrade Software Coordinators, the Electronics Coordinator, Computing Coordinator, and Physics Coordinator, plus chairs of any Task-forces and/or Sub-committees appointed by the Upgrade Coordinator to resolve or oversee specific upgrade-related issues and activities.

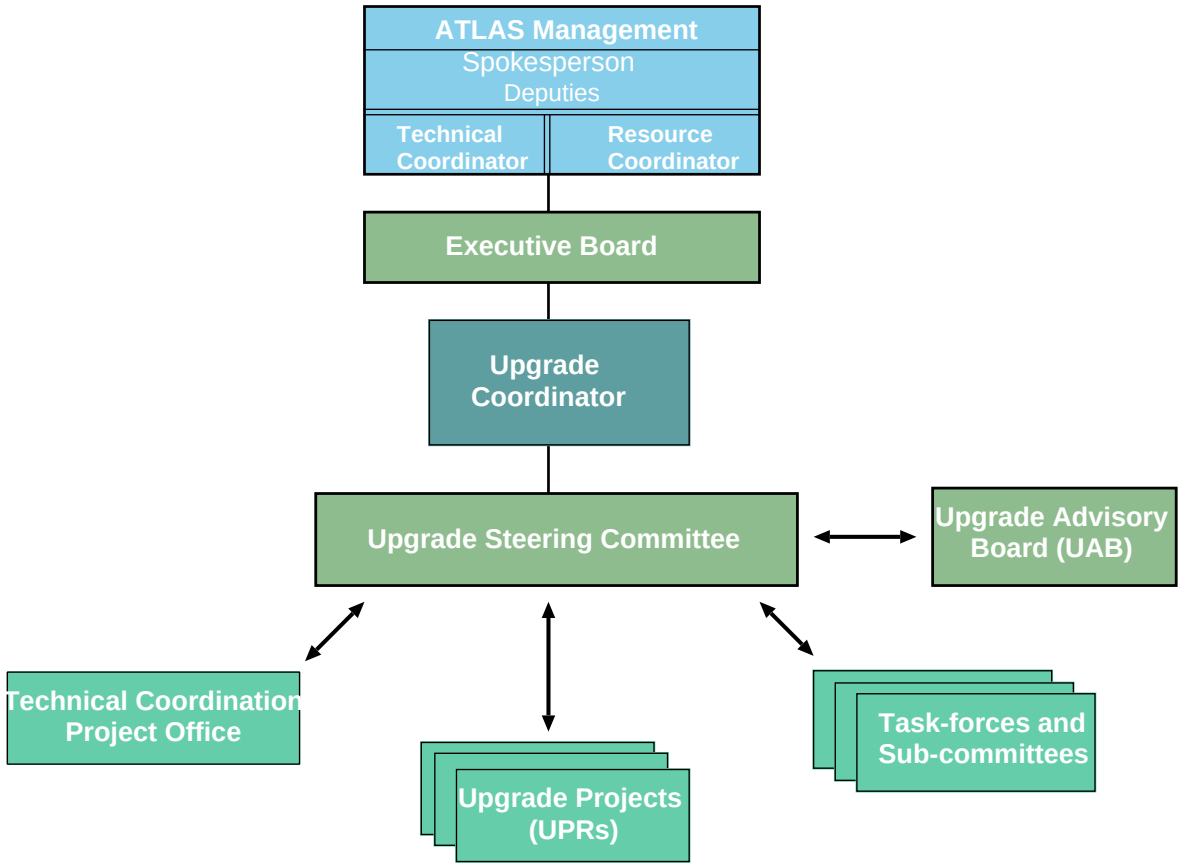

Figure 72. A schematic view of the ATLAS Upgrade organisation.

X.2 Project Phases

Each major component of the Phase-II upgrade starts as an R&D project inside the relevant system in ATLAS. The project then proceeds through a sequence of steps, which are indicated schematically in Fig. 73. Once the R&D project reaches an appropriately mature state, the community prepares a comprehensive document describing the project, and undergoes an Initial Design Review (IDR). This review should verify that the overall performance and technical requirements for the Upgrade PRoject (UPR) are clearly defined and that the initial design, as described in the documents that constitute the UPR proposal, is technically sound and corresponds to the requirements. It also examines the initial cost estimate, preliminary schedule and milestones up to and including the writing of a Technical Design Report (TDR).

The ATLAS Phase-II UPRs include the inner tracker (ITk) system, the LAr system, the TileCal system, the Muon system, and the Trigger and Data Acquisition (TDAQ) system. All of these systems, with the exception of the ITk, are formally embedded in the existing system organisations for the present ATLAS detector. The ITk is sufficiently different from the existing Inner Detector that a new system has been started for this project.

After a given UPR passes the IDR review, all interested institutes participate in a kick-off meeting, where they can express their interest in different aspects of the UPR. After this process has been completed, and an appropriate level of interest demonstrated, the Upgrade Coordinator brings the project to the ATLAS EB for approval. Finally, the ATLAS management and the Upgrade Coordinator bring the project to the Collaboration Board for endorsement. At the time of writing, only the ITk project has passed through this process, which formalises the existence of an Institute Board (IB) (the ITk IB currently consists of 94 institutions - more than 50% of the total set of ATLAS institutions), and the appointment of an UPL. During 2016, all of the remaining Phase-II projects are expected to pass through this process, with the exception of the Forward project. Note that at the time of the IDR, many of the projects are still evaluating several options in order to develop optimal solutions for meeting all the necessary requirements. In almost all cases, these options will be reviewed and reduced to a single baseline by the time of the TDR.

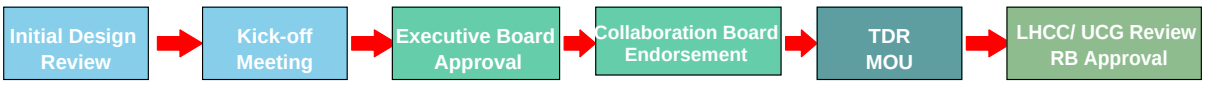

Figure 73. The internal ATLAS approval sequence of an Upgrade PRoject (UPR).

The present schedules for the IDR process for the remaining projects are the following: the TDAQ upgrade is scheduled to go through its IDR during Q1 2016, while the Muon upgrade will go through its IDR in Q2 2016, and the LAr and Tile upgrades will go through their IDRs in Q3 2016, thereby completing the transition of all of the elements of the Phase-II upgrade to the formal project level by the end of 2016 (again with the exception of the Forward project).

The detailed time-lines for each of the project TDRs have also been tentatively defined, although the IDR process provides an opportunity to revisit the proposed TDR schedules. In general, each project is expected to have a single TDR. In the current planning, the last of the TDRs would be submitted for review by the end of 2017. The only exception to the convention of one TDR per project arises for the ITk. In this case, an initial TDR for the Strip tracker, which will provide a detailed view of the Strip tracker design, and the associated mechanics, services, and infrastructure, while also providing a less detailed overview of the other components of the project, will be written first. This will be followed approximately one year later by a TDR for the Pixel tracker, which will also provide a coherent update on any changes which have taken place in the other parts of the project. This

two-step process is tailored to the long production time for the Strip tracker due to its very large area, which requires that it pass through the TDR process, followed by the formal interim MOU (iMOU) agreements necessary to spend construction money, at the earliest possible date (presently estimated to be during the first half of 2017). Since the Pixel tracker has a shorter construction time, it benefits significantly from additional time for finalising R&D, which also leads to a later date for the TDR. In addition to these two ITk TDRs, a related document is being prepared, which will discuss in detail the decommissioning and removal of the present Inner Detector. This will be a very complex process, involving a large number of services in activated regions which must be carefully removed, to prepare the way for the ITk installation. This document on ID decommissioning is expected to be ready on the timescale of the Pixel TDR.

The current dates for the TDRs are the following: the first TDR is the ITk Strip TDR, which is targeted for Q4 2016. Following this, the Muon TDR is targeted for Q2 2017, then the LAr and TileCal TDRs are targeted for Q3 2017, followed by the ITk Pixel and the TDAQ TDRs which are targeted for Q4 2017. It is anticipated that the planning of common items and infrastructure will be documented in a series of reports rather than a single TDR at a specific time. Past experience suggests that the sequence of TDRs defined above would allow the preparation and approval of all of the MOU needed for construction on a timescale of mid-2018.

Table 26 summarises the schedule for the IDRs, and for the submission dates for the TDRs, for each of the Phase-II UPRs.

Table 26. IDR and TDR schedule of the ATLAS Phase-II UPRs

Upgrade PRoject (UPR)	IDR	TDR
ITk-Strip	Q4 2014	Q4 2016
ITk-Pixel		Q4 2017
LAr	Q3 2016	Q3 2017
TileCal	Q3 2016	Q3 2017
Muon	Q2 2016	Q2 2017
TDAQ	Q1-2016	Q4 2017

X.3 Review Strategy

The management of a large and complex project like the ATLAS Phase-II upgrade requires a wide variety of tools to monitor the progress and ensure that all of the components are on schedule, have an acceptable cost, and meet the complex requirements defined during the TDR process. The monitoring of all aspects of the project progress is done using a variety of expert reviews, accompanied by rather detailed documentation. All reviews (except the internal project reviews), report to the USC, and then through the Upgrade Coordinator to the EB, in order to monitor progress and track problems.

X.3.1 Internal Reviews

As a given project begins to finalise many details of its technical design, the project leader of that project often organises internal reviews to assist the decision making and evaluation process. Generally the Upgrade Coordinator and a few outside experts are invited to attend these reviews to monitor the progress, and ensure coherence with global requirements across projects.

X.3.2 Review Office Reviews

Inside the Technical Coordination organisation in ATLAS, there is a formal review office, jointly chaired by an engineer and a physicist. This office organises reviews of all of the upgrade projects. Most of the reviews take place after the completion of the TDR process, but for a complex project such as ITk, it is also useful to take advantage of the wide-ranging expertise of the Review Office, which draws on a large pool of engineers and technically-oriented physicists to carry out its reviews, to assist with critical decisions during the TDR process as well.

For the post-TDR reviews, most of them fit the standardised template of the initial technical reviews (PDR and FDR), as well as the more complex production reviews (PRR). With the scale of the Phase-I and Phase-II projects, it has also proved useful to insert additional review steps into the process, for example a Specification Review prior to the PDR, in order to ensure that the basis for the preliminary design is well-defined and coherent with the project goals. For complex ASIC submissions involving multiple chips which must work closely together, and small-feature size processes with very high NRE costs for masks, a pre-submission review is often useful to go through last minute developments before launching the very expensive fabrication. Finally, given the multi-year production schedules for the large upgrade projects, it will be useful to organise Production Advancement Reviews (PARs) to monitor the progress of the production and avoid unpleasant schedule or technical surprises. All of these reviews involve formal reports, which are signed off by the review committee, Review Office management, and the Upgrade Coordinator, and then are stored in the Engineering & Equipment Data Management Service (EDMS) [73]

X.3.3 Strategic Upgrade Reviews

For the Phase-II upgrade, there are some complex decisions to be made where a combination of performance and physics assessments must be combined with the usual technical criteria for a given conceptual design (or designs) in order to reach an optimal decision. In this case, the Upgrade Coordinator, in consultation with the Review Office and the Technical Coordinator, puts together a review committee with the full range of necessary expertise to reach a decision. Examples which are already foreseen for the Phase-II upgrade include the decision on the final ITk layout, and in particular the balance between the number of space-points required in the region with $|\eta| < 2.7$ versus the extent of a very-forward extension which potentially has complex impacts on end-cap and forward calorimetry. A second example will be the decision whether or not to proceed with an sFCal, which involves balancing technical risks associated with the removal of the current FCal and installation of a new sFCal, versus the performance and physics advantages of an sFCal with greater radiation tolerance and finer segmentation. The report from such a review requires USC approval, and will be presented by the Upgrade Coordinator to the EB for endorsement.

X.3.4 IDR Process

The Initial Design Review (IDR) process, which is used to assess the initial design for feasibility, performance, and evaluate whether it meets the requirements in the overall context of the Phase-II upgrade program, has already been discussed earlier in this chapter. This process is organised jointly by the Technical Coordinator and the Upgrade Coordinator. A broad-based review committee is appointed to review the documentation for the initial design and performance of the project, and undertake detailed follow-up discussions with the community involved. This process typically takes place over a period of several months, culminating in a one-day formal review with presentations, and followed by a written report with recommendations and action items. Periodic updates are provided to the USC, which then is asked to approve the report of the review team. This report is

then also brought by the Upgrade Coordinator to the EB for approval, following the process outlined in the previous section.

In addition to these formal reviews of the components of each project, the overall status of all UPR is tracked through formal reports by the UPL to the monthly USC meetings, using a series of milestones. Discussions are just beginning in order to develop internal procedures across the different Phase-II UPR to provide a more comprehensive process for monitoring technical progress at the level of deliverables, and in close collaboration with the relevant management organisations inside the national communities, to track the corresponding financial status of each of the UPR.

Chapter XI

Performance and Physics

XI.1 Introduction

The physics programme for the HL-LHC includes comprehensive measurements of the Higgs boson properties in all its production and decay modes, as well as improved measurements of all relevant Standard Model processes and parameters including the study of rare Standard Model processes, and searches for phenomena beyond the Standard Model. The physics potential of each of the three detector scenarios is assessed by first studying the performance for a range of physics objects using fully simulated Monte Carlo events. Trigger and identification efficiencies, and the resolution for reconstructed object properties are then parametrised as simple functions which can be applied to the truth level particles in generated events of interest. In addition, jets from pile-up events are overlaid on the hard-scatter events. In this chapter, the performance studies are described first, followed by a discussion of the physics studies.

XI.2 Physics object performance

The performance of the three scoping scenarios for physics objects is assessed using fully simulated events from a number of Standard Model processes, including $Z \to \ell\ell$, $t\bar{t}$, and vector-boson fusion production of Higgs bosons with $H \to \gamma\gamma$. Minimum-bias pile-up events are overlaid on these hard-scatter events of interest. For example, for an instantaneous luminosity of $\mathcal{L} \simeq 7.5 \times 10^{34}\text{cm}^{-2}\text{s}^{-1}$, a value for the average pile-up, μ, is selected for each event from a uniform distribution in the range 190 to 210. The number of minimum-bias events to be superimposed is then sampled from a Poisson distribution with mean μ. The signals from interactions in previous bunch crossings are also added, using the same average μ. This is particularly important to model correctly the calorimeter response.

Samples are produced to allow the three different inner tracker geometries, corresponding to each of the scoping scenarios, to be studied. Full simulations of the LoI and LoI-VF ITk layouts described in Chapter IV are embedded in the Run 1 calorimeter and muon systems, and the simulated events are used to perform studies of the detector response. For the Middle and Low scenarios, hits in the ITk layers which are removed in the Middle and Low scoping scenarios are ignored in the track reconstruction. The reduced η-coverage in these scenarios is emulated by only using objects within the relevant geometrical region. Robustness studies are performed for each scenario, where an additional randomly selected 10% of the tracker modules are assumed to be inoperable.

Further studies of stand-alone muon performance are carried out using simulated data samples with the ATLAS Run 2 geometry where targeted modifications are made to emulate the different scoping scenarios.

The rate of pile-up jets is also assessed in fully simulated events. The “track confirmation” algorithm described in Section XI.2.7 is then used to identify jets from the hard-scatter process and reject jets which are associated with pile-up interaction vertices in the η-regions where track information can be used to link jets with the primary vertex.

The samples described so far are used for almost all of the performance studies described below, and do not account for the additional benefit of the the sFCal or HGTD detectors for the Reference scenario. The impact of the upgraded sFCal is estimated using dedicated fully simulated samples with the LoI tracker to give realistic material in front of the calorimeter, and where the Run 1 FCal is replaced with the sFCal. The performance of the HGTD for the Reference scenario is evaluated in a semi-analytic way.

The results of these studies, together with the trigger performance, are parametrised as simple functions which can be applied to generator level events for a range of physics processes. The impact of the sFCal and HGTD detectors are not included. These functions provide efficiencies, fake rates, and smearing of transverse energy or momentum and track impact parameters. They

also allow pile-up jets to be overlaid on other hard-scatter processes event-by-event.

XI.2.1 Trigger

Differences between the three scoping scenarios have a major impact on the trigger thresholds and efficiencies across the spectrum of physics objects. The potential improvements to the inner layer of the muon barrel have a direct effect on the muon trigger efficiency in terms of geometric coverage. The restrictions on trigger rates at each level, and the availability of track trigger information from L1Track and/or FTK++, also feed through to trigger thresholds, and the allowable rate of many trigger signatures, including tau, b-jet and general hadronic triggers. Three benchmark trigger menus have been defined to take the best possible advantage of each scenario, in each case assuming an instantaneous luminosity of $\mathcal{L} \simeq 7.5 \times 10^{34}\mathrm{cm}^{-2}\mathrm{s}^{-1}$ and a typical pile-up of $\mu \simeq 200$. These are described in detail in Section III.7.

XI.2.2 Tracking performance

Good tracking performance is critical to the reconstruction and identification of virtually all objects produced in p-p collisions. It is fundamental for the reconstruction of leptons and of primary and secondary vertices, and in pile-up mitigation. Unlike the calorimeters, the tracking detectors are not affected by particles from previous beam crossings. The vertexing performance is vital for the identification of b-jets (through secondary vertex reconstruction) and in order to link jets (especially in the forward region) to the correct primary vertex.

Two distinct effects of the layout choices on the tracking performance can to some extent be factorised: the impact of reducing the η-coverage of the tracking, and the degradation of the tracking performance due to a reduced number of strip layers. However, both effects contribute to global event features such as primary vertex finding, or the optimal evaluation of the missing transverse energy from all the objects in an event. The availability of tracking information at larger η for the Phase-II ITk brings many advantages in identifying physics objects and also in pile-up mitigation by linking objects to the primary vertex corresponding to the hard-scatter of interest. Primary vertex finding is discussed in Section XI.2.3.

The tracking performance of the three scoping layouts is studied using muons and pions in $Z \rightarrow \mu^+\mu^-$ events with an average pile-up of 200 events. The missing strip layers in the Middle and Low scenarios are simulated by masking hits in those layers when reconstructing tracks. In addition to evaluating the performance of the layouts when fully operational, the performance is also evaluated assuming a 10% hit loss from non-working modules to check the robustness of the layouts in case of failures. This hit loss is simulated by masking 10% of the remaining pixel and strip modules, chosen at random. The same random choice of modules is used for all samples. The performance for the Middle layout is inferred from the Reference layout for $2.7 < |\eta| < 3.2$.

Among the most important performance criteria for a tracking detector are tracking efficiency, impact parameter resolution and the rate at which “fake” tracks are reconstructed. Fake tracks do not closely match any single physical particle, but are instead from multiple different particles, and/or noise hits. Significant background contributions can arise due to such fake tracks, and so understanding and minimising the number of fake tracks is very important when designing a tracking detector. The efficiency, resolution and mis-reconstructed track fraction (fake rate) are defined as follows:

- **Efficiency**: The tracking efficiency is defined as the fraction of prompt muons or pions which produce matching tracks passing a track quality selection, optimised separately for each scoping scenario. The particles considered must be a true muon or pion, and satisfy $|d_0^{\text{truth}}| <$

1.0 mm and $|z_0^{\text{truth}}| < 150$ mm. Secondary particles produced in the Geant4 simulation are excluded. When measuring the efficiency as a function of η, the muons or pions must have $p_{\text{T}} > 4$ GeV. For the result as a function of p_{T}, muons or pions must have $p_{\text{T}} > 1$ GeV, $|\eta| < 4.0$ for the Reference layout, and $|\eta| < 2.7$ for the Middle and Low layouts.

In order to avoid counting fake tracks in the efficiency calculation, tracks are required to have a high probability of matching to a truth particle satisfying the above cuts. The *matching probability*, P_{match} takes into account that a track can have hits attached, that are generated by different particles and is defined as:

$$P_{\text{match}} = \frac{2N_{\text{common}}^{\text{pix}} + N_{\text{common}}^{\text{strip}}}{2N_{\text{track}}^{\text{pix}} + N_{\text{track}}^{\text{strip}}} \tag{1}$$

where $N_{\text{common}}^{\text{pix/strip}}$ is the number of pixel/strip-detector hits common to both the track and the particle to which it is being matched, and $N_{\text{track}}^{\text{pix/strip}}$ is the number of pixel/strip-detector hits assigned to the track. The factor of 2 included for N^{pix} arises due the the fact that each pixel layer provides one 2D measurement of the track whereas a double sided silicon layer provides two measurements.

The tracking efficiency, ϵ_{track}, is defined as the number of selected reconstructed tracks matched to a selected truth particle (satisfying the above cuts) with $P_{\text{match}} > 0.5$, divided by the number of selected truth particles (either muons or pions):

$$\epsilon_{\text{track}} = \frac{N_{\text{rec}}(\text{selected, matched})}{N_{\text{truth}}(\text{selected})} \tag{2}$$

- **Mis-reconstruction**: There is no unique way to define the rate at which fake tracks are produced, and many of the definitions are sensitive to details of the reconstruction. For the purposes of comparison in this note, the mis-reconstructed track fraction is used, defined as:

$$f_{\text{fake}} = \frac{N_{\text{rec}}(\text{selected, unmatched})}{N_{\text{rec}}(\text{selected})} \tag{3}$$

where $N_{\text{rec}}(\text{selected, unmatched})$ is the number of selected reconstructed tracks with $P_{\text{match}} < 0.5$, and the matching is to any charged truth particle.

- **Resolution**: Reconstructing tracks with a high efficiency and high purity is of limited use if the resolution in key track parameters is poor. The track parameters chosen in ATLAS are:
  - longitudinal and transverse impact parameter, z_0 and d_0;
  - transverse momentum, p_{T};
  - polar and azimuthal angle, θ and ϕ.

  The resolutions for these parameters can be obtained from simulation by comparing their reconstructed values for a given particle with the MC truth value. The tracks used to calculate the resolution are required to pass the same selection as for the efficiency calculation. Tracks must be matched to a truth muon or pion with $P_{\text{match}} > 0.5$ and $p_{\text{T}} > 4$ GeV .

  To define the resolution, the difference between the reconstructed and generated variable is computed for each selected track. The RMS of the distribution is taken as the parameter resolution σ. In order to limit the impact of outliers, the RMS is calculated using an iterative procedure within $\pm 5\times$ RMS of the previous iteration.

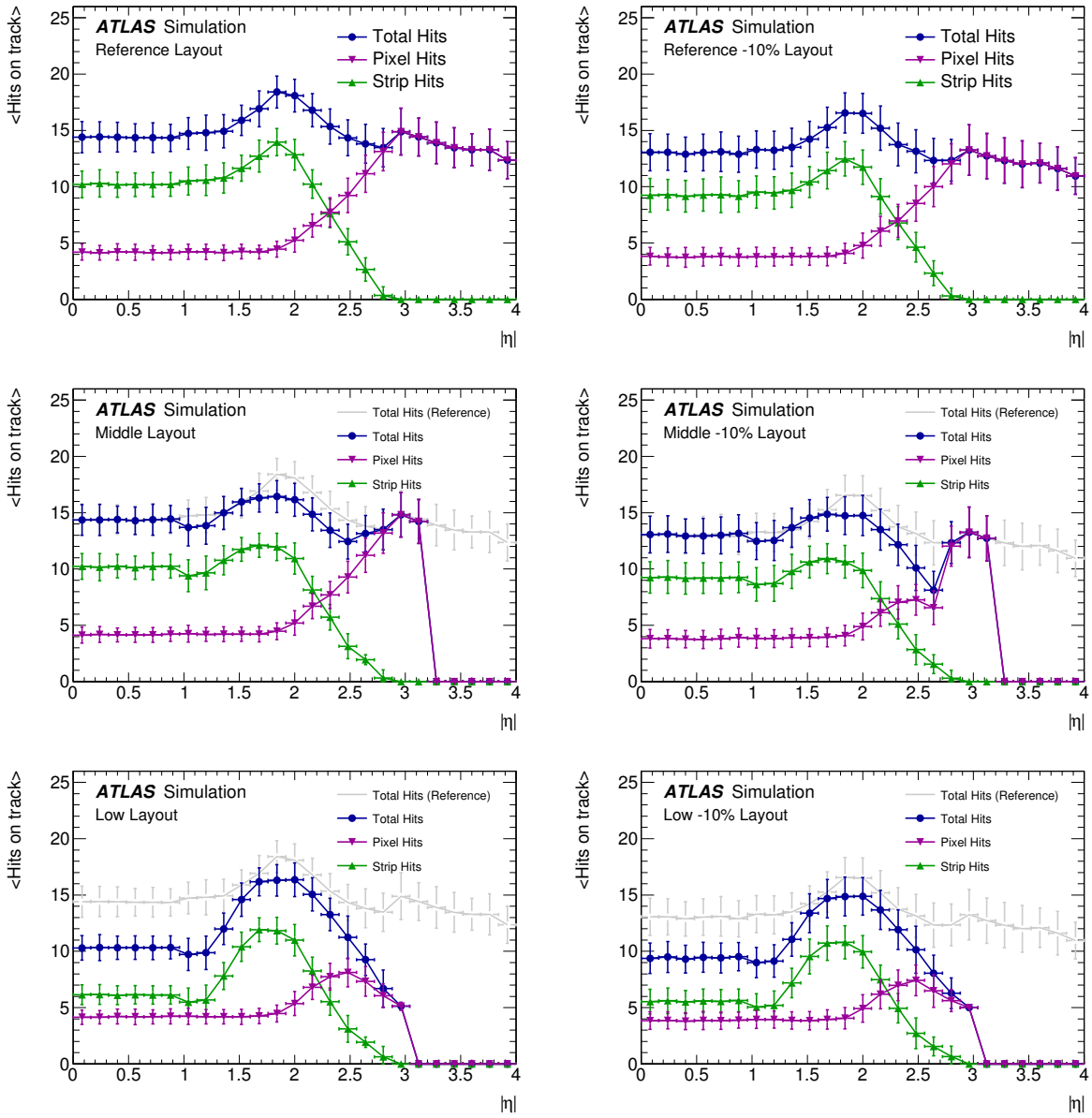

Figure 74. Mean number of hits on tracks for different layouts, for the strip detector (green), the pixel detector (purple), and the total number of hits (blue), for all tracks with $p_{\mathrm{T}} > 4$ GeV . The error bars show the RMS widths of the distributions of the number of hits. The number of hits in the fully working Reference layout are superimposed in each case in light grey.

The number of pixel and strip hits on muon tracks as a function of $|\eta|$ are shown in Fig. 74. The selection requirement on the number of hits on a track may also count in addition intersections through masked modules (either masked layers in the Middle or Low layouts or individual masked modules for the 10% hit loss). This distinguishes a known masked module from a missing hit, or "hole", which can be a powerful indicator for a mis-reconstructed track.

An optimal track selection takes into account the η-dependence of the available number of hits, otherwise the fake rate increases where more hits are available. This selection is optimised individually for each of the three scenarios, with and without the added 10% hit loss, typically requiring between 8 and 12 hits plus masked modules as a function of η. More hits are needed to improve performance in regions of high fake rate. In order to recover efficiency the cut can be relaxed in areas where fewer hits are expected, if these regions show low fake rate. For each region, the hit requirement is set such that the fake track fraction is kept below 1%, in order to provide a fair comparison of the performance of the different layouts. The hit cut is taken to be the tightest cut that does not give a significant decrease in the efficiency ($< 0.2\%$) compared to the loosest cut that would satisfy the requirement of the fake rate being below 1%. In addition, for these studies, tracks are required to have at most one hole in the pixel detector, $|d_0| < 1$ mm, $|z_0| < 150$ mm (i.e. to be consistent with originating from the luminous region) and are preselected with $p_{\mathrm{T}} > 1$ GeV.

The performance for reconstructed pion tracks is studied using the same track selection as for muons. Since layers which are absent in the Low and Middle scenarios remain in the simulation, and are removed from reconstruction simply by ignoring ('vetoing') hits in these layers, the resulting interactions within the detector material are still being simulated. The estimated performance for pions (and electrons) is therefore pessimistic (due to nuclear interactions and bremsstrahlung).

The tracking efficiency and fake rates for the three different scoping layouts, with and without the additional 10% masked modules, are presented in Figs. 75, 76 and 77. The fake fraction is evaluated for all tracks with reconstructed $p_{\mathrm{T}} > 1$ GeV. Note that the Middle layout results displayed in these and following tracking performance figures in this section only extend to $|\eta| < 2.7$. With 10% non-working modules, the typical average drop in efficiency for muons is less than 5% for the Reference, about 10% for the Middle and 15% for the Low scenario. The degradation shows no significant dependence on p_{T} or the number of vertices. In the Reference scenario, despite the high pile-up and extended η coverage, the muon track reconstruction efficiency is comparable with the Run 1 performance, which is $> 99\%$ for $p_{\mathrm{T}} > 10$ GeV [74]. As expected, the pion track reconstruction efficiency is lower, but follows similar trends. The mis-reconstructed track fraction is well below 1% for all η with the Reference layout. The shape as a function of $|\eta|$ is due to the different hits cuts applied in different $|\eta|$ bins. The tiny difference in fake rate at very low η between the Reference and Middle scenarios is an artefact of the modelling of service material in the simulation.

The d_0, z_0, ϕ, θ, q/p_{T} and p_{T} resolutions for muons in the three different scoping layouts, with and without the additional 10% masked modules, are presented in Fig. 78, and for pions in Fig. 79. The apparent slight improvement in position resolution, d_0, z_0 and ϕ in the Middle and Low scenarios is a reflection of the lower efficiency at low p_{T}. Lower p_{T} tracks have an intrinsically worse position resolution. The missing outer strip layers cause up to 40% degradation in p_{T}, since the lever arm for the p_{T} measurement is reduced.

The tracking performance of the Reference layer with $\mu = 200$ is excellent, with good efficiency across the full η range. The track parameter resolution is worse in the high-η region, but still useful for object identification and pile-up mitigation, as will be seen in the following sections. The layout is robust against up to 10% non-working modules. The robustness is partially lost with the Middle layout. Finding a balance between tracking efficiency and fake rate with the Low layout is very difficult, nor is this layout robust against module failures.

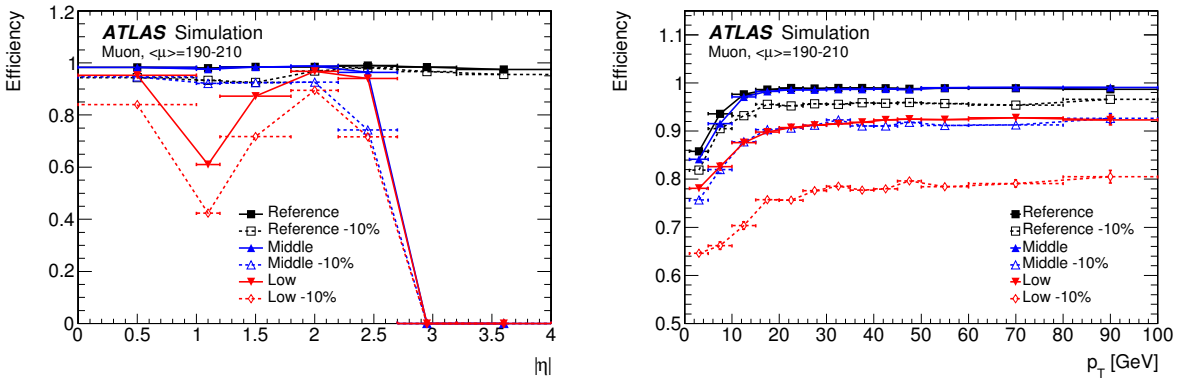

Figure 75. Efficiency for reconstructing prompt muons as a function of η (left) and p_{T} (right). MC statistical uncertainties are plotted, but are in many cases smaller than the symbol size.

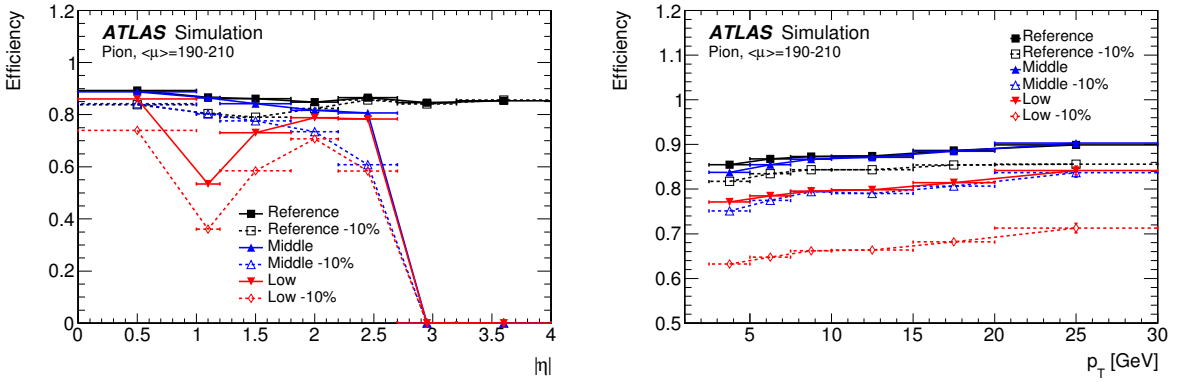

Figure 76. Efficiency for reconstructing prompt pions. The performance for the Middle layout is identical to the Reference for $2.7 < |\eta| < 3.2$. MC statistical uncertainties are plotted, but are in many cases smaller than the symbol size.

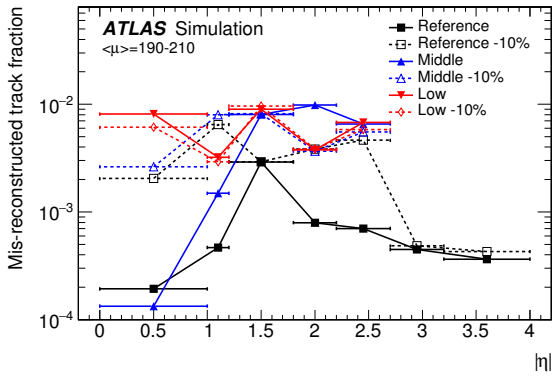

Figure 77. The mis-reconstructed track fraction as a function of η for tracks with reconstructed $p_{\mathrm{T}} > 1$ GeV. The performance for the Middle layout is identical to the Reference for $2.7 < |\eta| < 3.2$. MC statistical uncertainties are plotted, but are in many cases smaller than the symbol size.

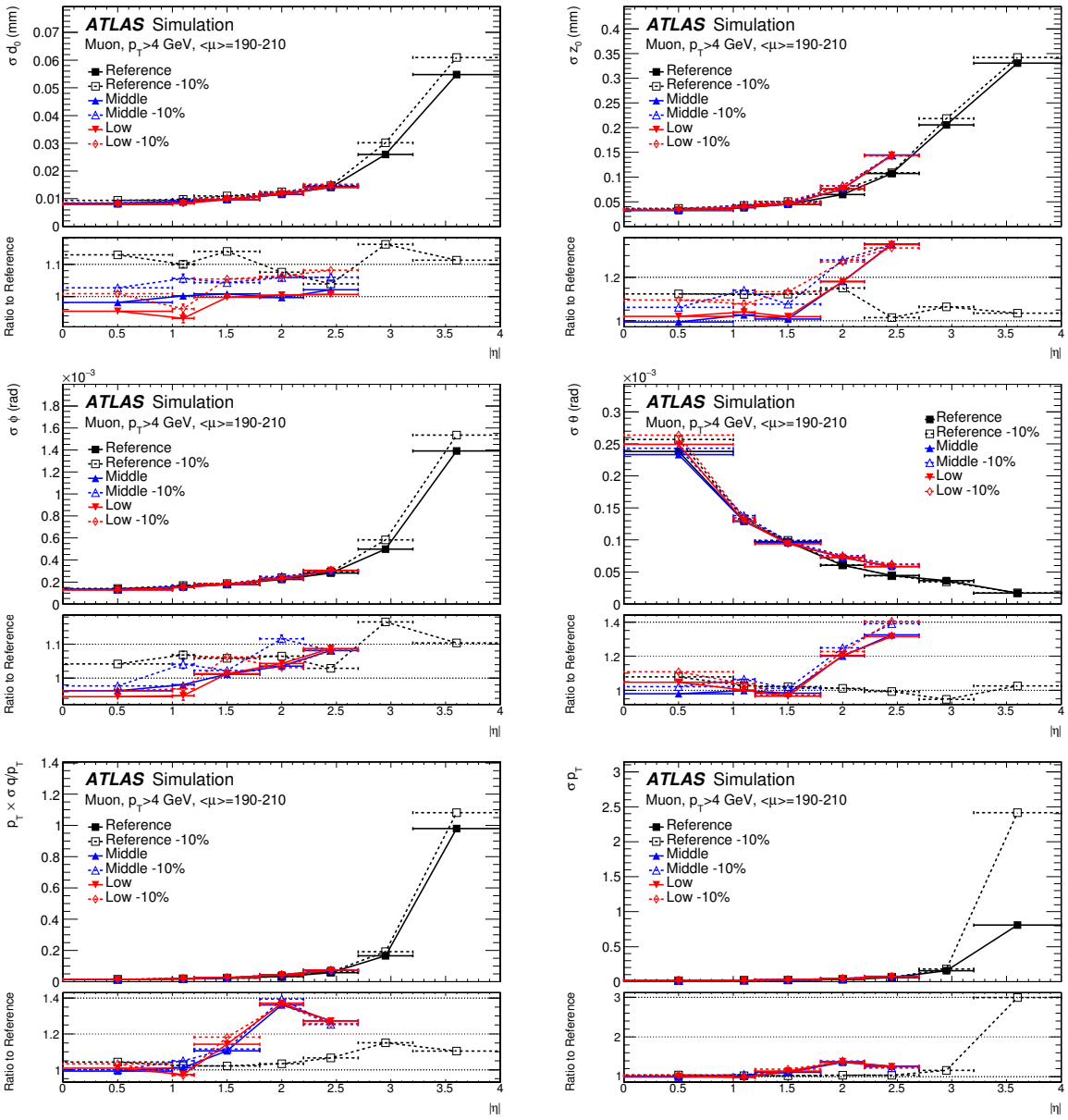

Figure 78. Resolution of the track parameters d_0, z_0, ϕ, θ, q/p_{T} and p_{T} for reconstructed muon tracks in $Z \rightarrow \mu\mu$ events, calculated by comparing the reconstructed values for a given particle with the truth value from the Monte Carlo simulation. The true muons are required to have $p_{\mathrm{T}} > 4$ GeV . The performance for the Middle layout is identical to the Reference for $2.7 < |\eta| < 3.2$. MC statistical uncertainties are plotted, but are in general much smaller than the symbol size.

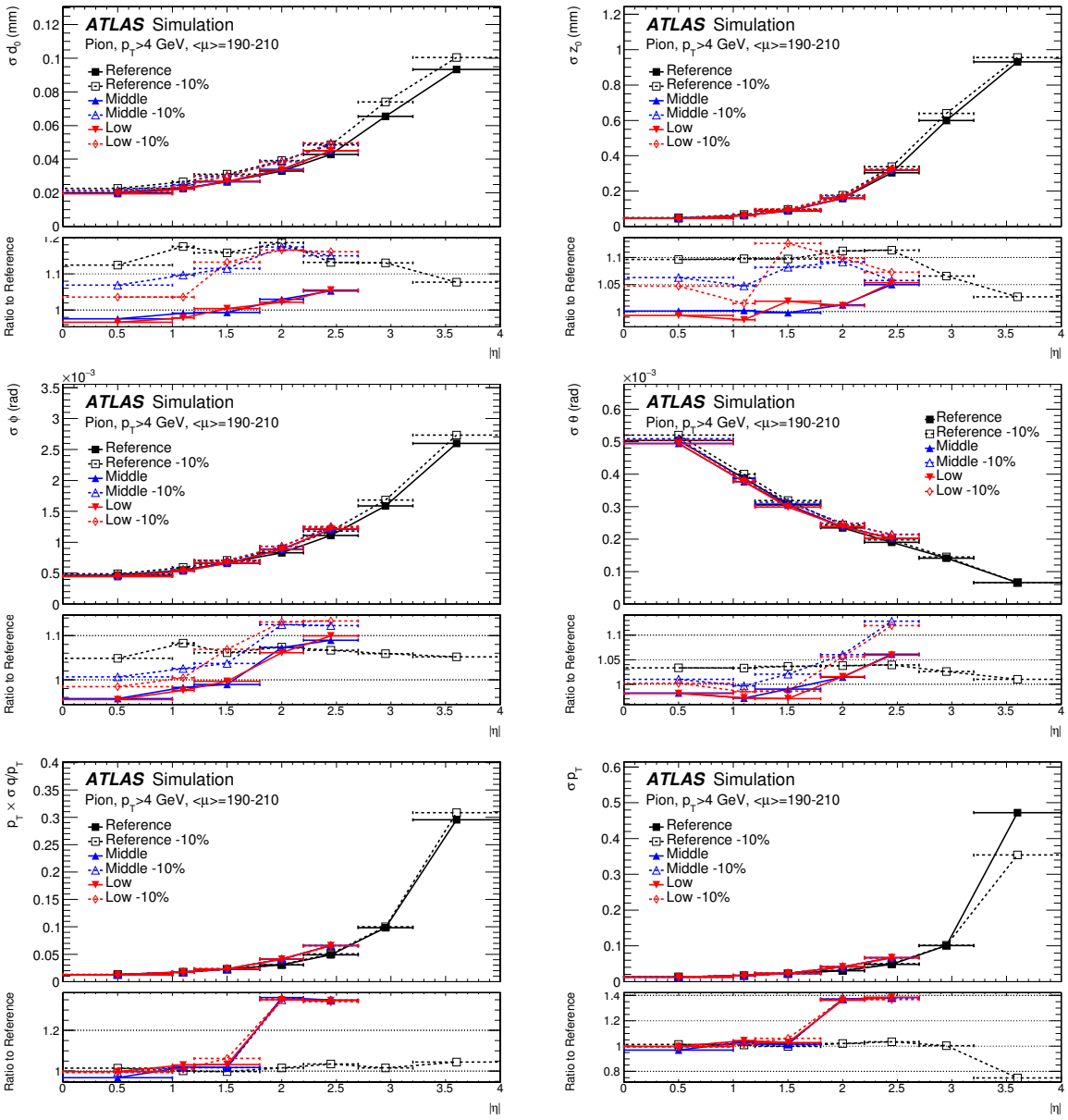

Figure 79. Resolution of the track parameters d_0, z_0, ϕ, θ, q/p_{T} and p_{T} for reconstructed pion tracks calculated by comparing the reconstructed values for a given particle with the truth value from the Monte Carlo simulation. The truth particles are required to have $p_{\mathrm{T}} > 4$ GeV . The performance for the Middle layout is identical to the Reference for $2.7 < |\eta| < 3.2$. MC statistical uncertainties are plotted, but are in general much smaller than the symbol size.

XI.2.3 Primary vertex finding

The performance of primary vertex finding is studied in samples of $t\bar{t}$, $Z \to \mu\mu$, and vector boson fusion (VBF) $H \to \gamma\gamma$ events with $\mu = 200$. These samples reflect quite different hard-scattering processes of interest in terms of charged particle multiplicity. VBF $H \to \gamma\gamma$ events are of particular interest for evaluating improvements in vertexing from the inclusion of forward tracks, since the VBF jets have large pseudo-rapidities.

A track selection independently optimised for vertex reconstruction applies η-dependent cuts on the numbers of hits, dead sensors and holes, and in addition requires $p_{\mathrm{T}} > 0.9$ GeV for $|\eta| < 2.7$ and $p_{\mathrm{T}} > 5$ GeV for $2.7 < |\eta| < 3.6$. The p_{T} threshold in the forward region is relatively high. The z_0 resolution for pions with $p_{\mathrm{T}} > 4$ GeV is in the range of 0.5 to 1.0 mm for $|\eta| > 2.7$ (see Fig. 79). However, once the primary vertex is identified, low momentum tracks with a small impact parameter with respect to the vertex can be included for example in determining whether a jet matches the primary vertex (see Section XI.2.7).

The following quantities are used to evaluate the vertexing performance of each ITk layout and signal process.

Reconstruction Efficiency: the efficiency for the hard-scatter interaction to be reconstructed as a vertex. The efficiency is normalised by the total number of generated interactions, i.e., with respect to the inclusive sample.

Identification Efficiency: the efficiency for the hard-scatter interaction to be reconstructed as the vertex with the highest $\Sigma\,(p_{\mathrm{T}}^{\mathrm{track}})^2$, where the summation includes all tracks used in the vertex reconstruction. The efficiency is also normalised by the total number of generated interactions (i.e., with respect to the inclusive sample).

z-Resolution: the position resolution of the reconstructed hard-scatter interaction, in the z direction. To extract the resolution, the distribution of $\Delta z = z_{\mathrm{reco}} - z_{\mathrm{true}}$ is fitted with a double Gaussian: $f(\Delta z) = A\exp(-(\Delta z)^2/2\sigma_A^2) + B\exp(-(\Delta z)^2/2\sigma_B^2)$. The quoted resolution is the weighted average of the two σ values, i.e. $\sigma = (A\sigma_A + B\sigma_B)/(A+B)$

Transverse Resolution: the position resolution of the hard-scatter interaction, in the x or y direction. The procedure for extracting the resolution is the same as for the z resolution.

Hard Scatter (HS)– Pile-Up (PU) Separation: the typical scale of the minimum resolvable distance between the hard-scatter vertex and nearby pile-up vertices. The separation of each HS-PU pair is measured as $\Delta z = z_{\mathrm{reco}}(HS) - z_{\mathrm{reco}}(PU)$, and the distribution of Δz is fitted by an Error function $1 + \mathrm{Erf}((\Delta z - d)/s)$, where d is the hard-scatter separation power.

Except for the identification efficiency, the vertexing performance does not depend strongly on the layout, but does vary with physics process, and is sensitive to the track selection defined. As shown in Fig. 80, with the selection defined above, the reconstruction efficiency is about 98 % for $t\bar{t}$, 94 % for $Z \to \mu\mu$ and 96 % for VBF $H \to \gamma\gamma$ events. The transverse resolution for the three processes is 6 μm, 7 μm and 8 μm, respectively, while the z-resolution is 16 μm for $t\bar{t}$ and 28 μm for the other two processes. The HS-PU separation power is typically 0.7 mm. In general, the performance in reconstruction efficiency, vertex resolution, and HS-PU separation power are consistent within a few per cent across the different layouts, with or without the 10% inefficiency in dead sensors, and comparing $\mu = 200$ with $\mu = 140$.

The vertex identification efficiency benefits from the inclusion of tracks in the forward region and thus shows the most significant variations across layouts. The impact from the forward extension on the identification efficiency depends on the physics processes, and is more sensitive to pile-up than

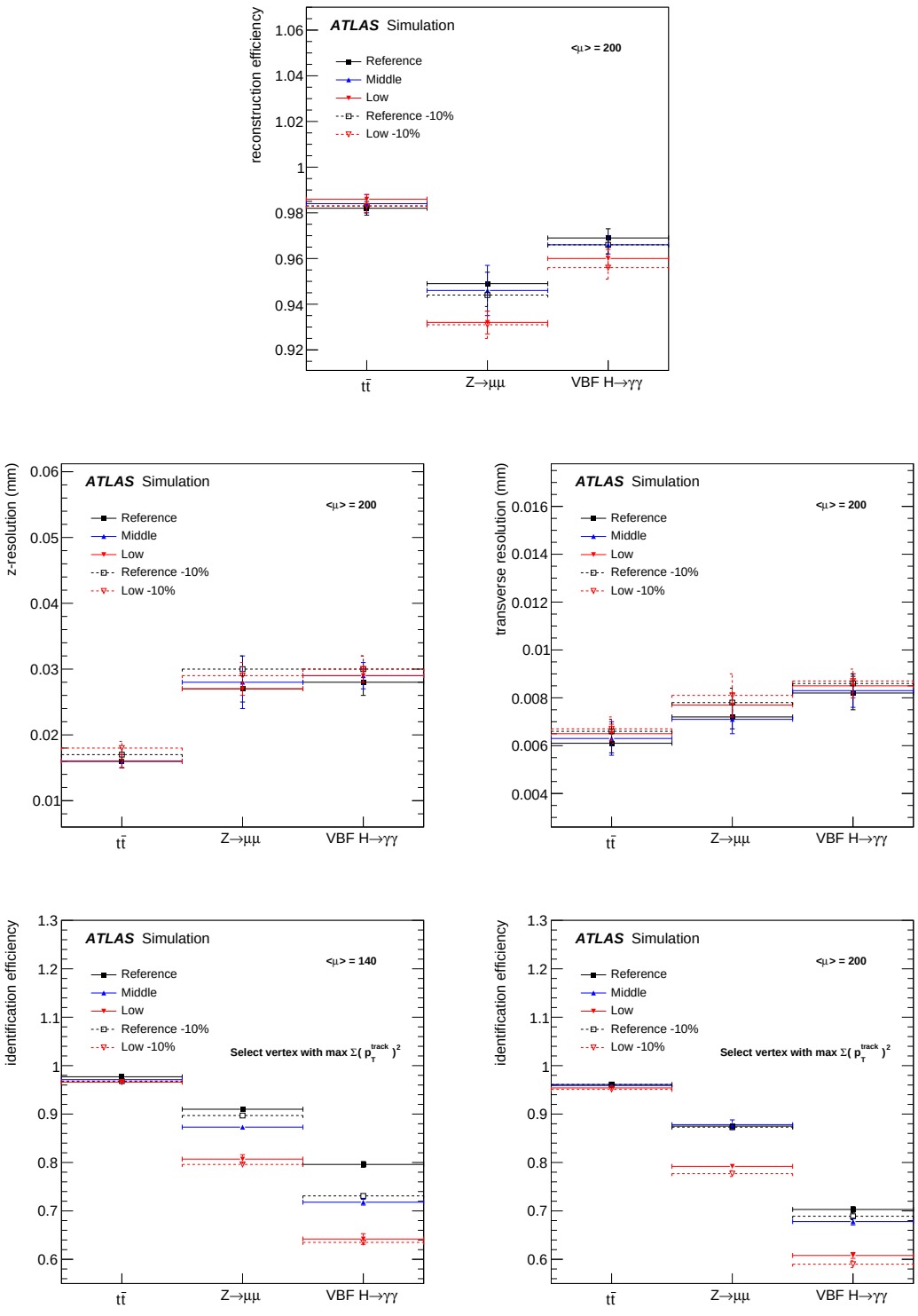

Figure 80. Vertexing performance for $t\bar{t}$, $Z \to \mu\mu$ and VBF $H \to \gamma\gamma$ events with μ=200. The reconstruction efficiency, z resolution, resolution of the transverse (x,y) coordinates and identification efficiency are shown (see text for the definitions of these quantities). In addition, the bottom left plot shows the identification efficiency with μ=140.

the vertex resolution and reconstruction efficiency. With $\mu = 200$, the identification efficiency for $t\bar{t}$ is about 95%, independent of the layout, because $t\bar{t}$ events events have most of their activity in the central region. Geometric acceptance effects have an impact on the efficiency for $Z \to \mu\mu$ events. Restricting the muon acceptance to $|\eta| < 2.7$ results in the observed 8% reduction in efficiency for the Low layout. For VBF $H \to \gamma\gamma$ events, the efficiency is degraded by 10% for the Low layout, since most of the activity in the tracking detector is in the forward region. The efficiency also drops by up to 10% from $\mu = 140$ to $\mu = 200$. It should be noted that the simple identification efficiency metric of $\Sigma\,(p_{\mathrm{T}}^{\mathrm{track}})^2$ used here can be improved with analysis specific selections, such as giving more weight to vertices close to the point of origin of identified leptons or b-jets. The calorimeter also provides pointing information for photons, which can be taken into account for processes such as VBF $H \to \gamma\gamma$. For VBF Higgs production with an invisible decay of the Higgs boson (which is expected to provide the strongest constraints on WIMPs in the low-mass regime) the vertex identification relies solely on the low p_{T} tracks from forward jets.

XI.2.4 Electron performance

The electron performance is evaluated with $Z \to ee$ events. Jets in these events and in other samples are used to study the fake rate and the relationship between the jet energy and the reconstructed fake electron energy.

The electron energy is measured using the calorimeter, with no information from the tracking. The energy resolution, quoted as the standard deviation of a Gaussian function fitted to the core of the distribution, is found to be rather insensitive to changes in the ITk material, and is parametrised as a function of electron energy and η. The energy resolutions for $\mu = 140$ and for $\mu = 200$ are shown in Fig. 81. The resolution with $\mu = 200$ is about 50% worse than that found in Run 1 at low $|\eta|$ [75]. However, the Run 1 resolution degrades up to $|\eta| = 2.5$, while with the reduced material in the ITk, it remains rather flat over this range. The typical resolution for a 30–50 GeV transverse energy electron with $|\eta| < 2.5$ and with $\mu = 200$ is 3–4%. It increases rapidly beyond $\eta = 2.5$ due to the reduced transverse segmentation of the calorimeter in this region.

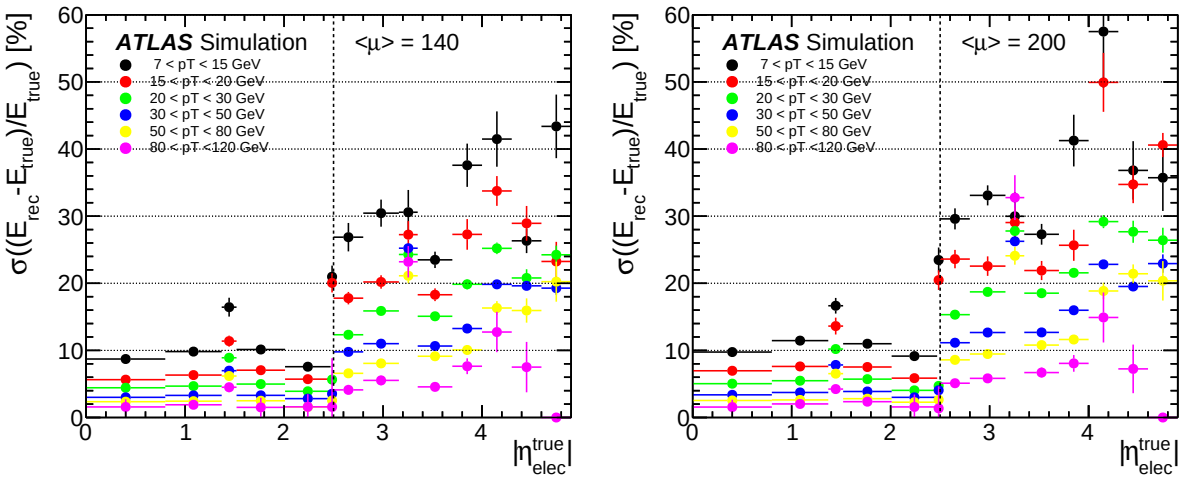

Figure 81. Energy resolution for electrons as a function of pseudo-rapidity and for different ranges of the electron transverse momentum p_T, for the Reference scenario with $\mu = 140$ (left) and $\mu = 200$ (right). The uncertainties are from MC statistics.

The efficiency for electron identification has been studied under different pile-up conditions and

for two different working points, *loose* and *tight*, corresponding to identification criteria with low and high purity, respectively. Tracks are required to have at least 10 hits or dead sensors for $|\eta| < 2.5$, and at least 8 hits or dead sensors for $|\eta| > 2.5$, with at most one hole in each case.

For central electrons, the cut-based identification menu developed for Run 2 has been used, without any further re-optimisation for higher pile-up conditions. Details can be found in Ref. [76]. Selection criteria using information from the Transition Radiation Tracker must be discarded, since this component is not present in the Phase-II detector.

For forward electrons ($|\eta| > 2.5$) in the electromagnetic end-cap and forward calorimeters, an identification method developed for 2012 Run 1 data is used. This exploits differences in the shower shapes of hadronic and electromagnetic energy depositions and a Fisher discriminant for the classification as background or signal. No re-optimisation of the Fisher discriminant, or more generally of the method, has been performed yet for large pile-up conditions. In the region $2.5 < |\eta| < 4.0$, for the Reference scenario, and $2.5 < |\eta| < 3.2$, for the Middle scenario the forward tracking information is used for the tight electron identification criteria. The closest forward track to the electron cluster in $\eta - \phi$ is matched to the cluster if $\Delta R < 0.06$ [2]. The absolute transverse impact parameter of the matched track is required to be $|d_0| < 1$ mm.

The efficiencies and fake rates are shown in Fig. 82 for both operating points, tight and loose, and for two pile-up values. The overall performance could be improved using more sophisticated algorithms such as those being developed for Run 2. However, even without a better algorithm, the relative impact of the different scoping scenarios can still be estimated.

In the central region ($|\eta| < 2.5$), the Reference scenario has a few percent higher efficiency than the Middle and Low scenarios. Within the simulated event statistics available for this study, the fake rates for the three scenarios are comparable.

In the forward region, the additional requirement of a track matching the electron cluster is included for the tight identification up to η = 3.2 and 4.0 for the Middle and Reference scenarios, respectively. This requirement improves the rejection of fake electrons by a factor of ~ 2, and reduces the identification efficiency by only 1 to 2%. These values are, however, limited by significant statistical uncertainty. The performance of the three scenarios is the same for η values larger than 4 since the tracker coverage never extends beyond $|\eta| = 4$.

The energy of a fake electron candidate reconstructed in a jet is different from the initial energy of the true jet. This behaviour is parametrised for use in physics analyses by rescaling the energy of the true jet so that it approximates the energy of fake electrons arising from true jets. Distributions of the difference between the energy of the reconstructed electron candidate and the energy of the true jet are determined from Monte Carlo simulation in bins of p_{T} and η. The updated electron identification efficiencies and energy resolutions have been implemented in the parametrised performance functions for physics studies.

XI.2.5 Photon reconstruction

For photons the choice of the layout mainly affects the efficiency for reconstructing photons that convert into an electron–positron pair within the tracking acceptance. The energy resolutions for unconverted photons and for photons with two correctly identified charged tracks are close to the resolution for electrons, and for the studies presented here are assumed to vary with pile-up in the same way. The resolution for incorrectly reconstructed converted photons is about 50% worse, since the appropriate correction for track energy loss is not applied.

The reconstruction of converted photons is studied in a sample of $ZH \to bb\gamma\gamma$ events for photons with $p_{\mathrm{T}} > 20$ GeV and $|\eta| < 2.37$ (referred to as “central photons” in what follows), corresponding

[2] The angular matching variable ΔR is defined by $\Delta R^2 = \Delta\eta^2 + \Delta\phi^2$

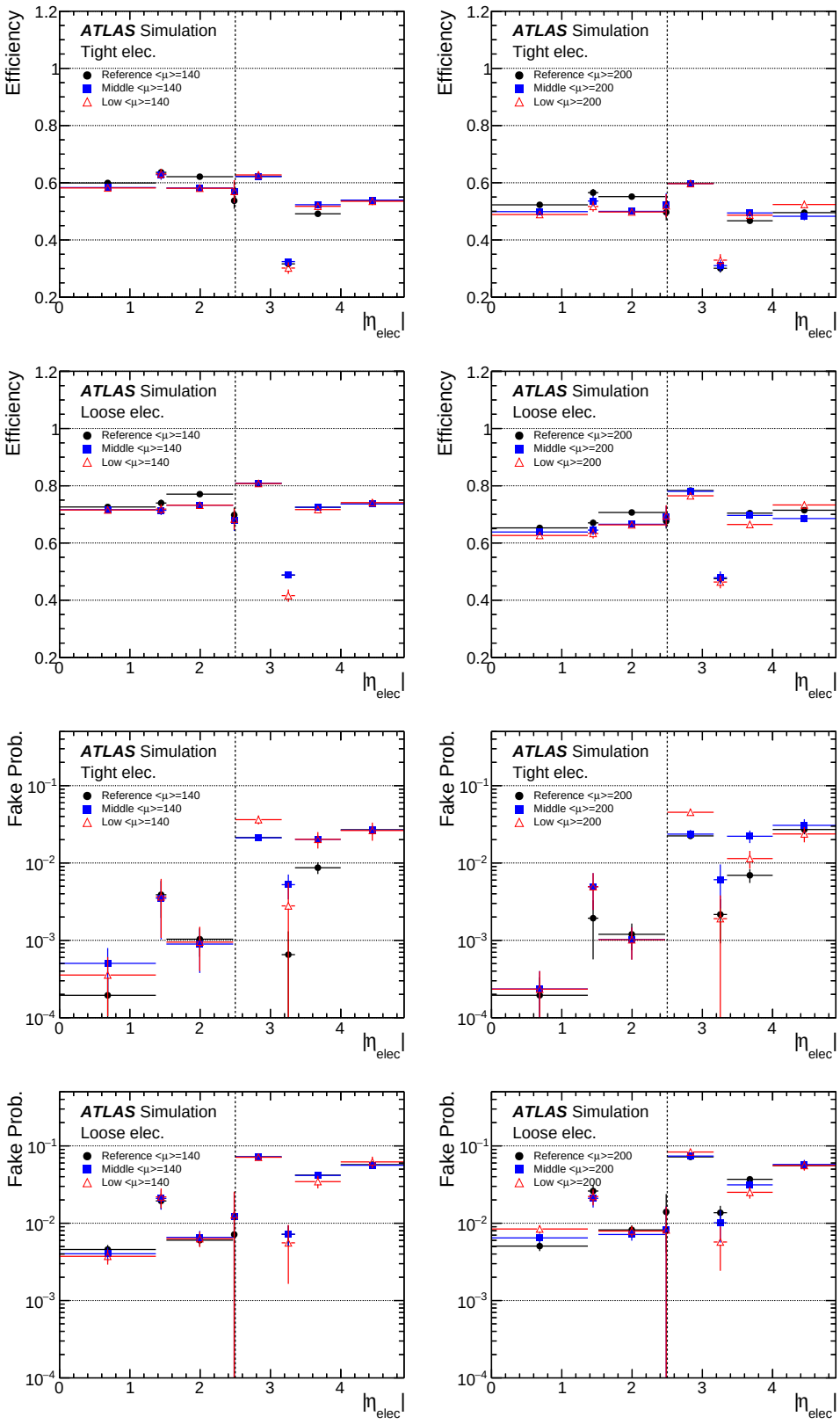

Figure 82. Identification efficiencies for true electrons (upper four plots) and the probability to find a fake electron in a jet (lower four plots) as a function of η, for transverse momentum of the reconstructed electron 20 GeV < p_{T} < 30 GeV, and with MC statistical uncertainties. In each group, the performance for $\mu = 140$ is shown on the left, and $\mu = 200$ on the right, for the tight (top) and loose (bottom) selections.

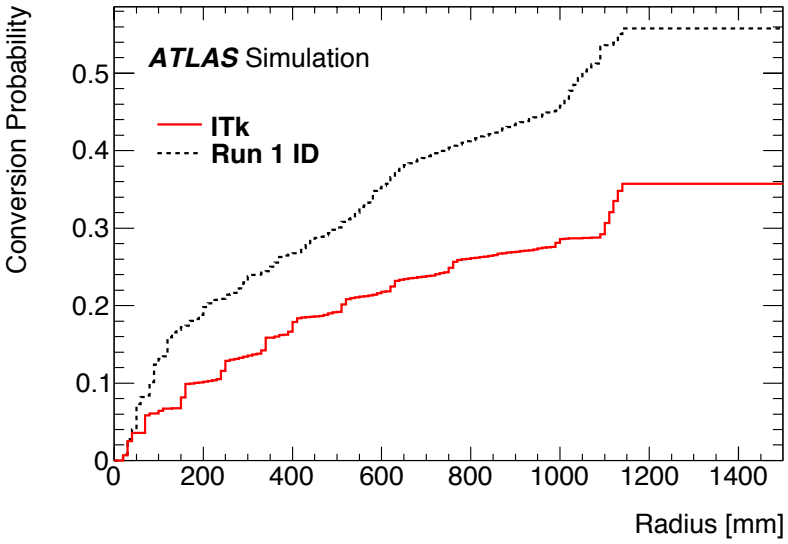

Figure 83. The cumulative probability of conversion as a function of radius for the Run 1 ATLAS ID and the planned ITk. The LoI layout is assumed for the ITk.

to the region for which the conversion reconstruction algorithm for the present ATLAS detector is optimised. A conversion track finding algorithm is developed for the ITk to improve the reconstruction efficiency of the tracks associated with conversions. This new algorithm runs after all other existing track finding algorithms, and takes the unused hits to build tracks with some loosened requirements, such as allowing tracks to have fewer hits, not to point back to the primary vertex, and to be seeded at larger radius than a standard track. An extension of the algorithm to larger pseudo-rapidity has not yet been developed for the extended ITk.

The ITk represents a major reduction in material upstream of the calorimeter compared to the present ATLAS ID. Figure 83 shows the conversion probability determined from the truth information, as a function of the radius, for the ID and the LoI ITk layout. In the ITk, 36% of photons convert, compared to 56% in the ID. Since the hit-masking technique is used to evaluate the Middle and Low scenarios, photons may convert in a layer (stub, disk or barrel) which should be absent. These photons are counted as unconverted. However, where 10% of additional modules are masked to simulate a non-functioning part of the detector, photons converting in these still count as converted. As a result, the fraction of converted photons is reduced from 36% in the Reference layout to about 34% in the Low scenario due to the missing strip barrel layers.

The central photon reconstruction efficiency and photon conversion reconstruction efficiency in different scenarios are shown in Table 27 for $\mu = 140$ and $\mu = 200$ pile-up conditions. For each scenario, both a nominal sample where all modules are functioning and a sample where 10% of modules are disabled are generated. For a sample of true photons, the photon reconstruction efficiency, ϵ_γ, is defined as the ratio of the number of reconstructed photons that can be matched to a true photon to the total number of photons, where a reconstructed photon passes the basic calorimeter selection requirements to be identified. This definition is independent of whether the photon converted in the ITk volume. The photon conversion reconstruction efficiency, ϵ_c, is defined as the ratio of the number of reconstructed converted photons that can be matched to a true converted photon to the number of true converted photons. The reconstructed conversions matching true converted photons are further divided into those reconstructed with a single track and those with two tracks, giving the

Table 27. The performance of conversion reconstruction for central photons for the scoping scenarios with all ITk modules working, or with 10% dead modules, and for two different pile-up conditions. The photon reconstruction efficiency, ϵ_γ, is the fraction of photons matching a suitable calorimeter cluster. The photon conversion reconstruction efficiency is ϵ_c. Reconstructed conversions have a fraction f_1 with a single track and f_2 with two tracks.

$\mu = 140$	Reference		Middle		Low	
	nominal	-10%	nominal	-10%	nominal	-10%
$\epsilon_\gamma(\%)$	98.7	98.7	98.7	98.6	98.6	98.7
$\epsilon_c(\%)$	48.0	41.5	47.1	39.9	36.2	31.5
$f_1(\%)$	40.1	41.0	41.6	42.6	39.8	40.8
$f_2(\%)$	59.9	59.0	58.4	57.4	60.2	59.2
$\mu = 200$	Reference		Middle		Low	
	nominal	-10%	nominal	-10%	nominal	-10%
$\epsilon_\gamma(\%)$	98.3	98.3	98.2	98.3	98.1	98.3
$\epsilon_c(\%)$	46.9	40.5	45.8	39.1	35.2	31.2
$f_1(\%)$	42.3	44.5	42.6	45.1	41.4	44.1
$f_2(\%)$	57.6	55.5	57.3	54.9	58.5	55.9

fractions f_1 and f_2.

The central photon reconstruction efficiency is about 98% for the different scenarios, regardless of the pile-up conditions and functional module fraction, reflecting the high cluster reconstruction efficiency in the electromagnetic calorimeter for both converted and unconverted photons, regardless of whether the tracks are reconstructed.

The photon conversion reconstruction efficiencies with $\mu = 200$ are 47%, 46%, and 35% with the nominal samples for the Reference, Middle, and Low scenarios, respectively, with a typical statistical uncertainty of 1%. This indicates that the removal of stub layers and the strip disks at $|z| = 2616$ mm has little impact on the conversion reconstruction. A 25% drop in the photon conversion reconstruction efficiency relative to the Reference and Middle scenarios is seen in the Low scenario. Disabling 10% of the modules in all three scenarios leads to a relative 15% drop in the photon conversion reconstruction efficiency. The photon conversion reconstruction efficiency is found to be similar for $\mu = 140$ and $\mu = 200$.

Figure 84 shows the true conversion vertex distribution for reconstructed converted photons as well as true converted photons. The conversion reconstruction efficiency begins to fall off with radius above about 400 mm, dropping to nearly zero by 700 mm.

The rate for electrons in a $Z \rightarrow ee$ sample to be incorrectly reconstructed as a converted photon is evaluated to be 2 to 3% in the absence of pile-up, roughly 1% each for 1-track and 2-track conversions, and the rate does not vary significantly with layout within the limited statistics available.

The photon energy resolution for physics studies is assumed to be the same as for electrons. The photon efficiency and angular resolutions remain the same as those used in Ref. [77]. No correction has been included for the degradation in energy resolution for misidentified converted photons in the Middle and Low scenarios.

The reduced material in the ITk compared to the Run 1 ATLAS detector results in fewer photons converting in the tracker volume. The relative degradation in performance of the Low scenario, in particular, demonstrates the need for sufficient a sufficient number of outer strip layers to have reliable reconstruction of converted photons, and similarly for other Standard or non-Standard particles which decay in the outer part of the tracking detector.

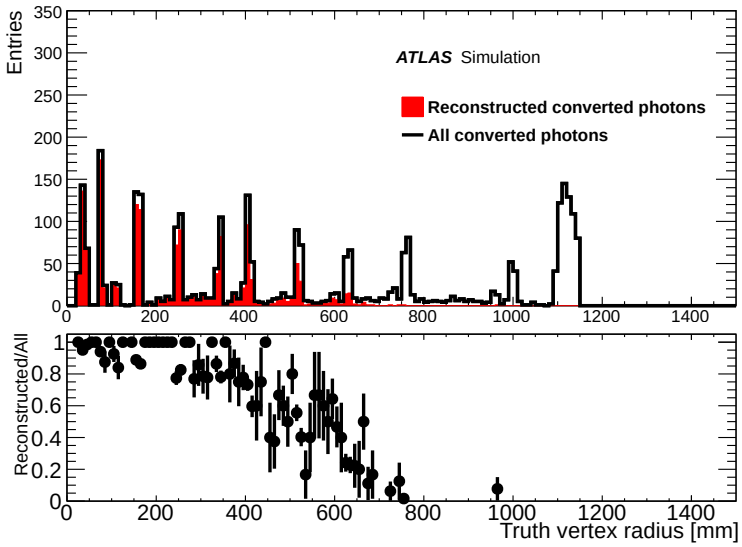

Figure 84. Distribution of true conversion vertex radius for reconstructed converted photons (solid black) and true converted photons (red) with $|\eta| < 2.37$ in the Reference layout, with average pile-up of $\mu = 200$ (top panel). The conversion reconstruction efficiency as a function of true radius (lower panel).

XI.2.6 Muon reconstruction and identification

The product of the muon trigger acceptance and efficiency in the barrel region will increase from approximately 65% in the Low scenario to approximately 95% in the Reference scenario or 80% in the Middle scenario, as explained in Section III.2.1. The new muon chambers in these scenarios are assumed not to change the momentum resolution of the muon spectrometer significantly. The addition of the high-η muon tagger (see Section VI.7) covering $2.7 < |\eta| < 4.0$ in the Reference scenario will allow muon identification to extend to this region. It is limited to $|\eta| < 2.7$ in the other scenarios. These muons are referred to as segment-tagged, since they consist of a full ITk track, which is extrapolated and matched to a track-segment found in the muon tagger. Note that the muon track segment does not have a measured momentum - the matching is performed using the location of the extrapolated ITk track intersection with the muon tagger. The extended coverage is of particular interest to measure charge asymmetries, in searches for rare processes, or to veto background with additional leptons for certain studies. It also improves the hermeticity with respect to forward muons for missing transverse momentum reconstruction.

The muon momentum resolution for lower momentum muons ($p_{\mathrm{T}} < 100$ GeV) is improved with the Phase-II tracker compared to the original ATLAS tracker. However, muon identification suffers from a reduced track finding efficiency, worse resolution and from worse performance of track isolation variables in the Middle and Low scenarios compared to the Reference scenario.

The muon momentum resolution for the muon spectrometer and ITk combined is shown in Fig. 85 for five representative pseudo-rapidity values. The effect of dropping strip layers has little impact on the resolution if the position of the outermost hit in the ITk is unchanged. The effect of removing the stub is visible at $|\eta| = 1.1$. The effect of the reduced bending field and much shorter lever arm is evident at larger $|\eta|$. The Middle scenario is indistinguishable from the Reference scenario for $|\eta| < 2.7$, apart from the region around $\eta = 1.1$ where it resembles the Low scenario. The efficiency and resolution effects are all included in the latest parametrised performance functions used for physics studies. However, the tracking inefficiencies shown in Fig. 75 are not taken into account,

assuming that a dedicated track finding seeded by a muon spectrometer segment could recover some of this inefficiency for the fully-operational scenarios. This assumption would not be robust against module failures - the inefficiencies with 10% dead modules are particularly severe for the Low scenario.

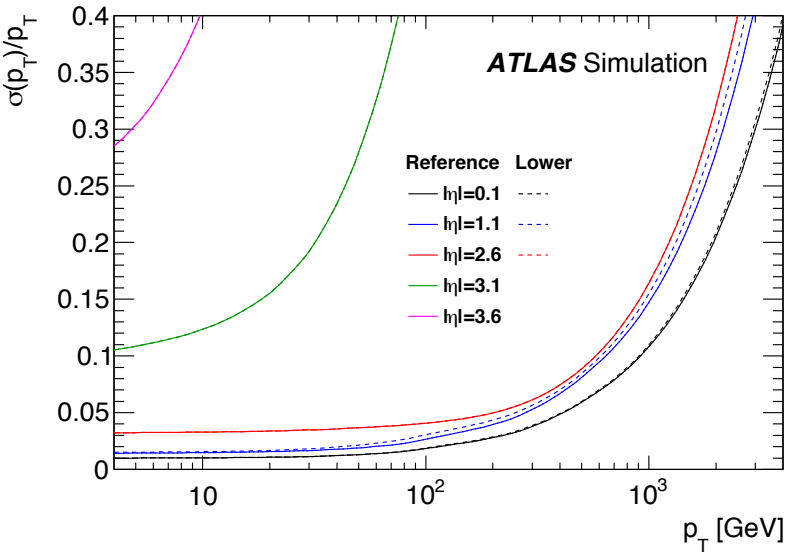

Figure 85. Momentum resolution combining the ITk and muon spectrometer measurements at several η values for the Reference and Low scenarios.

XI.2.7 Jet reconstruction and pile-up rejection

The jets considered here are reconstructed using the anti-k_t algorithm [78] with radius parameter $R = 0.4$, using as input energy clusters at the electromagnetic scale. These three-dimensional topo-clusters are built from topologically connected calorimeter cells that contain a significant signal above noise [79]. The noise thresholds are adjusted according to the expected level of pile-up.

XI.2.7.1 Jet energy scale

The Jet Energy Scale (JES) is applied as a calibration to transform the reconstructed jet energy to the best possible estimate of the true jet energy. It is assessed using a high statistics sample of di-jet events with the LoI geometry, for a typical pile-up of 140 and of 200.

The JES is insensitive to the small variations in material in front of the calorimeter of the different scoping scenarios. However, the JES algorithm includes a subtraction of the pile-up contribution, with a residual correction which depends on the number of interactions. The true number of interactions in an event is estimated from the number of reconstructed primary vertices, which strongly depends on the exact track selection requirements used in reconstructing primary vertices. The relationship between the number of reconstructed vertices and the true number of interactions in the event must therefore be taken into account for each scoping scenario. The JES performance was previously parametrised by an extrapolation from samples with $\mu \leq 40$ [80]. The new calibration including the pile-up subtraction term matches the previous extrapolation all the way up to μ of 200, and the previous parametrisation is retained for physics studies in this document.

XI.2.7.2 Pile-up jet rejection

Several techniques were developed in Run 1 to tag and suppress pile-up jets using tracking information. The variable considered here is R_{pT}, defined as the scalar p_{T} sum of the tracks that are associated with the jet and originate from the hard-scatter vertex divided by the fully calibrated jet p_{T}, including pile-up subtraction:

$$R_{pT} = \frac{\Sigma_i(p_{\mathrm{T}}^{\mathrm{track},i})}{p_{\mathrm{T}}^{\mathrm{jet}}} \tag{4}$$

Tracks are classified as originating from the hard-scatter vertex if their longitudinal impact parameter with respect to this vertex satisfies a loose, η-dependent requirement. Small values of R_{pT} arise for jets with small charged-particle p_{T} fractions originating from the hard-scatter vertex, which are therefore very likely to correspond to pile-up jets. In the following, reconstructed jets are defined as hard-scatter jets, if a truth jet associated with the hard-scatter vertex has $p_{\mathrm{T}}^{\mathrm{true}} > 10$ GeV and is found within $\Delta R = 0.3$ of the reconstructed jet. Reconstructed jets which are separated by more than $\Delta R = 0.6$ from any true jet with $p_{\mathrm{T}}^{\mathrm{true}} > 4$ GeV, are labelled as pile-up jets.

The distribution of the R_{pT} variable is shown in Fig. 86 for hard-scatter and pile-up jets with $40 < p_{\mathrm{T}} < 50$ GeV. The most important differences are at low values of R_{pT}. The efficiency of the R_{pT} cut for hard-scatter jets versus the efficiency for pile-up jets is shown in Fig. 87, where each curve represents a scan over the observable R_{pT} for jets in a range of $|\eta|$. For a particular η range, the curves for each scoping scenario are very similar if tracking information is available, so the figure only shows one curve for each region. The efficiency of the R_{pT} cut for hard-scatter (pile-up) jets is defined as the fraction of hard-scatter (pile-up) surviving the R_{pT} cut. For example, in the Reference scenario, the requirement $R_{pT} > 0.1$, as used in the evaluation of $E_{\mathrm{T}}^{\mathrm{miss}}$ (see Section XI.2.8), has an efficiency of 90 %, 86 % and 88 % for hard-scatter jets with $40 < p_{\mathrm{T}} < 50$ GeV, in the pseudo-rapidity regions $|\eta| < 2.4$, $2.4 < |\eta| < 3.2$ and $3.2 < |\eta| < 3.8$ respectively. The corresponding efficiencies for pile-up jets are 4 %, 6 % and 7 %. With tracking extended to $|\eta| < 4.0$, the pile-up rejection, defined as the inverse of the efficiency for pile-up jets, for radius $R = 0.4$ jets, is uniform in the forward region up to $|\eta| < 3.8$, and then starts to degrade for larger $|\eta|$. The optimal choice of the R_{pT} requirement depends on the physics analysis, and is discussed later.

Pile-up rejection using tracks is also important for triggering, where on-line tracking information will be available from L1Track or from FTK++. The impact of this is illustrated in Fig. 88 where p_{T} cuts of 4 and 8 GeV are shown. In the 8 GeV case, the curve only extends to a hard-scatter jet efficiency of 60% because many hard-scatter jets lack such high p_{T} tracks. For the Level-1 trigger only a modest rejection factor is needed and therefore the operating point is likely to be chosen to provide the highest possible hard-scatter efficiency.

XI.2.7.3 Pile-up jet simulation

The residual pile-up jets are taken into account in physics studies by superimposing such jets from full-simulation event samples onto the smeared hard-scatter events. A library of events containing pile-up jets is provided for different values of μ. The term “tracking confirmation” for jets is intended here as a generic name for future pile-up mitigation techniques and it represents the ability of the tracking information to disentangle jets originating from the primary vertex from jets originating from non-primary, i.e. pile-up, vertices. However, for the studies in this document, the R_{pT} method defined above is used. The efficiencies for hard-scatter and pile-up jets are derived from event samples based on full-simulation of the high luminosity environment. These efficiencies, once the pile-up jets are superimposed on a hard-scatter event, can be applied to all jets in order to investigate the effects of pile-up mitigation algorithms on the analysis. Analyses relying on good separation

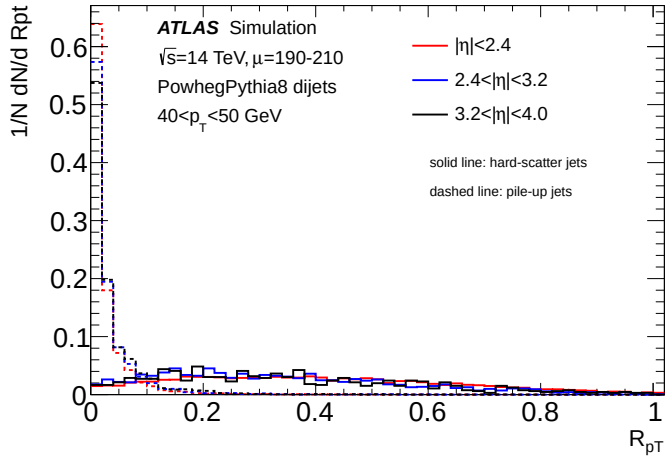

Figure 86. R_{pT} distribution for hard-scatter and pile-up jets with $40 < p_{\mathrm{T}} < 50$ GeV in different η regions.

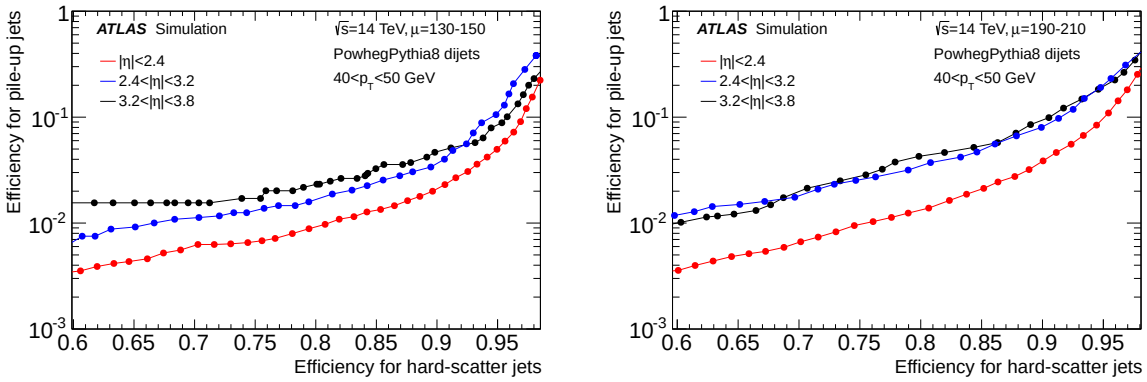

Figure 87. The efficiency for pile-up jets as a function of the efficiency for hard-scatter jets with $40 < p_{\mathrm{T}} < 50$ GeV using a track-matching algorithm for $\mu = 140$ (left) and $\mu = 200$ (right). The algorithm can be applied in $|\eta| < 2.4$ the Low scenario, $|\eta| < 3.2$ in the Middle scenario and $|\eta| < 3.8$ in the Reference scenario.

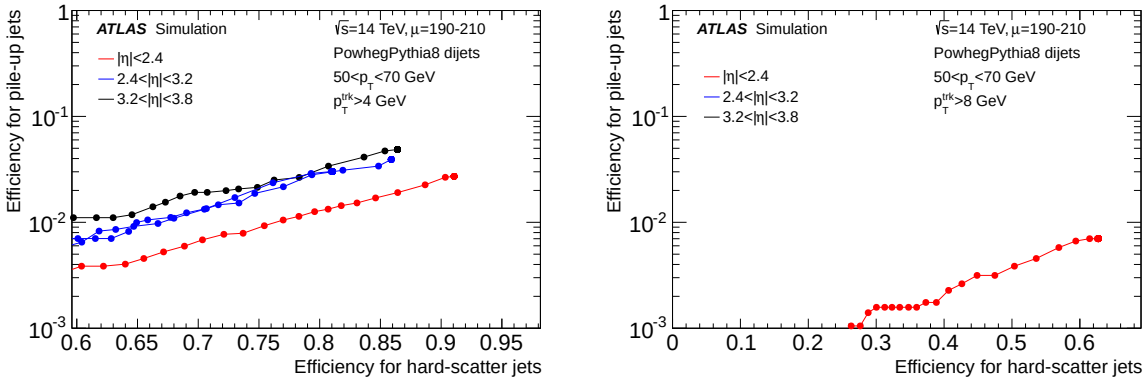

Figure 88. The efficiency for pile-up jets as a function of the efficiency for hard-scatter jets with $50 < p_{\mathrm{T}} < 70$ GeV using a track-matching algorithm for tracks with $p_{\mathrm{T}} > 4$ GeV which corresponds to the p_{T} cut used in L1Track in the Reference scenario (left), and for tracks with $p_{\mathrm{T}} > 8$ GeV which corresponds to the p_{T} cut used in L1Track in the Low scenario, which also only covers the central η region (right).

between hard-scatter jets and pile-up jets, or relying on exclusive jet selection, are expected to benefit from extending the η coverage for the tracking confirmation as far as possible. Several working points are provided. A requirement that the algorithm provides a fixed efficiency for hard-scatter jets of 70, 80 or 90 % over all valid ranges of p_{T} and η can be made. Alternatively, a fixed efficiency for pile-up jets of 2, 5 or 10 % can be required. The track confirmation algorithm is only applied for jets with $p_{\mathrm{T}} < 100$ GeV , as there is little pile-up jet contamination for higher values of jet p_{T}. Performance studies indicate that the 2% setting for pile-up jet efficiency presents a good compromise between pile-up rejection and hard-scatter efficiency. This is therefore adopted by the analyses presented here as the nominal working point. The effect of this tracking confirmation algorithm is illustrated in Fig. 89, where the inclusive distribution of pile-up jets is shown as a function of η for the different scoping scenarios. The benefit of the extended tracker coverage is evident for the Reference scenario with respect to the Middle and Low scenarios.

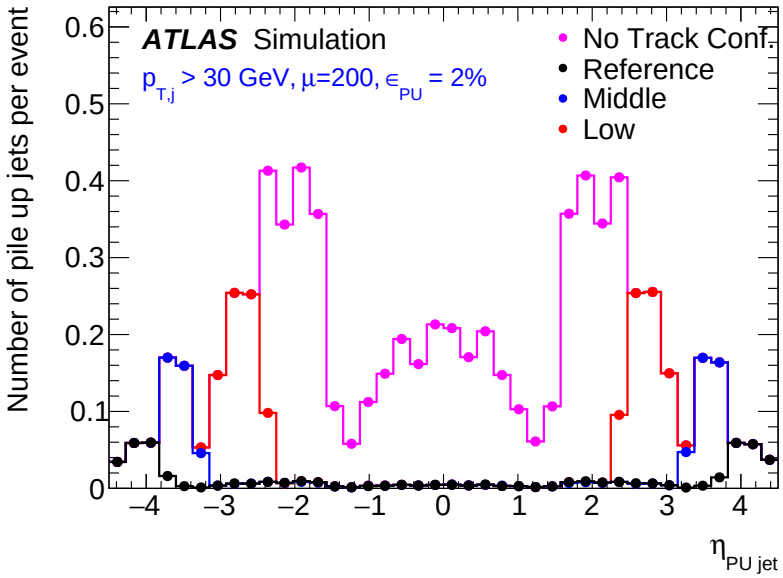

Figure 89. Distribution of the number of pile-up jets per event with no tracking confirmation (TC), and applying the TC algorithm tuned to give 2% pile-up jet acceptance, for each of the three scoping scenarios.

XI.2.7.4 Performance gains from the high-granularity sFCal

As described in Section V.4.2, a new forward calorimeter with smaller LAr gaps is proposed. This new detector will be read-out with four times finer transverse segmentation[3] in the first longitudinal layer (sFCal1) for $3.2 < |\eta| < 4.3$. The biggest improvements in terms of detector performance will come from the finer granularity in sFCal1.

The reduction in cell area by a factor of four results in a reduction of the pile-up noise RMS by a factor of ~ 2.5. This effect is illustrated in Fig. 90, where the total noise for the legacy FCal (left) and an upgraded sFCal (right) with increased granularity in sFCal1 is shown for $\mu \simeq 200$. The main effect, a reduction of the total noise of sFCal1 for $|\eta| < 4.3$, is clearly visible.

Note also the step in noise RMS at $|\eta| \simeq 4.3$ in the left plot, at the transition between the large area cells and the cells with an area four times smaller, in the present FCal.

[3]The current FCal1 is built with smaller unsummed cells for $|\eta| > 4.3$.

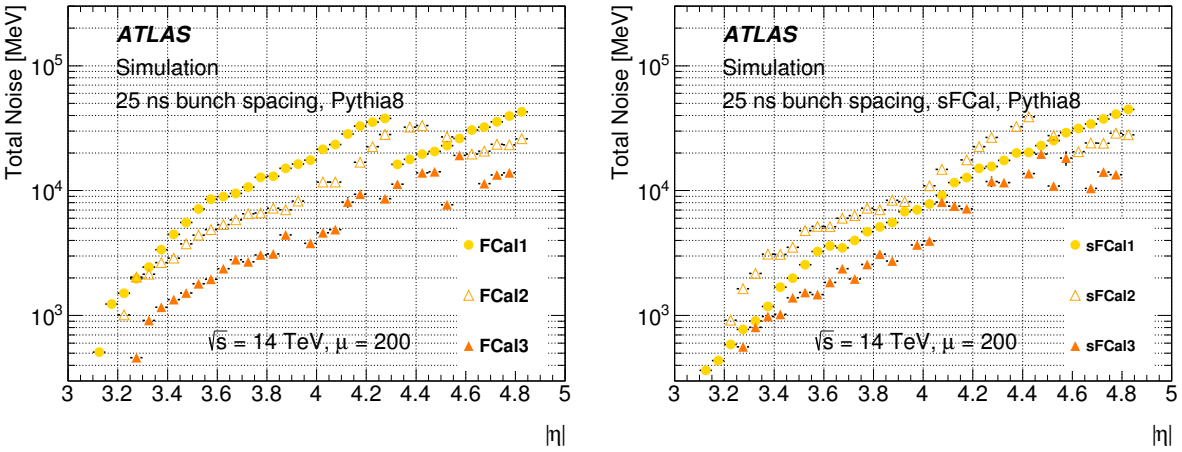

Figure 90. Calorimeter cell noise (electronic + pile-up) in the different longitudinal layers of the FCal (left) and sFCal (right) for $\mu \simeq 200$. Both simulations have been performed using PYTHIA8 [81] while the noise depicted in Fig. 44 has been derived from simulations using PYTHIA6.4 [82].

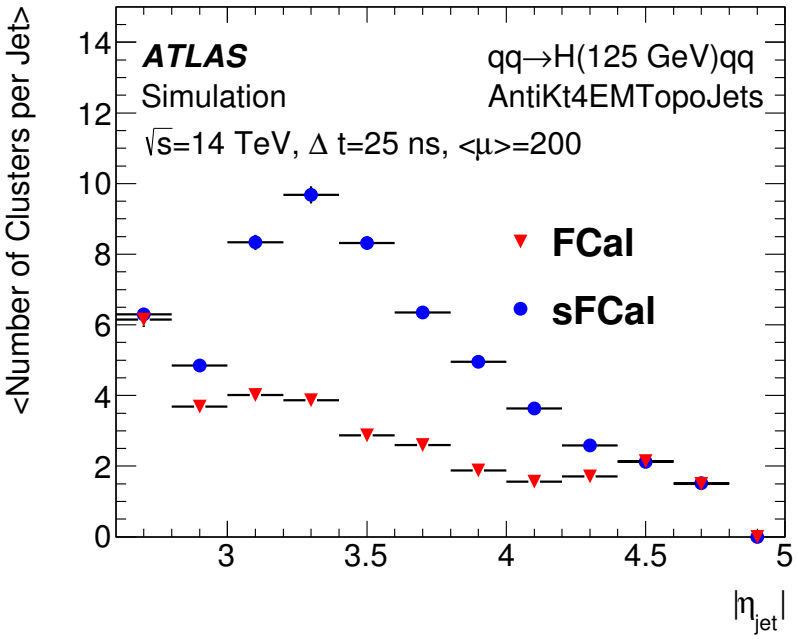

Figure 91. Average number of topo-cluster constituents per VBF tag-jet in the forward region as a function of $|\eta|$. The round dots indicate sFCal+ITk simulations; the triangles FCal+ITk simulations, both with $\mu = 200$. Jets with $R = 0.4$ at the e.m.-scale are matched to outgoing quarks from the VBF production of a 125 GeV mass Higgs boson within $\Delta R = 0.2$. The finer granularity sFCal1 leads to $2-3$ times more constituents in the region $3.2 < |\eta| < 4.3$ which provides better resolution of the substructure inside these jets. This information can be useful to reduce the impact of pile-up, and potentially to assist in distinguishing quark jets from gluon jets.

Extensive studies are being performed to quantify the expected performance improvements. Due to the substantially smaller noise RMS and the smaller cell sizes the number of topo-clusters in the forward region increases by roughly a factor 2-3, with each topo-cluster occupying a smaller volume. This is demonstrated in Fig. 91, which shows the average number of topo-cluster constituents per VBF tag-jet in the forward region as a function of $|\eta|$ for a sample of VBF production of a 125 GeV mass Higgs boson at a pile-up of $\mu = 200$. The higher number of topo-clusters leads to an improved reconstruction of the sub-structure in jets, better discrimination between the hard-scatter of interest and pile-up and hence better signal identification. Moreover it has been demonstrated in standalone single particle simulations without pile-up that a significant improvement of the φ-resolution can be reached. In case there is a very-forward extension of the ITk this will in turn translate into higher track-cluster matching efficiency and purity.

XI.2.7.5 Performance gains from the high granularity timing detector

A precision timing detector can provide the capability of identifying the vertex of origin for forward jets. Since pile-up vertices are produced at different z positions, particles from different vertices will travel different path lengths to reach the detector, arriving at different times. However, interactions also occur at different times. The spatial and time profiles of the interactions are given by the LHC bunch configuration. In Run 1, where the bunches collided almost head-on, the typical time spread of the pile-up interactions was of the order of hundreds of picoseconds, which is on the same order as the difference in time of flight of particles originating from vertices spread over a 5 cm beam-spot. Hence, the ability to resolve the vertex origin of particles using timing information is ultimately limited by the space-time pile-up density within bunches. A novel colliding scheme proposed for the HL-LHC upgrade, called crab-kissing [83], has the benefit of extending the spatial pile-up density profile while reducing the spread of the time density of pile-up interactions to very small values, enabling the use of timing information for pile-up jet tagging.

Figure 92 shows the particle arrival time spread of hard-scatter and pile-up particles for different values of the crab-kissing ψ angle, assuming that the z-position of the hard-scatter vertex is known. The curves in black correspond to the Run 1 LHC bunch configuration and show the very small separation for signal and pile-up due to the large time spread of collisions relative to the longitudinal spread of the bunch. The two crab-kissing configurations considered in this figure, corresponding to ψ angles of 2 mrad (blue) and 5 mrad (red), show a significant sharpening of the time distribution for hard-scatter particles, while maintaining a large spread in time for pile-up particles from the spatial position of the pile-up vertices.

In order to identify and reject pile-up jets, the time measurements need to be associated with the jets. The simplest approach is to consider the time of the highest p_{T} particle in the jet as an estimate of the jet time. In an alternative approach, the fraction f_t of time measurements within a certain window $[-t_c, t_c]$, defined as

$$f_t = \frac{\int_{-t_c}^{t_c} N_R(t)dt}{\int_{-\infty}^{\infty} N_R(t)dt}, \tag{5}$$

can be used as the discriminant. In order to enhance the sensitivity, only the number N_R of particles in the core of the jet with radius $R = 0.1$ is considered, and the time cut t_c is chosen to be 75 ps. While the choice of these parameters is based on the relevant distributions, a dedicated optimisation might provide better performance. Figure 93 shows the pile-up jet fake rate as a function of the hard-scatter jet selection efficiency obtained with the two different timing algorithms. The two discriminants provide complementary information. The jet time from the highest p_{T} particle provides better rejection of pile-up jets in the region with higher efficiency for hard-scatter jets, although

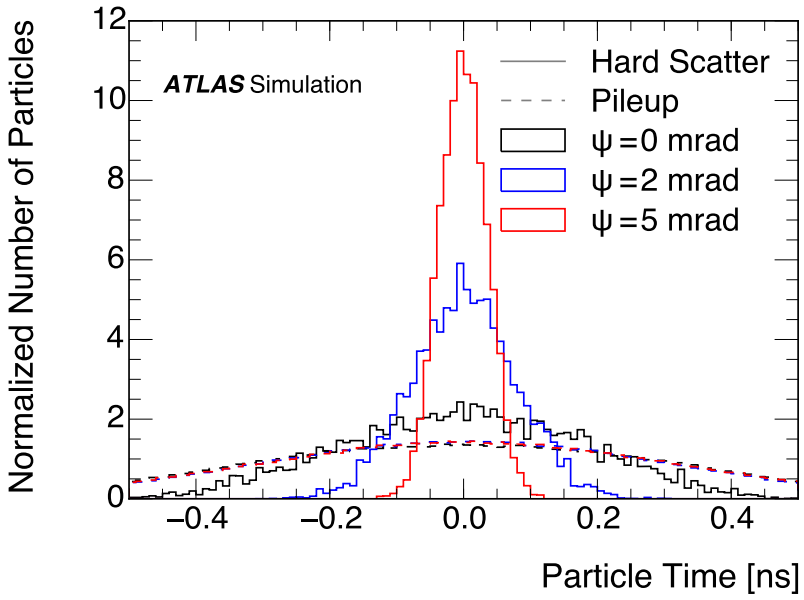

Figure 92. Arrival time spread for hard-scatter and pile-up particles for different bunch collision schemes (crab-kissing angle ψ), assuming that the z position of the hard-scatter vertex is known.

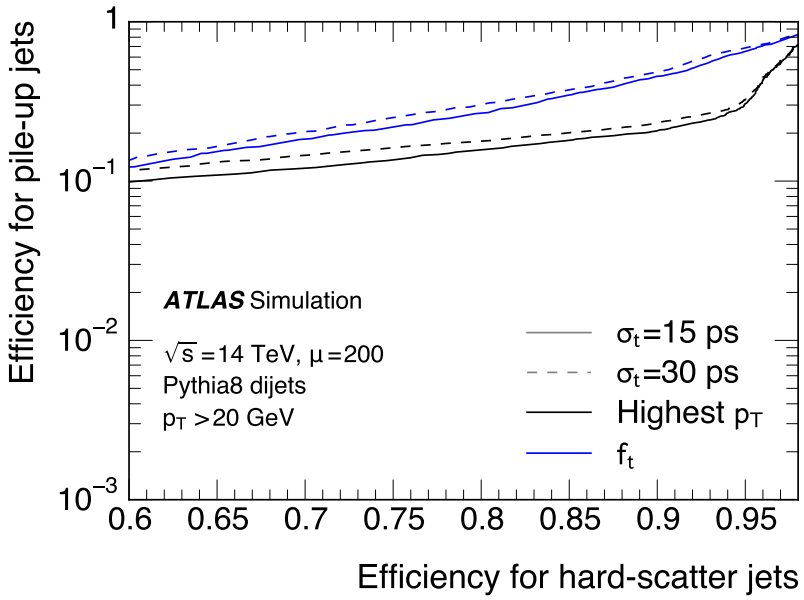

Figure 93. Efficiency for selecting pile-up jets as a function of the efficiency for selecting hard-scatter jets using the jet time from the highest p_{T} particle (black) and the time fraction f_t (blue) as discriminant, assuming a crab-kissing scheme with $\psi = 5$ mrad.

the time fraction f_t does perform better in the very low efficiency range. A combination of the two algorithms might provide improved performance over the whole efficiency range.

A timing detector with 30 ps resolution, operating with a crab-kissing scheme with $\psi = 5$ mrad, could achieve a fake rate of approximately 15% at 80% signal efficiency. It should be emphasised, however, that this is a first feasibility study with several limitations, and hence, these results are subject to potentially large uncertainties. Among the many simplifications are the lack of modelling of the jet energy resolution, the efficiency of the timing device to reconstruct low p_{T} particles, and uncertainties on the LHC reference time.

Other applications of a precision timing detector are under study, including more advanced jet-time tagging algorithms that do not rely on the crab-kissing scheme. One such handle is the fact that time measurements for particles corresponding to the same interaction yield the same values, within uncertainties. Therefore, considering the measurements within a jet, there are time regions as wide as the time resolution, where measurements are clustered. For stochastic pile-up jets, timing clusters will have similar densities, while for hard-scatter jets the highest density will correspond to the time measurements from hard-scatter particles. The performance of a discriminant using this technique degrades rapidly with the time resolution, since precise measurements are required to resolve nearby clusters.

The complementary information from a detector layer with excellent timing resolution is not yet taken into account in the physics studies presented in this document. Since pile-up mitigation is of key importance in the forward region, a timing layer to improve the separation of pile-up and hard-scatter jets when combined in an optimal way with tracking information is highly desirable.

XI.2.8 Missing transverse energy

Missing transverse energy is a global event quantity. The $E_{\mathrm{T}}^{\mathrm{miss}}$ resolution depends on identifying all the objects in an event, including leptons, photons and jets, as well as accounting for the soft term from particles which do not constitute high-p_{T} objects. A complete evaluation of the $E_{\mathrm{T}}^{\mathrm{miss}}$ resolution would therefore depend on all aspects of the scoping scenarios, across the full η-range, including changes in lepton, photon and jet energy resolutions. For previous studies the $E_{\mathrm{T}}^{\mathrm{miss}}$ resolution was parametrised as a function of the scalar sum of energy in an event [84], including an average contribution from pile-up activity. This estimate has been improved by taking into account the impact on the resolution of rejecting pile-up jets using tracking variables in each scoping scenario. A requirement of $R_{pT} > 0.1$ is applied to all jets, giving a significant improvement in the $E_{\mathrm{T}}^{\mathrm{miss}}$ resolution for the Reference scenario, compared to the Middle and Low scenarios. The chosen $E_{\mathrm{T}}^{\mathrm{miss}}$ variable uses a track soft term [85], and there is also a modest contribution from the improvement in the evaluation of this contribution when including tracks at larger $|\eta|$, but the dominant effect is from the removal of pile-up jets. The $E_{\mathrm{T}}^{\mathrm{miss}}$ resolution derived from fully simulated $t\bar{t}$ events with average $\mu = 200$ as a function of ΣE_{T} is shown in Fig. 94. The relative improvement in resolution grows with ΣE_{T}, until the Middle scenario is 40% worse than the Reference scenario, and the Low scenario is 70% worse for the most energetic events in the sample.

XI.2.9 Flavour tagging

The identification of b-quark jets, typically referred to as b-tagging, is evaluated for the different scoping scenarios in simulated $t\bar{t}$ events. Several algorithms have been investigated previously in order to validate b-tagging with the Phase-II detector and high pile-up [84]. These studies have been extended to larger values of $|\eta|$.

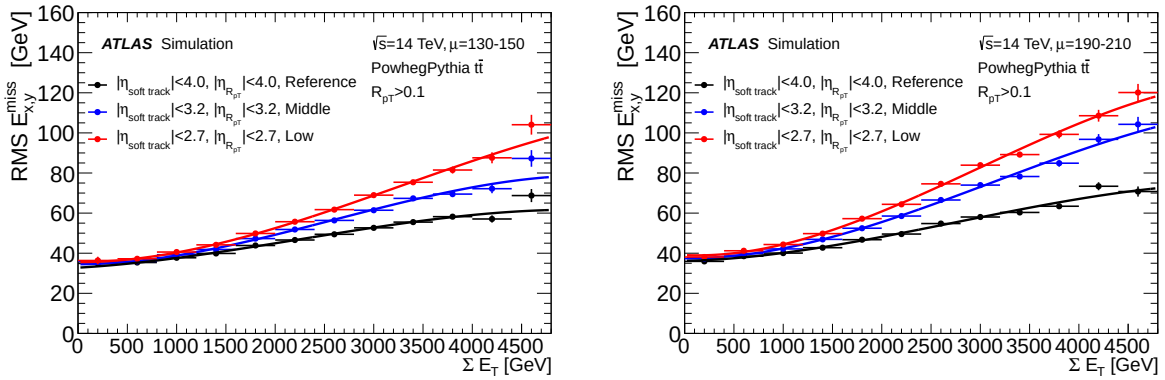

Figure 94. The resolutions of the x and y components of $E_{\mathrm{T}}^{\mathrm{miss}}$ in the three scoping scenarios for samples of $t\bar{t}$ events with $\mu = 140$ (left) and $\mu = 200$ (right). The resolutions are shown as a function of the scalar sum of total energy in the event, with MC statistical uncertainties.

All results here are quoted for the MV1 b-tagging algorithm [86], which combines information from track impact parameter and secondary vertex based algorithms in an artificial neural network. It is trained with b-jets as signal and light-flavour jets as background using Run 1 samples. Studies are underway to produce a b-tagging algorithm specifically optimised for the high luminosity LHC. The performance of the MV1 b-tagging algorithm is determined as a function of jet flavour, p_{T}, and $|\eta|$ for the three different scoping scenarios using fully simulated samples of $t\bar{t}$ events with pile-up.

It is required that a primary vertex is reconstructed in the event and in the case of several candidate vertices, the primary vertex is defined as the vertex with the largest sum of squared transverse momenta of the associated tracks. To factorise the primary vertex finding efficiency from the measurement of the b-tagging performance, it is required that the selected primary vertex is matched to the true hard-scatter vertex. The vertices are considered matched if they are within $\Delta z = 1$ mm of the true vertex.

Jets are reconstructed as described in Section XI.2.7. To measure the b-tagging performance for hard-scatter jets, only jets which are matched to a parton from the top decay are considered. The matching is performed by requiring that the jet is within $\Delta R < 0.3$ of a parton from the top decay, with $p_{\mathrm{T}} > 15$ GeV. A flavour label is assigned by matching jets to the truth-level b and c quarks with $p_{\mathrm{T}} > 5$ GeV, in a ΔR cone of less than 0.3. If a b-quark is found within the cone the jet is labelled as a b-jet. If no b-quark is found, the search is repeated for c-quarks, then for τ leptons. If no match is found for b, c, or τ, the jet is labelled as a light-flavour jet. Pile-up jets are defined as jets which are not matched within a ΔR cone of less than 0.6 to a truth-jet with $p_{\mathrm{T}} > 4$ GeV from the hard-scatter process. Pile-up jets are not assigned a specific flavour label and are instead as a separate category to account for the mixture of flavours that they include.

When evaluating the flavour tagging performance the following metrics are of interest:

b-jet (c-jet) tagging efficiency The efficiency to select a b-jet (c-jet) calculated by the total number of b-jets (c-jets) which pass the b-tagging selection divided by the total number of b-jets (c-jets) in the sample.

Mis-tag rate The rate at which light-flavour jets pass the b-tagging selection, given by the total number of light-flavour jets which pass the b-tagging selection divided by the total number of light-flavour jets in the sample.

Light-flavour jet rejection This is the inverse of the mis-tag rate.

Pile-up tagging rate The rate at which pile-up jets pass the b-tagging selection, given by the total number of pile-up jets which pass the b-tagging selection divided by the total number of pile-up jets in the sample.

The b-tagging performance is measured as a function of p_{T} and $|\eta|$ for b, c, light-flavour and pile-up jets, providing 'efficiency maps' of the probability to tag a jet of a given flavour, p_{T} and $|\eta|$. Most of the simulated samples have 50,000 events for a particular layout and pile-up. Due to these limited statistics, it is necessary to parametrise the efficiency to achieve smooth and continuous maps. A two dimensional fit is carried out as a function of p_{T} and $|\eta|$ using the binned efficiency measurements, and it is verified that there is a reasonable level of agreement between the parametrised and actual b-tagging efficiency.

Figure 95 illustrates the performance of the MV1 algorithm, showing the light-flavour jet rejection as a function of the b-tagging efficiency for the various detector scenarios. There is very little performance difference between the Reference and Middle scenarios for $|\eta|$<2.7, but a significant degradation is observed for the Low scenario. The degraded performance for the Low scenario is related to the tracking performance. The tracking performance in the Reference and Middle scenarios is very similar in terms of the efficiency and fake rate (see Figs. 76 and 77 respectively in Section XI.2.2), which suggests they should have very similar b-tagging performance, as is clearly seen in Fig. 95. However, when moving to the Low scenario, the tracking efficiency drops by 5% and the fake-rate increases by almost an order of magnitude. This degrades the b-tagging performance, leading to an increase in both the mis-tag and pile-up tagging rates for a fixed b-tagging efficiency of 70%. These studies did not use an optimised selection on the number of hits on a track as a function of η. A first cross-check indicates that adjusting this requirement in the Low scenario the mis-tag rate could be reduced by at most 30% around $|\eta| = 1.5$, while the b-tagging efficiency is almost unaffected. For comparison, in Run 1, the MV1 algorithm gave a light-jet rejection factor of about 130 for the 70% operating point [86].

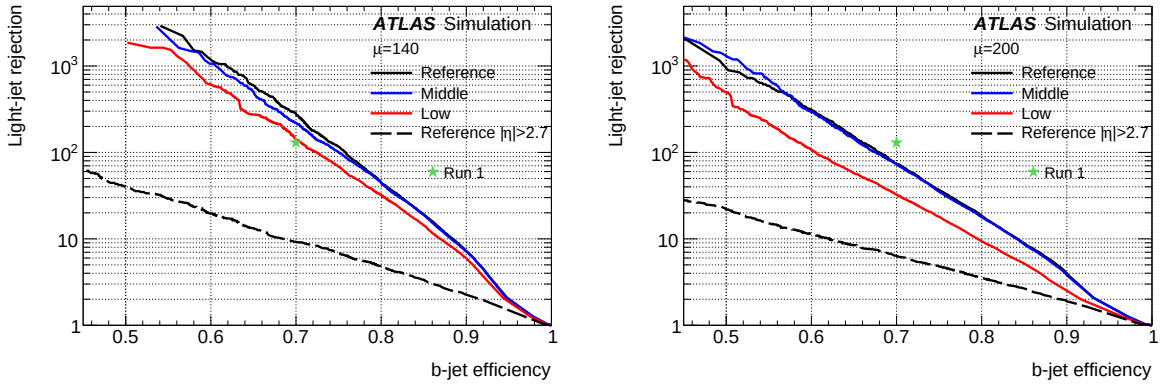

Figure 95. The light-flavour jet rejection versus the b-jet efficiency for the MV1 b-tagging algorithm in the Reference (black), Middle (blue) and Low (red) scenarios for a pile-up of 140 (left) and 200 (right) for jets with $p_{\mathrm{T}} > 20$ GeV and $|\eta| < 2.7$. The dashed curves are for jets in the Reference layout for $|\eta| > 2.7$. The equivalent Run 1 operating point is shown by a green star.

The performance of the tagging algorithm has also been tested under the assumption of a 10% module loss in both the Reference and Low scenarios. Figure 96 shows that a 10% module loss leads to a significant deterioration in the performance in both scenarios, due to the degradation of the tracking seen in Section XI.2.2. The performance as a function of η and p_{T} is also shown in Fig. 97. The working point giving an average efficiency of 70% for b-jets with $|\eta| < 2.7$ in $t\bar{t}$ events

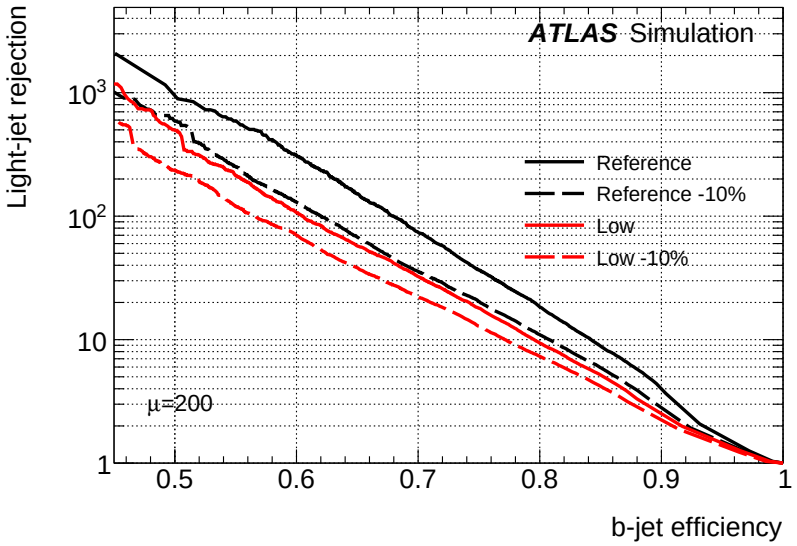

Figure 96. The light-flavour jet rejection versus the b-jet efficiency for the MV1 b-tagging algorithm in the Reference (black) and Low (red) scenarios for a pile-up of 200 for jets with $p_{\mathrm{T}} > 20$ GeV and $|\eta| < 2.7$. The solid line corresponds to full coverage while the dotted one to the case where 10% of modules are not operational.

is selected for each fully operational layout, and the same working point is used for the equivalent samples with 10% non-operational modules. The degradation in the tracking performance due to the 10% dead modules in the Reference scenario, results in a similar efficiency and fake-rate as the Low scenario. As therefore expected the b-tagging performance of the Reference scenario with 10% dead modules is very similar to the Low scenario. The tracking performance in the Low scenario with 10% dead modules, results in a further absolute loss of about 10% in the tracking efficiency for a similar fake-rate, which is reflected in the significant degradation in the b-tagging performance. The impact of the degradation in the Reference scenario case is however alleviated due to the higher initial baseline performance, ensuring a reasonable level of performance is maintained.

With the extension of the tracking in the forward region, it is found to be possible to b-tag jets with a reasonable performance up to an $|\eta|$ of about 3.5 with the Reference scenario compared to an $|\eta|$ of about 3.1 in the Middle and 2.7 in the Low scenarios.

XI.2.10 Tau performance

The main impact for final states including taus is expected to come from the restriction on trigger rates, and from the degraded tracking performance in the Middle and Low scoping scenarios with high pile-up. Work is in progress to develop a τ-reconstruction algorithm at large η to take advantage of the extended coverage of the Reference scenario.

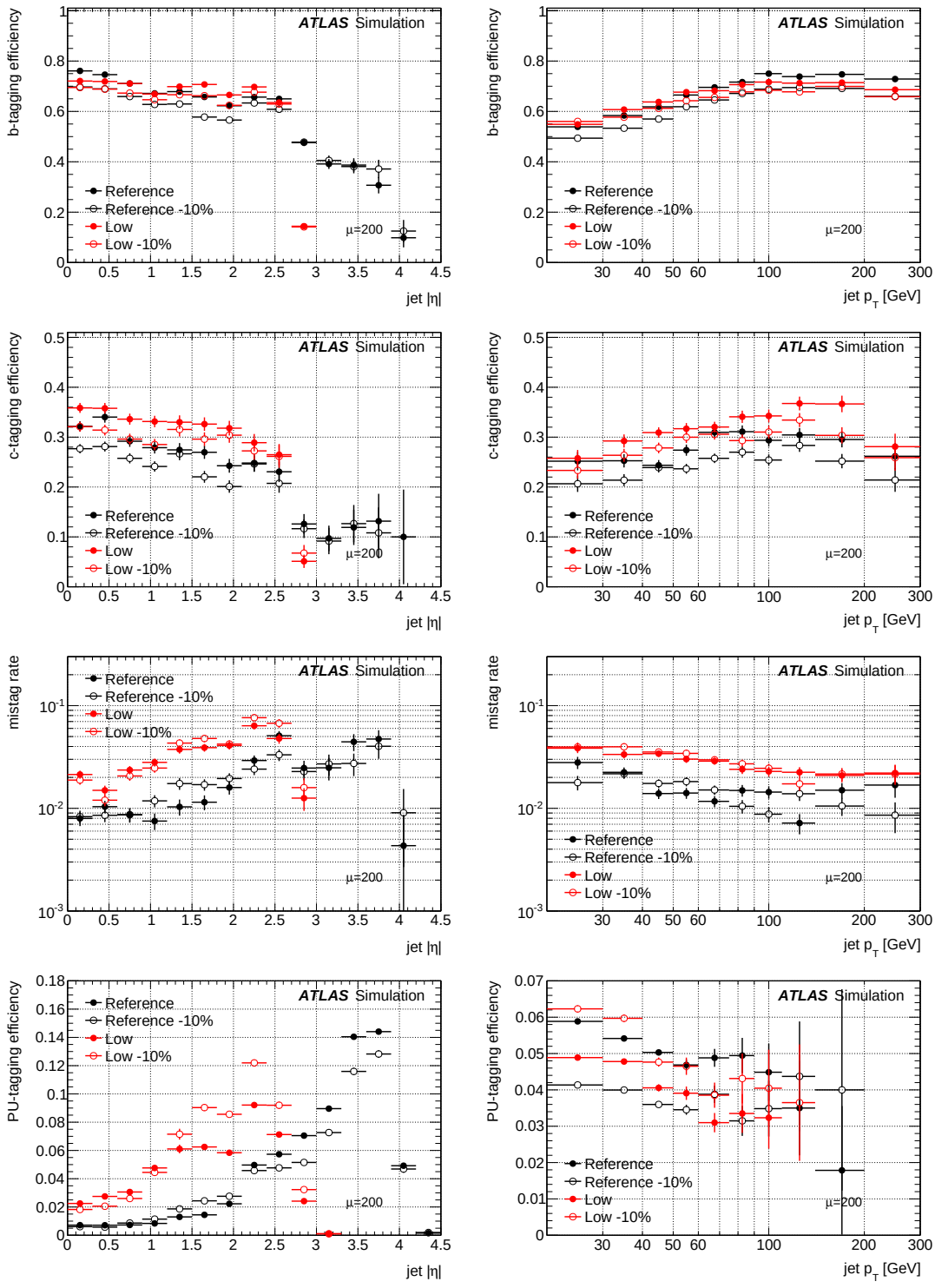

Figure 97. The rate of tagging jets in $t\bar{t}$ events with the 70% operating point of the MV1 b-tagging algorithm as a function of η (left) and p_{T} (right) for true b-jets, c-jets, light quark jets from the hard-scatter and pile-up jets (from top to bottom).

XI.3 Physics Potential and Selected Analyses

Several physics studies have been carried out to assess the impact of the object performance in the scoping scenarios. The aim is to pick some representative channels which illustrate the impact of the scenario-dependent performance of specific objects on a particular physics result.

Measurements of Higgs boson fiducial and differential cross-sections are an important ingredient of the HL-LHC physics programme. These are sophisticated analyses which are under development, and the potential improvements from the large data sample are not reflected in extrapolations of the precision in simpler variables such as the cross-section times branching ratio measurement (characterised as the uncertainty in the ratio μ to the Standard Model prediction). The potential gains are illustrated below for the $H \to ZZ^{(*)} \to \mu\mu\mu\mu$ channel. The rare decay mode $H \to \mu\mu$ was also considered; it can be observed with the full HL-LHC dataset with a significance larger than 8σ. The muons in this case are more central, coming directly from the Higgs boson decay, and the impact of the scoping scenarios on the signal significance is less marked than for the four-muon final state. High trigger efficiency with respect to the offline selection is crucial to select a large fraction of the events produced by this rare decay mode of the Higgs boson. While the Reference scenario ensures a trigger efficiency close to 100%, the Low scenario trigger efficiency is reduced to 92%. Furthermore, including muons that are reconstructed in the pseudo-rapidity region $2.5 < |\eta| < 4.0$ increases the overall signal yield by 10%.

The scoping scenarios will affect the precision with which most Higgs boson decay modes can be investigated. For example, tau-lepton identification at large η will allow extended fiducial measurements of the $H \to \tau\tau$ decay.

Distinguishing the different Higgs boson production measurements is an important part of understanding electroweak symmetry breaking. The largest cross-section is from gluon-gluon fusion. The next is about a factor of ten lower, by vector-boson fusion, which is characterised by the presence of forward jets from the hard scatter process, as well as the more central Higgs-boson decay products. The ability to reject pile-up jets plays a critical role here. This is true for any Higgs decay mode, and is illustrated here with the ZZ and WW final states. For the ZZ case, the most important aspect is to distinguish between ggF and VBF Higgs boson production. Other backgrounds are suppressed by a tight cut on the four-lepton invariant mass. For the VBF WW process, $t\bar{t}$ and other reducible backgrounds play a role. The analysis relies on a central jet veto and b-jet veto to reduce the background. The improved lepton and b-tagging performance will additionally help in identifying associated production of a Higgs boson with a W boson, Z boson or $t\bar{t}$ pair in the HL-LHC, and the full set of improvements will impact the measurement of Higgs boson pair production including decays to bb, $\tau\tau$ and $\gamma\gamma$.

Standard Model measurements will continue at the HL-LHC, with emphasis on differential cross-section measurements, for example to constrain anomalous gauge couplings. An example analysis of same-sign WW production is presented below, which takes advantage of the increased η coverage for lepton identification and also vetoing additional leptons to reject WZ and ZZ background. As for the VBF studies, this analysis also relies on tagging forward jets from the hard scatter process. An extension of the pseudo-rapidity coverage for lepton identification would also be beneficial for differential cross-section measurements of W and Z boson production, which would improve the experimental uncertainty of parton distribution functions at large x. This is a challenging analysis which will be investigated in future HL-LHC studies.

Numerous searches for physics beyond the Standard Model have been studied in building the case for the HL-LHC. Two examples are presented in this document. Searches for new physics also consider non-standard topologies. Section XI.2.5 illustrated the importance of the outer silicon detector layer for photon conversions. There are many new physics scenarios where charged or

neutral heavy long-lived particles exist. These have been searched for in Run 1 also via vertexing, using similar approaches as used here for conversion finding. The ability to find vertices at large radii is instrumental for such searches [87].

A search for chargino-neutralino production in a supersymmetric scenario where the electroweakinos decay via Higgs bosons to a final state with one lepton, two b-jets and moderate $E_{\mathrm{T}}^{\mathrm{miss}}$ is sensitive to the performance for these objects. High mass states such as Z' tend to produce central final states, and so do not benefit from the forward extensions. However, in the case of a search for $Z' \to t\bar{t}$ using a single lepton trigger, it is observed that both the signal and the background yields in the muon channel decrease by about 10% both from the Reference to the Middle and from the Middle to the Low scenario. This effective loss in luminosity does not lead to a change in sensitivity for this particular search, but would be relevant in other $t\bar{t}$ analyses. A search for resonant Higgs-boson pair production decaying to four b-jets also shows the impact of the improved b-tagging performance, and is described in detail below.

XI.3.1 Inclusive Higgs boson production with $H \to ZZ^{(*)} \to \mu^+\mu^-\mu^+\mu^-$

The impact of the various detector scenarios has been assessed by studying the variation of acceptance for Higgs boson production with the subsequent decay $H \to ZZ^{(*)} \to \mu^+\mu^-\mu^+\mu^-$. This section focuses on measuring the significance of this decay mode where the boson can be produced through any of the allowed Standard Model processes. The only background considered is the dominant contribution arising from irreducible $ZZ^{(*)}$ production. Additional backgrounds, *e.g.* Z+jet and $t\bar{t}$, which are not considered in this study, will have a small effect on the final result.

The object selection and performance depend on the scenario under consideration as documented in Section XI.2. The event selection is based on that developed for the Run 1 analysis [88], namely the event must contain four muons and their transverse momenta ordered in p_{T} are required to be greater than 20 GeV, 15 GeV, 10 GeV, and 6 GeV, respectively. The difference in $\eta - \phi$ space (ΔR) between each of the muons must be greater than 0.1. The pair with mass closest to the Z boson mass (m_{12}) is required to have $50 < m_{12} < 106$ GeV, and the other muon pair is required to have $12 < m_{34} < 115$ GeV. To ensure a good measurement of m_{12}, at least one of the muons from this pair is required to have a good resolution by lying in the region $|\eta| < 2.7$. As in the Run 1 analysis, a Z mass constraint is applied to m_{12}, however, the constraint used here is a simplified version. Compared to what is used in the Run 1 analyses this Z mass constraint uses the p_{T} resolution instead of the full covariance matrix, and only a limited mass range is considered. In a region of -21 GeV to $+30$ GeV around the Z mass, the Z line-shape given by a Breit-Wigner distribution is convoluted with the Z boson resolution described by a Gaussian distribution on an event-by-event basis. The width of the Gaussian distribution is defined by the p_{T} resolution of the two muons. After the most likely Z mass value is found the muon p_{T} rescaling factors are determined via a χ^2 test.

The overall acceptance after analysis selection is 47% for $|\eta| < 2.7$, and increases to 57% with $|\eta| < 4.0$, which corresponds to an acceptance gain of 21% and would allow an improved measurement of the differential cross-sections for a given integrated luminosity. Figure 98 shows the acceptance as a function of η with no detector requirements (100% efficiency) and after applying all the trigger and detector effects in the Reference scenario. The additional impact is also shown of allowing at most one or at most two of the muons from the Higgs boson to be segment-tagged (the only possible identification available in the regions $|\eta| < 0.1$ or $|\eta| > 2.7$).

The significance is then computed as the ratio of the number of signal events in the $\pm 1.5\sigma$ window centred at the reconstructed Higgs boson mass over the number of background events, where σ is the fitted mass resolution. Muon identification beyond $|\eta| = 2.7$ is only available in the Reference scenario. The corresponding resolutions are shown in three η bins in Table 28. As the

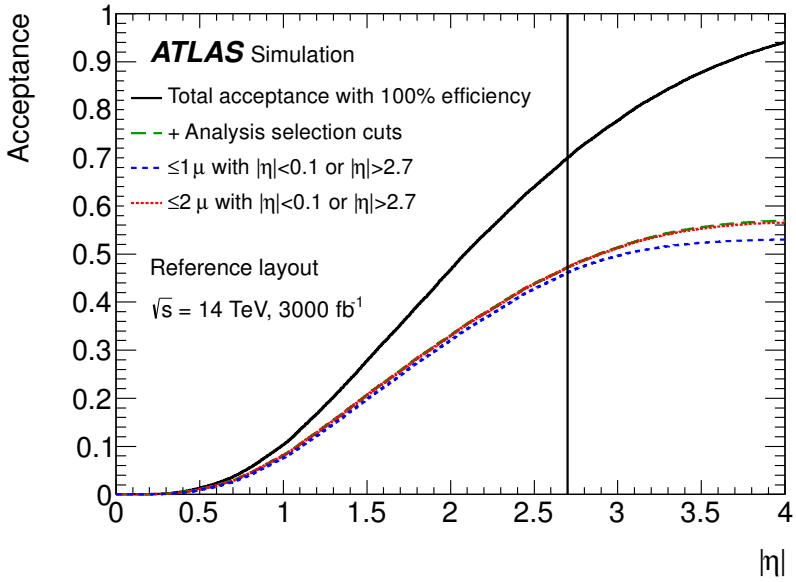

Figure 98. Acceptance of $H \to 4\mu$ events as a function of rapidity coverage in which the four muons from the Higgs decay are contained. Additional curves are shown for the categories in which at most one (blue) or two (red) of the muons are allowed to be segment-tagged by the muon detector (the only possible identification available in the regions $|\eta| < 0.1$ or $|\eta| > 2.7$), where the resolution is degraded compared to the central eta region. The vertical line indicates the acceptance to reconstruct muons in the Middle and Low layouts.

width is very similar for the three scenarios in the central η bin, the width as obtained from the fit in the Reference scenario is used for all scenarios. In the Reference scenario the results are computed by statistically combining the $|\eta|$ ranges [0; 2.7], [2.7; 3.2], and [3.2; 4.0]. These bins are motivated by the degradation of the muon resolution in the very forward region as the magnetic field produced by the solenoid surrounding the tracking detector decreases from its nominal field of 2 T to about 1 T at small radius where the $|\eta| = 4$ tracks provide their final measurements at the large z end of the tracking volume. It is observed that the yield of Higgs bosons is reduced by 18% in the Middle and 21% in the Low scenario (both scenarios only include the central η bin, but the trigger efficiency is further reduced in the Low scenario). The corresponding relative uncertainty on the signal strength ($\Delta\mu/\mu$) is reported in Table 29. The numbers for $\Delta\mu/\mu$ are slightly optimistic as the reducible background is not taken into account. In particular the background from $Z + \text{jet}$ production in the region $|\eta| > 2.7$ might have a significant contribution. For all the three layouts (the Middle and Low are identical for this analysis), a similar precision for the measurement is found with slightly better values of the relative uncertainty on the signal strength for the Reference scenario. This is driven by the increase of background due to the degraded muon resolution for $|\eta| > 2.7$ and the resulting broadening of the invariant mass peak (see Table 28). Despite this, the gain in the number of reconstructed Higgs bosons in the Reference scenario will allow higher statistics measurements of differential cross-sections, which are an important method to look for deviations from the SM Higgs hypothesis using effective field theory approaches.

XI.3.2 Studies of the VBF $H \to ZZ^{(*)} \to \ell^+\ell^-\ell^+\ell^-$ process

The complete set of measurements of Higgs boson properties with the HL-LHC data set includes measurements of differential cross-sections for specific Higgs boson production mechanisms Such

Table 28. Reconstructed Higgs boson mass and width for $H \to ZZ^{(*)} \to 4\mu$ in rapidity bins defined by the muon with the largest $|\eta|$ value for the Reference layout. The numbers are obtained from a fit of a Gaussian distribution in $\pm 1.5\sigma$ around the Higgs boson mass. The uncertainty given is the uncertainty of the fit result.

Coverage	Mass (GeV)	Width (GeV)
$\lvert\eta^{\mu}_{\text{max}}\rvert < 2.7$	124.95 ± 0.01	1.11 ± 0.01
$2.7 < \lvert\eta^{\mu}_{\text{max}}\rvert < 3.2$	125.31 ± 0.07	2.53 ± 0.08
$3.2 < \lvert\eta^{\mu}_{\text{max}}\rvert < 4.0$	125.89 ± 0.17	4.61 ± 0.23

Table 29. Expected number of events in a region of $\pm 1.5\sigma$ around the Higgs peak for 3000 fb^{-1} of data in the $H \to 4\mu$ and $ZZ^{(*)} \to 4\mu$ channel for the various layouts. The last row shows the relative uncertainty on the signal strength. As the width is very similar in the three layouts for $|\eta| < 2.7$ the width as obtained from a fit in the Reference layout is used here. The uncertainties correspond to the statistical uncertainties.

Scenario	$H \to 4\mu$	$ZZ^{(*)} \to 4\mu$	$\Delta\mu/\mu$
Reference	2551 ± 51	741 ± 27	0.022
Middle	2104 ± 46	351 ± 19	0.024
Low	2014 ± 45	336 ± 18	0.024

measurements require a clear identification and separation of events arising from the various Higgs boson production mechanisms. This section concerns the measurement of the signal strength $\Delta\mu/\mu$ for the channel $pp \to qqH$ with $H \to ZZ^* \to \ell^+\ell^-\ell^+\ell^-$). The production of Higgs bosons by vector boson fusion production (VBF) is a mechanism where two incoming quarks emit virtual W or Z bosons which fuse to form a Higgs boson. It is predicted to be the second largest contribution to the Higgs boson production cross-section, although it is still an order of magnitude smaller than Higgs boson production by the gluon-gluon fusion (ggF) mechanism. The latest study of expected sensitivity at the HL-LHC is documented in Ref. [89]. Based on the Run 1 analysis [88], the signal-to-background ratio for the VBF-enriched category is expected to be about 7. The focus of the current search is therefore to discriminate between the VBF signal and the signal where the Higgs boson is produced via gluon fusion in association with jets. In what follows the ggF production of Higgs bosons is considered to be a background process. Other contributions are considered negligible and thus discarded.

In this analysis, events are selected if they contain four leptons (electrons or muons) and two forward jets. The object performance depends on the scenario under consideration as documented in Section XI.2. The selection criteria applied in all three scoping scenarios are summarised in Table 30. Pile-up jets are superimposed on the hard-scatter event, taking the working point with pile-up mis-identification probability of 2%. Jets overlapping with selected leptons within a cone of radius $R = 0.2$ are discarded. Using a combination of single and di-lepton triggers, the overall trigger efficiency for these four lepton events is 96% for the Reference, 93% for the Middle, and 90% for the Low scenario.

Events are pre-selected if they contain at least one quadruplet of leptons consisting of two pairs of same-flavour opposite-charge leptons where the three highest p_{T} leptons satisfy $p_{\text{T}} > 20$, 15, 10 GeV. A candidate quadruplet is removed if $m_{\ell\ell} < 5$ GeV or $\Delta R_{\ell\ell} < 0.10$ (0.20) for any pair of same (different) flavour leptons in that quadruplet. The candidate quadruplet is then the one with the

Table 30. Common object selection criteria in the Reference, Middle, and Low scenarios for VBF $H \to ZZ^{(*)}$.

Variable	Applied criteria
Minimum ℓ (e, μ) p_{T} (GeV)	7, 6
Maximum ℓ (e, μ) $\lvert\eta\rvert$	2.47, 2.7
Minimum light-flavour jet p_{T} (GeV)	30
Maximum light-flavour jet $\lvert\eta\rvert$	4.5

leading and sub-leading mass closest to the Z mass. The QCD scale variation uncertainty in the ggF sample can become very large, O(100%), if tight VBF-like restrictions are imposed, enhancing the ggF + 2 jet contribution [90]. These uncertainties are limited to at most 15% by removing information on the shape of the transverse momentum of the system, $p_{T,Hjj}$, for values below 50 GeV from the BDT described below. Additional event requirements are reported in Table 31.

Table 31. Event selection criteria defining the signal region in the Reference, Middle, and Low scenarios for VBF $H \to ZZ^{(*)}$. The sub-leading Z candidate must have a mass greater than $m_{\mathrm{thresh.}}$, whose value used depends on the reconstructed 4ℓ mass, and varies from 12 to 50 GeV.

Variable	Applied criteria
Leading di-lepton mass (GeV)	$50 < m_{12} < 106$
Sub-leading di-lepton mass (GeV)	$m_{\mathrm{thresh.}} < m_{34} < 115$
Number of jets	≥ 2
m_{jj} (GeV)	> 130

After the full event selection is applied, a boosted decision tree (BDT) is used to discriminate the VBF signal from the ggF background. The BDT is based on the following six observables: invariant mass of the selected forward jets, m_{jj}; separation of these jets in η, $\Delta\eta_{\mathrm{jj}}$; transverse momentum of the Higgs boson plus jets, $p_{\mathrm{T},H\mathrm{jj}}$; transverse momentum of each of the jets, $p_{\mathrm{T,jet\,1}}$ and $p_{\mathrm{T,jet\,2}}$; and the Zeppenfeld variable $\eta_{ZZ}^{\mathrm{Zepp}} = \eta_{ZZ} - \left\langle \eta_{(\mathrm{jet\,1})}, \eta_{(\mathrm{jet\,2})} \right\rangle$. Figure 99 shows the resulting BDT output for the Reference, Middle, and Low scenarios. Events are then divided into three categories defined by a selection on the BDT output with bin edges [1, 0.8, 0.6, 0] and the negative log likelihood (NLL) minimisation technique is used to fit in all three bins simultaneously for the signal significance Z_0 and $\Delta\mu$ [4]. The same bin edges were found to be optimal in each scoping scenario. The NLL distribution width and statistical uncertainty factor are accounted for in the fits.

From Table 32 it is observed that Z_0 decreases by 5% and 14% in the Middle and Low scenarios, respectively, and the signal strength uncertainty $\Delta\mu/\mu$ increases by 2% and 6% when no theoretical uncertainties are considered. Including estimates of the QCD scale variation uncertainty, made using the Stewart-Tackmann approach, result in a deterioration of the significance of ~12% (2%) in the Low (Middle) scenario with respect to the Reference one, while the signal strength uncertainty degrades by ~11% (4%).

To make a precise measurement of the VBF process, it is necessary to determine the purity of the VBF dedicated selection. In Table 33 the pile-up contamination of the VBF and ggF Higgs boson

[4] The statistical significance is computed using the background-only p-value (p_0). The p_0 value is then converted to the corresponding number of standard deviations (σ) in a one-sided Gaussian test. This equivalent formulation is referred to as the local significance, Z_0.

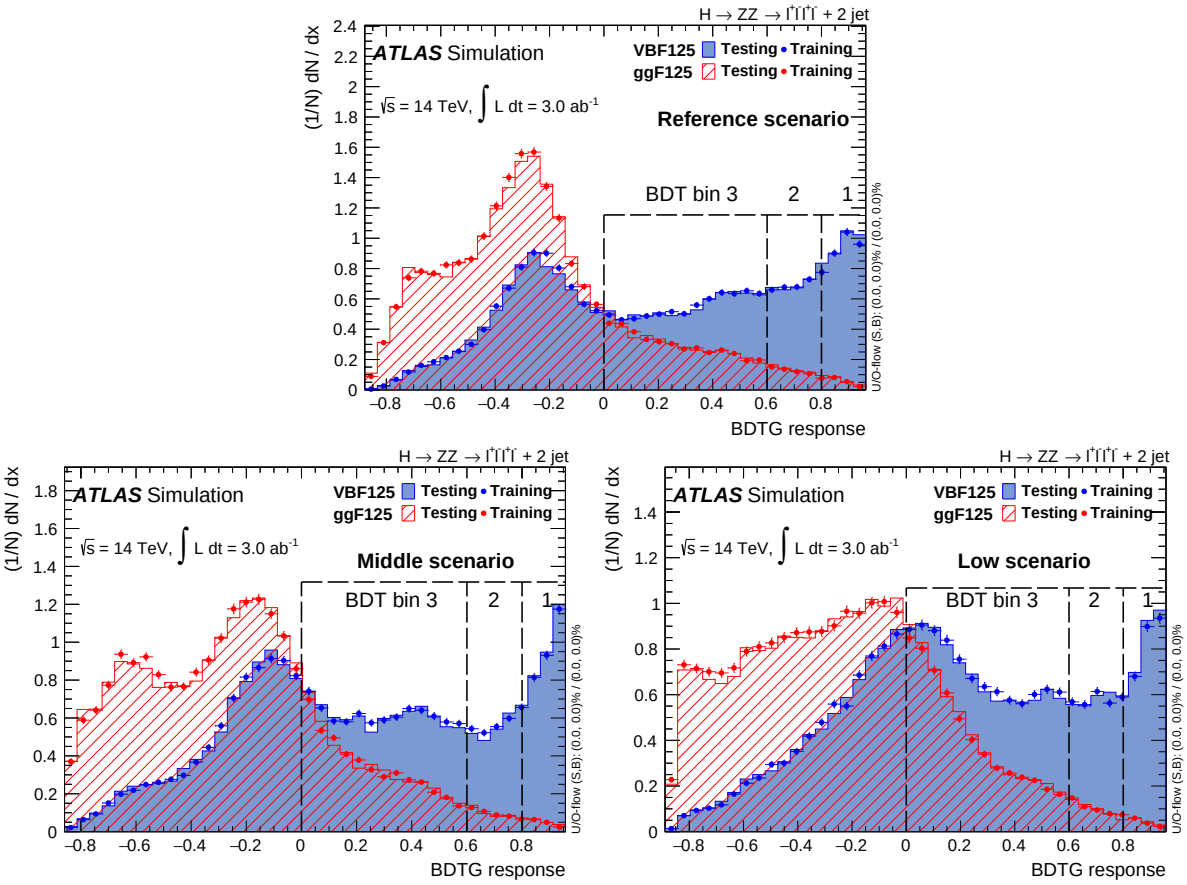

Figure 99. BDT output for for the Reference (top), Middle (bottom left), Low (bottom right) scenarios for the VBF $H \to ZZ^{(*)}$ analysis. The signal refers to VBF Higgs boson production and background refers to ggF production. The error bars show the Monte Carlo statistical uncertainty.

Table 32. The local Z_0-values and the precision on the combined signal strength $\Delta\mu/\mu$ in the Reference, Middle, and Low scenarios for VBF $H \to ZZ^{(*)}$ without and with the inclusion of theoretical uncertainties. The additional integrated luminosity, $\Delta\mathcal{I}$, to allow the $\Delta\mu/\mu$ precision in the Middle and Low scenarios to match the Reference scenario is also given.

Scoping Scenario	without theo. unc.			with theo. unc.		
	$\Delta\mu/\mu$	$\Delta\mathcal{I}$ (fb^{-1})	Z_0-value (σ)	$\Delta\mu/\mu$	$\Delta\mathcal{I}$ (fb^{-1})	Z_0-value (σ)
Reference scenario	0.134	–	11.41	0.167	–	7.64
Middle scenario	0.137	125	10.86	0.174	350	7.48
Low scenario	0.142	425	9.84	0.186	1000	6.75

production signals is shown. The contamination is reduced significantly in the Reference scenario with respect to the Middle and Low ones. This in turn allows for a much better discrimination between the VBF and the ggF signal, and hence a better potential for precision Higgs boson properties measurements in this production mode.

Table 33. Pile-up contamination of the VBF and ggF $H \to ZZ^{(*)}$ signal for the various scenarios in the three BDT output bins as defined in the text.

	Pile-up impurity (%)		
Scoping scenario	Bin 1	Bin 2	Bin 3
VBF Sample			
Reference	2.0	4.6	13.1
Middle	3.0	6.4	23.6
Low	5.2	12.0	38.7
ggF Sample			
Reference	23.2	37.9	52.1
Middle	24.0	43.4	65.0
Low	41.2	59.4	76.2

In conclusion, the Reference scenario brings several improvements over the Middle and Low scenarios. Due to the extension of the tracking confirmation to larger η values, it brings much better separation between the background, which has substantial pile-up contamination, and the signal. This will be especially important once systematic uncertainties on pile-up modelling and jet energy scale are taken into account.

XI.3.3 Studies of the VBF $H \to WW^{(*)} \to \ell\nu\ell\nu$ process

A high precision measurement of the vector-boson fusion production mode of the Higgs boson, with subsequent decay through the $H \to WW^{(*)} \to \ell\nu\ell\nu$ channel, enables the extraction of the vector boson coupling to the Higgs boson with a very small theoretical uncertainty arising from the production process. This measurement also provides a good benchmark for investigating the effects of the high pile-up environment. Due to the absence of a fully reconstructed final state (because of the final-state neutrinos) and the unique VBF topology, this measurement will be quite sensitive to the detector performance under HL-LHC conditions, since the analysis uses missing transverse momentum, forward jets without any jet activity in the central region and the veto of b-tagged jets for $t\bar{t}$ background rejection.

The result from the Run 1 cut-based analysis achieved an expected (observed) significance of 2.1 (3.0) σ for the $H \to WW^{(*)} \to \ell\nu\ell\nu$ channel [91]. The present analysis attempts to minimise the uncertainty on the VBF signal strength, and to improve the precision on the vector boson coupling constant determination in order to estimate possible residual contributions from BSM processes.

This analysis is performed in a different manner to the other physics analyses in this document. The fully simulated 8 TeV Monte Carlo samples are extrapolated to the 14 TeV conditions based on parton distribution function (PDF) re-weighting and emulation of the difference in performance of the ATLAS detector with the high pile-up environment. The signal is considered to be Higgs boson production through VBF and in associated production with a W and a Z boson (VH). The ggF production mode is considered as a background. The following background processes are

also considered: the irreducible SM WW production, $t\bar{t}$, single top ($tW/tb/tqb$), non-WW di-boson ($W\gamma^{(*)}/WZ/ZZ$), $Z/\gamma^* + \text{jets}$ and $W + \text{jets}$ backgrounds.

The selection closely follows the published strategy in order to suppress the large variety of backgrounds present in the final state with two forward jets, two leptons and $E_{\mathrm{T}}^{\mathrm{miss}}$. A single lepton trigger is required, and for the analysis, the leading lepton p_{T} is required to be at least 25 GeV, with the sub-leading lepton required to be at least 15 GeV. Jets are required to have $p_{\mathrm{T}} > 30$ GeV, overlap removal between jets and leptons is applied, and the event is rejected if any jet is b-tagged. Jets are then required to satisfy a track confirmation requirement to be considered further in the selection. The leading and sub-leading jet must have $p_{\mathrm{T}} > 70$ and 60 GeV, respectively. A requirement for reduced jet activity is implemented by the use of a veto on any additional jet with p_{T} above 30 GeV in the region between the two leading (so called tagging) VBF jets.

The trigger assumptions, jet momentum smearing, tracking confirmation and flavour efficiencies used are as described in Section XI.2. This holds for all objects but the leptons, where Run 1 performance assumptions are retained. The latter is expected to have a small impact on the comparison of the scoping scenarios.

Events with exactly two oppositely charged and different flavour ($e\mu + \mu e$) leptons passing a set of quality cuts are selected. The invariant mass of the leptons, m_{ll}, is required to be larger than 10 GeV to remove low mass resonances. The Drell-Yan and multi-jet backgrounds are suppressed with a cut on $E_{\mathrm{T}}^{\mathrm{miss}}$, which is defined using a combination of calorimeter and tracking information, as for the ATLAS Run 1 analysis. This variant of $E_{\mathrm{T}}^{\mathrm{miss}}$ is not part of the standard recommendations, but in the context of the present analysis, it is found to be more stable against pile-up, and to provide an improved scale, resolution and direction for the $E_{\mathrm{T}}^{\mathrm{miss}}$ with respect to the true $E_{\mathrm{T}}^{\mathrm{miss}}$ in the events with jets. The analysis is optimised to select events with the VBF topology, and the cuts applied are summarised in Table 34.

Table 34. Selection criteria common for all three scenarios used for the 14 TeV VBF $H \to WW^{(*)}$ analysis. The rapidity gap is the y range spanned by the two leading jets. The energy and p_{T} thresholds are in GeV.

Selection	Applied criteria
Pre-selection	Two isolated leptons ($\ell = e, \mu$) with opposite charge Leptons with $p_{\mathrm{T}}^{\text{lead}} > 25$ and $p_{\mathrm{T}}^{\text{sub-lead}} > 15$ $m_{\ell\ell} > 10$
$E_{\mathrm{T}}^{\mathrm{miss}}$	$E_{\mathrm{T}}^{\mathrm{miss}} > 20$
General selection	$p_{\mathrm{T}}^{\mathrm{jet}} > 70$ (60) lead (sub-lead) $N_{\mathrm{b-jet}} = 0$ $p_{\mathrm{T}}^{\mathrm{tot}} < 20$ $Z/\gamma^* \to \tau\tau$ veto (Collinear approx. $m_{\tau\tau} < 50$ GeV)
VBF topology	$m_{\mathrm{jj}} > 1250$ and $\lvert\eta_{\mathrm{jet}}\rvert > 2.0$, opposite hemisphere No jets ($p_{\mathrm{T}} > 30$) in rapidity gap Require both leptons in rapidity gap
$H \to WW^{(*)} \to \ell\nu\ell\nu$ topology	$m_{\ell\ell} < 60$ $\Delta\phi_{\ell\ell} < 1.8$ $m_{\mathrm{T}} < 1.07 \cdot m_H$

The Reference and Middle scenarios provide improved VBF signal efficiencies for the central jet veto, because the track confirmation algorithm eliminates many pile-up jets which would otherwise

result in vetoing signal events. The VBF signal-to-background ratio decreases from 0.49 (Reference) to 0.33 (Middle) to 0.23 (Low).

The distribution of the events in m_{T} is shown in Figure 100. The expected precision on the VBF $H \to WW^{(*)} \to e\nu\mu\nu$ signal strength measurement ($\Delta\mu/\mu$) has been obtained based on the the number of events remaining after the m_{T} cut. For the current results, the systematic uncertainties on the backgrounds are assumed to be 10%, except for the $W+\mathrm{jets}$ background, where an uncertainty of 20% is assumed. All uncertainties related to the Monte Carlo statistics are neglected for the extraction of the precision on the VBF signal strength measurement. The signal strength precision and significance are given by:

$$\Delta\mu/\mu = \frac{\sqrt{N_{\mathrm{sig}} + N_{\mathrm{bkg}} + \sum_{i=0}^{\mathrm{bkg}} \sigma_{i,\mathrm{bkg}}^2 + \sum_{i=0}^{\mathrm{sig}} \sigma_{i,\mathrm{sig}}^2}}{N_{\mathrm{sig}}}, \quad (6)$$

$$\text{Significance} = \frac{N_{\mathrm{sig}}}{\sqrt{N_{\mathrm{bkg}} + \sum_{i=0}^{\mathrm{bkg}} \sigma_{i,\mathrm{bkg}}^2}}. \quad (7)$$

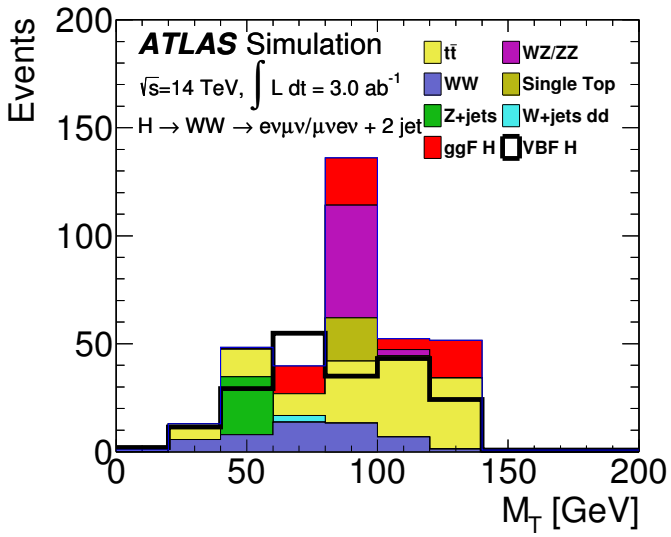

Figure 100. The m_{T} distribution for the VBF $H \to WW^{(*)}$ analysis in the Reference scenario after all the selection cuts for $\mu = 200$ with 3000 fb^{-1} total integrated luminosity.

The VBF significance and the uncertainty on the signal strength for the three scenarios are shown in Table 35 with and without the expected theoretical uncertainties at 14 TeV. The significance is degraded by 56 (33)% from the Reference to the Low (Middle) scenario and the $\Delta\mu/\mu$ degrades by 114 (43)% from the Reference to the Low (Middle) scenario in the case where the theoretical uncertainties are ignored. When including current theoretical uncertainties on ggF and VBF Higgs boson production, the significance is degraded by 53 (23)% from the Reference to the Low (Middle) scenario and the $\Delta\mu/\mu$ degrades by 95 (25)%. In the present analysis, the signal strength measurement of the Higgs boson in this channel is limited by background systematic uncertainties, and the deficiencies of the Middle and Low scenarios with their larger background contributions cannot simply be recovered with additional integrated luminosity. In order to achieve the best possible coupling measurement, the optimisation of the analysis focuses on the precision of the signal strength measurement, which results in lower significances than might otherwise be achievable. No

particular treatment aiming at distinguishing VBF from the ggF signal production, as proposed in Section XI.3.2 for $H \to ZZ^{(*)}$ decays, has been investigated here; consequently, the current large theoretical uncertainties reflect partly the large ggF contamination of this VBF $H \to WW^{(*)}$ measurement.

Table 35. The $\Delta\mu/\mu$ and significance for VBF $H \to WW^{(*)}$ are shown for the three scoping scenarios. Results with and without the theoretical uncertainties on the VBF or ggF Higgs boson production are included.

Scoping Scenario	without theo. unc.		with theo. unc.	
	$\Delta\mu/\mu$	Z_0-value (σ)	$\Delta\mu/\mu$	Z_0-value (σ)
Reference	0.14	8.0	0.20	5.7
Middle	0.20	5.4	0.25	4.4
Low	0.30	3.5	0.39	2.7

In conclusion, this analysis shows a large sensitivity to the three scoping scenarios. This arises primarily through the use of the b-jet veto and central jet veto. The evaluation of their individual contribution has to take into account the strong correlation between them. If the central jet veto is dropped for jets in the pseudo-rapidity region $|\eta| > 2.4$, a degradation of the uncertainty on the signal strength by 120% and 24% in the Low and Middle scenario, respectively, is observed with respect to the Reference scenario. This drop is explained by the lack of b-tagging in the very forward region of the Middle and Low scenarios. This illustrates the importance of b-tagging in the very forward region for physics processes where top-quark production represents an important background for precision measurements and for new physics searches.

Alternatively, if the b-tagging is released in the very forward region, the effect of the central jet veto can be evaluated. The result shows a degradation of the signal strength measurement by 94% and 50% in the Low and Middle scenario, respectively. A strong degradation of the measurement, due to pile-up jets that are not rejected by tracking confirmation, is expected also in the Middle scenario.

XI.3.4 Studies of $W^{\pm}W^{\pm}$ boson scattering in the final state with two same charge leptons and two jets

The measurement of vector boson scattering $VV \to VV$ with $V = W,Z$ by electroweak processes provides a unique window into the nature of the electroweak symmetry breaking mechanism as well as into potential new physics in the electroweak sector. The $W^{\pm}W^{\pm}$-electroweak scattering process is experimentally interesting since it offers the rare signature of two same-sign leptons with two forward jets ($W^{\pm}W^{\pm}jj$), and is a final state where the electroweak signal is comparable in size to that from QCD-induced processes, which are considered as a background here. With Run 1 data there is evidence of the electroweak cross-section, with a significance of 3.6 standard deviations, and the cross-section is statistically limited with a total uncertainty of about 30% [92].

In this analysis, events are selected if they contain two leptons (e/μ) with the same electric charge, two forward jets, and moderate missing transverse momentum. One of the leptons must pass the single lepton trigger. The object selection depends on the scenario under consideration as documented in Section XI.2 and it is summarised in Table 36. Pile-up jets are superimposed, and the track confirmation algorithm is applied to all jets, selecting the operating point with a pile-up jet

mis-identification probability of 2%. Good angular separation among objects is achieved by imposing $\Delta R_{\ell,\text{jet}} > 0.3$ and $\Delta R_{\ell,\ell'} > 0.3$

Table 36. Object selection criteria in the Reference, Middle, and Low scenarios for the same sign WW analysis.

Selection	Reference scenario	Middle scenario	Low scenario
Minimum lepton (e, μ) p_{T}	25	25	25
Maximum lepton (e, μ) $\lvert\eta\rvert$	4.0	3.2, 2.7	2.7
Minimum veto-lepton (e, μ) p_{T} (GeV)		7, 6	
Minimum jet p_{T} (GeV)		30	
Maximum jet $\lvert\eta\rvert$		4.5	

The major background in the VBS region of the 8 TeV $W^{\pm}W^{\pm}$ analysis [92] is the $WZ/\gamma^{*} + jj$ production where only two leptons were reconstructed. It comprises more than 50% of the total background. Additional background processes include events from $W^{\pm}W^{\pm}$-QCD production and those with charge mis-identification of leptons, leptons from hadron decays in jets, and photon conversions. The latter processes are estimated from data in the Run 1 analysis and are not simulated in the scope of this work. Their contribution is approximated by scaling up by a factor 1.7 [92] the sum of the $WZ/\gamma^{*} + jj$ and $W^{\pm}W^{\pm}$-QCD yields, independent of the scoping scenario.

Based on the Run 1 analysis, good signal-to-background discrimination is achieved by selecting events according to the criteria in Table 37. In addition a requirement based on the lepton centrality ζ [5] is also imposed to enhance the purity of the $W^{\pm}W^{\pm}$-electroweak signal relying on the relative kinematic signature between leptons and jets.

Table 37. Event selection criteria for the signal region for same sign WW electroweak production.

Selection	Electroweak Signal Region
Number of leptons	2
Number of jets	≥ 2
Third lepton veto	remove events with ≥ 3 veto-leptons
Di-lepton invariant mass $m_{\ell\ell'}$ (GeV)	> 20
Z-veto (GeV)	$\lvert m_{e,e} - m_{Z}\rvert > 10$
Di-jet invariant mass $m_{j,j}$ of highest p_{T} jets (GeV)	> 500
$\Delta\eta_{\text{j,j}}$ of highest p_{T} jets	> 2.4
$E_{\text{T}}^{\text{miss}}$ (GeV)	> 40

The signal significance is reported using Z_{σ_B} [6], which uses a Poissonian distribution for the signal and takes into account the background uncertainty with a Gaussian distribution. A background uncertainty of 15% is assumed for all calculations [92]. The precision on the cross-section measurement is derived using Equation 6.

[5] $\zeta = \min[\max(\eta_{\ell 1}, \eta_{\ell 2}) - \min(\eta_{j1}, \eta_{j2}), \max(\eta_{j1}, \eta_{j2}) - \min(\eta_{\ell 1}, \eta_{\ell 2})]$

[6] $Z_{\sigma_B} = \sqrt{2[(S+B)\log\frac{S+B}{B_0} + B_0 - S - B] + \frac{(B-B_0)^2}{\sigma_B^2}}$ where $B_0 = \frac{1}{2}(B - \sigma_B^2 + \sqrt{(B-\sigma_B^2)^2 + 4(S+B)\sigma_B^2})$

Figure 101 shows the leading and sub-leading jet η distribution in the signal region for the Reference, Middle, and Low scenarios. The significance Z_{σ_B} and the precision on the cross-section measurements are reported in Table 38 after the additional cut on lepton centrality is applied.

The precision of the cross-section measurement in the Reference scenario is 5.9% and it is reduced in the Middle and Low ones to 11% and 13%, respectively. There are two dominant effects causing this deterioration of performance. First, the limited lepton coverage in the Middle/Low scenario reduces the efficiency of suppressing the WZ background through the third-lepton veto by a factor of ∼2 with respect to the Reference scenario. Second, the limited η coverage of the tracker in the Middle and Low scenario causes a significant increase of the background with pile-up jets: the fraction of events where the selected jets originate from pile-up interactions increases from ∼18% in the Reference scenario to ∼23% (∼27%) in the Middle (Low) one.

In conclusion, there is a clear correlation between the extension of the tracker and the precision of the measurement and in the Reference scenario the cross-section measurement is more than twice as precise as in the Low scenario.

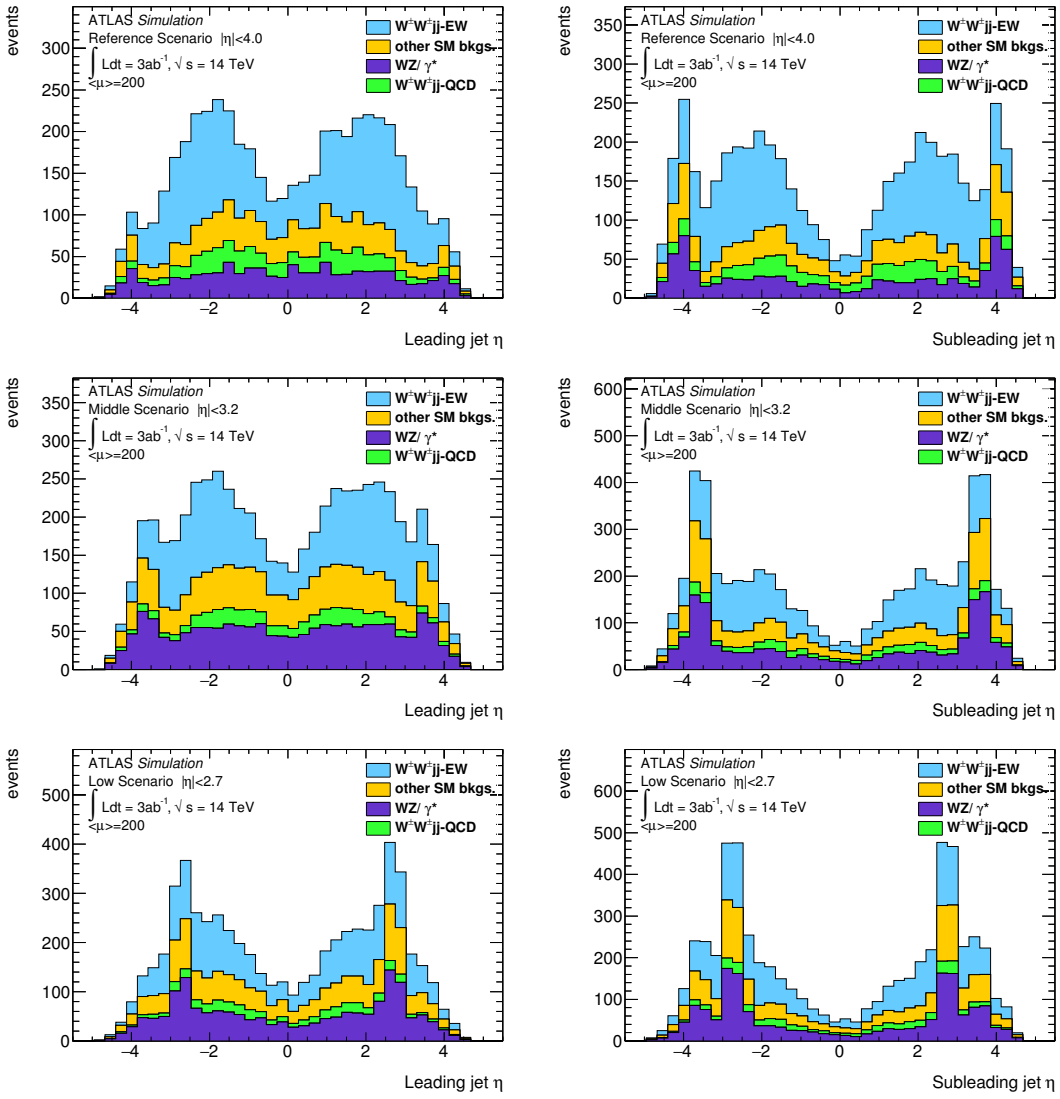

Figure 101. The leading jet (left) and sub-leading jet (right) η distributions for the Reference (top), Middle (centre), and Low (bottom) scenarios in the signal region for the same sign WW electroweak search.

Table 38. Significance Z_{σ_B} and uncertainty on the cross-section measurement in the Reference, Middle, and Low scenarios for the same sign WW electroweak search.

Scenario	Z_{σ_B}	$\Delta\sigma/\sigma$
Reference scenario	11.3 ± 0.6	5.9%
Middle scenario	6.06 ± 0.3	11%
Low scenario	5.02 ± 0.2	13%

XI.3.5 Search for charginos and neutralinos in final states with one lepton and two b-jets

Supersymmetric (SUSY) extensions of the SM naturally address the gauge hierarchy problem by postulating the existence of SUSY particles with spin differing by one-half unit with respect to that of their SM partner. If R-parity is conserved, SUSY particles can only be pair-produced and will eventually decay into SM particles and the lightest SUSY particle (LSP) which is stable. The charginos ($\tilde{\chi}^{\pm}_{i=1,2}$) and neutralinos ($\tilde{\chi}^{0}_{i=1,2,3,4}$) are the mass eigenstates formed from the linear superposition of the SUSY partners of the Higgs and electroweak gauge bosons. Based on naturalness arguments these electro-weakinos are expected to have masses in the hundreds of GeV range and thus to be within the reach of the HL-LHC. The search described in this document is for pair-production of a wino-like $\tilde{\chi}^{\pm}_{1}$ and wino-like $\tilde{\chi}^{0}_{2}$ with a subsequent decay into a W and a SM-like Higgs boson. The final states contain one isolated lepton, two jets consistent with the expected topology of b-quark decays, and significant missing transverse momentum due to the LSPs escaping detection. The electron isolation is defined with respect to the jets as $\Delta R(e, \text{jet}) > 0.2$ and the two b-jets must be the leading jets in the event. The object performance depends on the scenario under consideration as documented in Section XI.2. The selection is summarised in Table 39 where the momentum threshold on the lepton is raised to satisfy the single lepton trigger level. The η-coverage of leptons and b-tagged jets is not scenario-dependent since the signal is expected to be produced centrally in the detector. Since jets are limited to $|\eta| < 2.5$ with a 50 GeV threshold and the signal regions have 2 or 3 jets where the leading and the sub-leading jets are b-tagged, the impact of pile-up jets is negligible. The pile-up overlay and track confirmation are not applied.

Table 39. Object selection criteria in the Reference, Middle, and Low scenarios for the $1\ell bb$ SUSY search.

Scenario	Reference	Middle	Low
Minimum lepton (e, μ) p_{T} (GeV)	22, 20	28, 25	28, 25
Maximum lepton (e, μ) $\|\eta\|$		2.47 (2.4)	
Minimum b-jet p_{T} (GeV)		50	
Maximum b-jet $\|\eta\|$		2.5	
b-jet identification probability		70%	
Minimum light-flavour jet p_{T}		50	
Maximum light-flavour jet $\|\eta\|$		2.5	

The background is dominated by $t\bar{t}$, t, W+jets, and ttV production where V=W, Z, with contributions from Z+jets, VV and Vh. The signal-to-background discrimination is optimised on Z_0, the significance derived from the p_0 value as in Section XI.3.2. A coarse systematic uncertainty of 30%

on the total background is assumed, which is consistent with the uncertainties determined in the published Run 1 search [93]. The most significant observables to suppress the background and preserve the signal are the missing transverse momentum, the transverse mass m_{T} of the lepton and missing transverse momentum, and the boost-corrected contransverse mass m_{CT}, calculated from the b-jets [7]. Table 40 reports the signal region selection (in common for the Reference, Middle, and Low scenarios) and Fig. 102 shows the transverse mass of the signal and background events in signal region SR1.

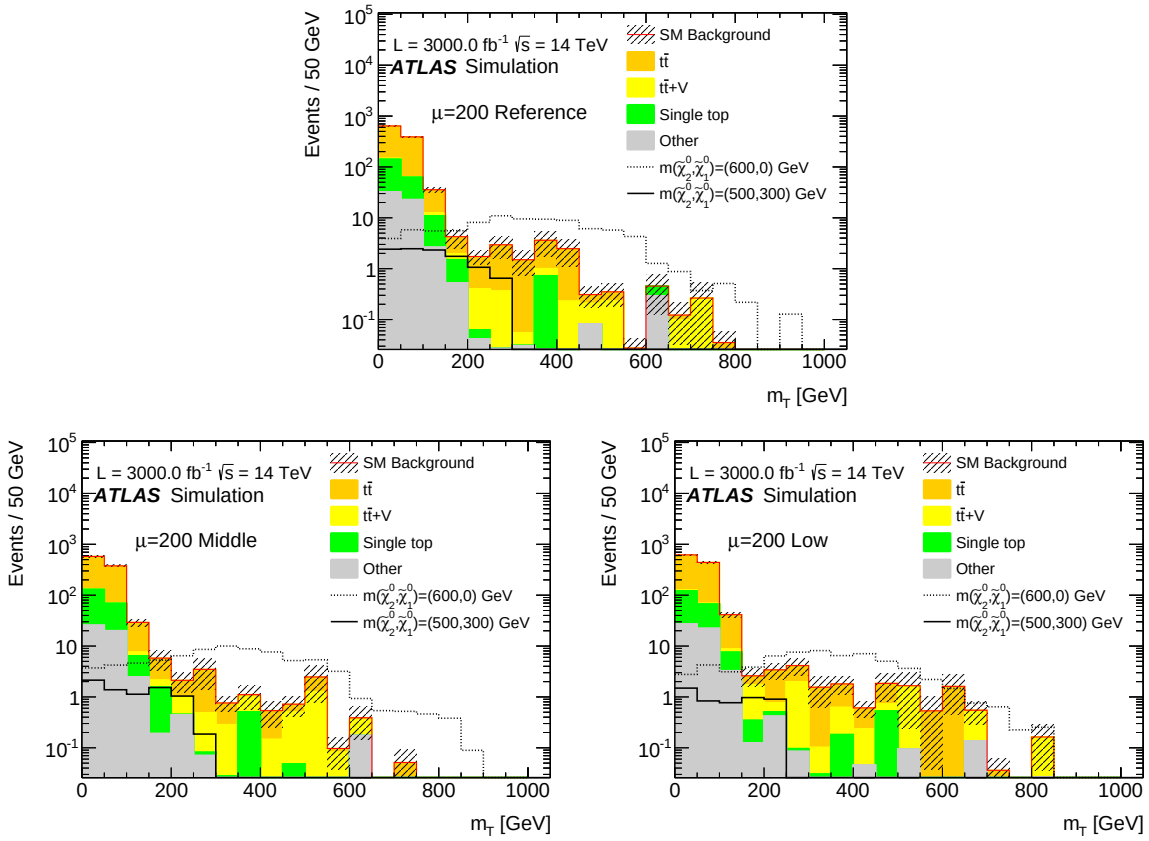

Figure 102. Distributions of the transverse mass after the SR1 selection (except for the transverse mass selection) in the Reference (upper), Middle (lower left) and Low (lower right) scenarios for the $1\ell bb$ SUSY search. The contributions from all SM backgrounds are shown, with the bands representing the total uncertainty. The distributions of the signal expected for two different models are also shown: the solid line corresponds to a signal with a 500 GeV $\tilde{\chi}_2^0,\tilde{\chi}_1^{\pm}$ and a 300 GeV $\tilde{\chi}_1^0$ neutralino, while the dashed line corresponds to a signal with 600 GeV $\tilde{\chi}_2^0,\tilde{\chi}_1^{\pm}$ and a massless $\tilde{\chi}_1^0$.

The discovery potential of the search corresponding to $Z_0 = 5$ is presented in Fig. 103 and in Table 41 for the Reference, Middle and Low scenarios. Mass-degenerate $\tilde{\chi}_2^0$ and $\tilde{\chi}_1^{\pm}$ with masses up to 850 GeV can be discovered at the HL-LHC for massless neutralinos. This significantly improves the current ATLAS Run 1 95% C.L. of 250 GeV [93] and is comparable to the latest projection given in Ref. [95]. The discovery reach is reduced to 770 and 675 GeV in the Middle and Low scenarios, respectively. Under the assumption of a detector based on the Middle (Low) scenario, 6000 fb^{-1} (12,000 fb^{-1}) would be needed to reach the discovery potential of the Reference scenario at 3000 fb^{-1}.

[7] The boost-corrected contransverse mass [94] is is bound from above by an analytical combination of particle masses, $m_{\mathrm{CT}}^{\mathrm{max}} = (m_{\mathrm{parent}}^2 - m_{\mathrm{daughter}}^2)/(m_{\mathrm{parent}})$

A mixture of factors contribute to this significant deterioration of the search reach in the Low and Middle scenario with respect to the Reference scenario. The single muon trigger efficiency reduces the signal and background yields in the muon channel by ∼20%, and a reduced b-tagging efficiency suppresses both yields. Although the same average b-tagging working point was used for each scenario, the variation of efficiency with p_{T} has an impact on the signal efficiency. In contrast the deterioration of the missing transverse momentum resolution (see Section XI.2.8) mainly leads to an increase in the background yields (dominated by softer missing transverse momentum with respect to that in the signal), and also reduces the discriminating power of the transverse mass observables.

Table 40. Event selection criteria defining the two signal regions used in the $1\ell bb$ SUSY search.

Selection	SR1	SR2
Number of leptons (e, μ)	1	
Number of b-jets	2	
m_{bb} (GeV)	105-135	105-135
Number of jets	2 or 3	2 or 3
m_{CT} (GeV)	>300	
m_{T} (GeV)	>180	>200
$E_{\mathrm{T}}^{\mathrm{miss}}$(GeV)	>400	>450

Table 41. Discovery potential (Z_0 = 5, massless $\tilde{\chi}_1^0$) in the Reference, Middle, and Low scenarios.

Discovery Potential	$\tilde{\chi}_2^0$,$\tilde{\chi}_1^{\pm}$ mass (GeV)
Reference scenario	850
Middle scenario	770
Low scenario	675

XI.3.6 Search for resonant pair production of Higgs bosons in the four b-jet final state

Many new physics models predict rates of Higgs boson pair production significantly higher than the Standard Model rate. For example, TeV scale resonances such as the first Kaluza-Klein (KK) excitation of the graviton G_{KK}^* predicted in the bulk Randall-Sundrum model or the heavy neutral scalar H of two-Higgs-doublet models can decay into pairs of Higgs bosons, hh. The study presented here focuses on the search for high-mass KK gravitons with each of the Higgs bosons decaying to $b\bar{b}$. In this study, the “boosted" search is emulated in which each of the Higgs boson decaying into a $b\bar{b}$ system is reconstructed with a large radius jet. Searches for hh resonances in this final state have recently been performed by the ATLAS Collaboration using the Run 1 data-set [96].

The search is based on jets reconstructed with the $\mathrm{anti}{-}k_t$ algorithm using the Monte Carlo collection of truth particles as input. The jet properties are parametrised as a function of the jet

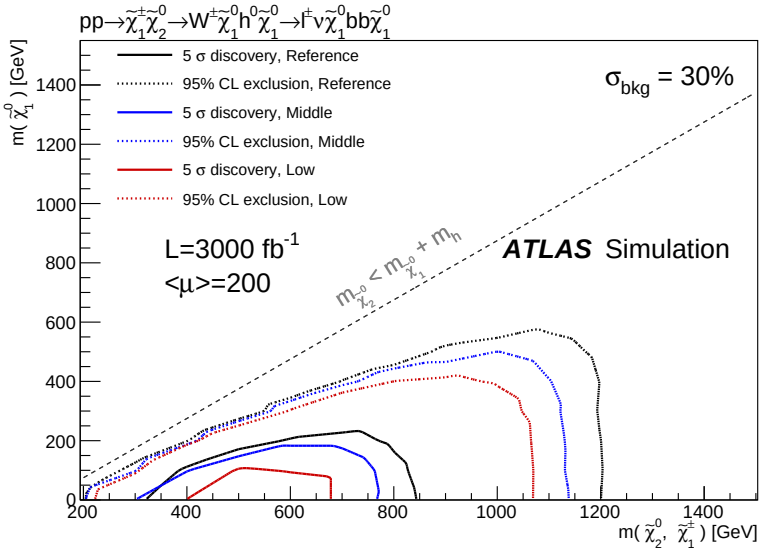

Figure 103. Discovery contour (Z_0 = 5, massless $\tilde{\chi}_1^0$) and exclusion limits (Z_0 = 1.64, massless $\tilde{\chi}_1^0$) for the 3000 fb^{-1} data-set in the $\tilde{\chi}_2^0$,$\tilde{\chi}_1^{\pm}$ and $\tilde{\chi}_1^0$ mass plane for the $1\ell bb$ SUSY search.

momentum and η, scenario, and pile-up condition as described in Section XI.2. Three different collections of jets are utilised:

- "Large-R" Jets: truth jets reconstructed with $R = 1.0$ are trimmed with an algorithm that relies on sub-jets reconstructed using the k_t algorithm with radius parameter $R_{\text{sub}} = 0.2$. The trimming algorithm removes sub-jets with p_{T} less than 5% of the large-R jet p_{T}. The mass of the large-R jets is smeared with a Gaussian of width equal to 8.5% of the truth jet mass.
- "Track" Jets: truth jets reconstructed with $R = 0.2$ serve as a proxy for "track" jets that are to be b-tagged. Track jets are considered to match large-R jets if they lie within $\Delta R < 1.2$.
- "Trigger" Jets: truth jets reconstructed with $R = 0.4$.

The details of the jet selection are provided in Table 42. Due to the high jet thresholds applied, the contribution of jets from pile-up interactions is considered negligible and no pile-up jets are superimposed on the hard scatter event in this analysis. The b-tagging algorithm working point corresponds to a b-tagging efficiency of 70% for jets with $|\eta| < 2.7$ in $t\bar{t}$ events. For jets with $p_{\text{T}} > 300$ GeV, a working point with constant efficiency for b-jets is adopted, taking into account the variation of c- and light-jet rejection as a function of p_{T}.

The dominant background process originates from multi-jet production. Optimal signal-to-background discrimination is achieved by applying the event selection described in Table 43, where track jets matched to the large-R jets must satisfy the b-tagging requirements. A "top-veto" is then imposed by rejecting events where the mass of any combination of the two track jets associated with either the leading or the sub-leading large-R jet with a third track jet is in the range 135−190 (125−190) GeV for the leading (sub-leading) larger R-jet. Finally, the signal region is formed by the ensemble of events satisfying X_{hh} <1.6 where X_{hh} is defined as:

$$X_{hh} = \sqrt{\left(\frac{m_{\text{J}}^{\text{lead}} - 124\ \text{GeV}}{0.1\, m_{\text{J}}^{\text{lead}}}\right)^2 + \left(\frac{m_{\text{J}}^{\text{subl}} - 115\ \text{GeV}}{0.1\, m_{\text{J}}^{\text{subl}}}\right)^2}. \quad (8)$$

Table 42. Common jet selection criteria in the Reference, Middle, and Low scenarios for the hh resonance search.

Variable	Applied criteria
Minimum large-R jet p_{T} (GeV)	400
Maximum large-R jet $\|\eta\|$	2.0
Minimum track jet p_{T} (GeV)	50
Maximum track jet $\|\eta\|$	2.5
Minimum trigger jet p_{T} (GeV)	50
Maximum trigger jet $\|\eta\|$	3.2

Table 43. Event selection criteria defining the hh signal region in the Reference, Middle, and Low scenarios.

Selection	Reference Scenario	Middle Scenario	Low Scenario
Number of large-R jets		2	
Minimum large-R jet p_{T}		500, 400 GeV	
$\Delta\eta$ between large-R jets		< 1.5	
Number of track jets		2	
matching each large-R jet			
b-jet identification probability		70%	
Trigger requirements:			
$\geq$1 jet with	$p_{\mathrm{T}} > 180$ GeV	$p_{\mathrm{T}} > 225$ GeV	$p_{\mathrm{T}} > 275$ GeV
OR $\geq$4 jets with	$p_{\mathrm{T}} > 75$ GeV	$p_{\mathrm{T}} > 85$ GeV	$p_{\mathrm{T}} > 90$ GeV
OR sum of jets with	$\Sigma p_{\mathrm{T}} > 500$ GeV	$\Sigma p_{\mathrm{T}} > 600$ GeV	$\Sigma p_{\mathrm{T}} > 750$ GeV

The invariant mass distribution of the two large-R jets is used to extract the signal from the background. In order to assess the signal significance, a sliding mass window region is defined around the resonance mass for each of the signal pole masses considered in the analysis and the significance is computed according to Equation 7. For illustration, the expected di-jet mass distribution is shown in Fig. 104 for events in the signal region for the Reference and Low scenarios. The expected sensitivity is reported in Table 44 while Fig. 105 shows the expected sensitivity for a $G^*_{\mathrm{KK}} \to hh$ signal with mass ranging from 1.5 to 2.5 TeV (in the context of the bulk Randall-Sundrum model with $k/\bar{M}_{\mathrm{Pl}} = 1.0$). There is no major difference between the significance in the Reference and the Middle scenario within the statistical uncertainties of the available Monte Carlo samples (leading to an apparent stronger significance in the Middle scenario with respect to the Reference one).

Table 44. Signal significance computed for background yield systematic uncertainties of 5% in the Reference, Middle, and Low scenarios.

Scenario	Significance ($M_{G^*_{KK}}$=2.0 TeV)
Reference scenario	4.4
Middle scenario	4.5
Low scenario	3.1

A significant loss of sensitivity is however observed in the Low scenario due to the large degra-

dation of the flavour-tagging performance compared with the other two scenarios. The Low scenario is in fact characterised by both smaller b-tagging efficiency at high p_{T} and reduced light- and c-jet rejection capabilities (Section XI.2.9). To reach the same significance as the other two scenarios, 2.4 times more integrated luminosity would be required. Furthermore, the Low scenario may not allow for a $5\ \sigma$ discovery in the mass range considered, depending on the magnitude of the systematic uncertainties in the background estimate.

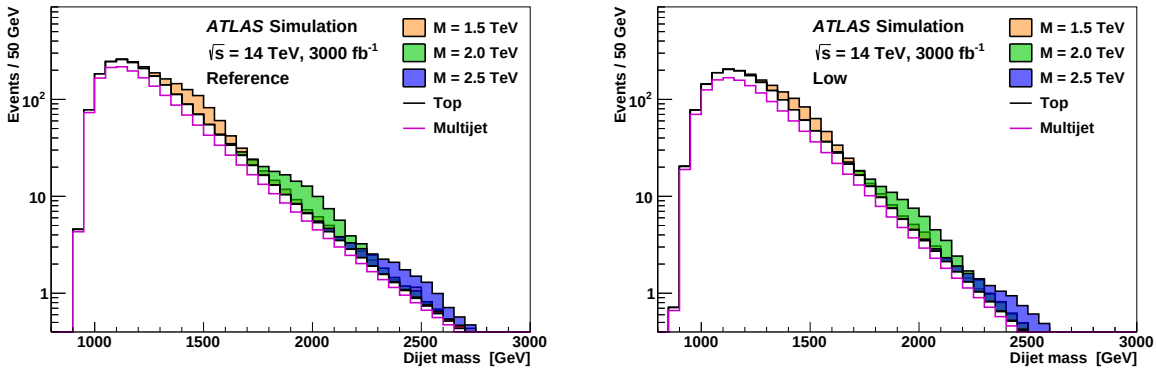

Figure 104. Expected di-jet mass distribution for events in the signal region in the Reference (left) and Low (right) scenarios.

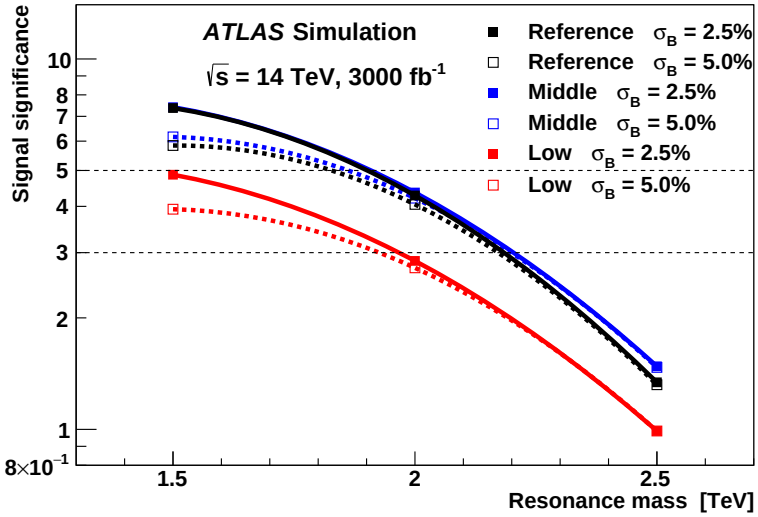

Figure 105. Expected signal significance for $G^*_{\mathrm{KK}} \to hh$ with 3000 fb^{-1}comparing the three different upgrade scenarios. Two different assumptions on the systematic uncertainty in the background yield are tested: 2.5% and 5.0%.

Chapter XII

Summary and Conclusions

The preceding chapters have described in some detail the proposed upgrades to ATLAS to face the challenges of the HL-LHC period. A broad and deep physics programme is anticipated in this period, a few highlights of which have been discussed in this document. The performance impact of the reduced funding scenarios has been delineated for object performance and selected final states. This final chapter collects the performance and physics messages developed in the document, and correlates them with the scoping scenario definitions to reach initial conclusions about performance and physics capability versus upgrade cost. It begins with a reminder of the Reference detector configuration, followed by a short summary of the components of the scoping scenarios, and the corresponding cost variations between scenarios. This description divides the different aspects of the ATLAS Phase-II upgrade into five logical groups of improvements which contain all of the significant contributions to the different scoping scenarios. The chapter proceeds to correlate the performance improvements described in detail in Section XI.2 with these five groups of detector upgrades. Next, a brief summary of the results for the selected benchmark physics processes and their scenario dependence, described in detail in Section XI.3, is given. In the conclusion, the performance and physics advantages of the Reference scenario, and the performance and physics disadvantages of the Low scenario, both relative to the Middle scenario, are briefly summarised.

The performance and physics studies presented in this document were performed assuming a data sample corresponding to 3000 fb^{-1} collected with a levelled instantaneous luminosity of $\mathcal{L} \simeq 7.5 \times 10^{34}\mathrm{cm}^{-2}\mathrm{s}^{-1}$, which results on average in 200 inelastic pp collisions per bunch crossing. The performance studies presented in Section XI.2 were carried out using detailed modelling of the ATLAS Phase-II detector where ever possible, and then the results were parametrised to provide a compact and simple representation of the performance of each physics object (tracks, electrons, muons, b-tagging, jets, and $E_{\mathrm{T}}^{\mathrm{miss}}$) for each scoping scenario. In addition, the trigger performance discussed in Section III.7 was used as part of the performance parametrisation. These parametrisations were then used to carry out the physics studies presented in Section XI.3. These physics studies for a selected set of benchmark analyses have been chosen to explore and quantify the impact of the object performance on physics in each of the scoping scenarios. Many physics studies are in progress, but were not mature enough to include in the present document.

XII.1 Summary of Scoping Scenarios

XII.1.1 Reference Detector

The Reference detector scenario presented in this document is described in Chapter II. A wide range of technical details are provided in Chapters III – VIII. A very brief summary of the key features follows:

- The Trigger and Data Acquisition system uses a two level hardware trigger (L0/L1) with enhanced specifications, including maximum L0/L1 rates of 1 MHz and 400 kHz respectively, and latencies of 10 μs and 60 μs respectively.
- The Inner Tracker consists of two sections. The outer section uses silicon micro-strip technology with the layout as defined in the ATLAS Phase-II LoI. The inner section is based on silicon pixel technology, and starts from the LoI layout, but extends the η-coverage from 2.7 to 4.0.
- The Calorimeter consists of two major systems. Liquid argon technology is used for the barrel electromagnetic calorimetry and all of the endcap and forward calorimetry, while scintillating Tiles are used for the barrel hadronic calorimetry. Both the LAr and Scintillating Tile Hadronic Calorimeter (TileCal) readout electronics will be upgraded to provide streaming of all data

off-detector at 40 MHz. A new sFCal forward calorimeter will be installed, with improved high luminosity performance and finer transverse segmentation. A new high-precision timing detector will be installed in the region $2.4 < |\eta| < 4.3$.

- The Muon upgrade focuses primarily on improved trigger performance, replacing almost all of the on-detector electronics, including the BI inner barrel region. In the BI region, the MDT precision chambers will be replaced by sMDT chambers to accomodate the installation of a layer of RPC trigger chambers. In addition, the MDT information will supplement the RPC information in the L0 trigger, providing an improved p_T resolution. Finally, a very-forward muon-tagger will be added in the region $2.6 < |\eta| < 4.0$.

XII.1.2 Components of Scoping Scenarios

The scoping scenarios defined by ATLAS represent a set of detector variations whose performance can be rapidly modelled within the framework of the existing Phase-II upgrade simulations, in order to provide timely performance and physics feedback on the three scenarios. They explore significant variations in the scope of the major cost drivers for the Phase-II upgrade, without being three separately optimised designs for ATLAS in the HL-LHC era. These scenarios were defined early in the scoping exercise to have estimated CORE costs close to the targets of 200 MCHF for the Low scenario, 235 MCHF for the Middle scenario, and 275 MCHF for the Reference scenario. An overview of the present costs for the three scenarios is presented in Chapter IX. The total costs are 200 MCHF for the Low scenario, 229 MCHF for the Middle scenario, and 271 MCHF for the Reference scenario. A more detailed description of the scoping scenarios is provided in Chapter II, but in this chapter, five groups of variations in scope will be used to organize the discussion of the impacts of the scoping on the performance and physics of the upgraded ATLAS detector.

The major cost drivers for the Phase-II upgrade are the ITk detector and the TDAQ system, which represent 60% of the total cost of the upgrade. The largest parts of the scoping variations therefore concentrate on large variations in these two critical systems.

For the ITk detector, the different scenarios explore substantial reductions in the large-radius silicon micro-strip system, since this system dominates the cost of the ITk detector. The details may be found in Chapter IV. The reductions include dropping one disc per side, one full barrel layer, and one side of two other barrel layers. In addition, reductions in the η-coverage of the small-radius silicon pixel system from $|\eta| = 4.0$ in the Reference scenario, to $|\eta| = 3.2$ in the Middle scenario, and $|\eta| = 2.7$ in the Low scenario, are explored. The total ITk costs in the three scenarios are 120.4 MCHF for the Reference, 113.3 MCHF for the Middle scenario, and 96.8 MCHF for the Low scenario. The reductions in the silicon pixel system contribute only 5.7 MCHF to the total difference of 23.6 MCHF between the Reference and Low scenarios.

For the TDAQ system, the different scenarios explore substantial reductions in the specifications for the major cost drivers. The details may be found in Chapter III. The major cost drivers are the L1Track and FTK++ associative memory tracking engines, plus the DAQ/EF networks and related computing resources. The reductions in the specifications include reducing the p_T and η range for the track reconstruction in L1Track and FTK++, plus reductions in the maximum allowed L0/L1 trigger rates and the EF output rate. The total TDAQ costs in the three scenarios are 43.3 MCHF for the Reference, 31.9 MCHF for the Middle scenario, and 25.1 MCHF for the Low scenario.

In addition to these two major variations, three more modest sets of variations are made in the following areas (this simplified description covers essentially all of the components which are changed in the different scenarios):

For the LAr calorimeter, the upgrade to the improved sFCal with finer segmentation and better high luminosity performance is removed from the Middle and Low scenarios, reducing the LAr cost

by 11.8 MCHF once tooling costs are included. The details may be found in Chapter V.

For the Muon barrel, the Reference scenario contains the upgraded innermost BI barrel layer with new on-detector electronics plus the new sMDT chambers with a new RPC layer. For the Middle scenario, only half of the BI layer is upgraded (the half at largest η), since this is the part of the BI layer with the highest rates and which is also the easiest to access and upgrade. For the Low scenario, none of the BI improvements are made. The total cost reduction from the Reference to the Low scenario is 10.4 MCHF, including technical labor costs. The details may be found in Chapter VI.

The two large-η opportunities, which are not yet well-developed at the technical level, are grouped together due to their more conceptual status. These are the very-forward muon-tagger described in Chapter VI, and the high-precision timing detector described in Chapter V. The total cost for these two upgrades is 7.1 MCHF.

XII.2 Impact on Physics Object Performance

This section correlates the variations of physics object performance, discussed in detail in Section XI.2, with the components of the scoping scenarios, organized into five logical groups, for the Phase-II upgrade. The performance for different scenarios has been summarised already in Section XI.2, and the scenario dependence of a selection of benchmark physics analyses has been summarised in Section XI.3. This section instead focuses on the connection between the specific detector upgrades and the performance benefits and losses.

XII.2.1 ITk Impacts

There are two components of the scope variations in the ITk system. The first is the reduction of the number of barrel layers and endcap discs in the large radius Strip system in the Middle and Low scenarios. The second is the reduction in the η-coverage of the Pixel system from $|\eta| = 4.0$ to $|\eta| = 3.2$ in the Middle scenario and to $|\eta| = 2.7$ in the Low scenario.

For the Strip sub-system, the Reference scenario gives excellent performance. It is the only scenario in which, for muons, the tracking efficiency is very high and the mis-reconstruction rate is well below the target value of 1%, reaching a value of less than 0.1% almost everywhere (see Figs. 75–77). When removing a random subset of 10% of the modules, this scenario shows a modest reduction in efficiency of a few percent, demonstrating that it provides robust tracking performance at $\mu = 200$, and provides roughly the minimum number of space points for robust track reconstruction. There are reductions in performance observed in the Middle scenario in the mis-reconstruction rate for tracks, particularly in the region where the stub layer has been removed. In addition, the loss in efficiency when removing a random subset of 10% of the modules is close to 10%, so this scenario is significantly less robust than the Reference scenario. For the Low scenario, performance and physics studies strongly disfavour this scenario. There are very significant reductions in performance for tracking efficiency (and the efficiency changes very substantially with removal of modules), for vertex ID efficiency, for b-tagging efficiency and light-quark rejection, and for conversion reconstruction efficiency.

For the Pixel sub-system, the Reference scenario, with η-coverage extended to 4.0 compared to η-coverage to only 2.7 in the original LoI layout, provides substantial capability above and beyond the Middle and Low scenarios. The dominant effect appears in the area of pile-up mitigation, which is an essential capability for operation at the very high μ values of the HL-LHC. In the Reference scenario, after applying the criteria described in Subsection XI.2.7 to all jets with $p_T > 30$ GeV, the average number of pile-up jets remaining per event is about 0.3. In the Middle scenario, this increases to about 1 jet per event, and in the Low scenario, it increases to about 2.5 jets per event.

In addition, these extra pile-up jets are all in the η region where most of the forward signal jets produced in vector-boson fusion or vector-boson scattering processes are expected (see Fig. 89). In addition, the missing transverse energy resolution benefits strongly from the removal of pile-up jets, as described in Subsection XI.2.8. The Reference scenario shows a substantially reduced growth in missing transverse energy resolution as a function of the total transverse energy in the event (see Fig. 94). It also shows a much smaller degradation in missing transverse energy resolution when μ increases from 140 to 200, so the measurement is more robust against very high pile-up conditions. The Middle scenario shows an intermediate performance for this measurement, and the Low scenario shows a substantially worse performance. Finally, the additional η-coverage is important for very-forward lepton ID (for both electrons and muons in the Reference scenario), and for very-forward b-jet tagging or b-jet vetoing (see Fig. 95).

XII.2.2 TDAQ Impacts

The Run 1 experience with triggering in ATLAS over a wide range of luminosities, and carrying out a comprehensive measurement and search physics programme, strongly supports the lower-threshold trigger strategy of the Reference scenario. This strategy allows a very inclusive approach to triggering, provides the widest access to a broad range of final states, and simplifies precise efficiency determinations with minimal dependence on details of the underlying physics processes. It is clear that in addition to the focus of the HL-LHC programme on the high-mass frontier, there is a very strong focus on precision physics to search for deviations from SM physics using EFT approaches, including understanding Higgs couplings and differential distributions, using di-boson and tri-boson final states to deeply probe the Electroweak theory, and a wide range of other SM investigations, all with very high statistics. Designing a trigger system to collect the largest and most inclusive samples of these “low-mass” bosons (W, Z, and H), in all of their decay modes, will provide major benefits for the full ensemble of measurements and searches at HL-LHC.

The trigger performance studies reported in Section III.7 indicate that the Reference scenario successfully provides a comprehensive set of low-threshold triggers (see Table 8). The Middle scenario requires substantial increases in trigger thresholds when compared to the Reference scenario. This occurs because of the reduction in the maximum L1 rate from 400 kHz to 200 kHz, and the reduction of the maximum EF acceptance rate from 10 kHz to 5 kHz.

Beyond raised thresholds, roughly 50% of the cost reduction between the Reference scenario and the Middle scenario arises from the reduction of η-coverage in the L1Track trigger and the FTK++ component of the higher-level trigger from $\eta = 4.0$ to 3.2, and the reduction in maximum L1 rate. Support for the extended η-coverage of the ITk in the hardware components of the trigger is essential to bring the offline benefits of large coverage described already in the performance and physics sections to the online trigger menus.

Finally, the HL-LHC physics programme requires that hadronic triggers, which are based on jets of different radii, H_T, missing transverse energy, hadronically decaying tau leptons, and heavy-flavour b/c-jets, are fully integrated into the trigger menu with low thresholds. This requires a powerful L1 tracking trigger, high throughput tracking capability in the EF through the FTK++ component, and high-bandwidth DAQ infrastructure. The Reference scenario provides the necessary trigger and data acquisition hardware to achieve these goals, while the Middle and Low scenarios require substantial reductions in L1Track, L1Global, FTK++, and the DAQ/EF networking infrastructure, which result in the higher trigger menu thresholds discussed above.

XII.2.3 LAr Impacts

The Reference scenario, which includes a finely-segmented sFCal containing several improvements to increase its performance at the high instantaneous luminosity values of HL-LHC, is expected to continue providing excellent calorimeter performance out to $\eta = 4.9$. The sFCal provides electron and jet measurements in a region that is critical for reconstruction of the very-forward jets produced in vector-boson fusion and vector-boson scattering. In combination with the ITk design in the reference scenario, it is expected to provide improved forward electron performance in this region as well. The impact of the change in segmentation, present only in the case where sFCal is installed, has not been fully evaluated yet. First indications are visible in the event displays and cell noise distributions shown in Section V.4.1, and the distribution of cluster multiplicity shown in Section XI.2. An ongoing simulation programme is expected to provide more comprehensive performance results, and indications of physics benefits, in the coming months. In the Middle and Low scenarios, which do not include this upgrade, Run 4 will bring some degradation of the FCal performance relative to that observed in Run 1, particularly in the highest η regions. Clearly there will be no benefits from improved segmentation without sFCal. The decision to construct and install an sFCal is not purely a financial question. Because of the risks associated with opening the Endcap Cryostat in order to remove the old FCal and install the new sFCal, a careful consideration of performance and physics benefits against the non-negligible risks of this upgrade will be necessary.

XII.2.4 Muon Impacts

The Reference detector includes substantial improvements over the muon upgrade presented in the LoI, due primarily to the upgrades to the innermost barrel layer. Recent detailed evaluations of the required chamber removal/insertion or displacement procedures, based on 3D models of ATLAS, have shown that this challenging upgrade of the muon system is feasible, although certainly not easy. The improvements include the replacement of the on-chamber electronics on the innermost barrel layer of the muon system known as BI, and the addition of a new RPC layer in this region, providing trigger capability on all three barrel muon layers (in the current ATLAS detector, only the middle and outer layers have RPCs). The addition of the RPC layer provides a dramatic improvement in the barrel muon trigger efficiency, which increases from an expected 65% in the Low scenario (without these upgrades) to 95% for the Reference scenario. The Middle scenario only performs this upgrade on the half of the BI system at the large η ends of the barrel region, where the rates are highest and the access is easiest, and thereby provides an intermediate trigger efficiency of 80% (see Section III.2.1).

XII.2.5 Impacts of Large-η Opportunities

For the two upgrades discussed in this sub-section, the designs are still at a largely conceptual level. Nevertheless, there is significant potential for these upgrades to contribute to the HL-LHC physics programme of ATLAS, and hence they are included in the Reference scenario.

The very-forward muon-tagger, which covers the region $2.6 < \eta < 4.0$, provides muon segments which can be matched with tracks in the extended ITk to provide muon candidates. The extended coverage associated with this upgrade can be valuable for reconstructing low-mass final states whose decay products are produced with a very broad η distribution. It also extends the η-coverage for vetoing additional leptons from backgrounds.

The precision timing detector, which covers the region $2.4 < \eta < 4.3$, is intended to provide further mitigation of pile-up in this critical very-forward region. Initial studies indicate that there is the potential to provide significant additional pile-up reduction in this region when the collision scheme used

by HL-LHC is based on the so-called ‘’crab-kissing” scheme, which provides a very narrow collision time distribution. Studies are on-going to improve the algorithms and evaluate the performance for other collision schemes. The correlation between the pile-up reduction from tracking, which was discussed at length in Section XI.2, and the additional pile-up reduction available from a timing detector, is also being studied.

XII.3 Summary of Physics Studies

The impact of the scoping scenarios on the physics object performance propagates into the physics potential of the HL-LHC. In general, the Reference scenario offers the most open trigger and detector acceptance, highest efficiencies, and best background rejection, allowing the most comprehensive measurements of fiducial and differential cross-sections. These benefits do not always translate into an improvement in simple performance metrics such as the precision of a total cross-section measurement. However, three example analyses probing Higgs production mechanisms or electroweak symmetry breaking have been presented. These are summarised in Table 45.

Table 45. Estimated uncertainty, for each of the scoping scenarios, on the 125 GeV Higgs boson signal strength produced by VBF processes and reconstructed in the $H \to WW^{(*)} \to \ell\nu\ell\nu$ and $H \to ZZ^{(*)} \to \ell\ell\ell\ell$ decay final states (second and third column), and on the measurement of the same-sign $W^{\pm}W^{\pm}$ boson scattering cross section (last column).

Scenario	VBF $H \to WW^{(*)}$	VBF $H \to ZZ^{(*)}$	VBS ss$W^{\pm}W^{\pm}$
Reference	0.14	0.134	0.059
Middle	0.20	0.137	0.11
Low	0.30	0.142	0.13

The vector boson fusion (VBF) production of a Higgs boson, followed by the decay $H \to WW^{(*)} \to \ell\nu\ell\nu$, is one of the most important channels for the study of this production mechanism. The precision of the signal strength measurement in the Middle (Low) scenario is 40% (100%) worse than in the Reference scenario. This is due to the degradation in the central-jet-veto efficiency as the pile-up jet rejection becomes less effective, and the less performant b-jet veto, which allows a greater contamination from $t\bar{t}$ background.

The analysis of VBF production of a Higgs boson, followed by the decay $H \to ZZ^{(*)} \to \ell\ell\ell\ell$ is qualitatively different. The dominant backgrounds are $V+\text{jets}$ and ZZ continuum production, which can be strongly reduced thanks to the high mass-resolution for this fully reconstructed final state. There is no need to use the central-jet-veto, which is essential in the WW final state. The main task of the analysis is then to distinguish Higgs bosons from the gluon-gluon-fusion process from the VBF signal. In addition, the contamination from pile-up jets is less important, because the multi-variate analysis being used strongly suppresses contributions from pile-up jets. The measurement precision decreases by only 6% in the Low scenario compared to the result in the Reference scenario. If current theoretical uncertainties in the ggF production mode are taken into account, the difference increases to 11%.

The measurement of electroweak vector boson scattering (VBS) $VV \to VV$ with $V = W, Z$ provides a unique window into the nature of the electroweak symmetry breaking mechanism as well as into potential new physics in the electroweak sector. This analysis has been performed in the same-sign WW final state, since the QCD processes which contribute to this final state are comparable in magnitude to the electroweak production of this final state, whereas in other final states, the QCD

processes are much larger than the electroweak production modes of interest. This makes the same-sign WW final state the most promising process to use in achieving a precise understanding of VBS processes at the HL-LHC. The precision of the cross-section measurement in the Reference scenario is 6%, and is a factor of 1.9 (2.2) worse in the Middle (Low) scenario. This degradation is largely explained by the reduced acceptance for lepton reconstruction in the Middle and Low layouts, which reduces the effectiveness of the lepton-veto, and by the larger fraction of pile-up jets at large rapidities which survive pile-up rejection cuts as the tracking coverage is decreased.

Along with the precision program, one of the main goals of the HL-LHC is to continue the search for new physics beyond the SM. Two illustrative analyses are summarised in Table 46. Among the best motivated theories of BSM physics is Supersymmetry. The electro-weakinos are expected to be the lighest supersymmetric particles and to be within the reach of the LHC. When pair produced, the chargino and neutralino can decay into a final state with one lepton, two b-jets and missing transverse momentum. The deterioration of the trigger performance in the Middle and Low scenarios with respect to the Reference scenario has a major impact reducing the discovery potential from 850, to 700 and 675 GeV respectively. To reach the same sensitivity accessible with the Reference scenario with 3000 fb^{-1} a data sample corresponding to 6000 fb^{-1} and 12000 fb^{-1} would be needed in the Middle and Low scenario, respectively.

Many new physics models predict high mass resonances leading to pair production of boosted particles. For example, this may lead to rates of Higgs boson pair production significantly higher than the Standard Model expectation. A search for heavy resonances decaying into two Higgs bosons, each subsequentally decaying into two b-jets, leads to final states with two large-radius boosted jets in opposite hemispheres of the detector. Each large-radius jet should contain two b-tagged jets making the search vulnerable to reduced b-tagging performance at high p_{T}. A significant loss of sensitivity is observed in the Low scenario compared with the Reference and Middle scenarios. To reach the same sensitivity accessible in the Reference scenario with 3000 fb^{-1} a data sample of 7200 fb^{-1} is needed assuming the Low Scenario.

Table 46. Mass limits and significances for searches of new phenomena in SUSY $\chi_1^{\pm}\chi_2^o \to \ell b\bar{b} + X$ and BSM $HH \to b\bar{b}b\bar{b}$ ($M_{G^*_{KK}}$=2.0 TeV). For both analyses the equivalent integrated luminosity needed in the Middle and Low scenario configurations to reach the same result as in the Reference scenario is given.

Scenario	SUSY $\chi_1^{\pm}\chi_2^o \to \ell b\bar{b} + X$		BSM $HH \to b\bar{b}b\bar{b}(M_{G^*_{KK}}$=2.0 TeV)	
	Mass (GeV)	$\mathcal{L}^{\mathrm{int}}_{\mathrm{equiv.}}$ [fb^{-1}]	Significance	$\mathcal{L}^{\mathrm{int}}_{\mathrm{equiv.}}$ [fb^{-1}]
Reference	850	3000	4.4	3000
Middle	770	6000	4.5	
Low	675	12000	3.1	7200

XII.4 Conclusions

The exciting physics program of ATLAS at the HL-LHC spans precision measurements of the Higgs boson, probing electroweak symmetry breaking further by studying longitudinal vector boson fusion and scattering processes, and continuing searches for new physics both at higher masses and in rare processes. Furthermore, detailed studies of any previously discovered beyond-the-Standard-Model phenomena will be essential. The Reference scenario presented will provide a powerful detector for these studies as outlined in a selected set of benchmark cases summarised above, based on the excellent physics object performances detailed earlier.

The Reference scenario has many advantages relative to the Middle scenario. These include the following significant items:

- The thresholds for key triggers in the simplified trigger menu, including the single electron, single muon, the di-lepton triggers for $e\mu$, $\mu\mu$, and $\tau\tau$, the single jet, the multi-jet, the H_T, the $E_{\mathrm{T}}^{\mathrm{miss}}$, and the jet+$E_{\mathrm{T}}^{\mathrm{miss}}$ triggers are significantly lower in the Reference scenario.
- The efficiency for the single muon, and the di-lepton $e\mu$ and $\mu\mu$ triggers is significantly higher. For the single muon case, the efficiency is 95% in the Reference scenario compared to 80% in the Middle scenario, almost a 20% improvement.
- The ITk performance for reconstructing single muons in a high pile-up event is better. Although the nominal efficiency is almost identical, the rate for mis-reconstructed tracks is significantly lower, never higher than 0.1% compared to 1% for the Middle scenario. In addition, the impact on the efficiency for 10% dead modules is only a few percent in the Reference scenario instead of almost 10% in the Middle scenario, so it is a more robust tracker.
- The inclusion of lepton tagging over the widest η-range (more electrons due to the larger ITk η-coverage, more muons due to the ITk coverage and the inclusion of the muon-tagger) is important. This leads to improved statistics in the $H \to 4\mu$ and $H \to \mu\mu$ analyses, and improved rejection of multi-lepton backgrounds in the SM VBS same-sign $W^{\pm}W^{\pm}$ analysis.
- The inclusion of b/c-tagging over the widest η range leads to improved b-veto performance to suppress $t\bar{t}$ background in the $H \to WW^{(*)} \to \ell\nu\ell\nu$ analysis.
- Improved pile-up jet rejection, and correspondingly improved $E_{\mathrm{T}}^{\mathrm{miss}}$ resolution, in the Reference scenario leads to a reduction of the impact of pile-up on analyses which require jets and $E_{\mathrm{T}}^{\mathrm{miss}}$ at the high μ conditions of the HL-LHC. Examples include the measurement of forward jets required by the Higgs boson and SM analyses summarised in Table 45, and the $E_{\mathrm{T}}^{\mathrm{miss}}$ resolution required for the SUSY analysis in Table 46.

By comparison, the Low scenario has many significant disadvantages when compared to the Middle scenario.

- The ITk performance for reconstructing single muons is poor, with a nominal efficiency of only 90%, and a lack of robustness, with a reduction in efficiency by a further 15% when 10% of the modules are dead.
- The ITk performance shows substantial reductions in the vertex ID efficiency, the conversion reconstruction efficiency, and the light-quark rejection for the b-tagging algorithm in the Low scenario compared to the Middle scenario.
- The Low scenario has significantly reduced pile-up jet rejection and much poorer $E_{\mathrm{T}}^{\mathrm{miss}}$ resolution as a function of total transverse energy. The $E_{\mathrm{T}}^{\mathrm{miss}}$ performance also degrades more significantly when μ increases from 140 to 200.
- The barrel muon trigger has a substantially lower efficiency due to the reduced RPC gains required to extend the lifetime of these chambers at the HL-LHC, combined with the lack of redundant RPC planes in this scenario.

These features lead to poorer precision or significance for all of the benchmark analyses in the Low scenario compared to the Middle scenario. Combining these disadvantages together, it is clear that the Low scenario represents a detector which is far from optimal for the rich HL-LHC physics programme at $\mu = 140$ and even more clearly so at $\mu = 200$.

The combined advantages of the Reference detector over the Middle scenario means that it provides substantially enhanced physics capability. This is demonstrated by the results summarised in Table 45, and is further quantified in Table 46 in the column indicating the required integrated luminosity necessary to achieve the Reference scenario search result in the Middle or Low scenarios.

Operational scenarios with integrated luminosities much greater than 3000 fb^{-1}, which would require years of additional operation of the HL-LHC, are clearly far more costly than the differences in cost between the scoping scenarios discussed here. In summary, the Reference detector provides a much-improved and powerful configuration of the ATLAS experiment well-matched to the extensive and exciting physics programme in the HL-LHC era.

Glossary

ADC Analog-to-Digital Converter. 65–69, 71, 74, 78

AFP ATLAS Forward Physics. 117, 118, 122

ALARA *As Low As Reasonable Achievable* symbol. 125, 129, 141

ALFA Absolute Luminosity For ATLAS. 117

AM Associative Memory. 29–31

AMC Advanced Mezzanine Card. 69

ARM Advanced Reduced Instruction Set Computer (RISC) Machines. 111

ASD Amplifier-Shaper Discriminator ASIC. 102–104

ASIC Application-Specific Integrated Circuit. vi, 7, 8, 29, 45, 49, 50, 55–57, 64–66, 68–71, 77, 78, 93, 102, 103, 106, 107, 114, 155

ATCA Advanced Telecom Computing Architecture. 23, 69, 72, 82, 139, 140

BC Bunch Crossing. 8

BCID Bunch Crossing IDentification. 18

BDT Boosted Decision Tree. 22

BEE Barrel/End-cap Extra station layer. 99

BI Barrel Inner layer. 11–13, 17, 18, 98, 99, 101, 102, 106, 108, 133, 206, 207, 209

BiCMOS Bipolar Complementary Metal-Oxide Semiconductor. 66, 67

BIL Barrel Inner Large chamber sector. 11, 133

BIS Barrel Inner Small chamber sector. 11, 133

BIS7 BIS chamber in sector #7. See BIS78 project. 114

BIS78 Barrel Inner Small sector #7,8. It is an approved ATLAS Phase-I upgrade project, consisting in the insertion of new RPC BI stations, which allows for an increase of the current detector coverage up to 96%. 99, 104, 106, 108, 114

BIS8 BIS chamber in sector #8. See BIS78 project. 114

BJT Bipolar Junction Transistor. 106

BM Barrel Middle layer. 12, 13, 98, 102, 111

BMG BMG refers to 12 sMDT chambers to be installed in the feet of the ATLAS detector (sectors 12/14) in the LHC 2016/2017 winter shutdown in order to cover acceptance gaps in that region. 114

BML Barrel Middle Large chamber sector. 99, 133

BMS Barrel Middle Small chamber sector. 99

BO Barrel Outer layer. 12, 13, 98, 102, 111

BOL Barrel Outer Large chamber sector. 99

BOS Barrel Outer Small chamber sector. 99

BW Big Wheel. 109, 134

CiS Charge-injection-Scan. 75, 76

CMOS Complementary Metal-Oxide Semiconductor. 7, 37, 45, 54, 55, 58, 67, 93, 102, 104

COTS Commercial Off-The-Shelf component. 64, 65, 75, 78

CPU Central Processing Unit. 19, 22, 25, 29, 33

CSM Chamber Service Module. 101, 102, 113, 133

CTP Central Trigger Processor. 16, 17, 21–23, 29, 33

DAC Digital-to-Analog Converter. 70

DAQ Data Acquisition. 16, 29, 30, 41, 63, 65–67, 75, 78, 80, 141, 147, 206, 208

DB Daughter-board. 75, 76, 82

DC-DC Direct Current to Direct Current. 52, 55, 58

DC/DC See DC-DC. 70

DCS Detector Control System. 56, 58, 80, 141

DCT Data Collector Transmitter. 102, 104

EB Executive Board. 152–156

EBA Tile Extended Barrel A-side. 134

EBC Tile Extended Barrel C-side. 134

ECFA European Committee for Future Acceleartors. 6

EDMS Engineering & Equipment Data Management Service. 155

EDUSAFE EDUSAFE is a 4-year Marie Curie ITN project that provides training for 10 Early Stage Researchers and 2 Experienced Researchers. 130

EE Extended End-cap layer. 12

EEL End-cap Extended Large chamber sector. 99

EEPROM Electrically Erasable Programmable Read-Only Memory. 113

EES End-cap Extended Small chamber sector. 99, 133

EF Event Filter. 8, 17, 18, 21–28, 30, 33, 206, 208

eFEX electron Feature EXtractor trigger processor. 19, 20

EI End-cap Inner layer. 98, 101, 104

EIL End-cap Inner Large chamber sector. 99, 133

ELMB Embedded Local Monitor Board. 113, 141

ELMB++ upgraded ELMB. 141

EM End-cap Middle layer. 12, 13, 98, 102, 111

EMB Electromagnetic Barrel Calorimeter. 10, 65

EMEC Electromagnetic End-cap Calorimeter. 10, 65, 87

EML End-cap Middle Large chamber sector. 99

EMS End-cap Middle Small chamber sector. 99

EO End-cap Outer layer. 12, 13, 98, 102, 134

EOS End-cap Outer Small chamber sector. 99

EoS End of Structure. 51, 56, 57

FATALIC Front-end for Atlas TilecAL IC. 78

FCal Forward Calorimeter. 10, 11, 63, 70, 83–91, 131, 138, 155, 158, 177, 178, 209

FCal1 FCal module #1. 10, 84, 85, 87, 88, 177

FCal2 FCal module #2. 84, 85

FCal3 FCal module #3. 84, 85

FDR Final Design Review. 33, 148, 155

FE Front-End. 56, 80–82, 106, 108, 113

FEB Front-End Board. vii, 64, 80, 82

FEB-2 upgraded Front-End Board. 65–70, 72, 73, 85, 86

FEC Front-End Crate. 85, 86

FELIX Front-End Link Interface eXchange. 16, 17, 23, 24, 30, 33, 65, 68, 72, 102

FESOC Front-End System-On-Chip. 68, 69

FEX Feature EXtractor trigger processor. 19–21, 23

FLUKA Monte Carlo program used to simulate electromagnetic and hadronic particle showers in the ATLAS detector. Used for radiation calculations symbol. 125

FPGA Field-Programmable Gate Array. 7, 8, 19, 20, 22–24, 28–31, 55, 64, 65, 67, 69–72, 76–78, 82, 102, 104, 111, 114

FTE Full-Time Equivalent. 148

FTK Fast TracKer trigger. 8, 15, 25, 29–31

FTK++ upgraded Fast TracKer trigger. v, 8, 9, 21, 23, 25–31, 147, 159, 175, 206, 208

FWHM Full Width at Half Maximum. 75

FZ Float Zone. 47, 49

GBLD GBT Laser Driver. 50

GBT Giga-Bit Transceiver project. 17, 23, 30, 50, 56, 76, 77, 102

GBTx Giga-Bit Transmitter. 50, 77

gFEX global Feature EXtractor trigger processor. 19, 20

GIF Gamma Irradiation Facility. 111

GIF++ upgraded Gamma Irradiation Facility (GIF). 108, 111

GOL Giga-Bit Optical Link. 102

GPU Graphics Processing Unit. 22, 29

HCC Hybrid Controller Chip. 50, 54, 55

HEC Hadronic End-cap Calorimeter. 10, 63–65, 70, 72, 85, 87

HGTD High Granuarity Timing Detector. vii, 63, 91, 92, 95, 96, 147, 158

HL-LHC High Luminosity LHC. vi, vii, 2, 4–8, 10, 11, 15, 20, 26, 35, 37, 47, 50, 52, 54, 59, 63–65, 70, 71, 73–75, 79, 80, 83, 85, 87, 89, 92, 98, 100–102, 105, 106, 109, 112, 113, 117, 118, 125, 126, 131, 137, 140, 158, 179, 192, 198, 199, 205–213

HLT High-Level Trigger. 8, 22, 25, 29, 109

HV High Voltage. vii, 10, 37, 52, 53, 55, 57, 58, 63, 74, 78, 80–83, 85, 87, 105, 114

HV-CMOS High Voltage CMOS. 93

HVPS High Voltage Power Supply. 90

IB Institute Board. 153

IBL Insertable B-Layer. 7, 8, 42, 45–47, 54, 55, 57, 61, 90, 136

IC Integrated Circuit. 78

ID Inner tracking Detector. 7, 35, 37, 42, 52, 58–61, 92, 125, 129–131, 133, 140–143, 154, 171

IDR Initial Design Review. 71, 73, 79, 89, 91, 95, 96, 114, 148, 153–155

iMOU interim MOU. 154

IP Interaction Point. 89, 104, 117, 119, 125, 128

ITk Inner Tracker. viii, 4, 10, 13, 15, 18, 20, 21, 24, 25, 27, 30, 35–40, 42, 45–47, 50, 52–61, 64, 92, 130, 131, 133, 134, 137, 139–143, 147, 150, 152–155, 158, 159, 166, 168, 171, 173, 174, 178, 179, 206–209, 212

JD ATLAS Shielding Disc. The JD is a shielding structure that supports and shields the muon chambers in the Muon small wheel, and returns the flux of the super-conductive solenoid magnetic field. 111

JES Jet Energy Scale. 174

JFET Junction Field-Effect Transistor. 52

jFEX jet Feature EXtractor trigger processor. 19, 20

JM ATLAS Moderator Shielding. The JM is a shielding structure on the front-face of the end-cap LAr calorimeter to protect the inner detector from back-splash of neutrons fom the calorimeter. 89

JTT The JTT shielding is part of the JT. It is a cylindical structure made of ductile cast iron that surrounds the beam-pipe in the end-cap toroids. It consists of four plug pieces of cast iron and polyethylene layers doped with B_2O_3 which acts as neutron shielding. The photons created in the polyethylene layer are absorbed by the stainless steel bore tube of the end-cap toroid that supports the shielding. 129

L0 Level-0 trigger. 8, 11–13, 15–30, 33, 50, 54, 64–66, 73, 75, 98, 100–104, 109, 110, 147, 205, 206

L1 Level-1 trigger. 7, 8, 11, 13, 15–18, 20–27, 29, 30, 50, 64–67, 70, 98, 100–102, 104, 109, 118, 147, 205, 206, 208

L1Global Level-1 Global Trigger. 15, 16, 20–25, 28, 29, 208

L1Track Level-1 Track Trigger. 8, 15, 20–31, 159, 175, 176, 206, 208

LAr Liquid Argon. vii, 7, 11, 18–22, 29, 63–73, 83–93, 95, 96, 129, 133, 134, 137, 138, 140, 142, 143, 147, 153, 154, 177, 205, 206

LBA Tile Long Barrel A-side. 134

LBC Tile Long Barrel C-side. 134

LDPB LAr Digital Processing Board. 65, 69, 71

LDPS LAr Digital Processing System. 23, 71

LEP Large Electron Positron collider. 142

LGAD Low-Gain Avalanche Detector. 93, 96

LHC Large Hadron Collider. 2, 4–6, 15, 26, 64, 65, 67, 71, 83, 84, 98, 100, 104, 105, 109, 112, 117–119, 121, 137, 141, 179, 181, 182

LHC-RRB LHC Research Review Board. 2, 4

LHCC LHC Experiment Committee. 2, 79, 145, 148

LoI Letter of Intent. 4, 6, 8, 10, 22, 23, 27, 35–37, 40, 41, 45, 52, 57, 58, 84, 158, 171, 174, 205, 209

LoI-VF ITk layout in the Reference scenario, with coverage up to $|\eta| \leq 4.0$. 35, 37–40, 42, 52, 55, 158

lpGBT Low Power GBT transmitter. 68, 71

lpGBTx Low Power GBT transmitter. 50

LPPR LAr Pre-PRocessor. 68, 69, 71, 72

LSB Least Significant Bit. 109

LTDB LAr Trigger Digitizer Board. 23, 64, 65

LUCID LUminosity Cherenkov Integrating Detector. 117, 119, 121, 122

LUCROD LUCID Readout Driver. 121

LV Low Voltage. 37, 52, 53, 55, 57, 58, 75, 114

LVPS Low Voltage Power Supply. 65, 70, 72, 75, 80, 81

MB Motherboard. 75, 76, 78, 82

MCP Multi-Channel Plate. 93

MDT Monitored Drift Tube. vii, viii, 11–13, 15–19, 22, 28, 30, 32, 98, 99, 101–104, 106, 108–114, 131, 133, 134, 147, 206

MiniFCal Mini Forward-Calorimeter. vii, 11, 63, 83, 86–93, 134, 137, 138, 143, 147

MIP Minimum Ionising Particle. 93

MOSFET Metal-Oxide Semiconductor Field-Effect Transistor. 52, 70

MOU Memorandum Of Understanding. 145, 148, 154

MPO Multi-Fiber Push On. 69

MS Muon Spectrometer. 98, 113

MTP Medium Term Plan. 5, 125

MuCTPI Muon to CTP Interface. 17, 23, 29

NIC Network Interface Card. 23

NIEL Non-ionising Energy Loss. 65, 80

NMR Nuclear Magnetic Resonance. 58

NRE Non Recurring Engineering. 31, 57, 155

NSW New Small Wheel. 7, 11, 13, 15–19, 23, 28–30, 98, 101, 102, 104, 106, 108, 109

PAR Production Advancement Review. 155

PC Personal Computer. 72

PCB Printed Circuit Board. 31, 69, 77, 82

PCI Peripheral Component Interconnect. 23

PCIe PCI Express. 23, 24

pCVD poly-Crystalline Vapour Deposited. 87, 88

PDR Preliminary Design Review. 33, 148, 155

PL Detector sub-system Project Leader. 152

PMT Photomultiplier Tube. 73, 75, 76, 78–82, 119–121, 134

POL Point of load regulator. 75

PP1 Patch Panel #1. 57

PP2 Patch Panel #2. 57, 58

PRR Production Readiness Review. 33, 148, 155

PWM Pulse Width Modulator. 113

QA Quality Assurance. 52, 53, 59, 61

QC Quality Control. 52

QIE "Charge Integrator and Encoder" ASIC. 78

QSFP Quad Small Form-Factor Pluggable. 76, 78

ROD Read-Out Driver. 15, 24, 74, 102

RoI Region of Interest. 15, 18, 20, 21, 23, 25, 32

RP Roman Pots. 117

RPC Resistive Plate Chamber. vii, 11–13, 17, 18, 28, 98–100, 102–110, 112–114, 131, 133, 138, 140, 142, 147, 206, 207, 209, 212

S/N Signal-to-Noise ratio. 93

SAR Successive Approximation Register. 67, 68

SCT Semiconductor Tracker. 55, 61

SDX1 Access building on top of the USA15 underground experimental hall. It provides personnel access and access for services to the underground area via the second main shaft (PX15). 139, 141

SEE Single Event Effect. 65, 66, 69, 80

SEU Single Event Upset. 55, 73, 75

sFCal upgraded small-gap Forward Calorimeter. x, 10, 63, 83–87, 89–91, 131, 134, 138, 143, 147, 155, 158, 177, 178, 206, 209

sFCal1 sFCal module #1. 10, 85, 88, 177, 178

sFCal3 sFCal module #3. 86

SFO Sub-Farm Output. 25

SL Sector Logic. 102–104

sMDT small tube diameter MDT. 11–13, 99, 104, 108, 113, 114, 133, 206, 207

SNDR Signal to Noise and Distortion Ratio. 68

SoI Silicon-on-Insulator. 70

SP Serial Powering. 41, 43, 45, 47, 52, 58

SR1 Surface building for system integration tests before installation in the experimental hall. 141, 142

sTGC small Thin Gap Chamber. 12, 13, 98, 99, 109, 113

SW Small Wheel. 130

SX1 Main Surface building above the underground UX15 experimental hall. 139

TAN Target Absorber Neutral: absorber for the neutral particles leaving the IP. It is located just in front of the D1 separation / recombination dipole magnet on the side facing the IP.. 118, 119

TAS Target Absorber Secondaries: absorber for particles leaving the IP at large angles. It is located just in front of the Q1 triplet quadrupole magnet on the side facing the IP. 119, 121, 125, 129–131, 134, 137

TAXS upgraded TAS absorbers. 131, 134

TC ATLAS Technical Coordination. 124, 125, 129, 137–139, 142

TDAQ Trigger and Data Acquisition. 4, 8, 9, 15, 19, 27, 28, 30–33, 37, 50, 80, 147, 153, 154, 206

TDC Time-to-Digital Converter. 101, 102, 109

TDR Technical Design Report. 2, 4, 19, 28, 30, 33, 37, 53–55, 57–61, 71, 73, 79, 80, 89, 91, 95, 96, 114, 145, 146, 148, 150, 153–155

TGC Thin Gap Chamber. 12, 17–19, 28, 98, 100, 101, 104, 108–110, 112, 113, 131, 134, 147

TID Total Ionising Dose. 65, 80

TileCal Scintillating Tile Hadronic Calorimeter. 63, 80, 154, 205

TilePPR Tile Calorimeter Pre-Processor. 75, 77–82

TRT Transition Radiation Tracker. 35

TTC Timing, Trigger and Control system. 24, 30, 56, 63, 68, 72, 77, 78, 102

UCG Upgrade Cost Group. 2, 145, 148

Upgreade Coordinator Upgrade Coordinator. 152–154

UPL Upgrade Project Leader. 152, 153, 156

UPR Upgrade PRoject. 153, 154, 156

UPS Uninterruptible Power Supply. 124, 139

US15 underground service area. 114

USA15 main underground electronics cavern. 18, 101, 102, 104, 108, 109, 114, 139, 140

USC Upgrade Steering Committee. 152, 154–156

UX15 underground experimental cavern. 114, 124, 129, 130, 132, 140

VA Liquid Argon End-cap calorimeter beam-pipe section. 137, 143

VAX Vacuum Assembly Support. 121, 137

VCSEL Vertical Cavity Surface-Emitting Laser. 50, 68

VI Inner Tracker beam-pipe section. 137, 142

VJ Forward Shielding beam-pipe section. 137

VL+ Versatile Link PLUS. 68, 71

VME Versa Module Eurocard. 139

VT End-cap Toroid beam-pipe section. 137

WBS Work Breakdown Structure. 30, 33, 56, 113, 143, 146, 147

ZDC Zero-Degree Calorimeter. 117–119, 122

References

[1] ATLAS Collaboration, *Letter of Intent for the Phase-II Upgrade of the ATLAS Experiment*, CERN-LHCC-2012-022. LHCC-I-023. 2, 4, 6, 8, 15, 23, 27, 84, 102

[2] S. Bertolucci, *Status and Plans for the LHC Experiments*, LHC RRB 40th Meeting April 2015 . http://indico.cern.ch/event/359409/session/1/contribution/8/material/slides/0.pdf. 2, 4, 9, 10, 12

[3] *ECFA High Luminosity LHC Experiments Workshop: Physics and Technology Challenges. 94th Plenary ECFA meeting*, ECFA-13-284. https://cds.cern.ch/record/1631032. 4, 6, 35

[4] *ECFA High Luminosity LHC Experiments Workshop - Physics and Technology Decelopments Summary submitted to ECFA2014. 96th Plenary ECFA meeting*, ECFA-15-289. https://cds.cern.ch/record/1983664. 4, 6, 35

[5] *HL-LHC High Luminosity Large Hadron Collider: The HL-LHC project*, . http://hilumilhc.web.cern.ch/about/hl-lhc-project. 5, 125

[6] R. Heuer, *LHC Schedule according to MTP2015*, CERN Council 76th session, 18-19 June 2015 . http://indico.cern.ch/event/397373/session/0/contribution/9/2/material/slides/0.pdf. 5, 125

[7] *Projections for measurements of Higgs boson signal strengths and coupling parameters with the ATLAS detector at a HL-LHC*, . https://cds.cern.ch/record/1956710. 6

[8] ATLAS Collaboration, *Technical Design Report for the Phase-I Upgrade of the ATLAS TDAQ System*, CERN-LHCC-2013-018 . 7, 19, 23, 24, 26

[9] ATLAS Collaboration, *ATLAS Liquid Argon Calorimeter Phase-I Upgrade Technical Design Report*, CERN-LHCC-2013-017 . 7, 19

[10] ATLAS Collaboration, *New Small Wheel Technical Design Report*, CERN-LHCC-2013-006 . 7, 15

[11] ATLAS Collaboration, *Technical Design Report Fast TracKer (FTK)* , CERN-LHCC-2013-007 . 8, 15

[12] ATLAS Collaboration, *Letter of Intent for the Phase-I Upgrade of the ATLAS Experiment*, CERN-LHCC-2011-012. LHCC-I-020. 15

[13] *RD-53 Collaboration Home*, . http://rd53.web.cern.ch/RD53/. 45, 53

[14] The Versatile Link PLUS project, https://espace.cern.ch/project-Versatile-Link-Plus. 46, 50, 68

[15] N. Buchanan, L. Chen, D. Gingrich, S. Liu, H. Chen, et al., *Design and implementation of the Front End Board for the readout of the ATLAS liquid argon calorimeters*, JINST **3** (2008) P03004. 64

[16] Liquid Argon Back End Electronics Collaboration, A. Bazan et al., *ATLAS liquid argon calorimeter back end electronics*, JINST **2** (2007) P06002. 64

[17] ATLAS Collaboration, *ATLAS Liquid Argon Calorimeter Phase-I Upgrade Technical Design Report*, Tech. Rep. CERN-LHCC-2013-017. ATLAS-TDR-022, CERN, Geneva, Sep, 2013. https://cds.cern.ch/record/1602230. 64, 66, 69

[18] N. Buchanan, L. Chen, D. Gingrich, S. Liu, H. Chen, et al., *Radiation qualification of the front-end electronics for the readout of the ATLAS liquid argon calorimeters*, JINST **3** (2008) P10005. 64

[19] ATLAS Collaboration, *Letter of Intent for the Phase-II Upgrade of the ATLAS Experiment*, Tech. Rep. CERN-LHCC-2012-022. LHCC-I-023, CERN, Geneva, Dec, 2012. https://cds.cern.ch/record/1502664. 64

[20] D. Gingrich, G. Lachat, J. Pinfold, J. Soukoup, D. Axen, et al., *Construction, assembly and testing of the ATLAS hadronic end-cap calorimeter*, JINST **2** (2007) P05005. 64

[21] F. Ahmadov et al., *Upgrade plans for the Hadronic-Endcap Calorimeter of ATLAS for the high luminosity stage of the LHC*, Tech. Rep. ATL-COM-LARG-2013-002 (to be replaced with PUB note), CERN, Geneva, Feb, 2013. https://cds.cern.ch/record/1517088. 64, 85

[22] F. Lanni et al., *Report of the 2013 Radiation Estimate Task Force*, Tech. Rep. ATU-GE-ER-0005, EDMS 1293497, CERN, 2013. 64

[23] J. P. Grohs and S. Stärz, *AREUS*, Tech. Rep. ATL-LARG-INT-2014-003, CERN, Geneva, Jul, 2014. https://cds.cern.ch/record/1745502. 65

[24] H. Xu, Y. Zhou, Y. Chiu, D. Gong, T. Liu, and J. Ye, *High-speed, high-resolution, radiation-tolerant SAR ADCs for particle physics experiments*, Journal of Instrumentation **10** (2015) no. 04, C04035. http://stacks.iop.org/1748-0221/10/i=04/a=C04035. 66, 68, 69

[25] J. Kuppambatti, J. Ban, T. Andeen, P. Kinget, and G. Brooijmans, *A radiation-hard dual channel 4-bit pipeline for a 12-bit 40 MS/s ADC prototypewith extended dynamic range for the ATLAS Liquid Argon Calorimeter readout electronics upgradeat the CERN LHC*, JINST **8** (2013) P09008, arXiv:1308.0028 [physics.ins-det]. 66, 68

[26] Fatah Rarbi,*PEALL4: A 4-channel, 12-bit, 40-MSPS, Power Efficient and Low Latency SAR ADC*, TWEPP Conference 2014. 66, 68

[27] F. Liang, D. Gong, S. Hou, T. Liu, C. Liu, D. S. Su, P. K. Teng, A. C. Xiang, J. Ye, and G. Jin, *The design of 8-Gbps VCSEL drivers for ATLAS liquid Argon calorimeter upgrade*, Journal of Instrumentation **8** (2013) no. 01, C01031. http://stacks.iop.org/1748-0221/8/i=01/a=C01031. 68, 69

[28] Paulo Moreira, *GBT Project: Present & Future*, ACES 2014 - Fourth Common ATLAS CMS Electronics Workshop for LHC Upgrades, CERN 2014, https://indico.cern.ch/event/287628. 68

[29] ALTERA Corporation, *Arria 10 Device Overview*, Tech. Rep. 2015.06.15, 2015. https://www.altera.com. 69

[30] Xilinx Inc., *UltraScale Architecture and Product Overview*, Tech. Rep. DS890 (v2.1), 2015. http://www.xilinx.com. 69

[31] A. Affolder, B. Allongue, G. Blanchot, F. Faccio, C. Fuentes, A. Greenall, and S. Michelis, *DC-DC converters with reduced mass for trackers at the HL-LHC*, Journal of Instrumentation **6** (2011) no. 11, C11035. http://stacks.iop.org/1748-0221/6/i=11/a=C11035. 70

[32] J. Abdallah et al., *Design, construction and installation of the ATLAS hadronic barrel scintillator-tile calorimeter*, Tech. Rep. ATL-TILECAL-PUB-2008-001, ATL-COM-TILECAL-2007-019, ATLAS TileCal, 2008. 73

[33] ATLAS TileCal Collaboration, J. Abdallah et al., *The optical instrumentation of the ATLAS tile calorimeter*, JINST **8** (2013) P01005. 73

[34] ATLAS Collaboration, G. Aad et al., *The ATLAS Experiment at the CERN Large Hadron Collider*, JINST **3** (2008) S08003. 73, 101, 104

[35] K. Anderson, A. Gupta, F. Merritt, M. Oreglia, J. Pilcher, et al., *Design of the front-end analog electronics for the ATLAS tile calorimeter*, Nucl.Instrum.Meth. **A551** (2005) 469–476. 74

[36] F. Tang, K. Anderson, G. Drake, J. Genat, M. Oreglia, et al., *Design of the front-end readout electronics for ATLAS Tile Calorimeter at the sLHC*, IEEE Trans.Nucl.Sci. **60** (2013) 1255–1259. 75

[37] F. Carrio, *Upgrade for the ATLAS Tile Calorimeter Readout Electronics at the High Luminosity LHC*, Nucl.Instrum.Meth. **A718** (2012) . http://www.sciencedirect.com/science/article/pii/S0168900212014052. 75

[38] ATLAS Collaboration, S. Muschter et al., *Development of a readout link board for the demonstrator of the ATLAS Tile calorimeter upgrade*, JINST **8** (2013) C03025. 75

[39] G. Drake, W. Fernando, R. Stanek, and D. Underwood, *Modulator based high bandwidth optical readout for HEP detectors*, JINST **8** (2013) C02023. 76

[40] P. Moreira, *The GBT, a proposed architecture for multi-Gbps data transmission in high energy physics*, p. 71, Topical Workshop on Electronics for Particle Physics (TWEPP07). 2007. http://indico.cern.ch/getFile.py/access?contribId=71&sessionId=16&resId=0&materialId=paper&confId=11994. 76

[41] J. Hoff, *SMQIE: The Shower Max QIE chip*, Tech. Rep. FERMILAB-TM-2075, 1999. 78

[42] N. Pillet, *FATALIC, a wide dynamic range integrated circuit for the tilecal VFE Atlas upgrade*, Proceedings of TWEPP 2011 (2011) . 78

[43] F. Vazeille, T. Theveneaux-Pelzer, G. Drake, R. Bonnefoy, and E. Sahuc, *NIEL and TID certifications of the active dividers of the Tile Calorimeter of the ATLAS detector for the Phase II upgrade*, Tech. Rep. ATL-TILECAL-INT-2015-001, CERN, Geneva, Jan, 2015. https://cds.cern.ch/record/1980942. 80

[44] F. Vazeille, T. Theveneaux-Pelzer, G. Drake, R. Bonnefoy, and E. Sahuc, *NIEL and TID certifications of the active dividers of the Tile Calorimeter of the ATLAS detector for the Phase II upgrade*, Tech. Rep. ATL-COM-TILECAL-2014-074, CERN, Geneva, Nov, 2014. https://cds.cern.ch/record/1966942. 80

[45] G. Drake and R. Stanek, *Summary of Radiation Testing of the V7.3.1 ATLAS TileCal LVPS Bricks*, Tech. Rep. ATL-COM-TILECAL-2012-019, CERN, Geneva, May, 2012. https://cds.cern.ch/record/1453424. 80

[46] R. Bonnefoy, R. Chadelas, D. Lambert, R. Madar, E. Sahuc, and F. Vazeille, *Performances of a Remote High Voltage Power Supply for the Phase II Upgrade of the ATLAS Tile Calorimeter*, Tech. Rep. ATL-COM-TILECAL-2014-082, CERN, Geneva, Nov, 2014. https://cds.cern.ch/record/1972544. 80

[47] G. Drake, B. Stanek, and J. Kierstead, *Stability of QSFP Transceivers in LANSCE n Beam*, Tech. Rep. ATL-TILECAL-INT-2014-003, CERN, Geneva, Feb, 2014. https://cds.cern.ch/record/1648449. 80

[48] ATLAS Liquid Argon Endcap Collaboration, A. Glatte et al., *Liquid argon calorimeter performance at high rates*, Nucl.Instrum.Meth. **A669** (2012) 47–65. 83

[49] D. Axen et al., *Diamond detector irradiation tests at TRIUMF*, Journal of Instrumentation **6** (2011) no. 05, P05011. http://stacks.iop.org/1748-0221/6/i=05/a=P05011. 87, 88

[50] *CALICE: The Silicon Tungsten ECAL*, . https://twiki.cern.ch/twiki/bin/view/CALICE/SiWEcal. 93

[51] The NA62 Collaboration, *2015 NA62 Status Report to the CERN SPSC*, Tech. Rep. CERN-SPSC-2015-012/SPSC-SR-157, 2015. http://na62.web.cern.ch/NA62/Documents/SPSC-SR-157_2015.pdf. 93

[52] N. Cartiglia, *Timing Performance of Silicon and Diamond Tracking Systems*, Tech. Rep. Workshop on requirements for future detector technologies in view of FCC-hh, 2015. http://indico.cern.ch/event/358198/session/1/contribution/4/material/slides/0.pdf. 93

[53] ATLAS CMOS Pixel Collaboration, B. Ristic, *Measurements on HV-CMOS Active Sensors After Irradiation to HL-LHC fluences*, JINST **10** (2015) no. 04, C04007, arXiv:1412.1589 [hep-ex]. 93

[54] ATLAS Collaboration, M. Aleksa et al., *Rate Effects in High-Resolution Drift Chambers*, Nucl.Instrum.Meth. **A446** (2000) 435. 101

[55] ATLAS Collaboration, S. Horvat et al., *Operation of the ATLAS Muon Drift-Tube Chambers at High Background Rates and in Magnetic Fields*, IEEE trans. on Nucl. Science Instr. **53, 2** (2006) 562. 101

[56] P. Moreira et al., *The GBT-SerDes ASIC prototype*, JINST **5** (2010) C11022. 102

[57] ATLAS Collaboration, *Performance of the ATLAS muon trigger in pp collisions at* $\sqrt{s} = 8$ *TeV*, Eur.Phys.J. **C75** (2015) no. 3, 120, arXiv:1408.3179 [hep-ex]. 104

[58] G. Aielli, M. Alviggi, V. Ammosov, M. Bianco, M. Biglietti, et al., *New results on ATLAS RPC's aging at CERN's GIF*, IEEE Trans.Nucl.Sci. **53** (2006) 567–571. 105

[59] R. Cardarelli, G. Aielli, P. Camarri, A. Di Ciaccio, L. Di Stante, et al., *Performance of RPCs and diamond detectors using a new very fast low noise preamplifier*, JINST **8** (2013) P01003. 106

[60] L. Paolozzi, G. Aielli, R. Cardarelli, A. Di Ciaccio, L. Di Stante, et al., *Test for upgrading the RPCs at very high counting rate*, PoS **RPC2012** (2012) 065. 106

[61] B. Bittner, J. Dubbert, O. Kortner, H. Kroha, F. Legger, R. Richter, O. Biebel, A. Engl, R. Hertenberger, and F. Rauscher, *Development of muon drift-tube detectors for high-luminosity upgrades of the Large Hadron Collider*, Nucl. Instrum. Meth. **A617** (2010) 169–172. 108

[62] H. Kroha et al., *Construction and test of a full prototype drift-tube chamber for the upgrade of the ATLAS muon spectrometer at high LHC luminosities*, Nucl. Instrum. Meth. **A718** (2013) 427–428. 108

[63] R. Cardarelli, L. D. Stante, B. Liberti, L. Paolozzi, E. Pastori, et al., *New RPC gas mixtures for large area apparatuses*, JINST **9** (2014) no. 11, C11003. 108

[64] ATLAS Collaboration, *ATLAS muon spectrometer: Technical design report*, . 110

[65] J. Dubbert, S. Horvat, O. Kortner, H. Kroha, and R. Richter, *Upgrade of the ATLAS Muon Trigger for the SLHC*, JINST **5** (2010) C12016, arXiv:1011.0163 [physics.ins-det]. 109

[66] P. Schwegler, O. Kortner, H. Kroha, and R. Richter, *Improvement of the L1 trigger for the ATLAS muon spectrometer at high luminosity*, Nucl. Instrum. Meth. **A718** (2013) 245–247. 109

[67] H. Kroha and S. Nowak (on behalf of the ATLAS Muon Collaboration), *A Highly Selective First-Level Muon Trigger With MDT Chamber Data for ATLAS at HL-LHC*, in *Proceedings of the 13th Pisa Meeting on Advanced Detectors, La Biodola. Isola d'Elba, Italy, 24-30 May 2015*. 2015. Submitted to NIMA, ATL-MUON-PROC02015-005. 111

[68] T.T. Böhlen, F. Cerutti, M.P.W. Chin, A. Fassò, A. Ferrari, P.G. Ortega, A. Mairani, P.R. Sala, G. Smirnov and V. Vlachoudis, *The FLUKA Code: Developments and Challenges for High Energy and Medical Applications*, Nuclear Data Sheets **120** (2014) no. 211-214, . 125

[69] A. Ferrari, P.R. Sala, A. Fassò and J. Ranft, *FLUKA: a multi-particle transport code*, tech. rep., 2005. 125

[70] The HiLumi LHC Collaboration, *HL-LHC Preliminary Design Report: Deliverable D1.5*, Tech. Rep. CERN-ACC-2014-0300, November, 2014. https://cds.cern.ch/record/1972604/. 125

[71] O. Beltramello et al, *Radiation protection: New Results for LS2 and Beyond*, tech. rep., October, 2014. https://indico.cern.ch/event/315626/session/2/contribution/55/attachments/605645/833487/2014_ECFA_ATLAS_CMS.pdf. ECFA 2014 workshop. 125, 126

[72] http://edusafe.web.cern.ch/edusafe/site.php. 130

[73] https://edms.cern.ch. 155

[74] ATLAS Collaboration, G. Aad et al., *Measurement of the muon reconstruction performance of the ATLAS detector using 2011 and 2012 LHC proto proton collision data*, Eur. Phys. J. **C74** (2014) no. 11, 3130, arXiv:1407.3935 [hep-ex]. 162

[75] ATLAS Collaboration, G. Aad et al., *Electron and photon energy calibration with the ATLAS detector using LHC Run 1 data*, Eur. Phys. J. **C74** (2014) no. 10, 3071, arXiv:1407.5063 [hep-ex]. 168

[76] ATLAS Collaboration, *Electron efficiency measurements with the ATLAS detector using the 2012 LHC proton-proton collision data*, . https://cds.cern.ch/record/1706245. 169

[77] ATLAS Collaboration, *Prospects for measuring Higgs pair production in the channel $H(\rightarrow \gamma\gamma)H(\rightarrow b\bar{b})$ using the ATLAS detector at the HL-LHC*, . https://cds.cern.ch/record/1956733. 172

[78] M. Cacciari, G. P. Salam, and G. Soyez, *The Anti-k(t) jet clustering algorithm*, JHEP **04** (2008) 063, arXiv:0802.1189 [hep-ph]. 174

[79] ATLAS Collaboration, *Jet energy scale and its systematic uncertainty in proton-proton collisions at sqrt(s)=7 TeV with ATLAS 2011 data*, . https://cds.cern.ch/record/1509552. 174

[80] ATLAS Collaboration, *Performance assumptions for an upgraded ATLAS detector at a High-Luminosity LHC*, . https://cds.cern.ch/record/1527529. 174

[81] T. Sjostrand, S. Mrenna, and P. Z. Skands, *A Brief Introduction to PYTHIA 8.1*, Comput. Phys. Commun. **178** (2008) 852–867, arXiv:0710.3820 [hep-ph]. 178

[82] T. Sjostrand, S. Mrenna, and P. Z. Skands, *PYTHIA 6.4 physics and manual*, JHEP **0605** (2006) 026, hep-ph/0603175. http://dx.doi.org/10.1088/1126-6708/2006/05/026. 178

[83] S. Fartoukh, *Pile up management at the high-luminosity LHC and introduction to the crab-kissing concept*, Phys. Rev. ST Accel. Beams **17** (2014) no. 11, 111001. 179

[84] ATLAS Collaboration, *Performance assumptions based on full simulation for an upgraded ATLAS detector at a High-Luminosity LHC*, . https://cds.cern.ch/record/1604420. 181

[85] ATLAS Collaboration, *Expected performance of missing transverse momentum reconstruction for the ATLAS detector at $\sqrt{s} = 13$ TeV*, . https://cds.cern.ch/record/2037700. 181

[86] ATLAS Collaboration, *Calibration of the performance of b-tagging for c and light-flavour jets in the 2012 ATLAS data*, ATLAS-CONF-2014-046. http://cds.cern.ch/record/1741020. 182, 183

[87] ATLAS Collaboration, G. Aad et al., *Search for massive, long-lived particles using multitrack displaced vertices or displaced lepton pairs in pp collisions at $\sqrt{s}$ = 8 TeV with the ATLAS detector*, arXiv:1504.05162 [hep-ex]. 187

[88] ATLAS Collaboration, *Measurements of Higgs boson production and couplings in the four-lepton channel in pp collisions at center-of-mass energies of 7 and 8 TeV with the ATLAS detector*, Phys. Rev. D **91** (2015) 012006, arXiv:1408.5191 [hep-ph]. 187, 189

[89] ATLAS Collaboration, *Projections for measurements of Higgs boson signal strengths and coupling parameters with the ATLAS detector at the HL-LHC*, . https://cds.cern.ch/record/1956710. 189

[90] S. Gangal and F. J. Tackmann, *Next-to-leading-order uncertainties in Higgs+2 jets from gluon fusion*, Phys. Rev. **D87** (2013) no. 9, 093008, arXiv:1302.5437 [hep-ph]. 190

[91] ATLAS Collaboration, G. Aad et al., *Observation and measurement of Higgs boson decays to WW^* with the ATLAS detector*, Phys. Rev. **D92** (2015) no. 1, 012006, arXiv:1412.2641 [hep-ex]. 192

[92] ATLAS Collaboration, *Evidence for Electroweak Production of $W^{\pm}W^{\pm}jj$ in pp collisions at $\sqrt{8}$ TeV with the ATLAS detector*, Phys. Rev. Lett. **113** (2014) 141803, arXiv:1405.6241 [hep-ph]. 195, 196

[93] ATLAS Collaboration, *Search for direct pair production of a chargino and a neutralino decaying to the 125 GeV Higgs boson in $\sqrt{s}$ = 8 TeV pp collisions with the ATLAS detector*, Eur. Phys. J. C **75** (2015) 208, arXiv:1501.07110 [hep-ph]. 199

[94] D. Tovey, *On measuring the masses of pair-produced semi-invisibly decaying particles at hadron colliders*, JHEP **04** (2008) 034, arXiv:0802.2879 [hep-ph]. 199

[95] ATLAS Collaboration, *Prospect for a search for direct pair production of a chargino and a neutralino decaying via a W boson and the lightest Higgs boson in final states with one lepton, two b-jets and missing transverse momentum at the high luminosity LHC with the ATLAS Detector*, . https://cds.cern.ch/record/2038565. 199

[96] ATLAS Collaboration, *Search for Higgs boson pair production in the $b\bar{b}b\bar{b}$ final state from pp collisions at $\sqrt{s} = 8$ TeV with the ATLAS detector*, arXiv:1506.00285. 200